DET NATURVIDENSKABELIGE FAKULTET
KØBENHAVNS UNIVERSITET

Production and Interrogation of Metastable Magnesium Atoms: Towards an Atomic Clock

by

Brian Bak Jensen

Thesis submitted in partial fulfilment
of the requirements for the degree of
Doctor of Philosophy

The Niels Bohr Institute
University of Copenhagen

2009

Preface

The following thesis describes the work I have performed during my Ph.d. study at the Niels Bohr Institute at the Copenhagen University. First of all I would like to acknowledge the finanical support from the Lundbeck Foundation. It is to me remarkable that a danish company can and are willing to support fundamental research. The labs I worked in is lead by Jan. W. Thomsen. At the beginning of my stay with the group we were told by the university that we were to move the labs. The supposed relocating of the labs were delayed severral times. This has required us to make several changes to the equipment like mounting optics on breadboards for easy movement of the setup. Here at the end of my Ph.d it is still unclear if we are to move or not. The infrastructure was not the only problems to overcome that had little to do with physics.

All these problems have required creative solutions and taught me a great deal. These problems have forced us to find creative ways to solve problems which I am sure will help me in future situations.

Though the lab required a lot of work I have found time to spend with the family. I also enjoyed the time I spend on Badminton, Football, and Battlefield with my fellow colleges. A lot of the time I worked in the lab my fellow Ph.d student Kasper T. Therkildsen was there as we overcame problems of all kinds. Kjeld Jensen provided with a lot of technical assistance during my stay at the lab. I am also thankful to Anders Brush who helped in the lab as well as helping me with this thesis.

Contents

Publications

The following publications were produced during this ph.d. and can be seen on the following pages.

- Measurement of the Spin-forbidden Decay rate $(3s3d)^1D_2 \rightarrow (3s3p)^3P_{2,1}$ in ^{24}Mg
  K. T. Therkildsen, B. B. Jensen, C. P. Ryder, N. Malossi, and J. W. Thomsen
  Phys. Rev. A **79**, 034501 (2009).

- Measurement of the 3s3p $^3P_1$ lifetime in magnesium using a magneto-optical trap
  P. L. Hansen, K. T. Therkildsen, N. Malossi, B. B. Jensen, E. D. van Ooijen, A. Brusch, J. H. Müller, J. Hald, and J. W. Thomsen
  Physical Review A **77**, 062502 (2008).

- Amplification and ASE suppression in a polarization-maintaining ytterbium-doped all-solid photonic bandgap fibre
  C. B. Olausson, C. I. Falk, J. K. Lyngsø, B. B. Jensen, K. T. Therkildsen, J. W. Thomsen, K. P. Hansen, A. Bjarklev and J. Broeng
  Optics Express **16**, 13657 (2008).

- Metastable Magnesium fluorescence spectroscopy using a frequency-stabilized 517 nm laser
  Ming He, Brian Bak Jensen, Kasper T. Therkildsen, Anders Brusch, Jan W. Thomsen
  Optics Express, Vol. 17 Issue 9, pp.7682-7687 (2009).

- Isotope shifts of the (3s3p)3P0,1,2-(3s4s)3S1 Mg I transitions
  Ming He, Kasper T. Therkildsen, Brian B. Jensen, Anders Brusch, Jan W. Thomsen, and Sergey G. Porsev
  Phys. Rev. A 80, 024501 (2009)

- Iodine spectroscopy based on metastable Mg I spectroscopy of (3s3p) 3P - (3s4s) 3S transitions
  Ming He, Brian B. Jensen, Anders Brusch, Kasper T. Therkildsen, and Jan W. Thomsen
  Submitted to Optics Express (2009).

- Experimental determination of the ^{24}Mg I (3s3p)3P2 lifetime B. B. Jensen, He Ming, K. Gunnarsson, M. H. Madsen, A. Brusch, J. Hald, and J. W. Thomsen
  Pending submission PRL (2009)

CHAPTER 1

Introduction

For many years atomic and molecular transitions have been studied and with the invention of laser sources has accelerated these studies. These studies gives the possibility to test theoretical models of atoms and molecules. The hydrogen atom with a single electron orbiting the nucleus is the simplest atom to model and has therefore been studied in great detail. The alkali elements Li, Na, K, Cs and Ra can be considered one electron systems as they have one electron orbiting closed shells. They all have strong transitions and are popular for laser cooling as their wavelengths are easily accessible. A complication arises when doing more detailed spectroscopy of the alkali atoms. Due to the nuclear spin the atom often have hyperfine splitting of the levels. These systems will thus not offer a that can easily be modeled. When studying quantum mechanics several levels will quickly make calculations complicated or impossible to solve analytically. This has raised interest in the second group of elements in the periodic table, The alkaline earth elements, which have two electrons in the outer shell. All of the bosonic isotopes of the alkaline earth elements have zero nuclear spin I = 0 [1] which means the states have no hyperfine splitting. For example magnesium has no fine J = 0 and hyperfine splitting of the ground state, ie, F = 0. For magnesium the $^1S_0$, $^1P_1$ and $^1D_2$ is in a ladder system and the $^1D_2$ level has the highest energy. Atoms in the $^1D_2$ state are able to decay to the $^3P_{0,1,2}$ states. For some of the other alkaline earth elements the $^1D_2$ state is below the $^1P_1$ state

which cause atoms to decay our of the main cooling cycle ($^1S_0$ - $^1P_1$).

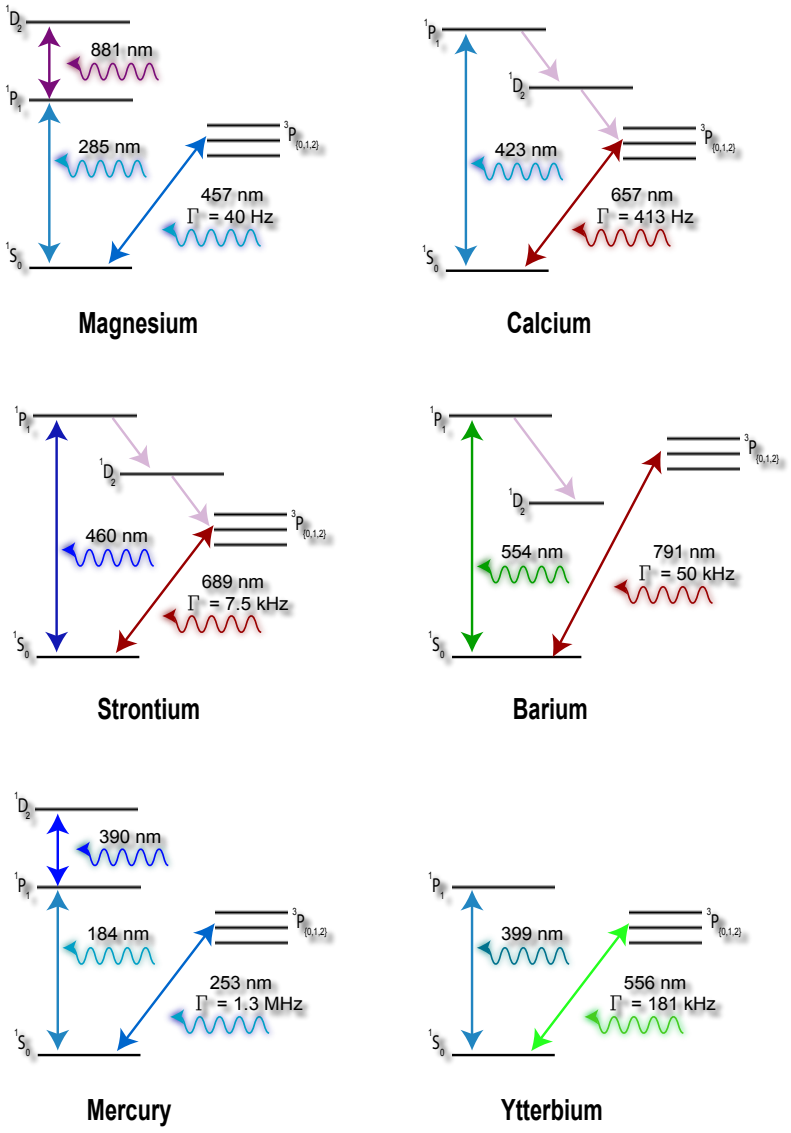

Figure 1.1: *The level diagram of the Alkaline Earth element Mg, Ca, Sr, Ba and the two alkaline earth like elements Yb and Hg. For each element the Einstein coefficient of the intercombination line is shown.*

Not only does the alkaline earth elements have simpler energy levels from the ground state but the two electrons also give rise to strong singlet-singlet and triplet-triplet transitions. In figure 1.1 the strong transitions between the $^1S_0$ and the $^1P_1$ state are shown. For decreasing atomic number, Z, the main transition decreases in wavelength. Contrary to the alkali elements there are few lasers capable of lasing at the wavelengths needed to drive the main transitions in the alkaline earth elements. In order to generate light for many of the transitions seen in figure 1.1, frequency doubling is required for these elements. Since the Einstein coefficient is proportional to $1/\lambda^3$, higher intensities are also required in order to saturate the transition. For some of the UV wavelengths seen in figure 1.1 there is also significant absorption through glass, air and coatings.

The weak transitions are of particular interest in high resolution spectroscopy such as atomic clocks [2], [3], [4], [5], [6], [7], [8]. As seen in figure 1.1 all the singlet-triplet transitions displayed are all at optical wavelengths and the intercombination line of magnesium has the weakest transition of the displayed alkaline earth elements.

Currently there are several groups working with ultra cold alkaline earth atoms. The different energy levels of the alkaline earth elements are shown in figure 1.1. Beryllium has not been laser cooled and no groups are working toward a clock based on Be. Two groups are working with magnesium toward an optical atomic clock. Calcium has three groups with realized atomic clocks. Strontium based atomic clocks has been realized and ten groups are currently pursuing strontium. Due to the level structure of barium none of the transitions from the ground state are closed transitions which means it is difficult to laser cool. Radium has been laser cooled but all Rn isotopes are radioactive [9].

We have chosen to work toward a optical atomic clock based on magnesium because it has some of the longest lived atomic states. Furthermore the insensitivity to black body radiation makes it promising for a high accuracy clock. The work described in this thesis is based on the 3 isotopes of magnesium atoms (^{24}Mg,^{25}Mg and ^{26}Mg) with the natural abundances 78%, 10% and 11% respectively [10].

1.1 Magnesium as a candidate for an optical atomic clock

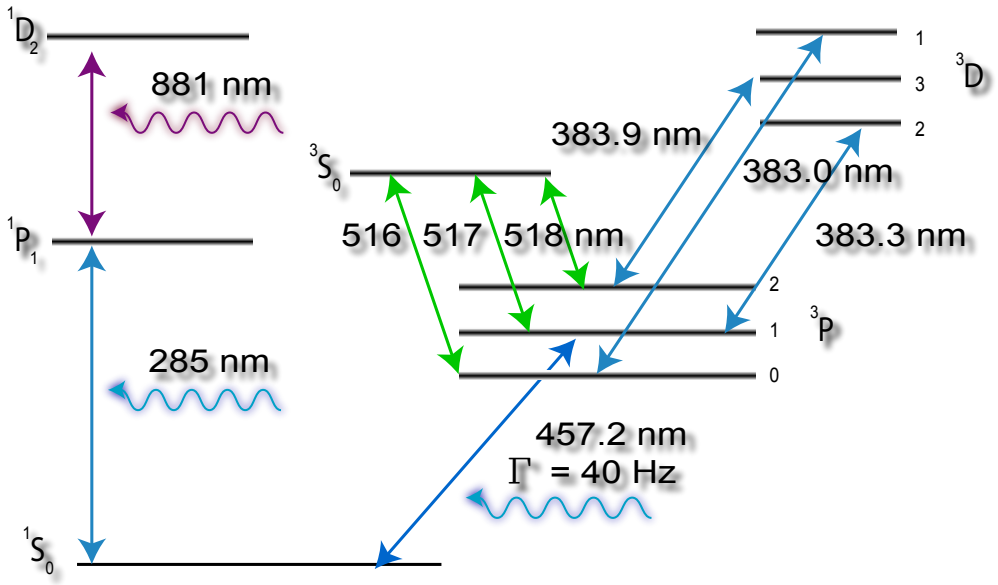

Figure 1.2: *The level diagram of magnesium. The singlet states are on the left and the triplet states are to the right.*

Laser cooling of neutral atoms was first suggested by Hänsch and Schawlow [11]. The alkaline earth elements (Be, Mg, Ca, Sr, Ba, Ra) are of particular interest to us because of the level structure, see Figure 1.2. Since magnesium is a two electron system, the level structure is divided into singlet and triplet states. Transitions between a singlet state and a triplet state requires a spin-flip to occur and as a consequence has lower decay rates [12]. These transitions open up for the possibility to do high precision measurements like that used in atomic clocks [13], [14], [15].

The strong electric dipole transition between the singlet states $(3s^2)^1S_0$ and $(3s3p)^1P_1$ with a linewidth of 79 MHz allows for laser cooling and with almost no leaks to other states it is nearly a ideal two level system. In contrast the intercombination line, which is a transition between the singlet

state $(3s^2)^1S_0$ and the triplet $(3s3p)^3P_1$ state, has a linewidth of 40 Hz.

In order to do spectroscopy on magnesium it is possible to use a gas cell containing magnesium vapor or use an effusive oven and probe the beam of magnesium escaping the oven. The advantage of probing a thermal beam is the reduced doppler effect when probing transversely to the propagating direction of the atomic beam. There are, however, a few limitations. An atomic beam can be collimated but there will most often be a transverse doppler broadening larger then the natural linewidth of the transitions being probed. If the atomic beam is collimated or cooled in the transverse plane it is possible to reduce the doppler effect. Even if the doppler effect was negligible it would still be almost impossible to obtain resolutions comparable to the natural linewidth of the intercombination line of 40 Hz. This is because of the limited time the atom stays in the interaction region with the optical beam. The interaction time, τ put a limit on the resolution given roughly by FWHM$\sim 1/\tau$ depending on the exact beam profile. A probe beam with a interaction zone of 1 m will give a transition broadening of about 1 kHz.

There are advantages to a beamline, like the large signal from many atoms passing through the interaction region. This is especially the case when the transition being probed is not a closed transition as the transit time is in the order of μs and the lifetime typically ns which would allow for thousands of cycles. We realized a beamline generating a beam of metastable magnesium atoms. The beamline was used for carrying out spectroscopy on the metastable states as well as provide us with a frequency reference for more recent experiments, see chapter 4.

In 1987 the first MOT was realized [16] allowing for cooling and trapping of neutral atoms. One of the huge advantages of a cold sample of atoms compared to the beamline is the reduction of the doppler effect by many orders of magnitude. This reduced doppler effect open up for the possibility to do high precision spectroscopy. Laser cooling has resulted in a breakthrough for the measurement of frequency and time with untold precision [17], [18], [19], [20]. A myriad of new cooling techniques were discovered and explained (for a review see e.g. [21], [22], [23], [24], [25], [26], [27]).The development of atomic clocks followed and with that the ongoing quest for

higher precision clocks. High precision spectroscopy also allows for new measurements of physical properties such as cold collisions [28], [29], [12], molecular photo-association [30] [31] [32], atomic dipole moments [33] [34], high precision spectroscopy [35] and theory of laser cooling [36]. The measurement of the exact lifetimes of the atomic states allows theoretical models to be improved. In chapter 5 I describe how a cold sample of metastable magnesium was realized and properties such as the long lifetime was measured. The measurement of the $(3s3p)^3P_2$ lifetime was realized by utilizing our UV MOT setup. This amazing technique of laser cooling allows atoms to be trapped and confined for long periods of time allowing interrogation times of seconds without significant doppler broadening [36]. One of the longest measured atomic lifetimes ever measured is presented in section 5.4. The atoms were confined in the magnetic trap and allows a sample of metastable magnesium to be trapped. In the experiment atoms decaying are observed directly and the measured lifetime was found to be $1914 \pm 40 \pm 191$ seconds. The statistical error of ± 40 seconds could be reduced further, however, the accuracy is limited by the systematic error of ± 191 seconds. The $(3s3p)^3P_0$ state has a even lower decay rate back to the ground state which was not measured here as we are unable to confine the atoms. Magnesium also have promising features such as a weak sensitivity to black body radiation making it a promising candidate for high precision atomic clocks, see section 2.2.

For magnesium one of the biggest challenges is the lack of suitable transitions that allows laser cooling down to μK temperatures. The lowest temperatures reached with laser cooling in magnesium is about 4 mK using the $(3s^1)^1S_0$ - $(3s3p)^1P_1$ transition which is above the theoretical doppler temperature of 2 mK. The intercombination line with a linewidth of 40 Hz will have a very small maximum light force corresponding to a acceleration of ~ 2.7 m/s^2. This imply a capture velocity of a 457 nm MOT would be about 0.2 m/s. Unlike Sr, where the light forces on the intercombination line is just strong enough to hold the atoms against gravity, they would not be confined for magnesium. One option that remains is trapping the magnesium atoms in a dipole trap and cool them using the intercombination line. At the moment the lack of good cooling transitions from the ground state and the subsequent

high temperature obtained for magnesium is one of the biggest problems we face. Some of the transitions from the metastable states are quite promising for laser cooling down to μK temperatures and are described in more details.

1.2 Outline of Thesis

Chapter 2 contains a brief summary of the physics behind the transitions, Black Body Radiation, and laser cooling.

Chapter 3 gives a description of the laser systems used in the experiments.

Chapter 4 contains the first experimental setup of the beamline and the experiments performed with it.

Chapter 5 describe the UV MOT setup and the experiments that was performed on the UV MOT.

Chapter 6 describes the work done on cooling metastable magnesium on the triplet-triplet transitions.

Chapter 7 contains the conclusion and outline.

CHAPTER 2

Properties of Alkaline Earth Elements

Alkaline earth elements consisting of group two in the periodic table Are two level atoms. The alkaline earth like elements such as Yb and Hg with two electrons inthe outer shell can also be considered two electron systems. Such systems can be considered two electron system similar to Helium. The two outer electrons leads to a splitting of the energy levels into singlet and triplet states.

2.1 Transitions and selection rules

The interest in the 2 electron system is partly because of the transitions between the singlet and triplet states. These transitions are forbidden contrary to the dipole allowed transitions between singlets that are also present in magnesium. The presence of dipole forbidden and dipole allowed transitions from the ground state make two electron systems particularly interesting in high resolution spectroscopy. The reason for this is the possibility to laser cool the transition as well as probe the very narrow transitions from $(3s^2)^1S_0$, $m_j = 0$ to $(3s3p)^3P_{0,1,2}$ $m_j = 0$. I will give a brief summary of the physics behind the transitions and give examples of useful transitions in magnesium. Let us consider a two level atom with state $|\psi_a\rangle$ and $|\psi_b\rangle$. When such a atom is placed in a electromagnetic field it will evolve between state $|\psi_a\rangle$ and $|\psi_b\rangle$.

It is possible to study the time-dependent Shrödinger equation to solve the equation of motion for the system. When describing transitions between the two states we introduce the matrix element $M_a b$ given by

$$M_{ba} = \sum_{i}^{n} \langle \psi_b | \exp(-i\mathbf{k} \cdot \mathbf{r}_i) \hat{\epsilon} \cdot \Delta | \psi_a \rangle \tag{2.1}$$

where $\mathbf{k}$ is the propagation vector, $\hat{\epsilon}$ is the polarisation vector, and summed over the n electrons. This matrix element M_{ba} is used to describe the transitions between the state $|\psi_a\rangle$ and $|\psi_b\rangle$. In many cases of interest the matrix can be simplified by expanding the exponential $\exp(-i\mathbf{k} \cdot \mathbf{r})$ as

$$\exp(-i\mathbf{k} \cdot \mathbf{r}) = 1 + (-i\mathbf{k} \cdot \mathbf{r}) + \frac{1}{2!}(-i\mathbf{k} \cdot \mathbf{r})^2 + ... \tag{2.2}$$

Considering strong optical transitions, the atomic wave function extends in the order of a Ångstrøm, however, the electromagnetic field for optical transitions are on the order of thousands of Ångstrøm. In this case we can safely replace $\exp(-i\mathbf{k} \cdot \mathbf{r})$ with unity. This is called the electric dipole approximation [37]. The first term in 2.2 gives rise to the electric dipole moment which is by far the strongest. Due to properties of the wave functions not all entries of the matrix element M_{ab} are non-zero. For example the wavefunction can be shown to be even or odd when l is even or odd for the electric dipole. The electric dipole can therefore only connect states of opposite parity. By using similar properties this leads to selection rules for the different transitions. The selection rules for the first terms in the expansion can be seen in table 2.1. This include the first term describing the electric dipole moment (E1), the second term describing the magnetic dipole moment (M1), the third term describing the electric quadrupole moment (E2), and the last term shown here describing the magnetic quadrupole (M2).

As stated earlier magnesium has several interested transitions of the types

Electric dipole (E1) ("allowed")	Magnetic dipole (M1) ("forbidden")	Electric quadrupole (E2) ("forbidden")	Magnetic quadrupole (M2) ("forbidden")
ΔJ=0,$\pm$1 (except 0$\leftrightarrow$0)	ΔJ=0,$\pm$1 (except 0$\leftrightarrow$0)	ΔJ=0,$\pm$1,$\pm$2 (except 0$\leftrightarrow$0)	ΔJ=0,$\pm$1,$\pm$2 (except 0$\leftrightarrow$0)
ΔM=0,$\pm$1 (except 0$\leftrightarrow$0 when ΔJ=0)	ΔM=0,$\pm$1 (except 0$\leftrightarrow$0) when ΔJ=0)	ΔM=0,$\pm$1,$\pm$2	ΔM=0,$\pm$1,$\pm$2
Parity change	No parity change	No parity change	Parity change
	for LS coupling only $\Delta S = 0$		
One electron jumping, with ΔL=$\pm$1, Δn arbitrary	No change in electron configuration;i.e., for all electrons ΔL=0, Δn=0	No change in electron configuration;or one electron jumping with ΔL=0, Δn arbitrary	One electron jumping, with ΔL=$\pm$1, Δn arbitrary

Table 2.1: *Different types of electric and magnetic transitions between two states. The first four terms from the exponential expansion 2.2 is shown here*

stated in table 2.1. The 285 nm transition is a very strong electric dipole transition with a linewidth of 79 MHz the scattering force from the transition can generate a light force corresponding to a acceleration of 10^7 m/s^2 for magnesium atoms. This allows us to capture a sufficient number of atoms directly from a thermal beam rather then slowing the atoms before capturing the atoms in a MOT. The capture velocity of the 285 nm MOT is about 50 m/s. Other electric dipole transitions like the 383 nm and 517 nm are equally suitable for cooling atoms in a MOT, see figure 1.2. Some of the more interested transitions are the transition from the ground state to the metastable states. The transition from the $(3s^2)^1S_0$ state to the $(3s3p)^3P_2$ state is a magnetic quadrupole (M2) transition. It is dipole forbidden because of ΔJ = +2. With a $\Delta L = \pm 1$ the Magnetic dipole (M1) and Electric quadrupole (M1) terms vanish as well.This means the most likely transition

of the remaining terms in the multipole expansion is the magnetic quadrupole (M2) transition. It also requires a low probability spin flip to occur with $\Delta S = \pm 1$.This gives the transition a linewidth of 80 μHz corresponding to a lifetime of about 2000 seconds which in atomic physics is quite a long time. In fact the $(3s3p)^3P_2$ state is one of the longest lived states with the M2 transition back to the ground state being the most probable decay channel. The measurement of the lifetime of the $(3s3p)^3P_2$ state is described in section 5.4.

The intercombination line from the $(3s^2)^1S_0$ ground state to the $(3s3p)^3P_1$ state is an allowed dipole transition however with $\Delta S = \pm 1$ it violates the LS coupling [38]. With a $\Delta S = \pm 1$ it is a semi-forbidden intermediate transition with a 40 Hz linewidth or a corresponding lifetime of about 4 ms [38].

2.2 Black Body Radiation

As seen in the previous section the transitions between states can have various probabilities of being excited by electromagnetic radiation. The transitions need not be excited by radiation from a laser but can also be excited by the presence of black body radiation from the surroundings [39]. This has implications when performing experiments in the laboratory when for example measuring on weak transitions. The very long lived metastable states can be optically pumped down to the ground state as the decay rate for the metastable states is extremely low. For a black body radiator the spectral energy density is given by planck's formula

$$\rho(\nu, T)d\nu = \frac{8\pi h\nu^3}{c^3}\frac{1}{e^{\frac{h\nu}{k_B T}} - 1}d\nu \tag{2.3}$$

The intensity of the radiation at the optical wavelengths is extremely low as can be seen in the plot of equation 2.3 in figure 2.1.

The BBR will not only cause optical pumping but it can also shift the

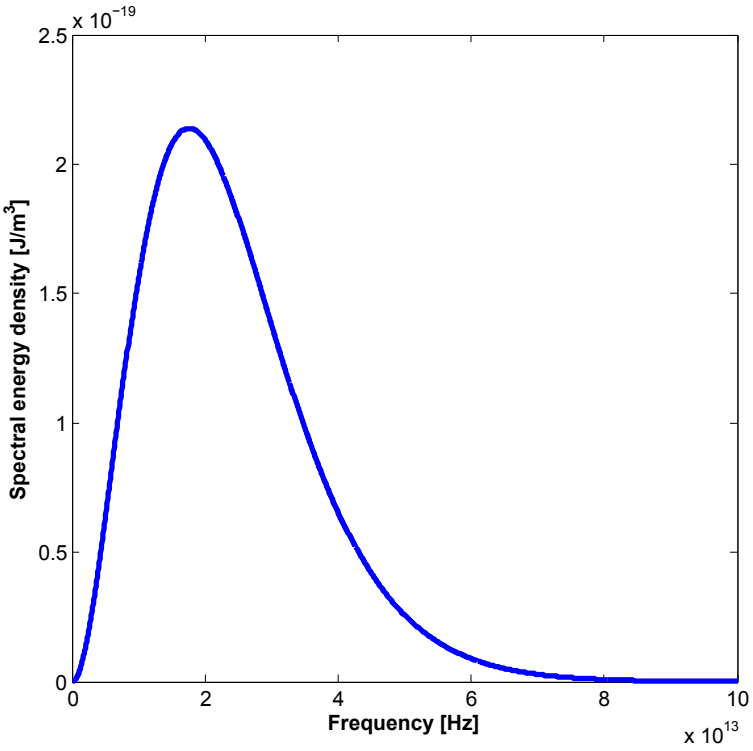

Figure 2.1: *The spectral energy density from at black body radiator at $T = 300$ K. The frequency of the 517 nm light and the 383 nm light is at $5.8 \cdot 10^{14}$ Hz and $7.8 \cdot 10^{14}$ Hz respectively.*

frequency of transitions. This is because of the AC Stark shift on atoms in a oscillating electromagnetic field. For an atom without a permanent dipole moment the shift of the m'th level is given by $\Delta E = \sum_n \frac{|\langle m|\vec{d}|n\rangle|^2}{E_m - E_n} \mathrm{E}^2$. This shift is the second order perturbation of the m'th level summed over the states n. The BBR shift therefore depends on the average squared amplitude of the electric field. The averaged squared amplitude of the electric field is found by integrating oven all frequencies

$$\langle E^2(t)\rangle = \frac{1}{\epsilon_0}\int_0^\infty \rho(\nu, T)d\nu \tag{2.4}$$

By inserting equation 2.3 into 2.5 this becomes

$$\langle E^2(t)\rangle = \frac{8\pi k^4 T^4}{\epsilon_0 c^3 h^3}\int_0^\infty \frac{\frac{h\nu}{kT}}{e^{\frac{h\nu}{kT}}-1} d\frac{h\nu}{kT} \tag{2.5}$$

$$= \frac{8\pi^5 k^4}{15 c^3 h^3 \epsilon_0} = \frac{4\sigma}{c\epsilon_0} T^4 \tag{2.6}$$

where I have used that $\int_0^\infty \frac{x^3}{e^x-1}dx = \pi^4/15$. The square amplitude electric field at T = 300 K is therefore $\langle E^2(t)\rangle = (832\ \mathrm{V/m})^2$. When doing high precision measurements on the clock transition this BBR shift leads to a systematic error given by the difference in shifts of the $^1S_0$ and $^3P_0$ state. This systematic error is shown for several alkaline earth elements in table 2.2. Magnesium has the lowest BBR shift of the elements listed in table 2.2 which makes it a interesting candidate for a improved accuracy atomic clock.

Atom	$\delta\nu_{BBR}$ (Hz)	ν_0 (Hz)	$\delta\nu_{BBR}/\nu_0$	Uncertainty
Mg	-0.258(7)	$6.55 \cdot 10^{14}$	$-3.9 \cdot 10^{-16}$	$1 \cdot 10^{-17}$
Ca	-1.171(17)	$4.54 \cdot 10^{14}$	$-2.6 \cdot 10^{-15}$	$4 \cdot 10^{-17}$
Sr	-2.354(32)	$4.29 \cdot 10^{14}$	$-5.5 \cdot 10^{-15}$	$7 \cdot 10^{-17}$
Yb	-1.34(13)	$5.18 \cdot 10^{14}$	$-2.6 \cdot 10^{-15}$	$3 \cdot 10^{-16}$

Table 2.2: *Black-body radiation shift for clock transitions between the lowest-energy $^3P_0$ and $^1S_0$ states in divalent atoms. $\delta\nu_{BBR}$ is the BBR shift at T = 300 K with our estimated uncertainties. ν_0 is the clock transition frequency, and $\delta\nu_{BBR}/\nu_0$ is the fractional contribution of the BBR shift. The last column lists fractional errors in the absolute transition frequencies induced by the uncertainties in the BBR shift. [39]*

2.3 Laser Cooling

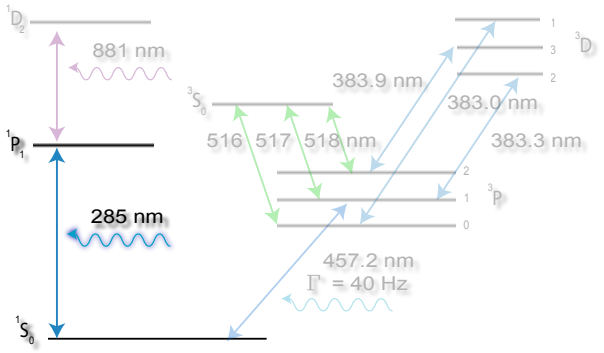

Figure 2.2: *A laser beam interacting with a two-level atom.*

In this section I will make a brief summary of laser cooling and give references to material for those unfamiliar with the theory. I will assume knowledge with the fundamental theory and it will not be described in details here.

I will consider a two level system with a single ground and excited state as seen in figure 2.2. The transition from the $(3s^2)^1S_0$ state to the $(3s3p)^1P_1$ states in magnesium can to a very good approximation be considered such a system. A laser beam that irradiates an atom has a probability to excite the transition given by:

$$\rho_{ee} = \frac{1}{2}\frac{s_0}{1+s_0+4\left(\frac{\delta-\bar{k}\cdot\bar{v}}{\Gamma}\right)^2} \tag{2.7}$$

where $s_0 = \mathrm{I}/\mathrm{I}_{sat}$ is the saturation parameter, δ is the detuning of the laser from the atomic resonance, k is the wavenumber, v is the velocity of the atoms relative to the laser source, and Γ is the linewidth of the transition. Now if the atom is moving toward a red detuned laser source the atom will see the light shifted toward the blue.

As the light is shifted toward the blue it will become closer to resonance

and there will be a increase in the scattering of photons. The scattering of photons lead to a momentum transfer. The force can then be written as $F = \frac{\Delta P}{\Delta T} = \hbar k \Gamma \rho_{ee}$ which combined with equation 2.7 can be written as

$$\langle \bar{F} \rangle = \frac{\hbar \bar{k} \Gamma}{2} \frac{s_0}{1 + s_0 + 4\left(\frac{\delta - \bar{k}\cdot\bar{v}}{\Gamma}\right)^2} \tag{2.8}$$

This force is the scattering force which can be used for slowing or cooling of atoms.

For two counterpropagating beams the force can be written as [22]

$$\begin{aligned} \langle \bar{F}_{total} \rangle &= \langle \bar{F}_+ \rangle + \langle \bar{F}_- \rangle \\ &= \frac{\hbar \bar{k} \Gamma}{2} \left(\frac{s_0}{1 + 2s_0 + 4\left(\frac{\delta - \bar{k}\cdot\bar{v}}{\Gamma}\right)^2} - \frac{s_0}{1 + 2s_0 + 4\left(\frac{\delta + \bar{k}\cdot\bar{v}}{\Gamma}\right)^2} \right) \\ &= \frac{\hbar \bar{k} \Gamma}{2} s_0 \frac{16\delta \frac{\bar{k}\cdot\bar{v}}{\Gamma^2}}{\left[1 + 2s_0 + 4\frac{\delta}{\Gamma^2} + 4\frac{\bar{k}\cdot\bar{v}}{\Gamma^2}\right]^2 - \left[8\delta \frac{\bar{k}\cdot\bar{v}}{\Gamma^2}\right]^2} \end{aligned} \tag{2.9}$$

For low velocities $v \ll \Gamma/k$ equation 2.9 can be written as

$$\langle \bar{F}_{total} \rangle \approx 8\hbar k^2 \frac{\delta}{\Gamma} \frac{s_0}{[1 + 2s_0 + (\frac{2\delta}{\Gamma})^2]^2} \bar{v} \equiv \alpha \bar{v} \tag{2.10}$$

and a plot of the resulting force can be seen in figure 2.3. For a red detuned laser ($\delta < 0$) one finds $\bar{F}_{om} = -\alpha \bar{v}$ which is a friction force. A region where the atoms experience such a force is called a optical molasse [40], [41]. Since the photons are quantized this give rise to brownian motion and heating of the atoms. The heating and the cooling of the atoms will reach a equilibrium temperature known as the doppler temperature given by $T_D = \hbar\Gamma/2k_B$ which for magnesium is 2 mK. The atoms in a molasse are not trapped in space and will diffuse over time. In order to create a central field which will confine the

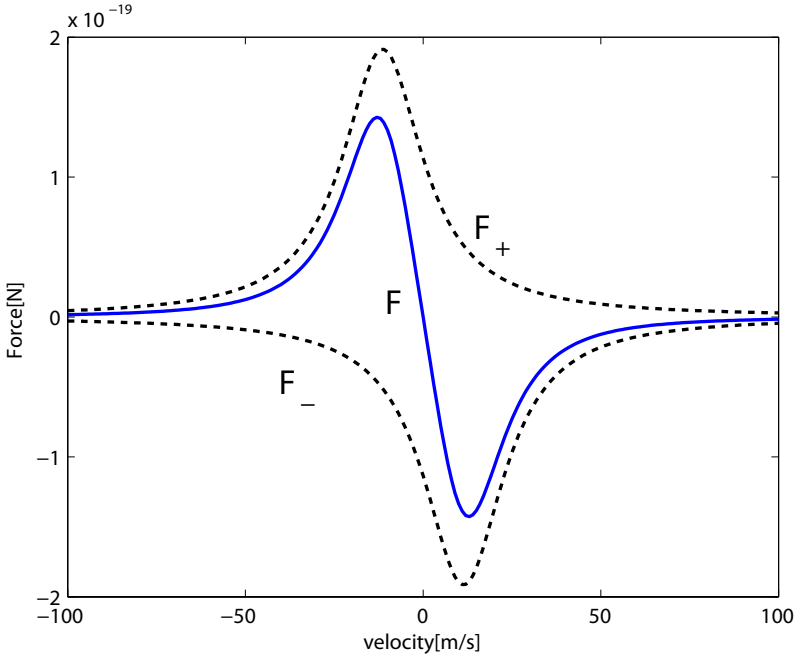

Figure 2.3: *Total force acting on an atom as function of the velocity for an optical molasses configuration together with the scattering forces created by the single laser beam.*

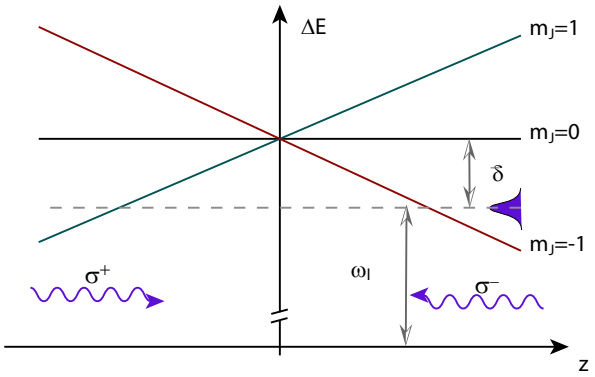

Figure 2.4: *Zeeman splitting as a function of spatial position. The Zeeman splitting depends linearly on the magnetic field, which is proportional to the distance from the center. For a negative detuning of the laserbeam, an atom positioned at $z > 0$ is pushed towards the center by the σ^--beam, while for $z < 0$ it is pushed towards the center by the σ^+-beam.*

atoms to a region in space a magnetic field and the polarization of the light is exploited. When combining the circular polarized light with a magnetic quadropole field this results in a mean force which has a spatial dependence. The spacial dependence is made in such a way that it becomes a central force. In figure 2.4 the 3 substates in $^3P_1$ is shown for magnesium and the magnetic field is choosen to be in the direction of the z-axis. The σ_- beam will become resonant with the $m_j = -1$ substate and the $m_j = -1$ substate will be shifted further away for z>0. This causes a net average force towards the center. Similar for atoms located at z<0 the atom will move close to resonance with the σ_+ light and there will be a net average force toward the center. If six laser beams are used a MOT can cool atoms down and confine them in a small region around B = 0.

For the MOT described above it is the light forces that confines the atoms near z = 0. Atoms can however also be trapped in the quadropole field without light forces. Atoms in a substate with a magnetic moment can either see a quadropole field as attractive or repulsive. For example metastable $^3P_2$ atoms in the $m_j = +1, +2$ substates are low field seekers and they will see a attractive potential in the center of a magnetic quadropole field. High field seekers are not possible to trap in a dc magnetic field.

CHAPTER 3

Laser systems

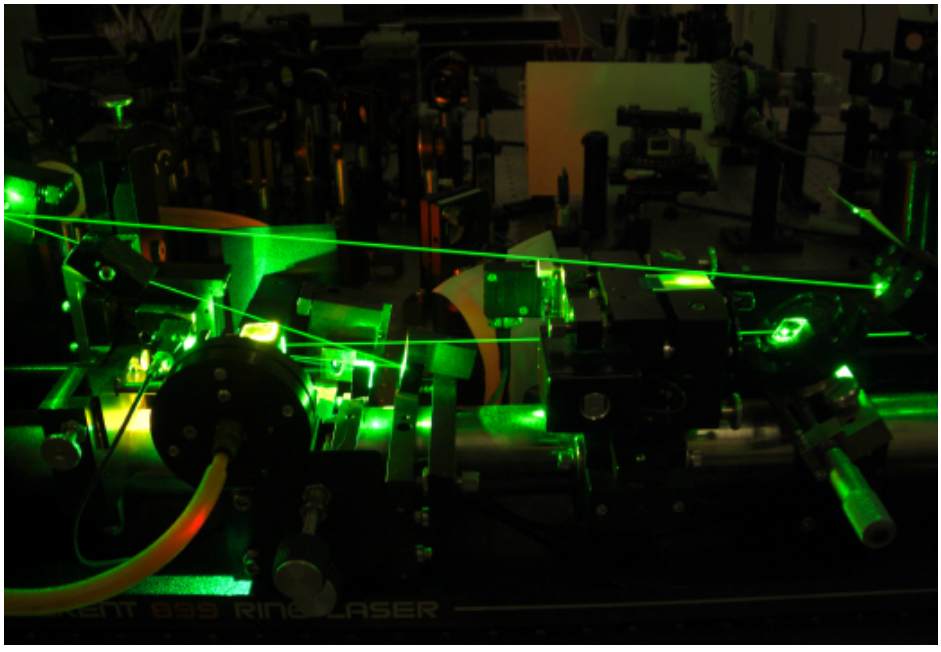

Figure 3.1: *The Coherent dye laser currently used in laser cooling magnesium atoms.*

During my stay at the Niels Bohr Institute I have worked with a lot of different laser systems. Familiarizing myself with the different types of lasers and studying the laser action in these systems is something that continues to fascinate me. It is the laser systems that take up most of our time when

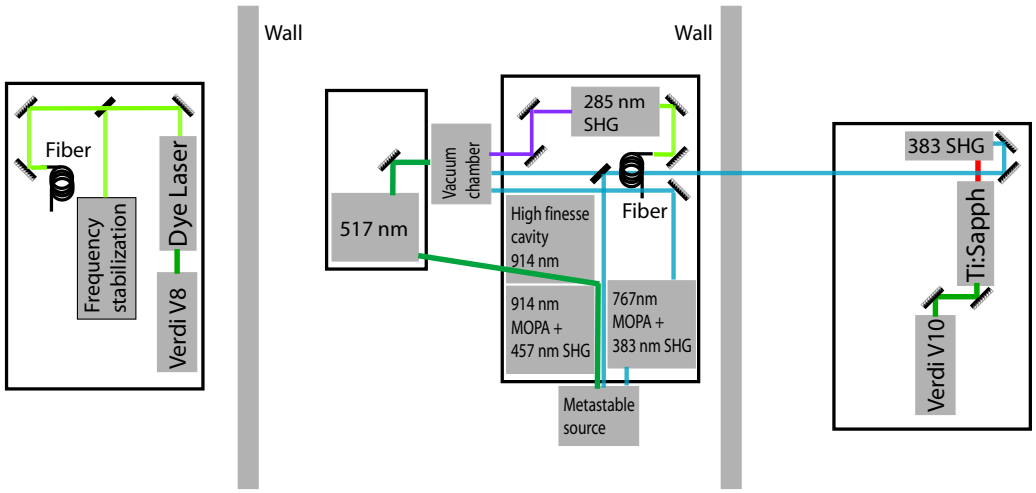

Figure 3.2: *The laser systems are located in three labs next to each other. The MOT chamber is located in the middle lab with the computers used to control the experiment. The lab on the right contain the beamline with one of the 383 nm lasers.*

working in the lab in order to get data from the experiments. Due to the number of Second Harmonic Generation (SHG) cavities used to run the experiment it is a challenge to get all of the different systems running at the same time.

In this section I will go through the various lasers I have worked with though some of them have been build before I came to the lab. For example the Dye laser is more then 20 years old and thus several people have worked with it over the years. Lately my fellow ph.d student Kasper T. Therkildsen worked with this laser and SHG cavity in order to improve the stability of the UV light. The 383 nm light sources were originally build at Danish Fundamental Metrology (DFM) but they have gone through several changes and I have worked quite a bit with them. The 457 nm laser for the clock transition is also originally from DFM however both the master and slave oscillator have been replaced along with much of the locking scheme for the Ultra High Finesse (UHF) cavity. Many of the changes to the setup has been done by Anders Brusch in order to improve the stabilization of the laser to the UHF cavity. He is also currently working on measurements of the magic

wavelength using this laser.

The 880 nm laser is the latest laser setup in the lab. This laser system now replace the older Ti:sapphire that was used for exciting the $^1P_1$ - $^1D_2$ transition. I used the Ti:sapphire laser to measure the decay rates out of the $(3s3d)^1D_2$ state to the $(3s3p)^3P_{1,2}$ state before it was replaced. The Ti:sapphire laser is described briefly for generating 383 nm light.

These laser systems are used in the experiments described in chapter 4, 5, and 6. The lasers are located in 3 different labs located next to each other as seen in figure 3.2.

3.1 UV light generation at 285 nm from a frequency stabilized dye laser.

The laser sytem used for cooling neutral magnesium on the $^1S_0$ - $^1P_1$ transition at 285 nm is based on a dye laser that is frequency stabilized to an iodine line. The dye used in the laser is Rhodamin 6G that is being pumped at 532 nm. The pump laser is a Coherent 10 W Verdi laser that is typically operated at a output power of 5.9 W. The dye laser typically generates about 1.4 W of output power at 570 nm. We have estimated the linewidth of the laser to be less then 5 MHz using a Fabry-Perrot cavity which is well below the natural linewidth of the $^1S_0$ - $^1P_1$ transition of 79 MHz.

The laser is locked to the R(115)20-1 absorbtion line of $^{127}I_2$ molecule [42] by polarization dependent frequency stabilization [43]. For the iodine lock about 100 mW of light is taken from the main beam by inserting a glass plate, as seen in figure 3.3. The glass plate generates two reflections, one from each air-glass interface, that is used as a pump and probe beam for the iodine lock. The setup of the iodine lock can be seen in figure 3.4. The linearly polarized probe beam is sent through a vapor cell containing $^{127}I_2$ and afterward sent onto a photo detector. The iodine will cause a drop in intensity on the photo detector when the laser is oscillating near an absorption line. The line will however be Doppler broadened since the cell contains a hot gas of molecules

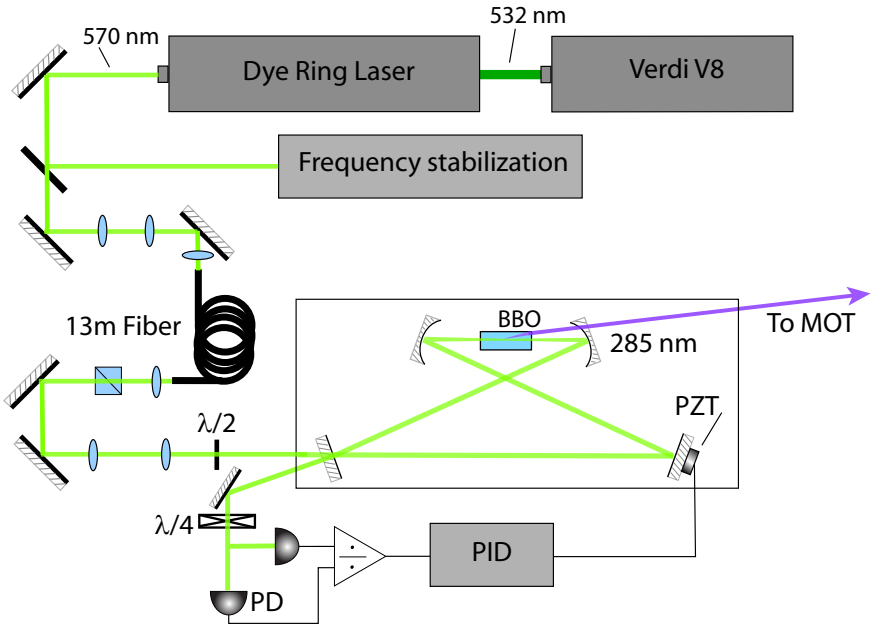

Figure 3.3: *Illustration of the 285 nm laser setup. A 532 nm diode laser pumps a dye ring laser to generate 570 nm light. A part of the beam is split off and sent to a frequency stabilization system. The other part is fiber coupled and sent to the frequency doubling cavity which is stabilized by a Hänsch-Couillaud scheme.*

with various velocities coaxial to the probe beam. In order to obtain a narrower structure the pump beam is sent counterpropagating to the probe beam. The presence of the pump beam can cause a depletion of a hyperfine level if the frequency, for a given velocity class, is on resonance with the absorption line. If the laser is resonant to a absorption line the pump and probe will be interacting with the same velocity class which is observable by a change in the intensity at the photo detector. This is caused by the change in the ground state population due to the presence of the pump beam. If the pump and probe beam both have the same frequency then the velocity class they both will be interacting with has V = 0. In order to increase the S/N ratio the polarization of the beams are exploited. The pump beam is changed to a circular polarization by inserting a $\lambda/4$ plate. Due to the

hyperfine splitting of the iodine transition this will cause a fast depletion of substates. When on resonance the pump beam will only induce transitions from m_K = -1 to m_K = 0 due to the atomic selection rules. The state m_K = -1 is therefore quickly depleted. The linear polarization of the probe is a superposition of left and righthanded polarizations with equal weights. When the light passes through the glass cell, only the σ_- is absorbed due to the optical pumping of the pump beam. In the linear basis, the polarization has a component in the horizontal plane which is then detected by the photodiode.

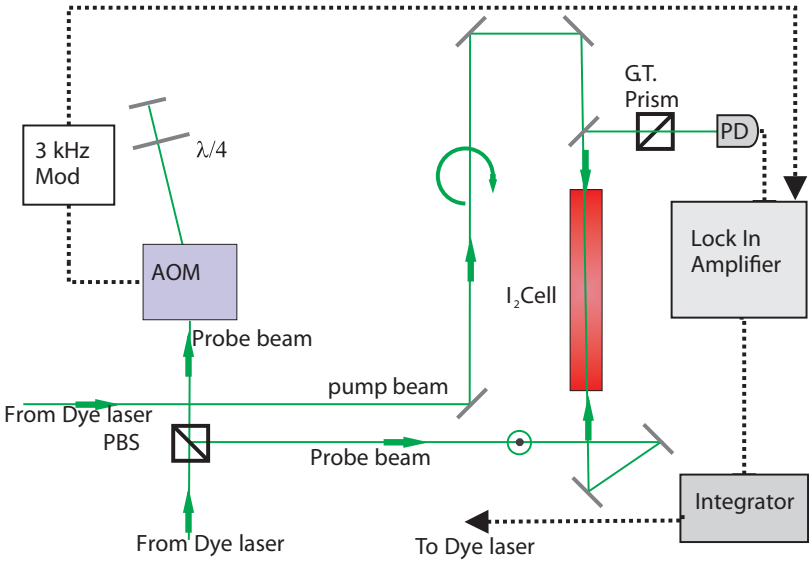

Figure 3.4: *Illustration of the polarization spectroscopy setup. The beam is split into two beams, pump and probe beam. The probe beam is double passed through an AOM and sent through a glass cell containing a gas of iodine. The horizontally polarized part of the probe beam is reflected on a beamsplitter and detected on a photodiode (PD). The pump beam is sent though the iodine glass cell.*

The main beam from the laser is sent into a optical fibre that guide the light into the lab next door that houses the main magnesium setup. The output fiber end is on a optical table with the Second Harmonic Generation (SHG) cavity containing a nonlinear β-BaB_2O_4 (BBO) crystal. The SHG cavity is a bowtie configuration where the light is coupled into the cavity through one of the two flat mirror [44]. The mirror used for coupling the

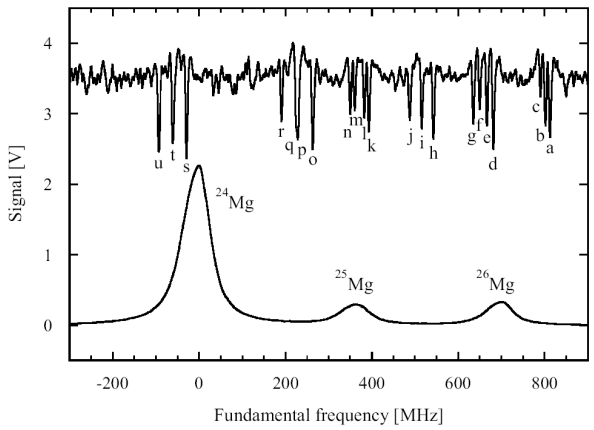

Figure 3.5: *Spectrum of iodine molecules together with the magnesium fluorescence as function of the fundamental frequency. The origin of the frequency axis is positioned at the maximum of the ^{24}Mg fluorescence [73].*

light into the cavity has a reflectance of about R = 97% in order to achieve impedance matching of the cavity. The cavity has two focal points. One is between the flat mirrors with a 150 μm waist. The second is between the curved mirrors with a 20 μm waist. The AR-coated BBO crystal is placed in the tight focus optimized to a crystal length of 5 mm which has a width and height of 3 mm by 3 mm. With about 700 mW light incident on the cavity the SHG cavity can generate about 50 mW UV light. The laser light from the dye laser is locked in frequency to the iodine lock and a cavity mode of the SHG cavity is locked to the laser frequency using a Hänsch-Couillaud locking scheme [45]. We use the Hänsch-Couillaud scheme because it requires simpler electronics then a Pound–Drever–Hall (PDH) locking scheme. The light from the SHG cavity is sent through a prism in order to separate the residual light at the fundamental frequency. Optics is also added after the SHG cavity to correct for the large walkoff of the BBO crystal. In order to switch the light on and off the UV beam is sent through a AOM driven at 200 MHz. The AOM not only shifts the frequency of the UV light but also acts as a spatial filter. The first order diffracted from the AOM is sent over to the MOT chamber while the other orders are blocked.

The estimated length of the SHG cavity is about 700 mm which gives it a Free Spectral Range (FSR) of 430 MHz. Such a small FSR cause the linewidth of a cavity mode to be $\Delta\nu = FSR/\mathfrak{F} = 6$ MHz. The laser frequency of the dye laser has been determined to have about 5 MHz linewidth by using a Fabry-pérot resonator. This means the fluctuations in laser frequency is comparable to the linewidth of a cavity mode. In order to avoid power fluctuations the laser linewidth should be much smaller then the cavity mode.

3.2 MOPA Laser System for UV light generation at 383 nm

For generation of light at 383 nm we currently have two laser systems. The first laser is a Master Oscillator Power Amplifier (MOPA) diode laser system shown in figure 3.6. The master laser is a diode laser set up in a Littrow configuration. The diode itself is a Eagleyard AR coated diode with a maximum output of 100 mW. The diode is typically run at 120 mA generation about 30 mW which extends the lifetime of the diode. The laser is kept running continuously for the duration of the lifetime estimated at about 10000 Hours. The laser output from the master is sent through a 40 dB isolator and then injected into a tapered diode amplifier. This amplifier is capable of generation up to 1.5 W output power at a current of 3 Amp. A second 40 dB isolator is placed after the amplifier in order to protect the laser system from feedback. It should be noted that during some of the experiments this isolation appeared not to be sufficient. The MOPA laser system is placed inside a plastic box in order to improve the stability of the frequency. The master diode laser and tapered diode amplifier is temperature stabilized to within a few mK.

The output of the MOPA laser was coupled into a second harmonic generation (SHG) cavity. The cavity is set up in a bowtie configuration with 2 curved mirrors and 2 flat mirrors. The curved mirrors have a focal length of

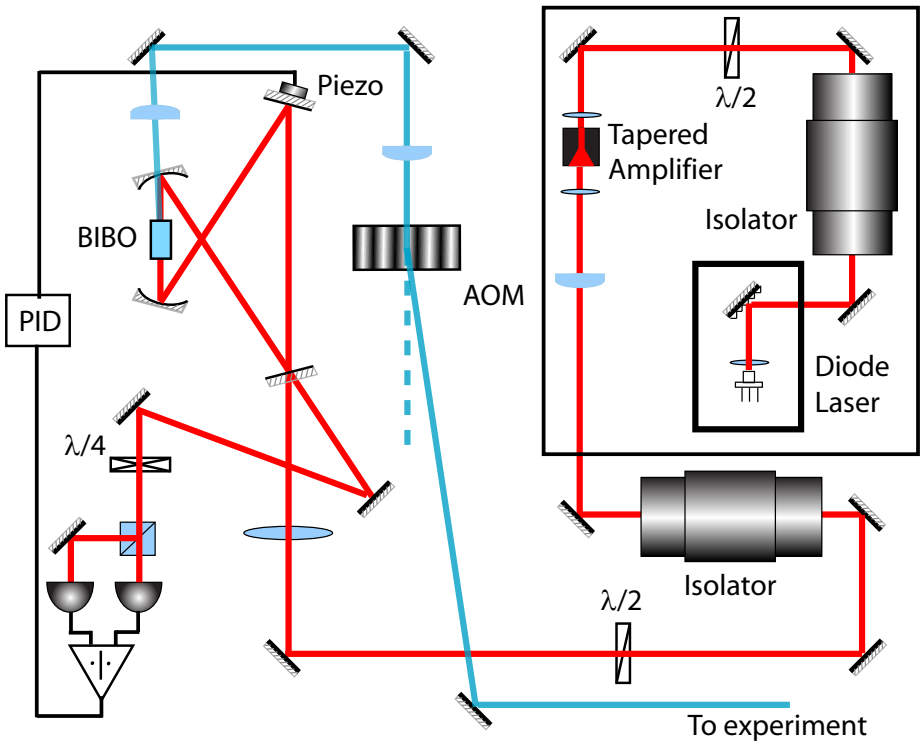

Figure 3.6: *Illustration of the 383 nm MOPA setup. The 766 nm beam is sent through an isolator to avoid feedback from the tapered amplifier. The output from the tapered amplifier passed another isolator before being coupled into the SHG cavity and up to 150 mW of 383 nm is generated. The beam reflected from the input coupling mirror is used for locking the length of the cavity using the Hänsch-Couillaud scheme.*

25 mm and the total length of the cavity is 215 mm giving it a FSR = 1.4 GHz. With a finesse of 100 this gives a linewidth of $\delta\nu \sim 14$ MHz which is much more then the laser linewidth. In this external enhancement cavity the laser frequency is frequency doubled using a AR-coated bismuth triborate crystal (BIBO, BiB_3O_6). The BiBO crystal has a higher nonlinearity then the lithium triborate (LBO) crystal however BIBO has what we believe to be thermal effects at high power [46]. A cavity mode is locked to the laser frequency by using a Hänsch-Couillaud locking scheme. For slow corrections of the laser frequency a error signal can be sent to the piezo controlling the grating position in the master laser. The bandwidth of the piezo driver is

up to 8 kHz and for fast correction to the frequency a signal can be sent to the diode current controller which has a bandwidth of 1 MHz. The typically generated 383 nm output is about 50 mW with a 600 mW IR power incident on the SHG cavity.

The second system used for generation 383 nm light is a Ti:Sapphire laser coupled into a similar cavity as the one described above. The pump laser used to excite the gain medium is a coherent 10W Verdi laser at 532 nm. The Ti:sapphire laser is difficult to get to operate due to a not so smart control box. The fast photodiodes that monitor the laser action have a 0.25 mm^2 active area making it very sensitive to alignment. A good feature is when it locks to the external cavity then the intrinsic linewidth of the laser is less then 100 KHz. Another useful feature is the tunability of the laser from 700 to 900 nm however this require the operator to change the mirrors. Normally a 600 mW output power can be obtained from the Ti:Sapphire laser.

When the 600 mW is coupled into the SHG cavity this typically generate about 50 mW of 383 nm light. The cavity is also a bowtie cavity with two curved mirrors having a radius of curvature of 25 mm. The reflectance of the input coupling mirror is 98%. The waist at the crystal position is about 20 μm and for coupling into the cavity the second waist is 200 μm. The larger secondary waist makes alignment of the laser more stable. The nonlinear crystal used in this setup is a 5 mm long brewster cut LBO crystal with a 3 mm by 3 mm aperture. The LBO crystal has a lower nonlinearity then the BIBO crystal however it has a lower walkoff and we have not observed any thermal effects in the crystal. The cavity is locked to the laser using a Hänsch-Couillaud locking scheme. Unfortunately using a brewster cut crystal is not the most alignment friendly setup as the crystal displaces the cavity beam. The daily alignment of the Ti:Sapphire and the associated beam steering when coupling into the SHG cavity makes this laser system quite challenging. The brewster cut crystal is optimized for the polarization of the fundamental frequency. Since the SHG generated light has the orthogonal polarization then this light is partly reflected internally in the crystal. The higher enhancement achieved for the fundamental frequency light is partly removed by the reduced transmission through the crystal of

the second harmonic light. For the experiments requiring only one source of 383 nm light the more reliable MOPA system was used.

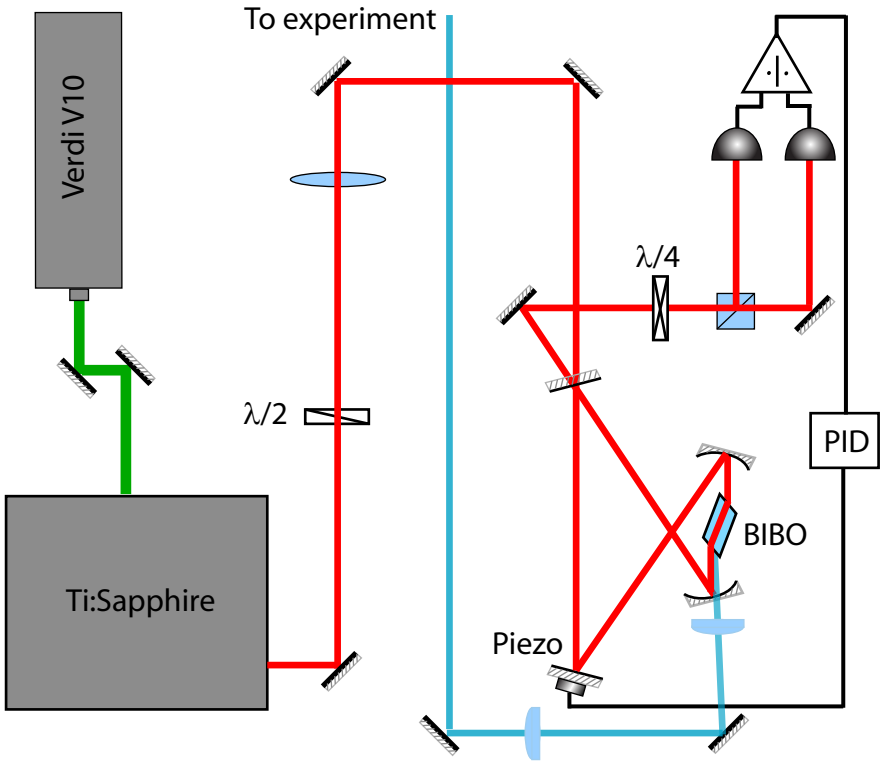

Figure 3.7: *Illustration of the 383 nm Ti:Sapphire setup. The output from the Ti:sapphire laser is coupled into the SHG cavity and up to 50 mW of 383 nm is generated using a Brewster cut BIBO crystal. The beam reflected from the input coupling mirror is used for stabilizing the length of the cavity using the Hänsch-Couillaud scheme.*

3.3 MOPA Laser System for blue light generation at 457 nm

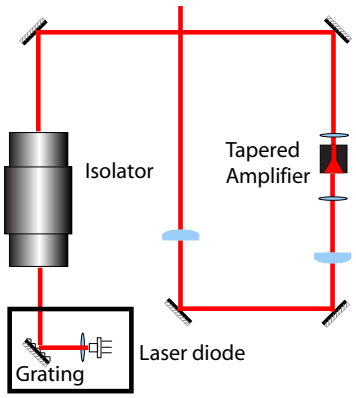

Figure 3.8: *Schematic of the MOPA setup with a master diode laser and a tapered amplifier.*

For probing the intercombination line we have a MOPA system at 914 nm that is frequency doubled to generate light at 457 nm. The MOPA system is shown in figure 3.8 and consist of a diode laser in a Littrow configuration. The power amplifier is a tapered diode amplifier that can boost a signal from 30 mW to 1 W. The grating mount has a piezo to make adjustments to the laser frequency. For high frequency modulation the current driver has a 1 MHz bandwidth modulating input.

The 914 nm laser system is placed inside a aluminium box that is acoustically isolated from the surroundings to avoid fluctuations in frequency. The MOPA and SHG cavity setup can be seen in figure 3.9. The output beam from the MOPA system is sent through a 60 dB isolator and then coupled into a fiber in order to ease daily alignment and improve the mode quality. The beam from the fiber is coupled into an external enhancement cavity containing a AR-coated potassium niobate crystal ($KNbO_3$) [46]. For SHG generation it is possible to obtain non-critical phase matching at a temperature of 143°. The $KNbO_3$ crystal is temperature stabilized in a small oven

consisting of copper for effective heat displacement and isolated using teflon. A thermistor records the temperature and electronics stabilize the temperature via a peltier element. In contrast to the 383 nm laser, where the SHG beam has walkoff, the SHG beam from the non-critical phasematched $KNbO_3$ has a nice gaussian profile. We typically generate an output power of about 50 mW at 457 nm. Similar to the SHG cavity of the 383 nm laser in section 3.2 the cavity generation 457 nm light uses a Hänsch-Couillaud locking scheme.

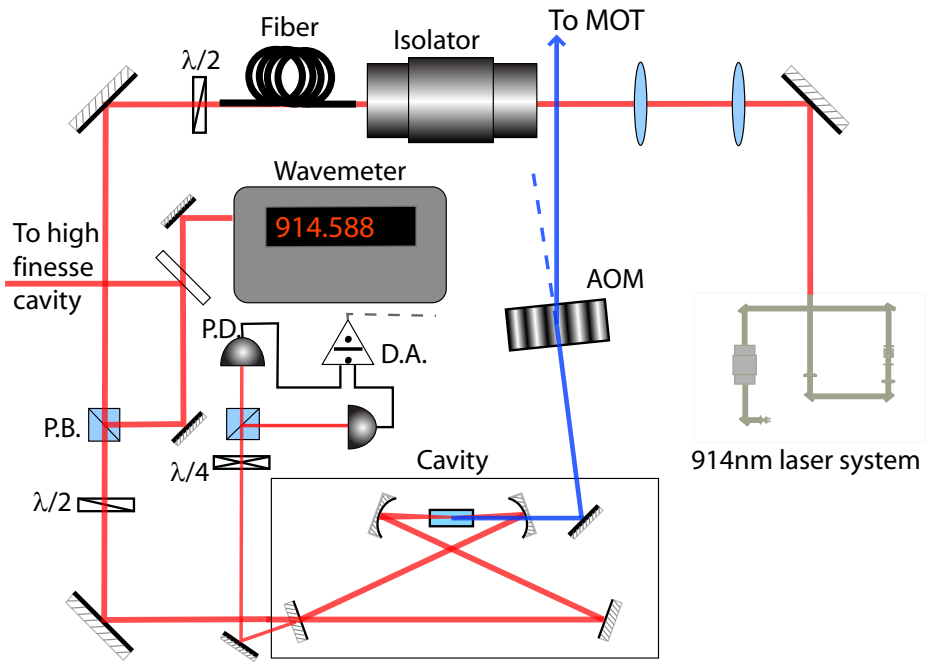

Figure 3.9: *Illustration of the 457 nm laser setup. The 914 nm beam is sent through an isolator to avoid feedback in the tapered amplifier and a fiber to clean the mode before coupling into the SHG cavity. A small part of the beam is reflected by a polarizing beam splitter cube and used for measuring the wavelength by a wave-meter and for stabilization to a high finesse cavity. The transmitted beam is injected into the SHG cavity. Typically 70 mW of 457 nm is generated. The beam reflected from the input coupler mirror is used for locking the length of the cavity using the Hänsch-Couillaud scheme.*

Before sending the blue light to the experiment it is sent through a AOM in order to switch the light on and off.

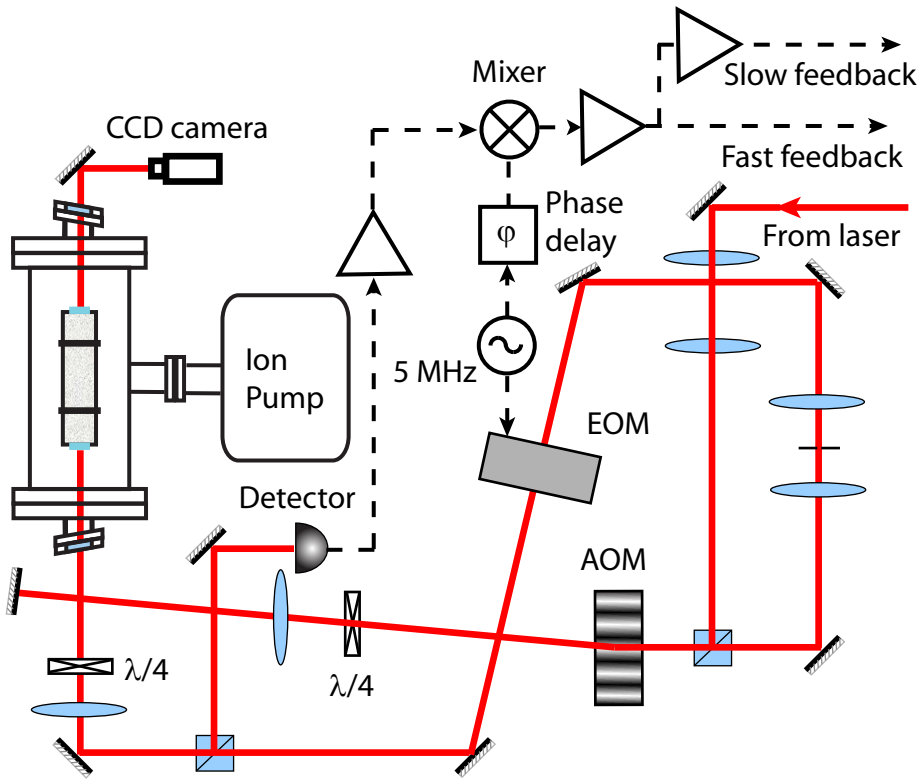

Figure 3.10: *Setup of the Pound–Drever–Hall (PDH) stabilization to a high finesse cavity. The 914 nm laser beam is double-passed through an AOM to have some frequency tunability with regards to the TEM_{00} mode of the high finesse cavity. Then the laser beam passes an electro optic modulator (EOM) which imprints 10 MHz frequency sidebands before being coupled into the high finesse cavity. The reflected light from the cavity is detected by a high bandwidth photodetector. The cavity error signal is phase-sensitively detected by the coherent mixing of the amplified photocurrent and the local oscillator signal (which drives the EOM) in a mixer. The loop filter provide additional gain, filtering and integration before sending the correction signal to the laser diode current and the piezo-mounted grating in the MOPA. The required dynamic range of the servo varies from the high frequency (700 kHz) to the low frequency region and therefore the signal is divided into two negative feedback loops. A slow feedback integrating loop to the grating PZT and a faster feedback loop applied to the laser diode current.*

The 457 nm laser is designed for probing the intercombination line. If spectroscopy is not to be limited by the linewidth of the laser, the laser needs

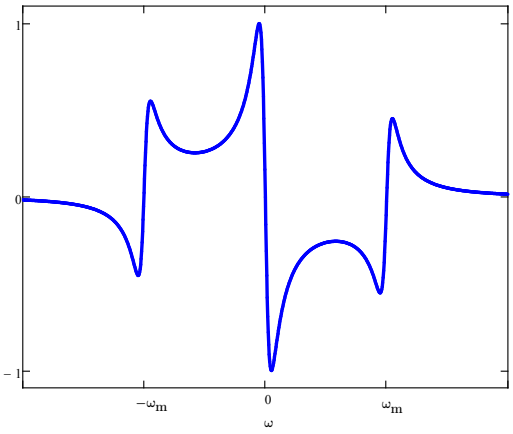

Figure 3.11: *Plot of the ideal PDH error signal.*

a linewidth smaller then the natural linewidth of the transition. In order to accomplish this we use a Pound–Drever–Hall (PDH) locking scheme [47] to lock the laser to a high finesse cavity as seen in figure 3.10. A small reflection of 914 nm light from the MOPA laser system in figure 3.9 is sent to the PDH lock. The beam is first double passed through a AOM driven at 200 - 300 MHz in order to tune the laser frequency to the exact frequency of a cavity mode. This is because the laser frequency is fixed to the frequency of the atomic transition being probed and since the ULE cavity length can not be varied the AOM is needed to cover 1 FSR. The beam from the AOM is thereafter sent through an EOM modulated at 10 MHz in order to generate the sidebands needed for the PDH lock. The beam is then sent onto the cavity in order to couple the light into a cavity mode. Because of the sidebands there will always be some reflected light off the cavity. The reflected light is counterpropagating to the incident light and in order to separate the reflected the beams we use a retarder plate and a polarization beamsplitter cube. The beam is then sent it onto a high bandwidth detector. The signal from the detector is sent through a double-balanced mixer where it is combined with the 10 MHz reference frequency provided by the local oscillator. The phase sensitive detection setup from the PDH lock generates an error signal similar to the one shown in figure 3.11 [48]. The resulting signal is integrated and

generate a fast output and a slow output that is then sent to the piezo and current driver to complete the PDH lock.

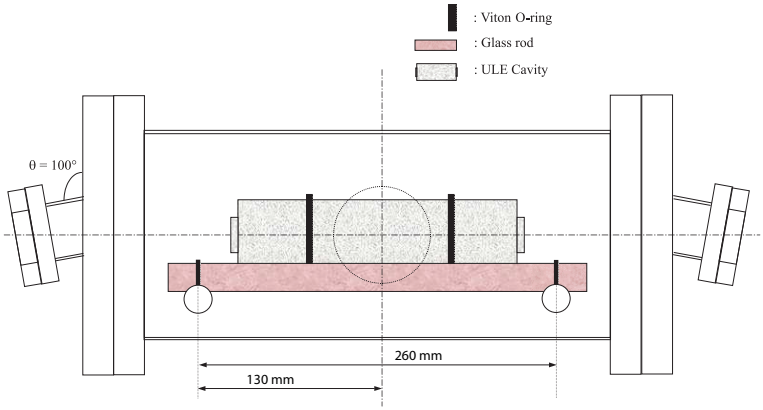

Figure 3.12: *Overview of the high finesse cavity. The high finesse cavity is non-confocal and consists of two high-reflection mirrors and a ULE (Ultra Low Expansion) glass spacer. The identical mirrors have a radius of curvature of 1000 mm. The spacer is 200 mm long and has a diameter of 50 mm. The high finesse cavity rests on two glass rods through a pair of Viton O-rings. The glass rods rest upon the steel shell. The setup is placed in a vacuum chamber which is evacuated to* $5 \cdot 10^{-9}$ *mbar by an ion pump citeK107.*

The ULE cavity is placed in a vacuum chamber as seen in figure 3.12 with a pressure of $5 \cdot 10^{-9}$ mbar. The pressure is maintained by a 100 l/s ion pump. The entire steel chamber is thermally stabilized using peltier elements in order to reduce variations to the optical length. To send light in and out of the chamber viewports are placed in each end and tilted in order to avoid interference from reflections from the windows. The cavity consist of a 200 mm long hollow glass rod made from ultra low expanding (ULE) glass. At each end of the glass rod a high reflecting curved mirror is attached with a focal length of 1000 mm making the cavity non-confocal. The FSR of the cavity is then found to be FSR $= c/2L = 750$ MHz. The finesse of the cavity has been estimated to be $\mathfrak{F} = \frac{c\pi\tau}{L} = 86000$ by fitting the ringdown of the cavity [46]. Coupling light into the cavity and then switching it off

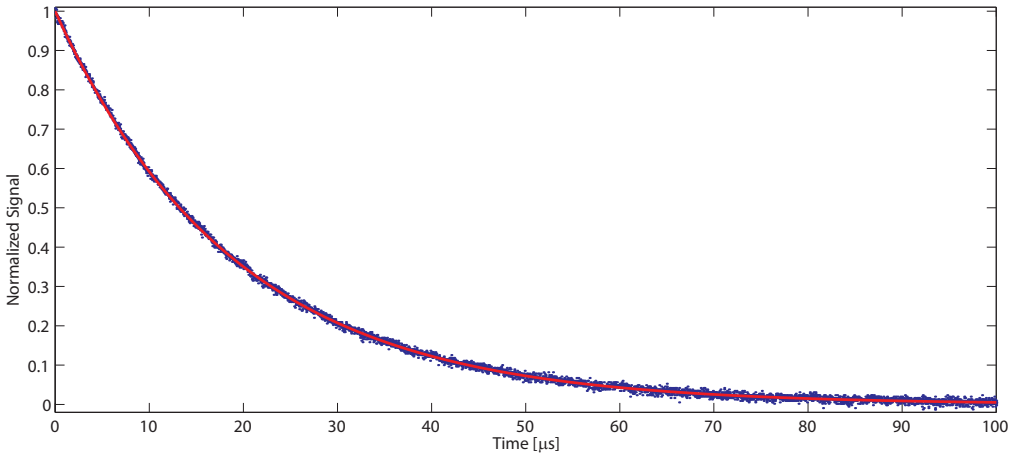

Figure 3.13: *Cavity ring down fitted to an exponential decay function resulting in a decay time of 19.0 μs giving a cavity linewidth of 8.4 kHz which corresponds to the value found in [46].*

allows us to measure the ringdown of the cavity giving it a linewidth of 8.4 kHz as seen in figure 3.13. The high finesse of the cavity cause the decay to be slow enough that the ringdown is detectable. To isolate the cavity from vibrations the cavity is placed on 2 glass rods through a pair of Viton O-rings. The glass rods rest on the vacuum chamber itself and the O-rings help to absorb vibrations. It is important that the temperature and thereby the cavity length is stabile since it takes along time for the cavity to settle.

3.4 MOPA Fibre Laser for green light generation at 517 nm

The 517 nm laser is used for exciting the $(3s3p)^3P_j$ - $(3s4s)^3S_1$ transitions and iodine spectroscopy. The laser is a MOPA system as the 383 nm laser and 457 nm laser however there are several key differences. The master is a AR-coated diode laser capable of delivering 100 mW. The diode is placed in a littrow configuration and typically generates 30 mW at 1034 nm. This

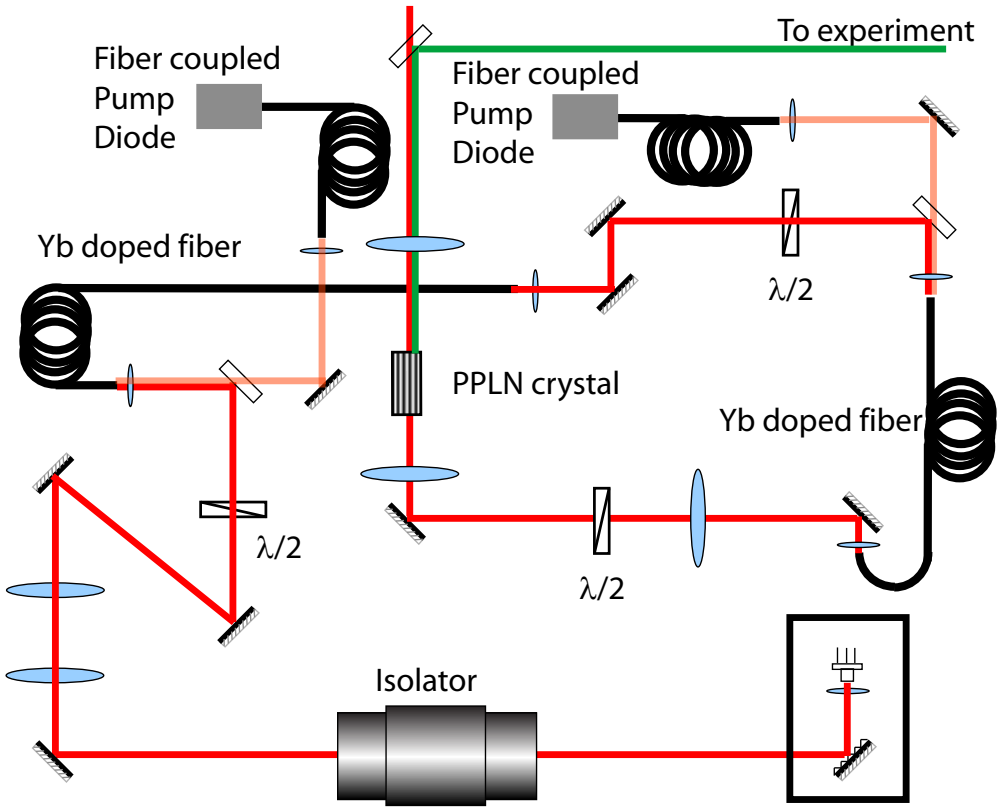

Figure 3.14: *Illustration of the 517 nm setup. The output from the 1034 nm external cavity diode laser is amplified by a two-stage Yb-doped fiber amplifier system and single pass frequency doubled using a periodically poled lithium niobate (PPLN) crystal.*

light is coupled into the core of a fiber as seen in figure 3.17. The fiber contains ytterbium in the core which is a rare earth element that act as a gain medium. The pump absorption in the core is 1200 dB/m and about 6 dB/m for the cladding. The use of a larger cladding which guide light at the pump wavelength makes the coupling easier especially for poor quality pump lasers. For each of the two amplifier stages we use a 2.5 m Ytterbium doped fiber. The absorption and emission cross-section for the gain medium is shown in figure 3.15 [49], [50]. As seen on figure 3.15 there is a large absorption at a wavelength around 980 nm. At 980 nm the gain medium act as a two level system were the emission and absorption cross-sections are equal [49]. We

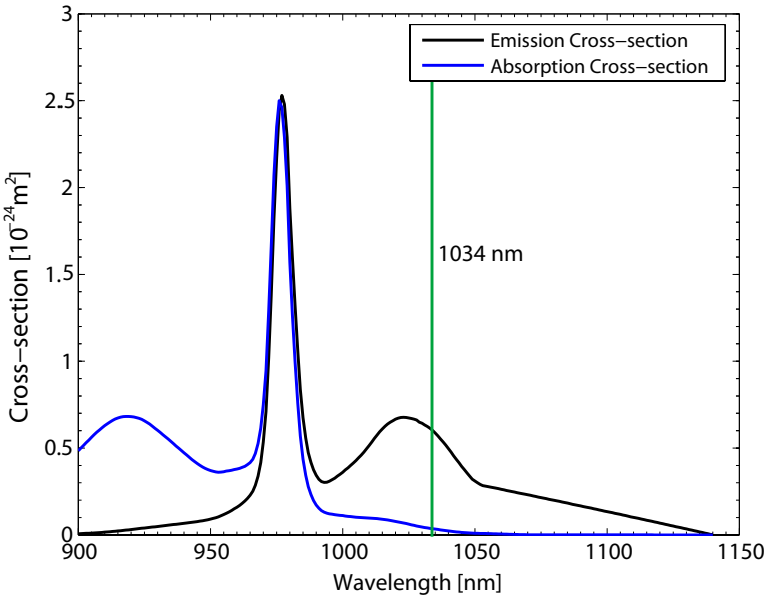

Figure 3.15: *The emission cross-section and absorption cross-section of ytterbium in a silica host material. At 1034 nm a non negligible absorbtion is present, making the fiber amplifiers sensitive to the length of the fibers.*

use a Lumics 8 W fibre coupled diode laser with a delivery fiber with a 100 μm core as pump laser. The pump laser is slightly tunable around 980 nm by changing the temperature. The delivery fiber has a NA of 0.22 which makes it easy to couple the light into the cladding of the doped ytterbium fiber. A 90 % coupling efficiency of the pump power into the cladding is easily achieved using a 1:1 imaging system. With the master laser seeding the fiber the doped fiber is pumped with about 4 W at 980 nm which generate 100 mW output at 1034 nm. In order to achieve 1.5 W at 1034 nm a second amplifier stage is used similar to the first stage. The output power after the second stage as a function of total pump power is shown in figure 3.16. Contrary to the tapered diode amplifiers a nice gaussian mode is obtained after the fiber amplifier with a output power of 1.5 W at 1034 nm. The laser beam is thereafter focused through a periodic poled Lithium Niobate crystal (PPLN) with a poling of 6.22 μm. This single pass through the PPLN generates up to 40 mW when the PPLN is properly phasematched [51], [52], [53]. Using a PPLN removes the need for a external enhancement cavity used in some

of our older systems like the 383 nm and 457 nm laser. The absence of a cavity that would need to be locked to the laser means the frequency of the laser can be changed rapidly without a drop in SHG output power. The SHG output power of the PPLN is also more stable where the cavity could loose the lock. This new design of a laser with a nice mode and stable output is a huge improvement compared to the older designs using SHG cavities.

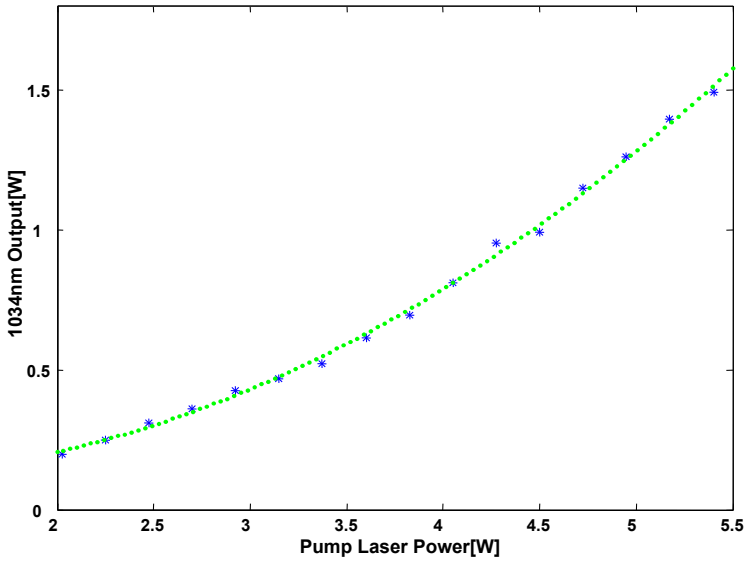

Figure 3.16: *1034 nm output of two-stage YDFA as a function of total pump power. 1.5 W of 1034 nm light is obtained. The green line is added as a guide for the eye.*

3.5 Littrow diode Laser at 881 nm

The 881 nm Laser system consist of a AR-coated diode placed in a Littrow configuration. The diode itself is capable of generation up to 100 mW of output power. The light from the diode is collimated using a f = 6.3 mm aspherical lens. The collimated light is sent onto a grating which allows the first order to be reflected back into the diode. Since the diode is AR-coated

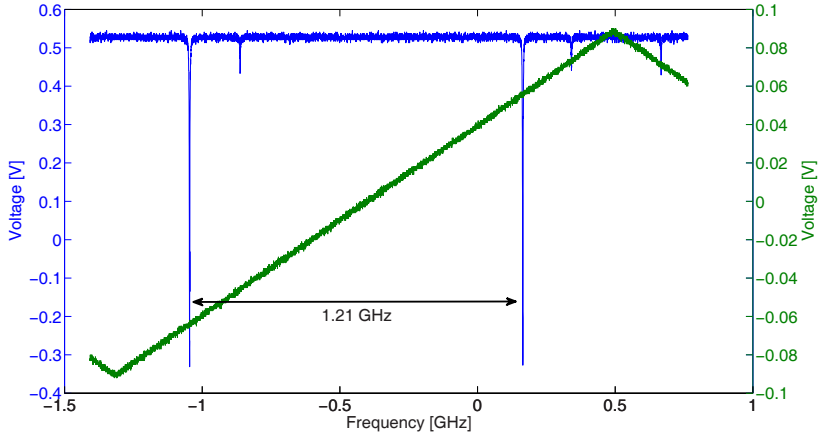

Figure 3.17: *Cavity modes are seen here when the 880 nm laser is scanned. The FSR of the cavity is measured to be 1.21 GHz with a 1.6 MHz linewidth.*

on the front the diode itself consist of one mirror and the gain medium. The grating act as the other mirror allowing power to build up in this extended cavity. The buildup is however low in order not to damage the coating of the diode. The typically efficiency of the grating allows 20% of the incident power to propagate into the first order. This is enough to force lasing in a single cavity mode as well as provide decent output power without damaging the diode. The alignment of the grating allows for the tunability of the system and with a piezo on the back of the grating mount allows the laser to be tuned. The laser beam from the diode laser is then sent through a 60 dB isolator. The beam is then split up into 2 beams where one is sent to a high finesse cavity. The laser is locked to a cavity mode which reduce the intrinsic linewidth of the laser to about 34 kHz. This is estimated by observing the error signal from the cavity lock. In order to change the frequency of the laser a piezo is placed on one of the mirrors in the cavity allowing the cavity length to be varied. This allows us to lock the laser in frequency as well as tune the laser in a controlled manner. The cavity is placed in a temperature stabilized vacuum chamber with a pressure of $1.5 \cdot 10^{-8}$ mbar. The second beam is sent through a AOM and the first order from the AOM is sent to the experiment allowing us to switch the beam on and off.

CHAPTER 4

Experiments with the metastable Mg beamline

One of the first experiments that was carried out on the metastable source was spectroscopy for determining isotope shifts and hyperfine splitting of relevant transitions. The position of the different transitions are important for the experiments carried out in the following chapters. These measurements are also improvements of older measured values. This chapter describe these measurements and the use of the setup as a frequency reference.

4.1 Experimental setup: Beamline

The generation of metastable magnesium was done using electron bombardment. Discharge beam sources have in the past been shown to be very efficient in the excitation of atomic beams of Ca [54], [55], Pb [56], Ba [57], [58], [59], Sr [60], Mg [61], [62]. We realized a source of metastable magnesium atoms in a similar fashion using the setup shown in figure 4.2. The efficiency is estimated to be as high as 40% which is consistent with previous experiments. The metastable source has a oven similar to the neutral magnesium source consisting of a hollow stainless steel cylinder with one opening as shown in figure 4.2 . A customized CF40 flange is used to seal the hole in the cylinder

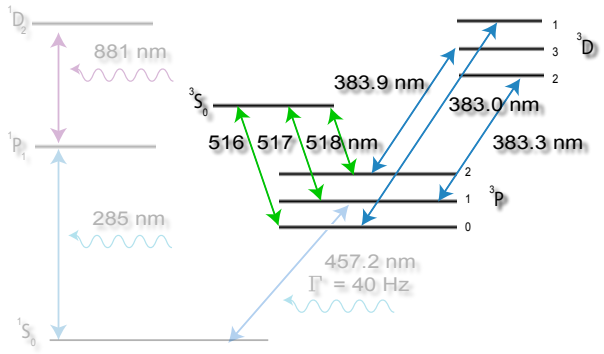

Figure 4.1: *Some of the relevant transitions between the triplet states are highlighted.*

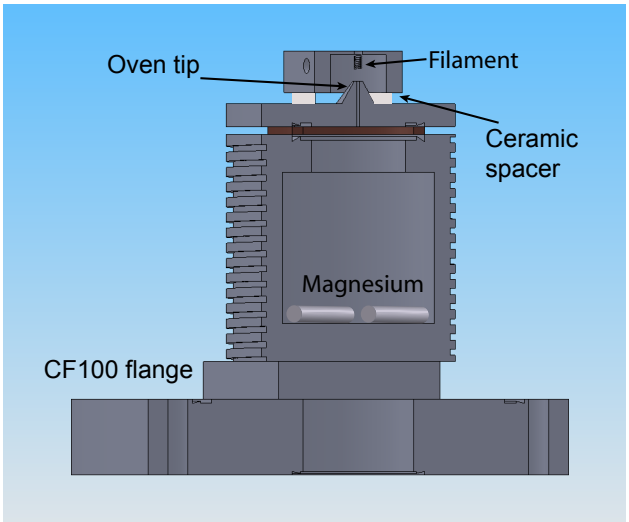

Figure 4.2: *The metastable source consists of an oven with a hole diameter of 2 mm and a $BaCO_3$ coated filament approximately 10 mm above the oven aperture. The oven has grooves for the heating wire to ensure optimal thermal contact and is thermally shielded by two stainless steel cylinders. The filament is shielded by a copper piece at the same potential as the filament. The metastable source is mounted on a CF100 flange using ceramic screws.*

with a appropriate knife milled into it. The flange has a 2 mm hole in the center as seen in the figure. When sealing the oven it was found that magnesium reacts with the copper gasket which generate a alloy that unfortunately has a melting point as low as 480 °C. The melting point of the alloy is lower

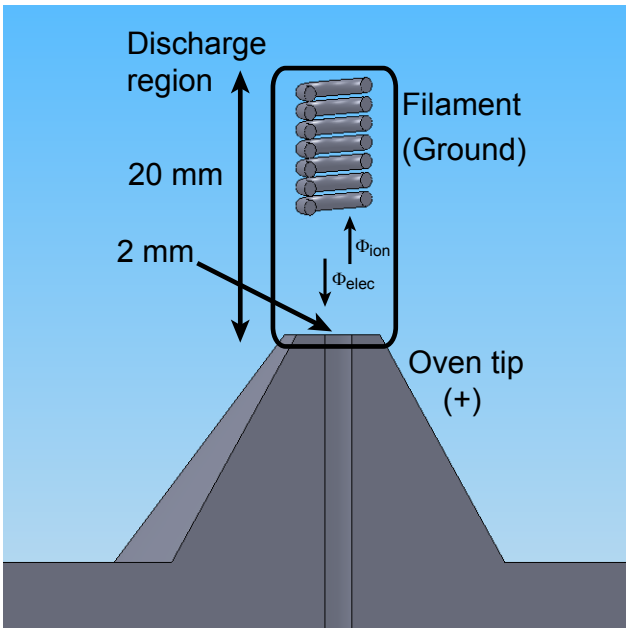

Figure 4.3: *Details of the discharge region defined by the filament and the oven aperture.*

then pure copper and pure magnesium. When the oven is heated to 520 °C and the magnesium vapor come in contact with the copper it generate the magnesium-copper alloy. Since the temperature is above the melting point of the alloy it is free to move away form the seal and into the oven interior. A Titanium gasket was manufactured to replace the copper gasket which did not corrode. The oven was heated by a resistance heating wiree that could bring the oven up to at least 800 °C. A filament was placed on top of the oven approximately 0.5 mm from the orifice of the oven. The filament coated with BaO would generate the initial electrons used to trigger the selfsustaining discharge. In order to generate free electrons the filament was heated by passing a current of 7.5 A through the wire. A voltage potential of 40 V was placed between the filament and the oven itself. The oven is isolated from the main chamber by using ceramic bolts in order to achieve a potential difference between the oven and the chamber. Without a magnesium flux this would typically generate a current of 0.5 mA between the filament and oven. As the oven is heated there is a increase in the flux of neutral magnesium

atoms coming out of the 2 mm hole. The flux at the typical operating temperature of 520 °C is about $5 \cdot 10^{17}$ atoms/s [44]. As the temperature of the oven is increased to 520 °C the magnesium vapor pressure in the oven reaches a flux where collisions with electrons are probable. Electrons moving through the neutral beam of magnesium cause inelastic collision. These collisions can cause a generation of ions given by [63]

$$\Phi_i = \sigma_i n_{crit} l I/e \tag{4.1}$$

where σ_i is the cross section for the inelastic collision, n_a is the neutral magnesium density, and l is the length of the electron path in the discharge region. The generation of ions cause the current between the filament and the oven to increase. As the electrons inelastically collide with magnesium atoms the generate ions and more free electrons. These new electrons can replace the need for the filament that generate electrons when hot. As the flux of neutral magnesium rise it will at some point reach a density where the discharge becomes selfsustained. This happens when the atomic density is large enough that the generated electrons from the ionization can maintain the neutral discharge condition

$$n_e = n_i \tag{4.2}$$

for a electron and ion flux given by

$$\Phi_{e^-} = n_{e^-} v_{e^-} \tag{4.3}$$
$$\Phi_i = n_i v_i \tag{4.4}$$
$$\Phi_{e^-} = \Phi_i + I/e \tag{4.5}$$

where Φ_{e^-} and Φ_i are the electron and ion densities.

The critical density of neutral magnesium can then be calculated [63]:

$$n_{crit} \geq \frac{v_i/v_{e^-}}{l\sigma_i} = \frac{\sqrt{m_e^-/m_i}}{l\sigma_i} \tag{4.6}$$

The critical density obtained using 4.6 is $n_{crit} = 5 \cdot 10^{12}$ which roughly corresponds to a oven temperature of 520 °C.

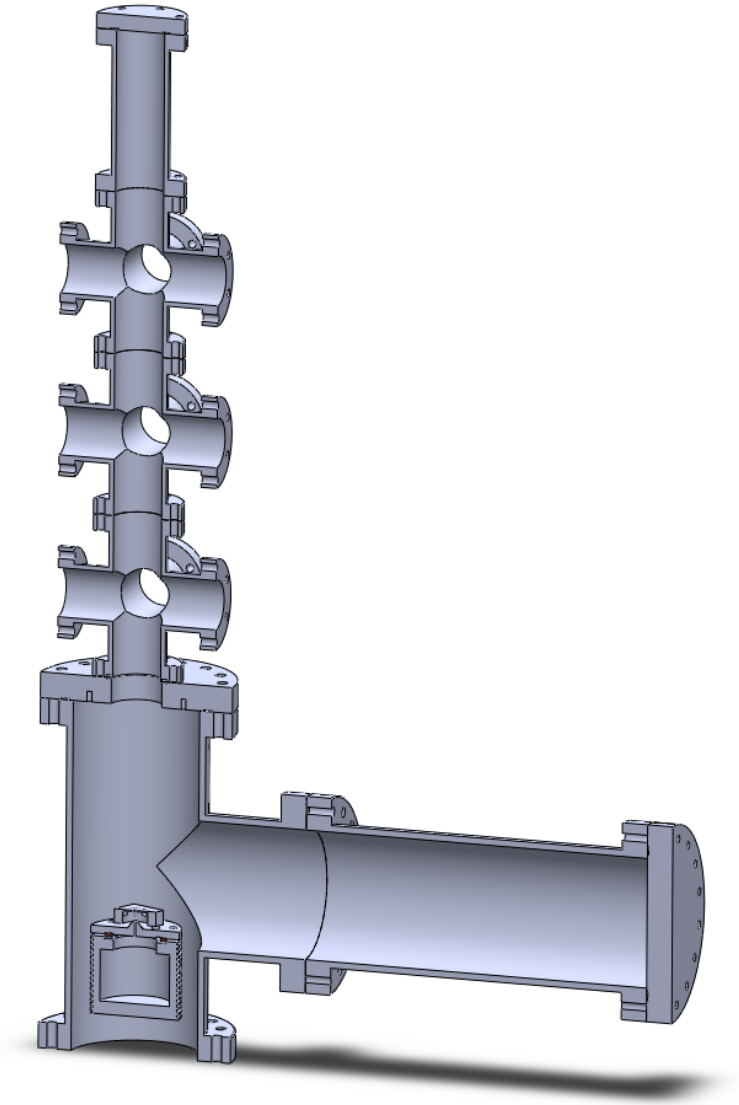

Figure 4.4: *The beamline consisting of the metastable oven generating a metastable beam which can be probed as is propagate past the 3 6-way connectors.*

For measuring the hyperfine splitting and isotope shift metastable source is placed in a beamline setup shown in figure 4.4. Along the beamline there are 12 viewports allowing optical access to the beam to monitor fluorescence.

The chamber is pumped using a 250 l/s turbo pump (Edwards EXT250) that maintains a pressure of about $2 \cdot 10^{-8}$ mbar in the oven section when the oven is operating. The metastable oven is operated at 520 °C which typically generate a flux of about 10^{13} atoms/s after a circular collimator 15 cm downstream. The oven temperature is increased untill the discharge becomes selfsustaining. In order to avoid using too much magnesium the flux is kept at or just above the flux needed to keep it selfsustaining. When the discharge becomes selfsustaining the current jumps up by more then a factor of 100 which at this current does generate a significant amount of heat around the orifice. With the additional heat from the discharge the power of the heating wires are typically reduced by 10%. The current running through the discharge, typically 1A with a potential difference of 25 V, is high enough to keep it running stable without damaging the oven, filament, and orifice. A picture of the discharge running at 1 A is shown in figure 4.5. When shutting down the discharge the output power of the heating wires is lowered so that the orifice with the discharge remains hot. Since the magnesium vapor inside the oven will condense on the coldest part of the steel cylinder then the area around the orifice will remain clear and we avoid blocking the nozzle.

Two of the viewports on the beamline have telescopes that image the beam of magnesium onto a Photo Multiplier Tube, (PMT) that generate a signal when the atoms are emitting fluorescence as seen in figure 4.4. These viewports are located 40 cm and 47 cm from the oven orifice and image a 5 mm * 5 mm and 1 mm * 1 mm wide area of the beam. The first PMT placed at a distance of 40 cm from the orifice observe the atomic beam which has a transverse velocity corresponding to a 65 MHz doppler broadening. The second PMT for observing the 383 nm fluorescence use a pinhole to increase the resolution. The 500 μm pinhole leads to a transverse doppler broadening, of the atomic beam, of about 35 MHz where the natural linewidth of these transitions are typically around 20 MHz.

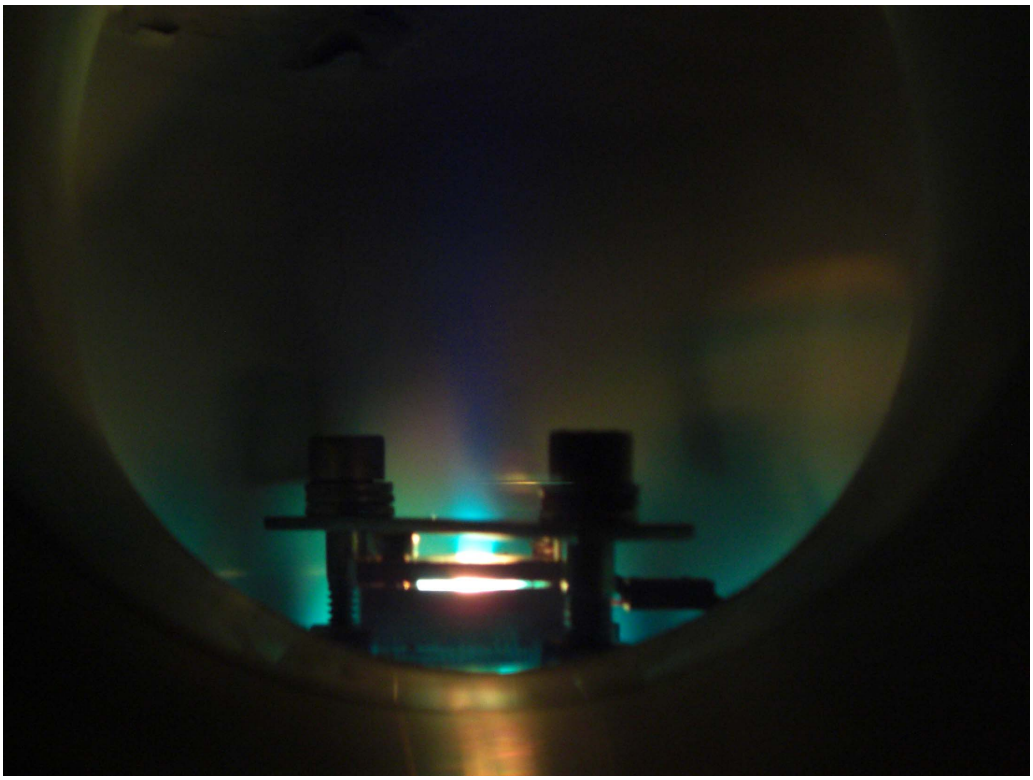

Figure 4.5: *Photo of the metastable oven. The green color from the* $^3S_1$ - $^3P_{0,1,2}$ *decay can be clearly seen. The faint blue jet that can be seen is from the 457nm* $^3P_1$ *decay to the ground state.*

4.2 Velocity distribution from the metastable source

The velocity distribution from the metastable source is non-maxwell-boltzman. This is due to elastic and inelastic collisions that happens to the atoms after they leave the oven. A theoretical description of the process can be found in [61], [62]. The velocity distribution was found to be of the form:

$$\rho_m(v) \quad = \quad B\left(\frac{v}{\alpha}\right)^{\gamma} e^{-\frac{v^2}{\alpha^2}-\frac{HI}{v}} \sinh(KI/v) \tag{4.7}$$

A plot of the theoretical velocity distribution of metastable atoms with parameters the fittet parameters, T = 520°C, H = 2840 $\frac{m}{s \cdot A}$, H/K = 0.7, I = 1A, $\gamma = 4$. The fitted plot the the experiments data can be seen in figure

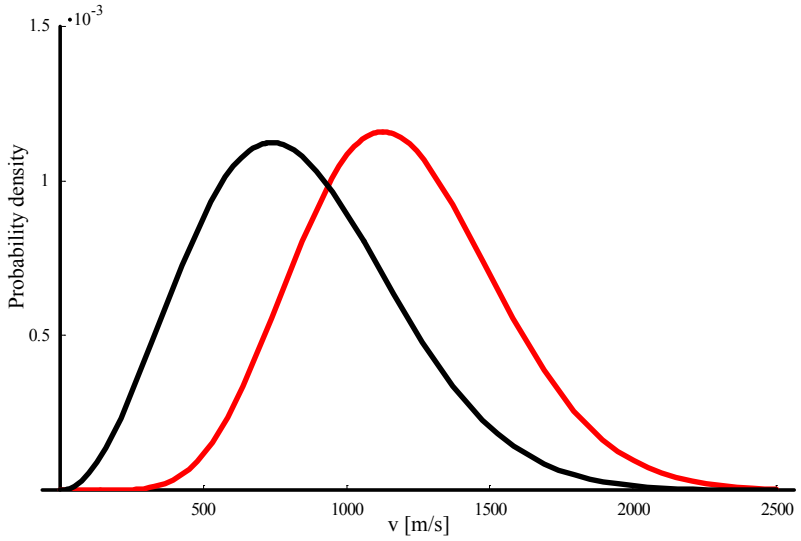

Figure 4.6: *Maxwell-Boltzmann velocity distribution (black) and velocity distribution given by equation 4.7 (red) with the typical parameters: T=520° C, H=2840* $\frac{m}{s \cdot A}$*, H/K=0.7, I=1A, γ=4. The velocity distribution of the metastable atoms is shifted towards higher velocities consistent with the expectation that the slow atoms are lost in the discharge region.*

4.6. A plot of a maxwell-boltzman with the same temperature is also shown in figure 4.6. It can be seen that there is a dramatic reduction of the number of slow atoms due to the long interaction time as they move through the discharge zone. We performed a measurement of the actual velocity distribution on the beamline by probing the atoms at a 45 deg angle. Scanning over a transition will now directly give to the velocity distribution using the relation $\delta_L = \bar{k} \cdot \bar{v} = kv\cos(\theta)$. The velocity distribution measured for 2 different currents is shown in figure 4.7. The maximum of the velocity distribution is found to be around 1000 m/s at a discharge current of 1 A. The shift to higher velocities is expected as the current through the discharge is increased from 0.5 A to 1 A. The lack of cold atoms in the thermal metastable beam is unfortunate when trapping atoms in a MOT.

We also tried to estimate the excitation efficiency of the discharge. This was done by probing the atomic beam with 285 nm light. The 285 nm laser was scanned and the $^1S_0$ - $^1P_1$ transition was observed as seen in figure

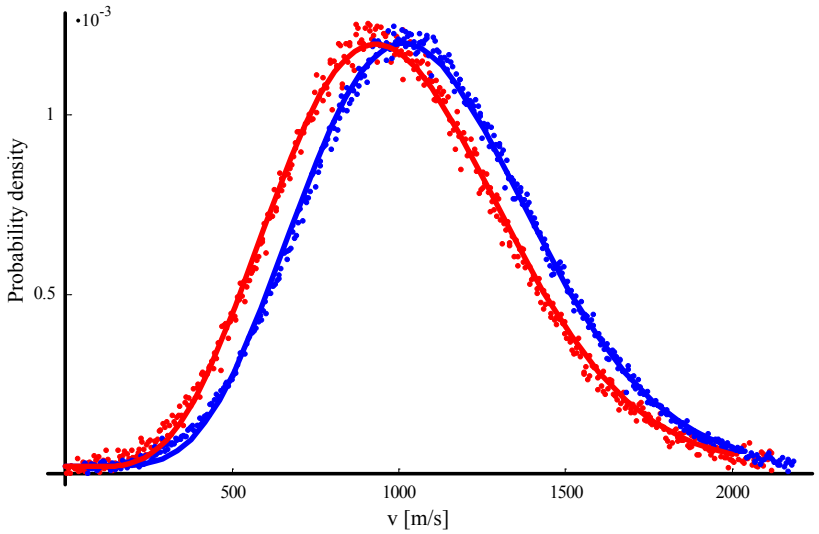

Figure 4.7: *Photomultiplier signal as a function of velocity (detuning) for two different discharge currents $I = 0.5$ A (red dots) and $I = 1$ A (blue dots) and the fits (solid) with the values: T=520° C, H=2840 $\frac{m}{s \cdot A}$, H/K=0.7, γ=4.*

4.8. When the discharge was turned on the 285 nm transition decreased by about 40%. Assuming that the atoms are either in the ground state or the metastable state this would indicate that at least 40% were transferred by the discharge to the metastable state. This however does not take into account a change in the total flux if some slow atoms were deflected out of the beam by the discharge or atoms decaying out of the metastable state before they could be probed.

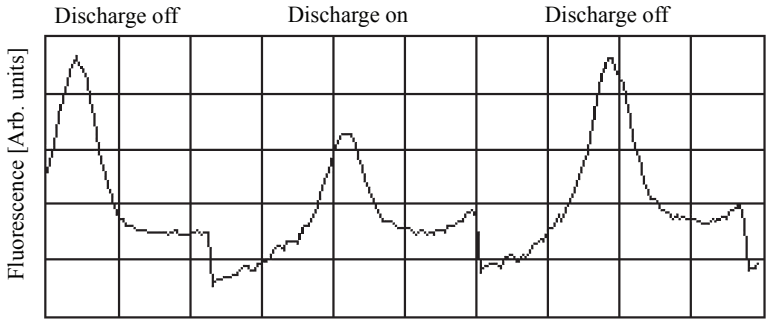

Figure 4.8: *285 nm fluorescence recorded while turning the metastable discharge on and off. An excitation efficiency of 40% is observed which is comparable to results obtained in [62].*

4.3 Measurements of the $(3s3p)^3P_j$ - $(3s4s)^3S_1$

Hyperfine splitting

In order to probe the clock transition it is necessary to probe the fermionic isotope of magnesium but since this isotope has a non-zero spin this leads to a hyperfine splitting of the energy levels, see section 2.1. In order to reach temperatures below the doppler limit of the UV transition it may be possible to cool on the triplet - triplet transitions. The hyperfine splitting of the ^3P_j - $^3S_1$ transition is interesting because the actual energy structure and hyperfine splitting is important for the possibility to do laser cooling on these transitions. Should we later choose to do laser cooling on these transitions then understanding the level structure is important. The number of lasers required in order to keep the metastable atoms in a cooling cycle depends on the spacing of the hyperfine splitting.

4.3.1 Setup

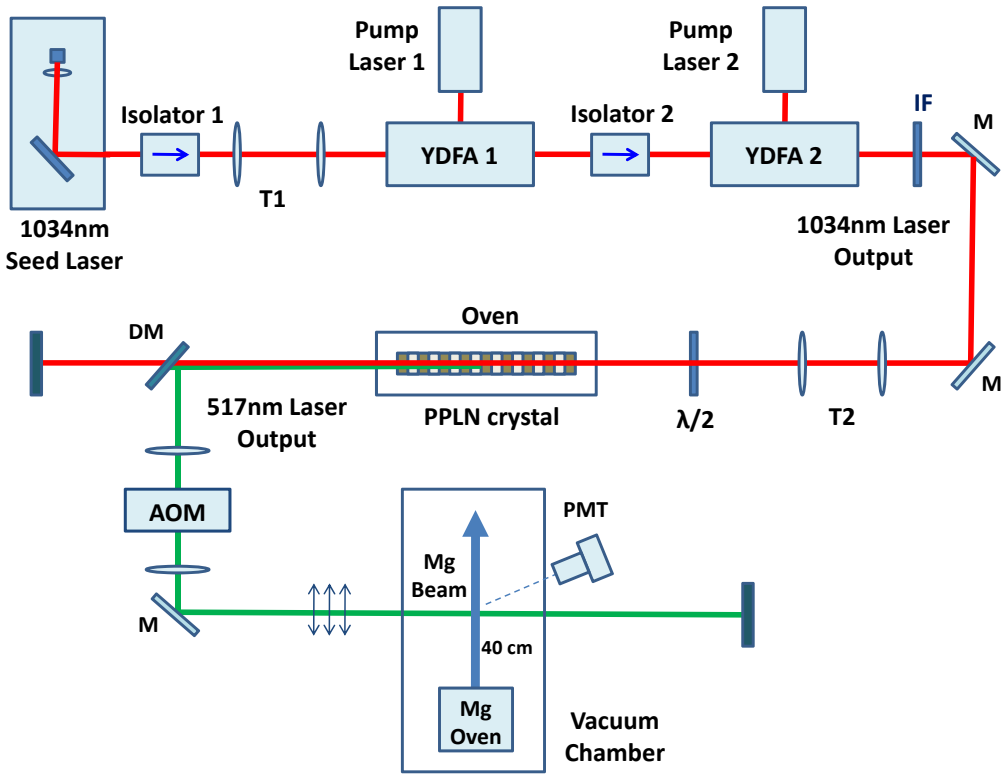

Figure 4.9: *Schematic diagram of 517 nm laser system: T, telescope; DM, dichromatic mirror; IF, interference filter; M, mirror; λ/2, half waveplates; AOM, acousto-optic modulator; PMT, photomultiplier tube. A two-stage YDFA system is used for 1034 nm laser amplification, and then there is the 517 nm second harmonic generation by PPLN crystal. For absorption spectroscopy of metastable magnesium beam, the distance between oven orifice and laser beam is 40 cm.*

The setup used to determine A($^3S_1$) and the isotope shifts is shown in figure 4.9. The laser was first calibrated by using the 0'order and 1'order from a AOM that was overlapped and used to calibrate the frequency scan. The AOM was efficient between 275 MHz - 400 MHz which was used during the calibration. The 517 nm beam was then passed through the viewport located 40 cm from the oven orifice. By scanning the peaks for different AOM frequencies allowed a calibration of the AOM as well as examining the

linearity of the scan. The laser scans were subsequently corrected for the nonlinearity of the scan. The AOM frequency was recorded using a precision counter with a uncertainty of ±1 kHz.

4.3.2 Results

We make the assumption that the hyperfine splitting is a perturbation of the fine splitting level. The energy of a $^3\mathrm{L}_J$ level can be written as [64]

$$\hbar\omega(^3L_J)_F = \hbar\omega_0(^3L_J) + \hbar\omega_1(^3L_J)_F \tag{4.8}$$

where J and F are the electronic and total angular-momentum quantum numbers, $\omega_0(^3L_J)$ is the energy level without nuclear spin and $\omega_1(^3L_J)_F$ is the first order hyperfine interaction energy. The first order hyperfine interaction energy is given by

$$\omega_1(^3L_J)_F = \frac{K}{2}A(^3L_J) + \frac{3K(K+1) - 4IJ(I+1)(J+1)}{8IJ(2I-1)(2J-1)}B(^3L_J) \tag{4.9}$$

where $K = F(F+I) - J(J+I) - I(I+1)$. Higher order terms in 4.8 and 4.9 are neglible and not included in this treatment. In figure 4.10 the spectra of the $^3\mathrm{P}_0$ - $^3\mathrm{S}_1$ transitions can be seen. The spectra is a average of 8 scans over the transitions and corrected for non-linearity of the laser scan.

A fit is made to the measured data and from the fit we calculate the hyperfine and isotope shifts. From the peaks $\mathrm{A}(^3S_1)$ is found to be 321.4±1.4 assuming $\mathrm{B}(^3S_1)$ is zero. The value of $\mathrm{B}(^3S_1)$ is of the order $\approx 10^{-6}$ and therefore negligible with our current resolution. The shifts of the ^{25}Mg and ^{26}Mg isotope relative to ^{24}Mg on the $^3\mathrm{P}_0$ - $^3\mathrm{S}_1$ transition where $\Delta^{24-25} = 205.7 \pm 1.5$ MHz and $\Delta^{24-26} = 391.3 \pm 1.7$ MHz. For the $^3\mathrm{P}_1$ - $^3\mathrm{S}_1$ transition shown in 4.11 the isotope shifts where measured to be $\Delta^{24-25} = 204.1 \pm 1.3$ MHz and $\Delta^{24-26} = 390.1 \pm 1.4$ MHz. The values of the isotope shift as well as theoretical data is shown in table 4.1.

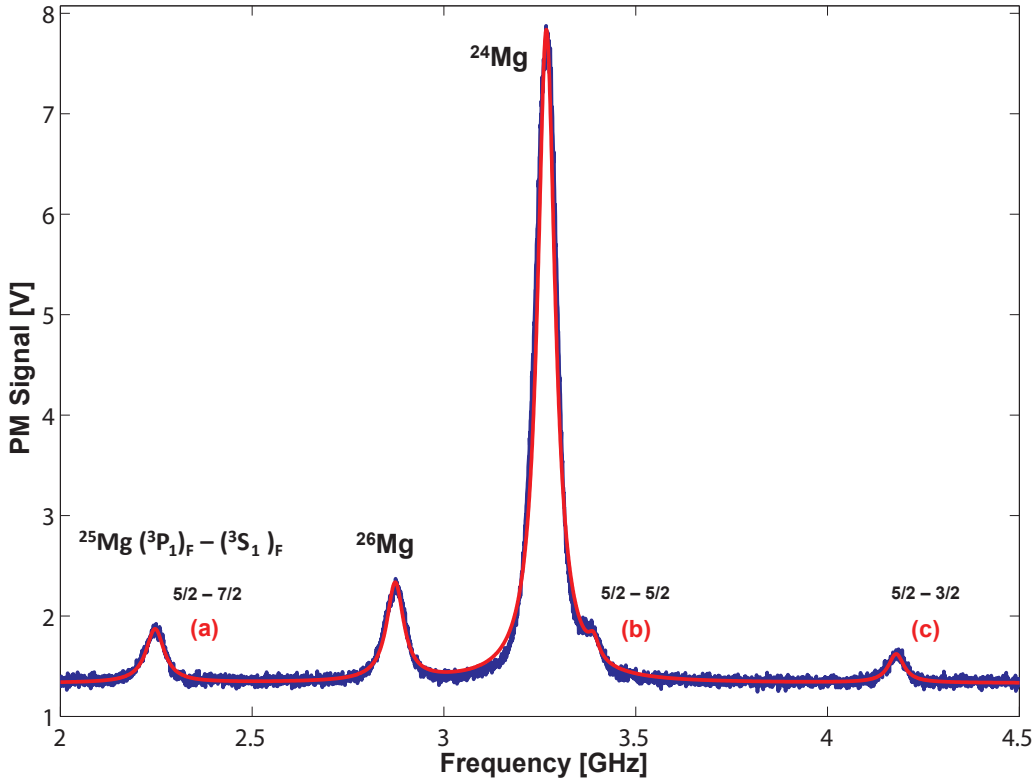

Figure 4.10: *The fluorescence signal from the $^3P_0$ - $^3S_1$ transitions. The blue curve represents the experimental data and the red curve is a fit to the data. The hyperfine transitions of ^{25}Mg $(^3P_0)_F$ - $(^3S_1)_F$ are indicated as (a) - (c).*

	^{3}P$_0$ - ^{3}S$_1$		^{3}P$_1$ - ^{3}S$_1$		
	Δ^{24-26} [MHz]	$\Delta^{24-25}[MHz]$	$\Delta^{24-26}[MHz]$	Δ^{24-25} [MHz]	$A(^3S_1)$ [MHz]
Ref. [65] (1949)	414 ± 9		366 ± 45		-322 ± 6
Ref. [66] (1978)	396 ± 6	210 ± 36	391 ± 4.5	201 ± 21	-329 ± 6
Ref. [67] (1990)	391 ± 10	214 ± 10	393 ± 10	215 ± 10	-322 ± 6
This work (2009)	391.3 ± 1.7	205.7 ± 1.5	390.1 ± 1.4	209.1 ± 1.3	-321.4 ± 1.9

Table 4.1: *Measured isotope shifts and $^3S_1$ hyperfine structure constant and comparison with previous measurements.*

4.3.3 Conclusion

The measured isotope shifts of Δ^{24-25} and Δ^{24-26} has been carried out and the measured values were in agreement with theoretical calculations. The associated errors have been improved by more then a factor 8 with respect

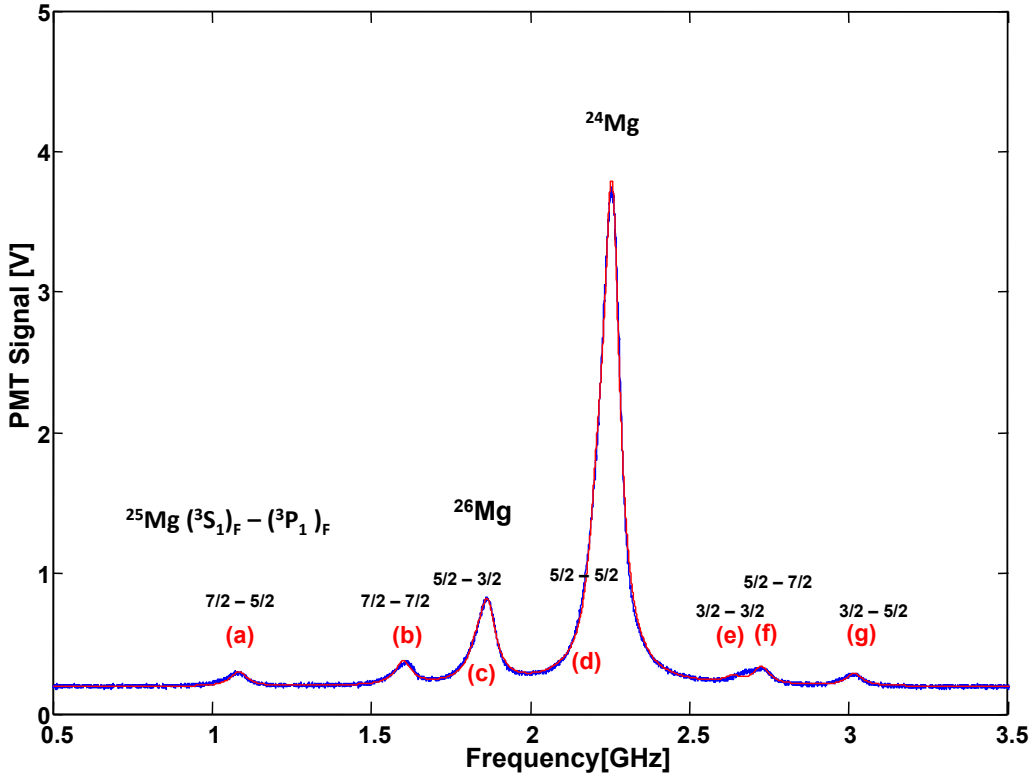

Figure 4.11: *The fluorescence signal from the* $^3P_1$ - $^3S_1$ *transitions. The blue curve represents the experimental data and the red curve is a fit to the data. The hyperfine transitions of* ^{25}Mg $(^3P_1)_F$ - $(^3S_1)_F$ *are indicated as (a) - (g).*

to earlier experiments. The measured value of A($^3S_1$) is the most accurate value measured so far and in agreement with theoretical calculations.

4.4 Measurements of the (3s3p)^{3}P$_j$ - (3s3d)^{3}D$_k$

Hyperfine splitting

The hyperfine splitting of ^{25}Mg on the ^{3}P$_j$ - ^{3}D$'_j$ transitions were investigated. These hyperfine splittings are of particular interest since they show unexpected peaks. The actual energy levels are also interesting for cooling purposes if ^{25}Mg is to be cooled. The reason ^{25}Mg is of particular interest is for metrology on the ^{1}S$_0$ - ^{3}P$_0$. For ^{24}Mg the ^{1}S$_0$ - ^{3}P$_0$ is too weak to be of practical use and so the more allowed ^{25}Mg fermionic isotope could be used. The simplest hyperfine splitting is from the ^{3}P$_0$ state however the hyperfine splitting of the ^{3}P$_2$ state is interesting since it provide closed transitions for laser cooling.

4.4.1 Experimental setup

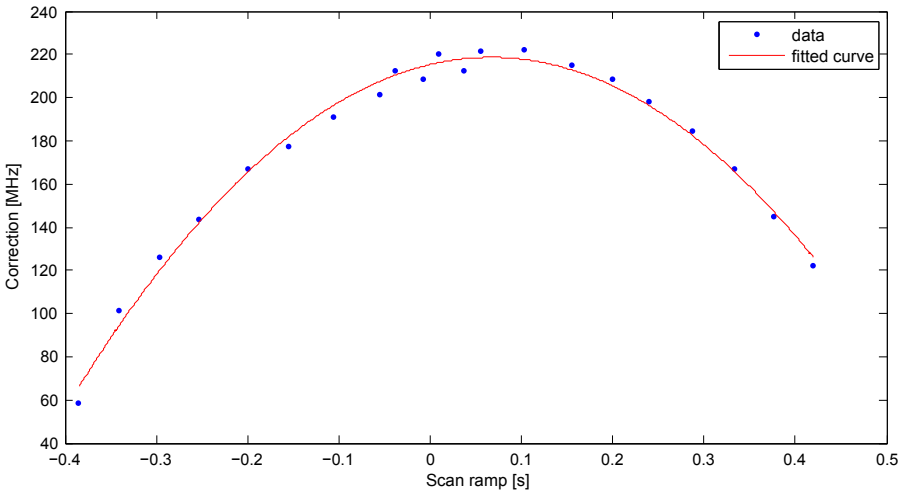

Figure 4.12: *The deviation from a linear scan ramp for the 383 nm laser in MHz. The scan has a span of 2.5 GHz which gives a 220 MHz deviation corresponding to roughly 10% deviation of a full scan.*

The setup is similar to the setup in 4.3. In order to probe the levels

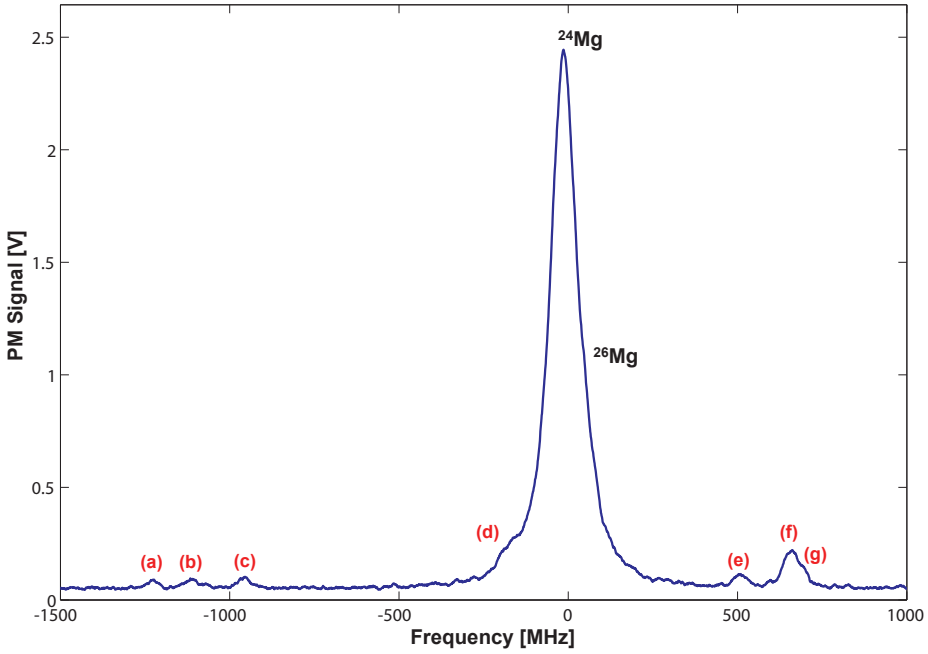

Figure 4.13: *The fluorescence signal from the* $^3P_0$ - $^3D_1$ *transitions. The blue curve represents the experimental data. The* ^{25}Mg *transitions are indicated as (a) - (g). (d) might contain more than one peak. At least 7 peaks are seen in contrast to the expected 3 hyperfine* ^{25}Mg *transitions:* $^3P_{05/2}$ - $^3D_{13/2,5/2,7/2}$.

around the ^3P_j - $^3D'_j$ the 383 nm laser described in section 3.2 was used to excite the atoms. The 383 nm beam from the laser was sent through a AOM which was operated at a frequency of around 80 - 110 MHZ. The 0'order and 1'order from the AOM was reflected back through the AOM which resulted in a beam that contained both orders, allowing for the possibility of doing a frequency calibration. When the metastable beam was probed the two orders produced two peaks for each allowed transition. Each set of peaks were all spaced by $2{\cdot}AOM_{freq}$ which made it possible to get a very accurate frequency calibration of the scan ramp. In order to improve the observed signal the AOM is amplitude modulated at 45 kHz by a high isolation switch and the PMT signal was passed through a lockin amplifier. A amplitude modulation was chosen due to beam steering if a frequency modulation was chosen. The scan ramp of the piezo/laser was found to be nonlinear and the frequency deviation from a linear scan is shown in figure 4.12. The deviation of 220

MHz on a 2.5 GHz scan corresponds roughly to a 10% deviation of the total displacement. A deviation of this magnitude is expected according to the piezo company (www.noliac.dk) and a linear operation of a piezo requires active measurement of the actual displacement so feedback can correct for deviations.

4.4.2 Results

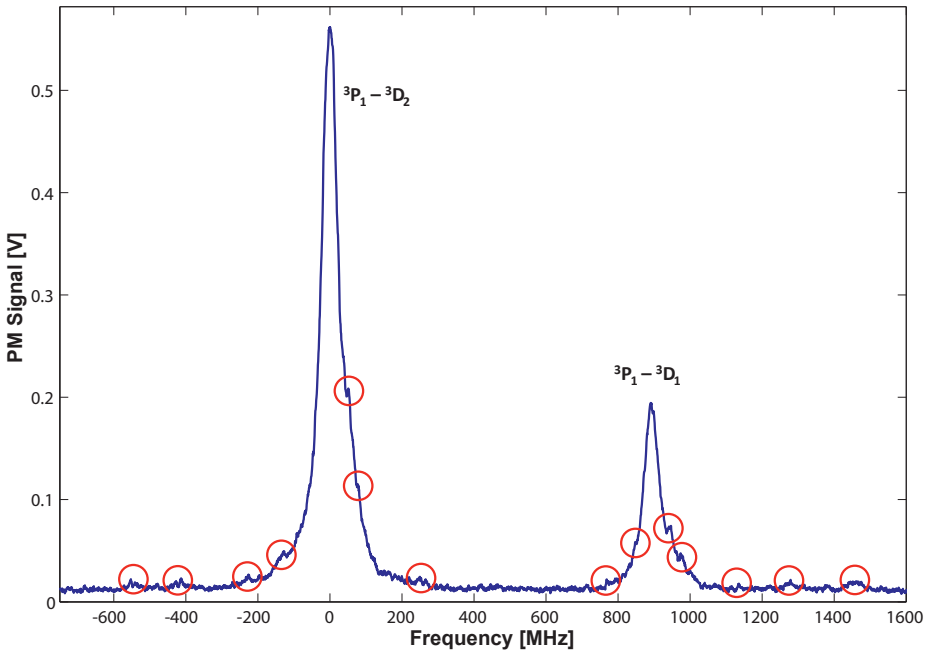

Figure 4.14: *The fluorescence signal from the $^3P_1$ - $^3D_{1,2}$ transitions. The blue curve represents the experimental data. The asymmetry of the ^{24}Mg peaks are due to overlap with ^{26}Mg. Possible ^{25}Mg transitions are indicated by a red circle.*

The simplest hyperfine splitting of ^{25}Mg on the ^{3}P$_j$ - ^{3}D$_k$ transitions is the ^{3}P$_0$ - ^{3}D$_1$ where the $(^3P_0)_{\frac{5}{2}}$ - $(^3D_1)_{\frac{3}{2},\frac{5}{2},\frac{7}{2}}$ should produce 3 lines. However as seen in figure 4.13 there are at lest 7 peaks visible in the spectrum. The main peak consist of a strong ^{24}Mg peak however the FWHM is about 65 MHz which is larger then the expected 35 MHz resolution of the detection optics. The peak can also be seen to be asymmetric and the ^{26}Mg peak

can be estimated to be 65 MHz by fitting. It is however not possible to determine the number of small ^{25}Mg peaks that are imbedded in the large peak. Currently we have no explanation for the extra peaks that are visible. The fact that they have been detected in a similar experiment 30 years ago would seem to rule out the possibility of contamination of the source.

The spectrum of the ^{3}P$_1$ - ^{3}D$_k$ and ^{3}P$_2$ - ^{3}D$_{k'}$ transitions have also been scanned, however, as seen in figure 4.14 the resolution does not allow the determination of the ^{25}Mg hyperfine peaks. For ^{3}P$_1$ - ^{3}D$_k$ one would predict 16 peaks however these are too weak to be resolved as seen in figure 4.14.

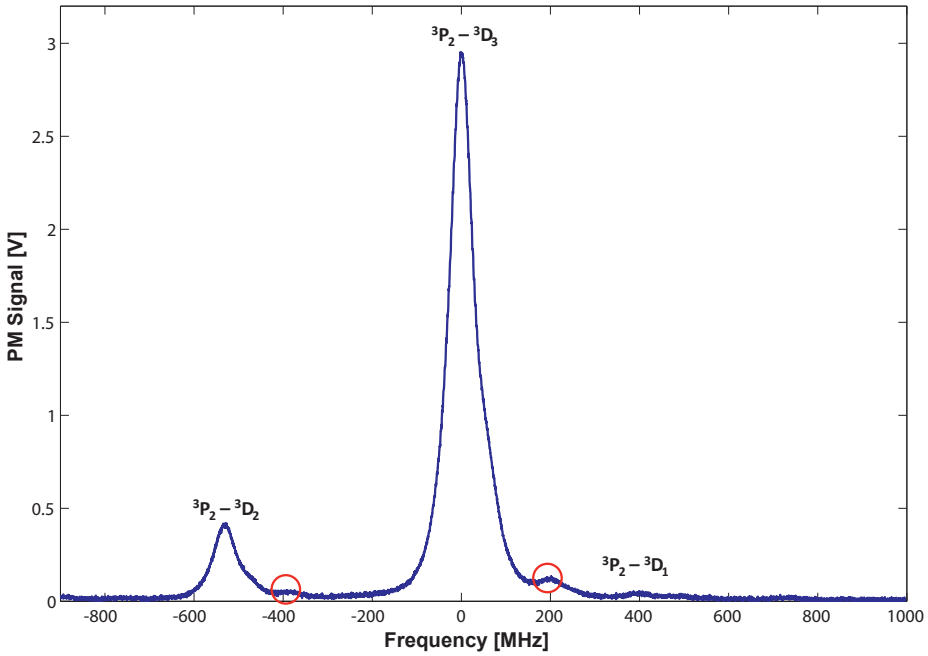

Figure 4.15: *The fluorescence signal from the $^3P_2$ - $^3D_{1,2,3}$ transitions. The blue curve represents the experimental data. The asymmetry of the ^{24}Mg peaks are due to overlap with ^{26}Mg. Possible ^{25}Mg transitions are indicated by a red circle. The spectrum is recorded without the use of a lock-in amplifier.*

4.4.3 Conclusion

The spectroscopy of the $(^3P_0)_{5/2}$ - $(^3D_1)_{3/2,5/2,7/2}$ transitions show several interesting features. The hyperfine splitting has several more peaks then theory predicts. Further studies of the hyperfine splitting is currently being conducted using optical pumping in two color experiments. There are also possibilities to study these transitions using a cold sample as described in the next chapter. With a cold sample of magnesium a pure ^{25}Mg sample can be probed which removes several peaks overlapping the ^{25}Mg peaks. This would make it easier to fit the small peaks from ^{25}Mg and impurities should not be present.

4.5 Level crossings in (3s3p)^{3}P$_2$-(3s3d)^{3}D$_j$

The last experiment done on the beamline was a measurement of the level crossings between the $^3P_2$ - ^3D_j transistions. The level crossings occur because of the zeeman shift of the different sublevels. Because the fine splitting of the ^3D_j states is only few hundreds of MHz and since the sublevels can have different lande g-factor some of these transitions can overlap. At a certain field strength, one interesting transistion is the $^3P_2$ - $^3D_3$ transition since this is later investigated for the possibility of cooling metastable atoms.

The fine splitting of the lower levels between the $^3P_{0,1,2}$ is 600 GHz and 1200 GHz which means they are of little concern. Unfortunately he fine splitting of the $^3D_1$ and $^3D_3$ is 380 MHz which can easily be zeeman shifted.

In order to measure the level crossings the beamline setup is used as described in 4.1. Two coils were placed on two of the viewports in a holmholtz configuration. The two coils generate a homogenous magnetic field at the location of the atomic beam where the 383 nm fluorescence is observed. The coils are serial connected to a 50 A current supply and the coils were determined to give 18 gauss when a current of 5 Amp were passed through them. The 383 nm beam was sent through the chamber with a linear polarization which consist of a superposition of a left and right circular polarization since

the beam was sent in coaxial to the magnetic field.

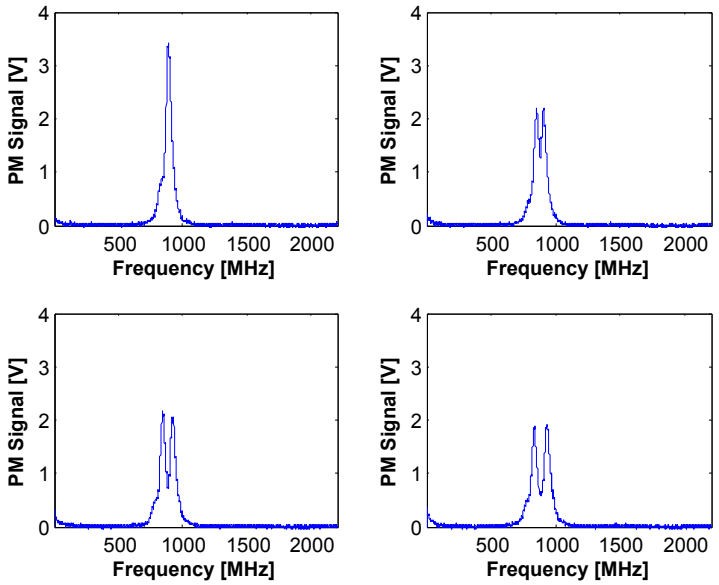

Figure 4.16: *Observed fluorescence for different field strength. The Current through the coils are 0 Amp, 3 Amp, 6 Amp, 9 Amp.*

The frequency of the 383 nm laser is then scanned back and fourth in order to see the transition $^3P_2$ - $^3D_3$. When a magnetic field is applied the substates are split up by the zeeman effect and when the laser is now scanned over the transitions each substate should be visible. As seen in figure 4.16 only two peaks are visible. This is because when probing the m_j - m_k most of these transitions are not closed and the lower state is quickly depleted and scatter only a few photons. The sublevel m_{+2} - m_{+3} can only decay back to m_{+2} and similar when exciting m_{-2} - m_{-3} the atoms return to the same lower substate and can scatter another photon. In figure 4.16 and 4.17 the zeeman shift is increased as the magnetic field is increased for each subsequent plot. When the current reaches 20 A one of the peaks disappear. This is when the zeeman shift of the $^3D_3$ m_{+3} and the $^3D_1$ m_{+1} substate overlap in energy. When the laser frequency excites the $^3P_2$ m_{+2} - $^3D_3$ m_{+3} it will at the same time excite the $^3P_2$ m_{+2} - $^3D_1$ m_{+1} transition. The crossing cause the number

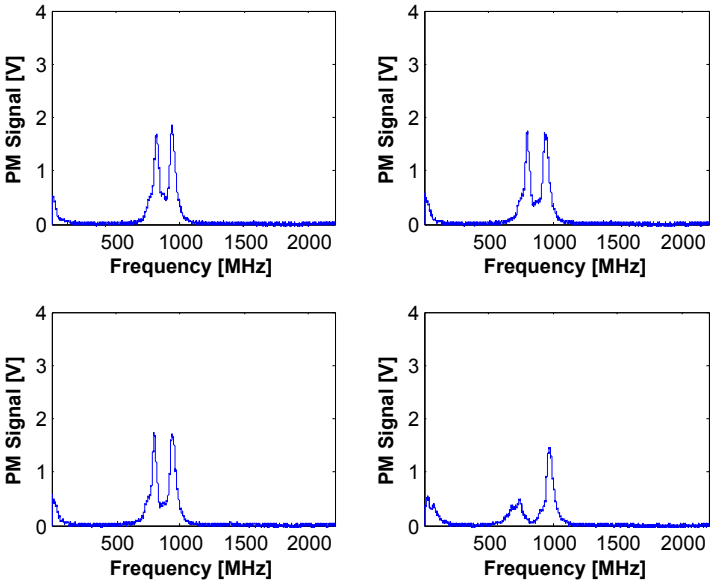

Figure 4.17: *Observed fluorescence for different field strength. The Current through the coils are 12 Amp, 15 Amp, 18 Amp, 21 Amp.*

of photons that can be scattered to drop as the atoms are optically pumped to the ^{3}D$_1$ m$_{+1}$ where they are lost. In order to calculate the level crossing I first plot the zeeman shift for each of the substates using

$$\Delta E_J = g_J m_J \mu_B B \tag{4.10}$$

This gives a crossing at

$$B = \frac{379\text{MHz}}{\Delta E_{^3D_3(+3)} - \Delta E_{^3D_1(+1)}} = 78 \text{ gauss} \tag{4.11}$$

The splitting of the ^{3}D$_{1,2,3}$ substates are shown in figure 4.18. The crossing of the ^{3}D$_3$ m_{+3} and the ^{3}D$_1$ m_{+1} at 78 gauss is circled in the figure where the two doted lined intersect. In figure 4.19 I have plotted the measured peak fluorescence when exciting the m_{+2} to m_{+3} transition as a function of the magnetic field. As expected the 383 nm fluorescence drops when the magnetic field reaches the level crossing. The dip was measured to be at

74 ± 5 gauss corresponding to 20.25 A of current through the coils. Similar for the σ_- polarization the $^3\mathrm{D}_3$ m_{-3} substate will cross the $^3\mathrm{D}_2$ m_{-1} substate at

$$B = \frac{532\mathrm{MHz}}{\Delta E_{^3D_3(-3)} - \Delta E_{^3D_1(-1)}} = 134 \text{ gauss} \tag{4.12}$$

The crossing of the $^3\mathrm{D}_3$ m_{-3} and the $^3\mathrm{D}_1$ m_{-1} substates at 134 gauss is circled in figure 4.18. This is however beyond the current of 36 A the helmholtz coils could handle. From figure 4.19 the fluorescence of the m_{-2} to m_{-2} transition up to a current of 36 A through the coil is shown corresponding to a magnetic field up to 130 gauss. The value however looks reasonable by extrapolating from the measured data.

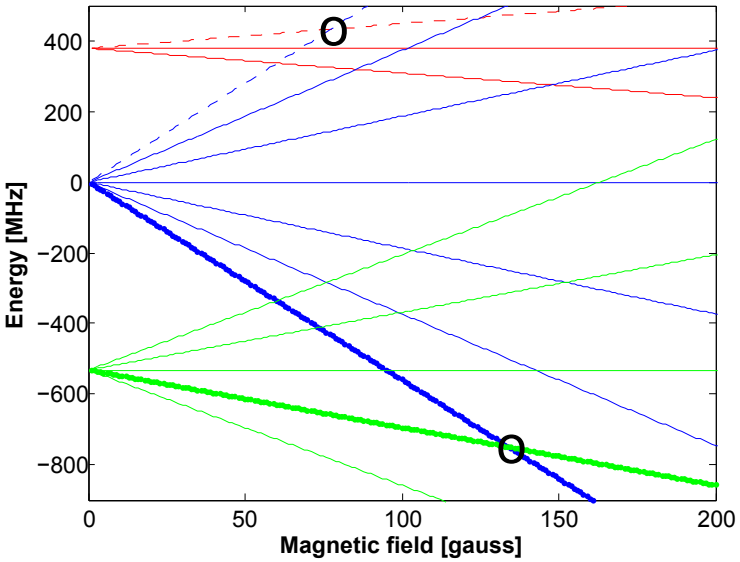

Figure 4.18: *Here the level crossings of the ^3D levels are shown. The crossing of $^3D_1$ m_{+1} with $^3D_3$ m_{+3} and the $^3D_1$ m_{+1} with $^3D_3$ m_{+3} are circled*

So far the 383 nm light that was used was linear polarized meaning that it is a superposition of both σ_+ and σ_- polarization. This allows the 383 nm light to drive both the $\Delta m_j = +1$ transition and the $\Delta m_j = -1$. If only one of the components is present this will have a dramatic effect on the observed

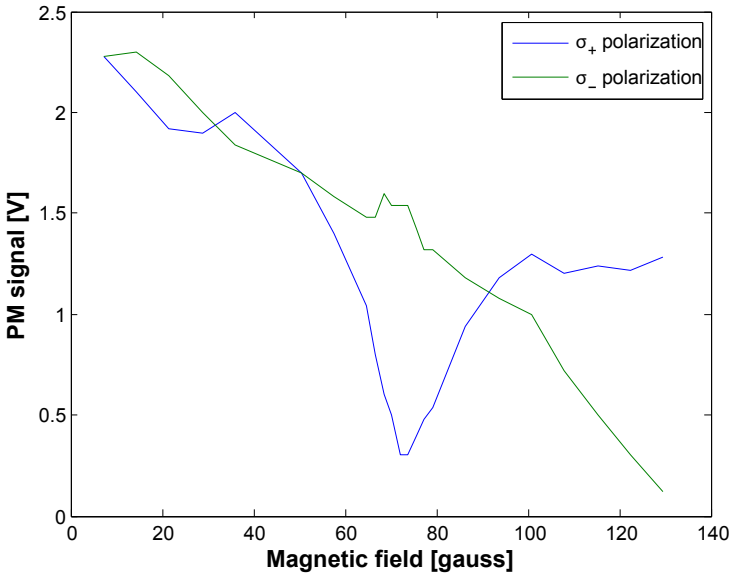

Figure 4.19: *The observed fluorescence when exciting the atoms with linearly polarized light. The level crossing at 78 gauss is clearly visible.*

spectrum. First only one peak will be present in the spectrum because the population of most of the substates will be depleted. If we first consider σ_+ light this will drive the $\Delta m_j = +1$ transitions with only the $m_j = +2$ to $m_j = +3$ being closed. Another interesting feature is when the magnetic field is increased to 78 gauss the $^3D_3$ m_{+3} and the $^3D_1$ m_{+1} substates cross. The observed fluorescence does however not drop as seen in figure 4.18. This is because of the $^3D_3$ m_{+3} to $^3D_1$ m_{+1} transition has $\Delta m_j = -1$ which the σ_+ light, due to conservation of angular momentum, can not excite. Since the $^3D_1$ ($m_j = +1$) is not excited as the magnetic field is increased to that of the levelcrossing the fluorescence remain constant. Similar for the other case where σ_- light is used the fluorescence of the $m_j = -2$ to $m_j = -3$ transition remain constant at the level crossing.

The polarization dependence was investigated by utilizing a $\lambda/4$ plate and the resulting fluorescence for the two polarizations can be seen in figure 4.20 and 4.21. Both polarizations show a constant fluorescence as a function of the magnetic field. In figure 4.20 the peaks at a current of 5, 10, 15, and

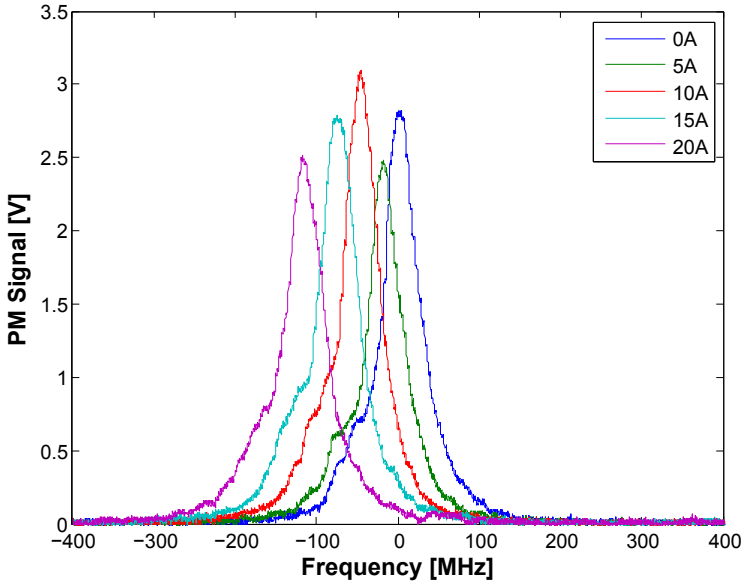

Figure 4.20: *Level crossing of the* ${}^3D_1(m_j = +1)$ *and* ${}^3D_3(m_j = +3)$ *state.*

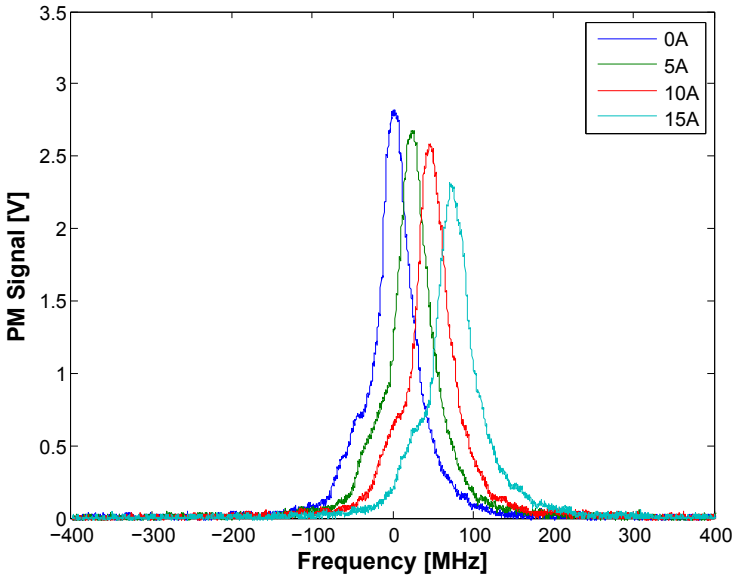

Figure 4.21: *Level crossing of the* ${}^3D_2(m_j = +1)$ *and* ${}^3D_3(m_j = +3)$ *state.*

20 A is shown. In figure 4.20 one of the peaks is shown for a current of 20 A correspond to 72 gauss close to the level crossing of $^3D_1(m_j{=}+1)$ and $^3D_3(m_j{=}+3)$. The transit time for atoms in the beam is roughly $\frac{0.01m}{1000m/s} = 10$ μs which is however quite a short time compared to the possible interrogation times of a MOT.

4.6 Frequency Stabilization of the 383 nm laser

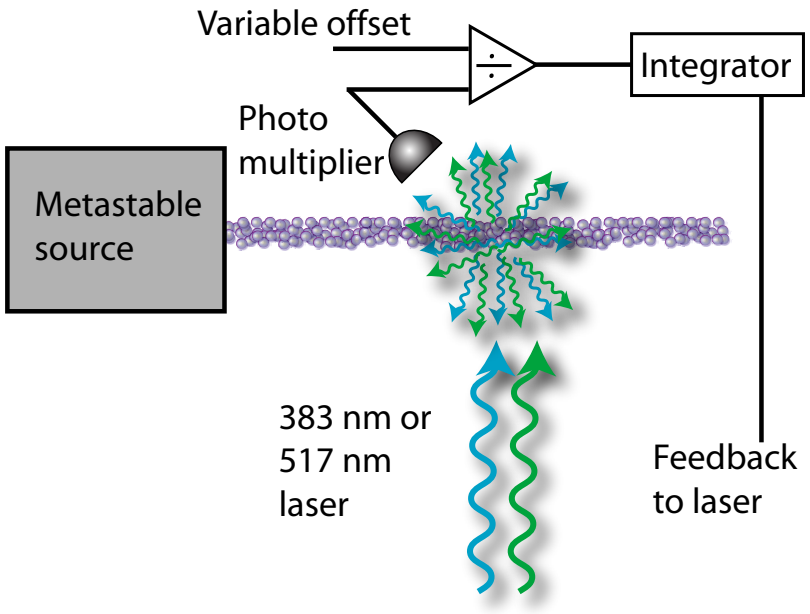

Figure 4.22: *The locking scheme for the beamline. The integrator has a slow integration time in order to average out power fluctuations from the SHG cavity.*

For some of the experiments conducted in the next chapters the 383 nm laser has to be frequency stabilized to an atomic transitions. This was achieved using the setup in section 4.1 and the locking scheme shown in figure 4.22. The 383 nm beam was single passed through the AOM and the 0'order was sent to the beamline for frequency reference. Since the following

experiments required the 383 nm light to be switched on and off the 1'order was sent to the experiment. In order to generate a modulation for the lockin amplifier the master laser was given a frequency modulation of 1 kHz and a amplitude of 1 MHz which would give both orders difracted form the AOM a frequency modulation. The modulation is well below the natural linewidth of 26 MHz that the $^3P_2$ - $^3D_3$ transition has. Since the laser is locked using an error signal generated from the derivative of the signal the zero point becomes independent of the 0'order power. Since the frequency lock is independent of power the lock is not disturbed when the AOM is switched on and off. The frequency lock is also unaffected by the power fluctuations from the SHG cavity.

As seen in section 4.5 the beamline has a pair of helmholtz coils that can generate a homogeneous magnetic field, at the interrogation zone, of 3.6 gauss/A with a maximum of 12 A at constant current or 30 A of current for short periods. With the laser locked to one of the peaks and using a $\lambda/4$ plate it is possible to frequency shift the laser. By rotating or varying the magnetic field it is possible to detune the laser about ± 60 MHz from the transition the laser is locked to.

4.7 Conclusion

A source of metastable magnesium atoms has been realized and a beamline chamber has been constructed for probing the source. The spectra of the relevant transitions has been investigated and the hyperfine splitting has been measured for the ^3P_j - $^3S_1$ in agreement with previous measurements. The isotope shift for the green transitions has been determined and are in agreement with previous measured values. Some of the hyperfine transitions in the ^3P_j - ^3D_k has been observed however not all of the transitions could be observed. The setup allows us to use it as a frequency reference for the experiments carried out in the following chapters.

CHAPTER 5

Experiments with cold Metastable ^{24}Mg in a Magnetic Trap

In the following chapter I will describe the experiments we did on and related to cold metastable magnesium. The experimental determination of the life-times of atomic states provide a sensitive test of theory. As some of the lower lying states are metastable these can effectively be considered ground states. Since some of them also have $J \neq 0$ they are able to be trapped in a magnetic field. This open up for the possibility to trap and condensate magnesium using magnetically trapped metastable atoms. It is therefore interesting to determine physical properties like the collision cross-section as the elastic and inelastic cross-sections are of great importance in such experiments.

In contrast to the beamline experiments having a confined sample of cold metastable magnesium allows for much longer interrogation times. One of the experiments we did on metastable ^{24}Mg was a measurement of the lifetime of the $^3P_2$ state. This state can radiatively decay down to the ground state, $^1S_0$ which is a forbidden transition. It is an electric dipole forbidden transition as well as magnetic dipole forbidden with a theoretically calculated lifetime of about 2000 s. This long lifetime would be nearly impossible to observe in a beam experiment however a cold sample of metastable magnesium could be probed long enough that the decaying atoms and the total number of atoms could be counted. These long interrogation times and cold temperatures is

what makes laser cooled and confining of atoms such a powerful tool. It opens up for the possibility of probing transitions for seconds allowing very weak transitions to be investigated like the $^1S_0$ - $^3P_0$ clock transition.

5.1 UV MOT setup

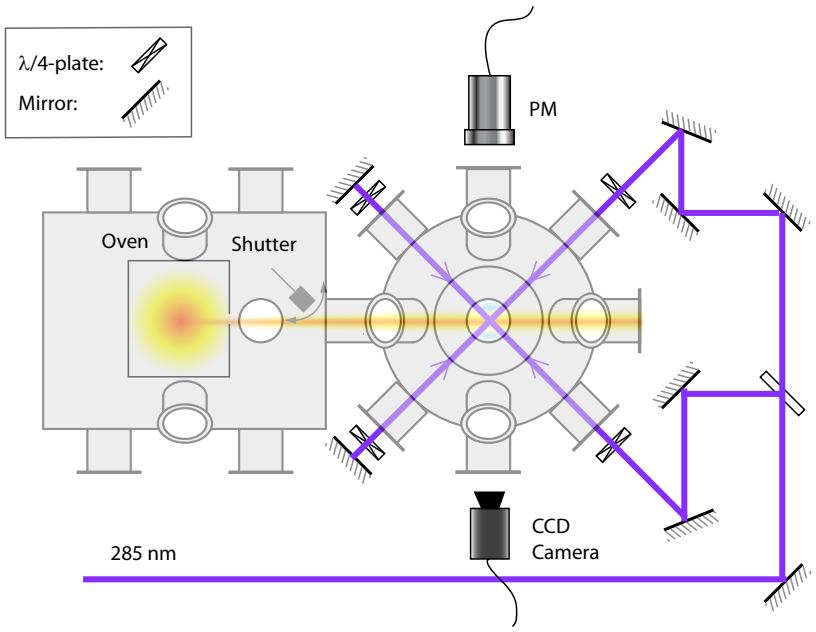

Figure 5.1: *The UV chamber showing here the UV beams that cool and confine the neutral Mg atoms.*

The experiment was carried out in the UV MOT Chamber as seen in figure 5.1 and the UV MOT setup is described in detail in [44], [68]. The vacuum in the oven chamber was typically $8 \cdot 10^{-9}$. The vacuum pressure of the oven chamber was achieved with a 250 l/s turbo pump (Edwards EXT250) while a 150 l/s Varian noble diode ionpump kept the MOT chamber at $3 \cdot 10^{-10}$ mbar. The CF40 flexible tube connecting the oven and MOT chamber had a 60 mm long differential pumping tube with a 4 mm in diameter hole that helped maintain a pressure difference between the chambers and allowed a

well collimated beam of magnesium into the MOT chamber. The distance from the oven orifice to the differential pumping tube was 90 mm and the distance from the oven orifice to the center of the MOT chamber was 260 mm. A mechanical shutter, placed in front of the differential tube, was used to switch the atomic beam on and off. The oven, consisting of a standard stainless steel container, was heated using thermal resistance wire up to a temperature of 710 K. At a temperature of 710 K the thermal beam of neutral magnesium would have a mean velocity of 790 m/s. With the geometry we have and a thermal beam divergence of 13 mrad this gives a 90 MHz transverse doppler broadening. The estimated capture velocity of the MOT is about 50 m/s.

The shutter consist of two coils that made a small piece of iron move back and forth as current through the coil was switched on. The atomic beam consisting of neutral magnesium would propagate across the MOT chamber and into a beam dump at the other end of the chamber. The atomic beam dump is a wedge shaped copper block that could be cooled using liquid nitrogen. This beam dump helped to reduce the background gas of magnesium in the MOT chamber.

Inside the chamber are two coils placed in a antiHelmholtz configuration that generate a magnetic quadropole field [69]. The copper coils were hollow allowing cooling water to flow through which allowed us to pass a current of up to 200 A through the coils. The magnetic field gradient generated by the coils were 1.4 gauss/(A cm) and their shape can be seen in figure 5.2. The shape of the MOT coils allowed beams from all 16 view ports to have a unobstructed line of sight to the MOT.

The main MOT chamber had 16 unobstructed view ports where 6 were used for the UV beams that generated a UV MOT. The fluorescence from the MOT was recorded using 2 R4007UV-3 photomultiplier tube (PMT) that were sensitive to the 285 nm light. One of the PMT was operated at 320 V supply voltage giving a low gain which allowed us to continuously observe the MOT. The second PMT observed MOT fluorescence through a telescope that had a 1 mm pinhole and a UV interference filter centered at 285 nm. The second PMT was operated up to a supply voltage of 800 V allowing

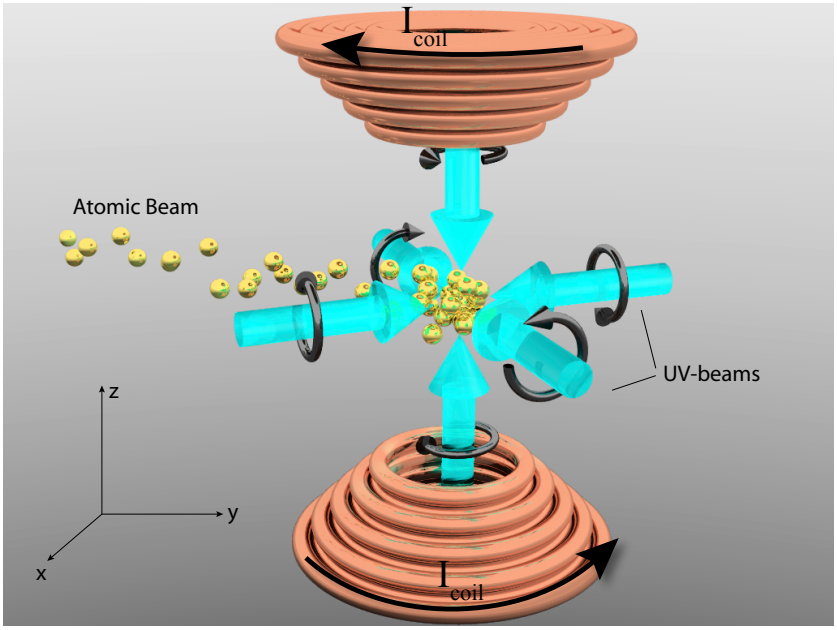

Figure 5.2: *Inside the chamber two coils are placed in a antihelmholtz configuration generating a quadropole field with a magnetic gradient of up to 280 gauss/cm.*

faint fluorescence to be observed. The second PMT was not always used and sometimes replaced with a CCD camera as seen in figure 5.1. In order not to damage the high gain PMT a high voltage switch was installed that allowed us to switch the supply voltage on and off in less then 1 μs.

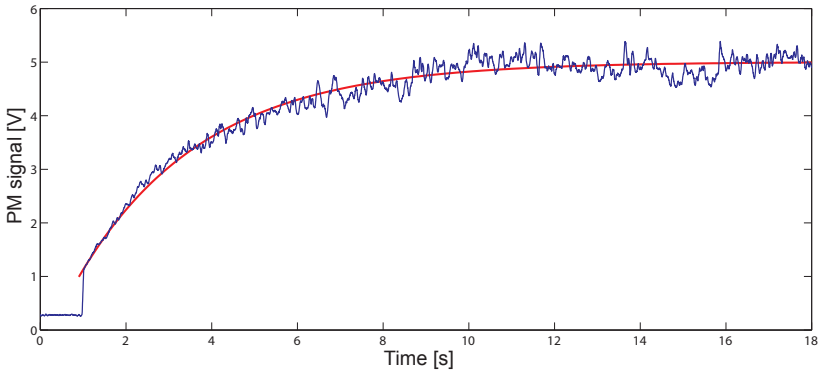

Figure 5.3: *Observed fluorescence on the low gain photomultiplier tube. The fit show a typical timescale of the load rate of about 2 seconds.*

Three beams from the 285 nm laser were sent into the chamber in the x,y and z axis. These beams were retroreflected which would generate a UV MOT when choosing appropriate polarizations. The beams were about 5 mm in diameter and with a magnetic gradient of 170 gauss/cm this gives a capture velocity of 50 m/s. Integrating the maxwell-boltzman distribution from 0 to V_{cap} gives a fraction of 10^{-5} of captured atoms from the thermal beam. At a oven temperature of 710 K the estimated flux is about 10^{12} s^{-1} giving a MOT load of $1.4 \cdot 10^7 s^{-1}$ [44], [70]. A plot of the fluorescence from the MOT is seen in figure 5.3 as atoms are loaded into the trap. When the MOT reaches equilibrium a total of $\sim 4 \cdot 10^7$ atoms are trapped in the UV MOT. The dominant loss from the MOT is two photon ionization where two 285 nm photons put the atoms into the continuum. The temperature has previously been measured by ballistic expansion which can be calculated, by using [71], [72], to 4 mK which is about twice the Doppler temperature.

The beam from the 880 nm laser, see section 3.5, was made to overlap the X-axis UV beam and a dichroic mirror on the other side of the chamber gave the possibility to retroreflect the beam. Just before entering the chamber a $\lambda/4$ plate could be inserted in order to investigate polarization dependencies.

To detect the metastable atoms a 383 nm laser was utilized that could optically pump the atoms into the $^3P_1$ state that would decay back to the ground state in 4 ms. In order to switch the laser beam on and off the beam was passed through a 275 MHZ AOM and the 1'order was sent to the experiment. The switching of the AOM was done with a high isolation switch (ZASWA-2-50DR+) from minicircuits giving a 95 dB isolation. The high isolation was later found to be crucial to the experiment. The 2000 s lifetime of the $^3P_2$ state meant that even faint light would cause a change to the measured lifetime. A mechanical shutter was later installed in addition to the AOM in order to completely block the light and scattered light from lenses, mirrors, etc. The 1'order beam was then overlapped with the 880 nm beam in the x-axis. This beam was single passed through the chamber. The 383 nm laser was frequency locked to the beamline as described in section 4.1. The laser was frequency modulated by a local oscillator sent to the current modulation on the diode control box. The width of the frequency

modulation was determined to be 1 MHz which is well below the 25 MHz natural linewidth of the $^3P_2$ to $^3D_3$ transition.

5.2 Measurement of the $(3s3p)^3P_1$ Lifetime

Magnesium has several long-lived metastable states. An accurate method for determining the lifetime of the metastable states are described in the following sections. The first lifetime we determined was that of the relatively short lived $(3s3p)^3P_1$ state. The method utilized the Magnesium UV MOT where atoms are trapped in the $(3s^2)^1S_0$ state. By optical pumping using the 457 nm laser, atoms in the ground state were excite to the $(3s3p)^3P_1$ state. Some of the atoms that were optically pumped into the $(3s3p)^3P_1$ state would be magnetically trapped in the magnetic quadropole trap. The magnetically trapped atoms would then decay back to the ground state where they would be recaptured by the UV MOT. This method allowed us to accurately determine the lifetime of the $(3s3p)^3P_1$ state which was found to be 4.4 $\pm$ 0.2 ms.

5.2.1 Experimental setup

This experiment is not the first to determine the lifetime of the $(3s3p)^3P_1$ state. The lifetime of the $(3s3p)^3P_1$ state has been measured several times and there still exist a discrepancy between the experimental determined lifetime and the theoretically calculated value.

The lasers used in the determination of the lifetime of the $(3s3p)^3P_1$ are the 457 nm laser and the 285 nm laser described in 3.1 and 3.3. The relevant atomic transitions are shown in figure 5.4.

The 285 nm UV MOT setup described in section 5.1 was used to trap and cool a sample of magnesium atoms down to about 4 mK. The cold sample of magnesium atoms in the $(3s^2)^1S_0$ state was then optically pumped by exposing the atoms to a 1 ms pulse of 457 nm light in order to excite

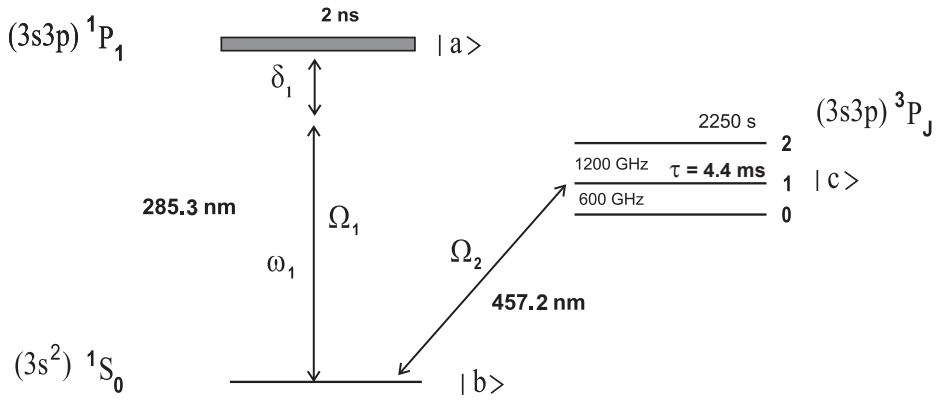

Figure 5.4: *Energy levels relevant for the lifetime measurement of the metastable (3s3p)$^3P_1$ state of the ^{24}Mg isotope. The involved levels are labeled $|a\rangle$, $|b\rangle$ and $|c\rangle$ respectively.*

them to the (3s3p)^{3}P$_1$ state. We transfer as much as 85% of the atoms in the UV MOT to the magnetically trapped (3s3p)^{3}P$_1$ |J = 1, m$_j$ = +1 $\rangle$ substate. Statistically and from symmetry about 1/3 of the atoms should be magnetically trapped. Because of the magnetic quadropole field the atoms in the MOT will be exposed to both σ_+ and σ_- light as they are located on both sides of B = 0. In order to boost the efficiency of the optical pumping into the magnetically trapped substate the atoms are displaced form the center of the MOT by making a small imbalance in the UV light force. By misalignment of the UV MOT and by opticcally pumping with circularly polarized light the atoms will only be pumped into 1 substate. We have solved the optical bloch equations (OBE) for the 3 level system shown in figure 5.4. The solution to the OBE can be seen in figure 5.5 for the 3 level V system.

The experiment start with a loaded UV MOT shown in part A in figure 5.5. As the 457 nm light is switched on the UV fluorescence in part B is seen to decrease to a new steady state. It can be shown that the UV fluorescence decay exponentially in part B [68]. The 457 nm light is then switched off after the atoms have reached a steady state. The 457 nm light is the turned off again and the steady state (3s3p)^{3}P$_1$ population will then start to decay

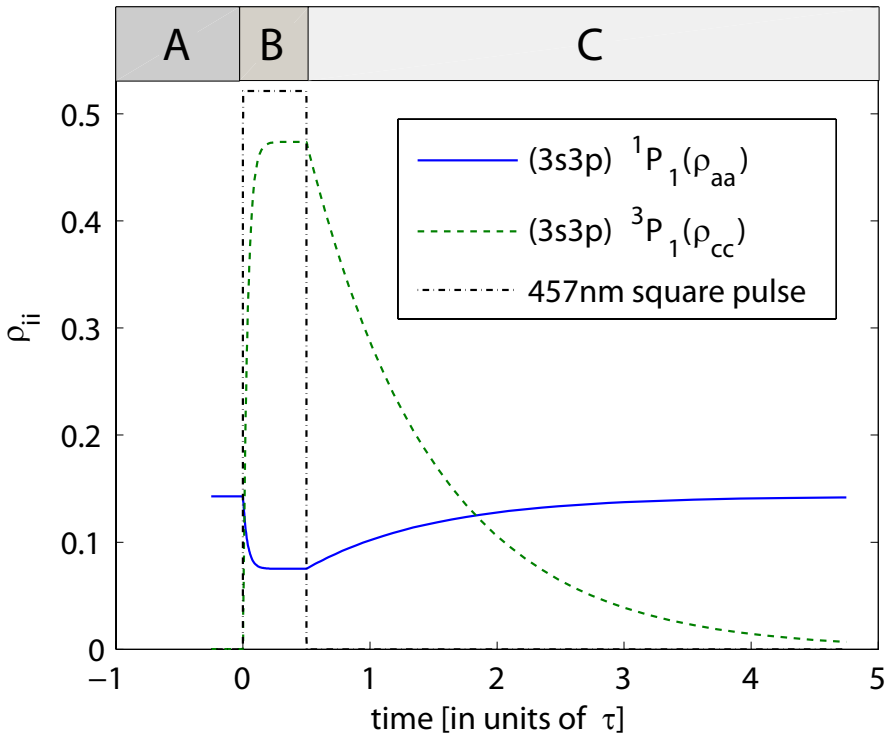

Figure 5.5: *The number of atoms in the excited $(3s3p)^1P_1$ (ρ_{aa}) and $(3s3p)^3P_1$ (ρ_{cc}) states during the pulsed experiment. Time is in units of τ. The signal monitored in our experiment is proportional to the fluorescence determined by (ρ_{aa}).*

as seen in part C. As the metastable atoms decay they are recaptured into the UV MOT and the UV fluorescence signal increases

$$S(t) = N_0(1 - e^{-t/\tau}), \tag{5.1}$$

with the time constant τ of the $(3s3p)^3P_1$ lifetime. The time evolution of the UV fluorescence signal is controlled by three time scales: the metastable state lifetime of 4 ms, the UV MOT lifetime of 4 s, and the magnetic trap lifetime of more then 20 s. The lifetime of the magnetic trap can be disregarded on the short timescale of 40 ms. The rate equation for the number of

atoms in the UV MOT is then given by:

$$\dot{N} = \frac{N_0}{\tau}(e^{-t/\tau}) - \alpha N(t) + L, \tag{5.2}$$

where N_0 is the number of metastable atoms trapped in the magnetic trap, and L is the load rate from the atomic beam. The solution of equation (5.2) becomes:

$$N(t) = \frac{\gamma_{cc}}{\gamma_{cc} - \alpha} N_0 \left(e^{-\alpha t} - e^{-\gamma_{cc} t}\right) + \frac{L}{\alpha}(1 - e^{-\alpha t}) \tag{5.3}$$

with $\gamma_{cc} = 1/\tau$. If the atomic shutter is closed during the measurement the last term of equation 5.3 is equal to zero.

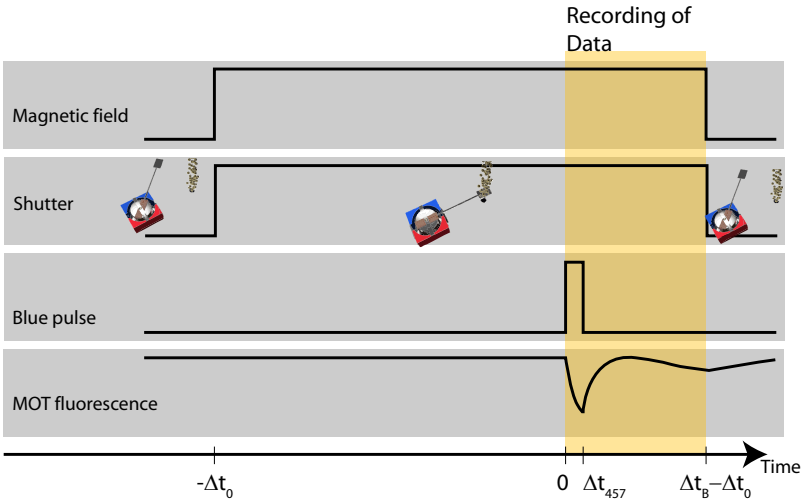

Figure 5.6: *Time-line of an experiment. The signals controlling the magnetic field and the shutter are started simultaneously. Due to the response time of the shutter, the blue pulse is not initiated before a few hundred milliseconds after the shutter signal. The time of the pulse, controlling the magnetic field and the shutter, is typically* 500 *ms, while the blue pulse lasts* $0.1 - 5$ *ms. The time of recording is* 100 *ms.*

In the actual experiment the 457 nm laser had a estimated linewidth of about 1 MHz. Due to power broadening, doppler effect, and zeeman shift

of the ground state atoms the metastable state is easily populated. In order to switch the 457 nm light on and off the light was sent through a AOM. The 457 nm beam has a diameter of 1.5 mm which is comparable in size with the UV MOT. The 457 nm beam is spatially overlapped with the UV beams and in the experiment were tested with both a single passed or a retroreflected beam. The experiment is controlled by a computer running a Labview program that execute a sequence in a loop. The four key parameter controlled by the computer is the magnetic field, atomic beam shutter, and 457 nm light pulse. The sequency for the experiment can be seen in figure 5.6.

5.2.2 Results

Figure, 5.7 shows data obtained when the experimental sequence shown in figure 5.6 is performed. The data obtained show the UV fluorescence just before the 457 nm light is flashed and subsequent dynamics. The discontinuous UV MOT fluorescence observed when the 457 nm light is turned on is due to scattered blue light. When the 457 nm light is switched off the UV MOT is seen to reload and this fluorescence is fitted. due to a poor serve loop on the UV SHG cavity large fluctuations are observed on UV intensity. In order to compensate for these fluctuations the fluorescence signal is divided with a normalized UV power signal from one of the UV beams. After 15 ms a weak decay of the UV fluorescence is observed due to linear losses from the 3 seconds lifetime of the MOT. The linear losses from the UV MOT are caused by two photon ionization [73] and collisions with the background gas. The Vacuum pressure in the MOT chamber was $3{\cdot}10^{-10}$ mbar when the experiment was performed.

In figure 5.7, the red curve is the fit to equation 5.3 which when fitted to the data gives a $\tau = 4.4$ ms lifetime. In total 80 measurements were obtained for different settings in order to investigate systematic effects. For example the effect of the magnetic gradient and recapture fraction was investigated. By using a $\lambda/4$ plate the polarization of the 457 nm light was tested and a clear difference between the two helicity could be observed on the recapture

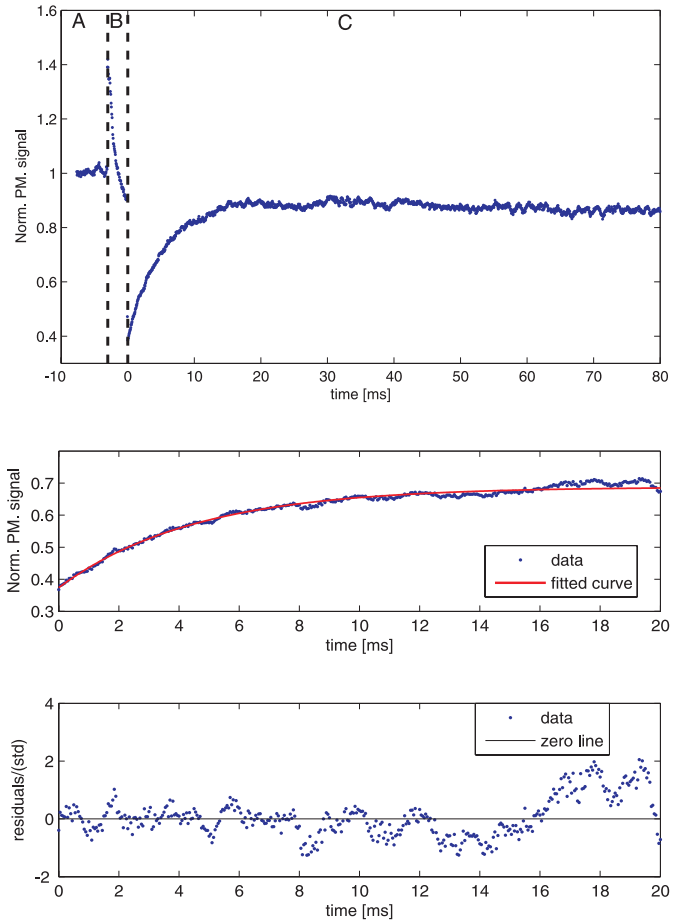

Figure 5.7: *Typical MOT fluorescence measurement, here normalized to the UV power level. The interval marked with dashed lines show the 457 nm pulse. As the 457 nm light is turned on, additional background photons are observed. After a load period of about 10 ms, the signal slowly decays due to the 4-5 second MOT lifetime. Lower two graphs: the red curve is a fit to equation (5.3), results in a lifetime of 4.4 ms. The lower part shows the residuals of the fit.*

fraction. The best signal to noise was obtained for the largest magnetic gradient. The 34 measurements performed at the maximum gradient tested (216 gauss/cm) were used in the quoted lifetime measurement.

From figure 5.7, when the UV fluorescence is subtracted from the fitted curve the residual signal is seen to fluctuate. These fluctuations are not due to

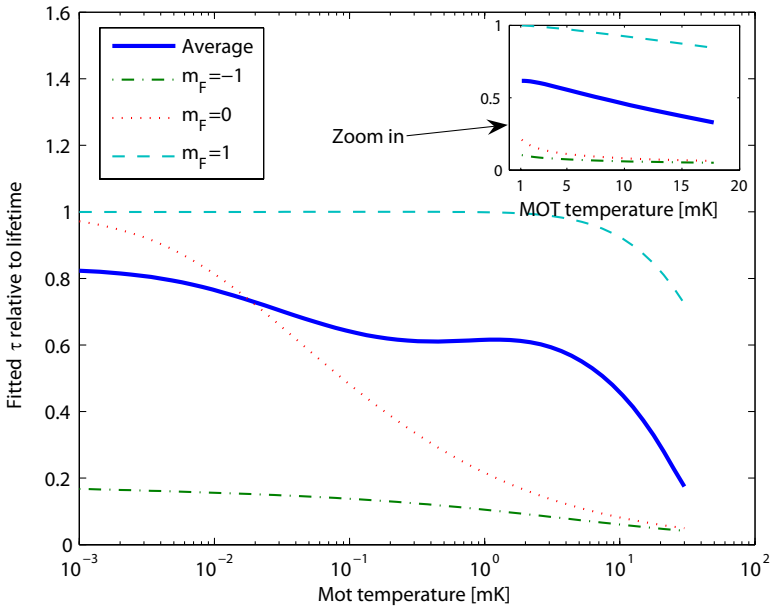

Figure 5.8: *Plot of the fitted values of the lifetime τ relative to the "true" lifetime (here set to 5 ms) based on the 1D simulation of the classical motion of the $^3P_1$ atoms as a function of the MOT temperature. The inset shows a zoom of the plot on a linear temperature scale [74]. It is seen that both for $m_F = 0$ and $m_F = -1$, the measurements are only about one tenth of the true lifetime. This leads to a measurement of τ made on the average signal of the three levels (assuming equal populations of the three magnetic substates), which is still significantly lower than the true lifetime.*

UV power fluctuations as these have been removed already by the normalized power signal. The fluctuations are believed to be frequency fluctuations of the dye laser. Frequency fluctuations will obviously cause a change to the observed UV fluorescence even when the UV power is constant. When the frequency is close to the corresponding lifetime it will cause shot to shot noise on the measured lifetime. The shot to shot noise result in a standard deviation of 0.9 ms for the 34 measurements. This gives a final result of $\tau = 4.4 \pm 0.16$ ms.

The UV power fluctuations and frequency modulation of the laser will affect the temperature of the MOT. The measured lifetime of the $(3s3p)^3P_1$ is dependent on the temperature. The relative long lifetime of the $(3s3p)^3P_1$

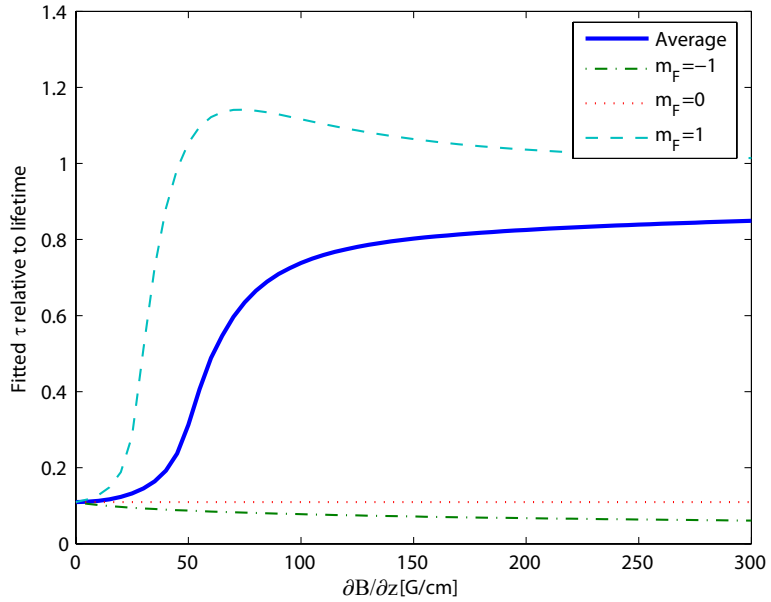

Figure 5.9: *Plot of the fitted values of τ relative to the lifetime as a function of the gradient of the magnetic field for a MOT temperature of 5 mK [74]. It is seen that both for $m_F = 0$ and $m_F = -1$, the measurements are only about one tenth of the true lifetime. This leads to a measurement of τ made on the average signal of the three levels, that is still significantly lower than the true lifetime. For $m_F = 1$, the measured τ is in good agreement with the true lifetime for gradients larger than 200 G/cm.*

state compared to the classical motion means some atoms will be able to escape the MOT region before decaying. This loss from the magnetic trap gives a dependence on the recapture rate. We therefore investigated these dependencies with a 1D simulation of classical motion of atoms in the trap. The recapture fraction is determined and is shown in figure 5.8. In the figure the recapture efficiency is shown when exciting the different substates. The magnetically trapped substate is of course insensitive to MOT temperature however the two untrapped substates are not. The substate $|J = 1, m_j = -1\rangle$ will see a repulsive force from the trap and so it will leave the MOT region faster then the $|J = 1, m_j = 0\rangle$ substate which has a higher recapture efficiency. From figure 5.8 it can also be seen that the polarization of the 457 nm light will have a strong dependence on the measured lifetime. Ideally

one would want to have a spin-polarized sample and expose them to circular polarized light exciting the $|J = 1, m_j = +1\rangle$ substate. The lifetime of the $(3s3p)^3P_1$ state also have a dependence on the magnetic field. Using the 1D simulation we have also investigated the magnetic gradient dependence on the lifetime and the result can be seen in figure 5.9. At very low magnetic gradients the 3 substates have similar recapture efficiency which for the measured UV fluorescence would fit to about $0.1{\cdot}\tau$. As the magnetic gradient is increased the magnetically trapped substate will begin to be recapture and a subsequent increase in the fitted lifetime. At a high magnetic gradient the measured lifetime will be the least sensitive. From figure 5.8 and 5.9 it is seen that a cold spin-polarized gas is preferable however because of these dependencies the lifetime must be assumed to be a lower limit.

In Table 5.1 the experimental and theoretical investigation of the $(3s3p)^3P_1$ lifetime are compared. The experimental determined lifetimes seem to be consistently higher then the theoretically calculated lifetimes. In our treatment we have assumed the decay from $(3s3p)^3P_1$ to $(3s^2)^1S_0$ to be the only decay channel which should be a good approximation.

Theoretical			Experimental		
'Reference	Year	τ [ms]	Reference	Year	τ [ms]
[75]	2004	2.8(1)	This work	2006	4.4(2)
[76]	2002	3.8	[79]	1992	5.3(7)
[77]	2001	3.6	[80]	1982	4.8(8)
[78]	1979	4.60(4)	[81]	1975	4.5(5)
			[82]	1975	4.0(2)

Table 5.1: *Collection of most recent calculated and measured $(3s3p)^3P_1$ lifetimes.*

5.2.3 Conclusion

In conclusion we have measured the metastable ^{24}Mg (3s3p)^{3}P$_1$ lifetime and found a value of 4.4 ± 0.2 ms. This measured lifetime is the most accurate to date as seen from table 5.1 and in good agreement with previous experimental determined lifetimes. The theoretical calculated values for the lifetime seem to be going toward shorter lifetimes increasing the discrepancy between theory and experiment which is at present not understood.

5.3 Measurement of the spin-forbidden decay rate $(3s3d)^1D_2 \rightarrow (3s3p)^3P_{1,2}$ in ^{24}Mg

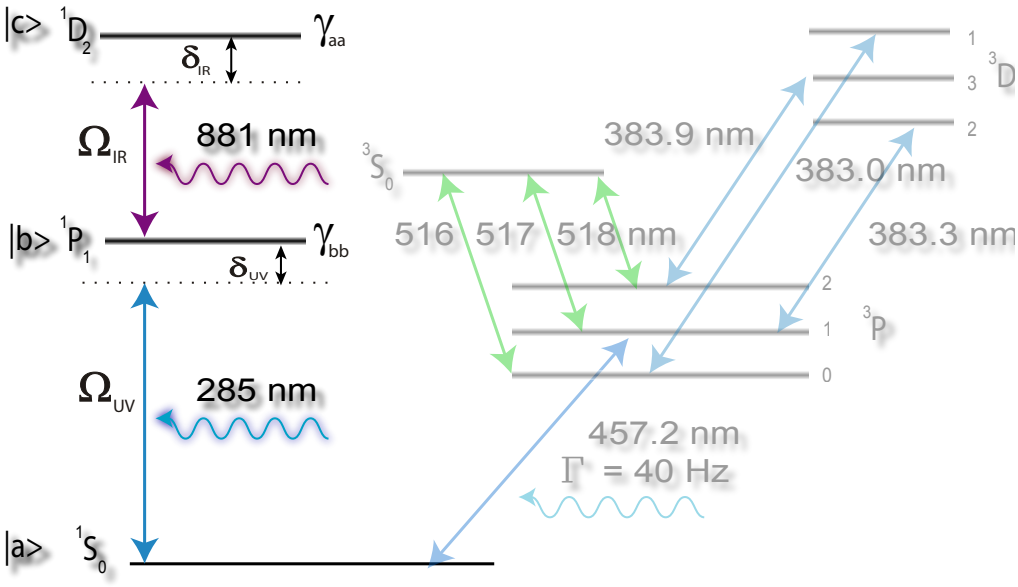

Figure 5.10: *The three level cascade system considered for magnesium. The lasers driving the UV and IR transitions is shown with the laser detuning δ_{UV} and δ_{IR}. The natural linewidth of the transitions is denoted γ_{aa} and γ_{bb}.*

Many attempts has been made to cool magnesium below the doppler temperature of the UV transition at 285 nm. A thorough investigation had already been carried out in the group on the two photon transition in order to investigate the possibility of two photon cooling , [68], [83]. The temperatures measured on Mg atoms cooled with the two photon transition shows a temperature close to the doppler temperature. The presence of a decay channel means that atoms being cooled by the two photon transition ie. excited to the $^1D_2$ state will have a probability to decay out of the cooling cycle and into the $^3P_{1,2}$ metastable states. This means that a reduction in atoms in the UV MOT is observed. Some of the atoms that decay out of the cooling cycle will however be confined by the MOT's magnetic quadrupole field. The

generation of metastable magnesium is done via a two photon transition that excited the ^{1}D$_2$ state which has a decay channel down to the ^{3}P$_{1,2}$ state. This decay requires a low probability spin flip to occur, from a singlet state to a triplet state, which gives this decay transition a 200 s^{-1} deacay constant.

In this section I will briefly describe the optical block equations used to describe the two photon transition. Followed by a description of the experiment done on the decay rates and the results.

For the case of the bosonic isotope ^{24}Mg the two photon transition on the cascade system ^{1}S$_0$ - ^{1}P$_1$ - ^{1}D$_2$ is considered as seen in figure 5.10. This system is nearly an ideal 3 level system with only a weak decay from the upper level. In figure 5.11 the notation is shown for the 3 level system. The states $|a>$, $|b>$ and $|c>$ correspond to the ^{1}S$_0$, ^{1}P$_1$ and ^{1}D$_2$. We use the 285 nm UV laser to drive the ^{1}S$_0$ - ^{1}P$_1$ transition and the 880 nm laser to drive the ^{1}P$_1$ - ^{1}D$_2$ transition. The corresponding laser frequencies of the two lasers are denoted ω_{UV} and ω_{IR}. For the UV transition the natural linewidth is 79 MHz which gives a doppler temperature of 1.9 mK. The natural linewidth of the upper state is much smaller then the UV linewidth which is what the two photon cooling takes advantage of. The two photon cooling is basically a Electromagnetically induced transparency (EIT) experiment where the purpose is to suppress the UV fluorescence in order to get a effective γ_{eff} smaller then that of the UV transition. The populations of $|a>$, $|b>$ and $|c>$ are described by the density matrix. The Optical Block Equations (OBE) give the equation of motion for the density matrix ρ. The time evolution of the density matrix is then solved for the hamiltonian of our system. The time evolution of the density matrix is then written as [84]

$$\dot{\rho} = -\frac{i}{\hbar}[\hat{H}, \rho] \tag{5.4}$$

The differential equations for each of the elements in the density matrix can

then be calculated using:

$$\dot{\rho}_{nm} = -\frac{i}{\hbar}\langle n|[\hat{H},\rho]|m\rangle \tag{5.5}$$

$$= \frac{i}{\hbar}\sum_k \langle n|\hat{H}|k\rangle\langle k|\rho|m - \langle n|\rho|k\rangle\langle k|\hat{H}|m\rangle \tag{5.6}$$

It is however necessary to include the spontaneous decay and the equation of motion for the density matrix can then be written:

$$\dot{\rho} = -\frac{i}{\hbar}[\hat{H},\rho] - \frac{1}{2}\{\gamma,\rho\} \tag{5.7}$$

where γ is the decay matrix. Assuming the off diagonal elements of the decay matrix to be zero then the OBE for the three level system can be written:

$$\begin{aligned}
\dot{\rho}_{aa} &= \frac{i\,\Omega_{IR}}{2}(\rho_{ba}-\rho_{ab}) - \gamma_{aa}\,\rho_{aa} \\
\dot{\rho}_{bb} &= \frac{i\,\Omega_{IR}}{2}(\rho_{ab}-\rho_{ba}) + \frac{i\,\Omega_{UV}}{2}(\rho_{cb}-\rho_{bc}) + \gamma_{aa}\,\rho_{aa} - \gamma_{bb}\,\rho_{bb} \\
\dot{\rho}_{cc} &= \frac{i\,\Omega_{UV}}{2}(\rho_{bc}-\rho_{cb}) + \gamma_{bb}\,\rho_{bb} \\
\dot{\rho}_{ab} &= i\,\delta_{IR}\,\rho_{ab} + \frac{i\,\Omega_{IR}}{2}(\rho_{bb}-\rho_{aa}) - \frac{i\,\Omega_{UV}}{2}\,\rho_{ac} - \frac{\gamma_{aa}\,\rho_{ab}}{2} - \frac{\gamma_{bb}\,\rho_{ab}}{2} \\
\dot{\rho}_{ba} &= -i\delta_{IR}\rho_{ba} - \frac{i\Omega_{IR}}{2}(\rho_{bb}-\rho_{aa}) + \frac{i\Omega_{UV}}{2}\,\rho_{ca} - \frac{\gamma_{aa}\rho_{ba}}{2} - \frac{\gamma_{bb}\rho_{ba}}{2} \\
\dot{\rho}_{ac} &= i\,(\delta_{UV}+\delta_{IR})\,\rho_{ac} + \frac{i\,\Omega_{IR}}{2}\,\rho_{bc} - \frac{i\,\Omega_{UV}}{2}\,\rho_{ab} - \frac{\gamma_{aa}}{2}\,\rho_{ac} \\
\dot{\rho}_{ca} &= -i\,(\delta_{UV}+\delta_{IR})\,\rho_{ca} - \frac{i\,\Omega_{IR}}{2}\,\rho_{cb} + \frac{i\,\Omega_{UV}}{2}\,\rho_{ba} - \frac{\gamma_{aa}}{2}\,\rho_{ca} \\
\dot{\rho}_{bc} &= i\,\delta_{UV}\,\rho_{bc} + \frac{i\,\Omega_{UV}}{2}(\rho_{cc}-\rho_{bb}) + \frac{i\,\Omega_{IR}}{2}\,\rho_{ac} - \frac{\gamma_{bb}}{2}\,\rho_{bc} \\
\dot{\rho}_{cb} &= -i\,\delta_{UV}\,\rho_{cb} - \frac{i\,\Omega_{UV}}{2}(\rho_{cc}-\rho_{bb}) - \frac{i\,\Omega_{IR}}{2}\,\rho_{ca} - \frac{\gamma_{bb}}{2}\,\rho_{bc}
\end{aligned}$$

The solution to the above differential equations can be solved numerically provided no loss out of the system:

$$\rho_{aa} + \rho_{bb} + \rho_{cc} = 1 \tag{5.8}$$

For the case of magnesium this is valid since the decay out of the system is weak compared to the lifetime of the ^{1}D$_2$ state. For the treatment here the system is assumed to be in a steady state giving $\dot{\rho} = 0$.

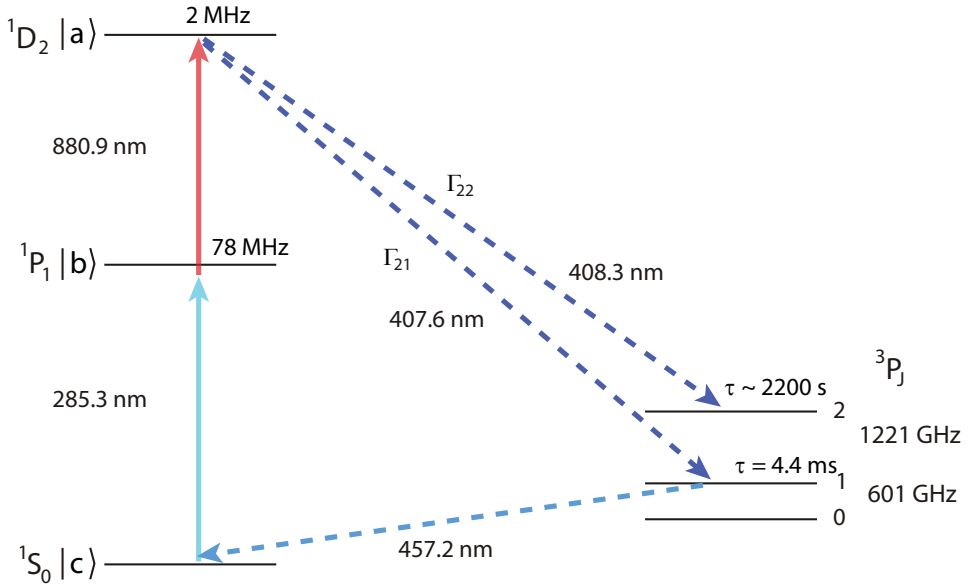

Figure 5.11: *Overview of the magnesium atom. Solid lines illustrate transitions excited with laser light, while dotted lines denote the measured decays.*

The decay out of the ^{1}D$_2$ to the triplet states is shown in figure 5.11 and Γ_{21} and Γ_{22} are the spin-forbidden decay rates out of the system. The rate equation for for the number of atoms in the MOT when the 880 nm light is on is:

$$\dot{N} = L - \rho_{aa}\,(\Gamma_{22} + \Gamma_{21})N - \alpha\, N \tag{5.9}$$

$$= L - N\,(\rho_{aa}(\Gamma_{22} + \Gamma_{21}) + \alpha) \tag{5.10}$$

As is the case in the experiment the number of atoms in the MOT is in a steady state $\dot{N} = 0$. With the steady state and when the 880 nm light is on equation 5.10 yields

$$N_{st} = \frac{L}{\rho_{aa}\left(\Gamma_{22} + \Gamma_{21}\right) + \alpha} \tag{5.11}$$

The rate equation giving the number of 285 nm photons with the 880 nm light on is then:

$$\begin{aligned} S^{on} &= \rho_{bb}^{on}\, N_{st}\, \Gamma_{bb} && (5.12)\\ &= \rho_{bb}^{on}\, \Gamma_{bb}\, \frac{L}{\rho_{aa}\left(\epsilon\, \Gamma_{21} + \Gamma_{22}\right) + \alpha^{on}} && (5.13)\\ &= \rho_{bb}^{on}\, \Gamma_{bb}\, \frac{\alpha^{off}\, N_0}{\rho_{aa}\left(\epsilon\, \Gamma_{21} + \Gamma_{22}\right) + \alpha^{on}} && (5.14) \end{aligned}$$

where α^{on} and α^{off} is the MOT loss when the 880 nm light is either on or off.

Since the experiment only takes a few seconds, the atoms decaying into the ^{3}P$_2$ state is considered to be lost. The atoms decaying into the ^{3}P$_1$ state is however not all lost. Those that decay into a magnetically trapped state will remain inside the MOT region and when decaying will be recaptured. The atoms in the ^{3}P$_1$ state are considered to be lost due to the high temperature of the MOT. The total decay rate is then modified to $\epsilon\, \Gamma_{21} + \Gamma_{22}$. The value of ϵ will have a strong dependence on the polarization of the UV and IR beam. If the 880 nm light is now switched on and off we can take the ratio:

$$\begin{aligned} \frac{S^{on}}{S^{off}} &= \frac{S^{on}}{\rho_{bb}^{off}\, \Gamma_{bb}\, N_0} && (5.15)\\ &= \frac{\rho_{bb}^{on}}{\rho_{bb}^{off}}\, \frac{\alpha^{off}}{\rho_{aa}\left(\epsilon\, \Gamma_{21} + \Gamma_{22}\right) + \alpha^{on}} && (5.16)\\ &= \frac{\alpha^{off}\, \rho_{bb}^{on}/\rho_{bb}^{off}}{\rho_{aa}\left(\epsilon\, \Gamma_{21} + \Gamma_{22}\right) + \alpha^{off}\, \frac{\rho_{bb}^{on}}{\rho_{bb}^{off}}} && (5.17) \end{aligned}$$

Since the photo ionization is proportional to α the relationship $\frac{\rho_{bb}^{on}}{\alpha^{on}} = \frac{\rho_{bb}^{off}}{\alpha^{off}}$ has been used.

These values basically only apply to a small region of the MOT since the zeeman effect from the magnetic quadroploe field from the MOT coils will shift the two transitions. It is therefore necessary to sum over the entire MOT. Since the optical transition is a lorentzian and the MOT distribution is that of a gaussing the resulting convolution is a Voight profile. This profile is used for all the calculations.

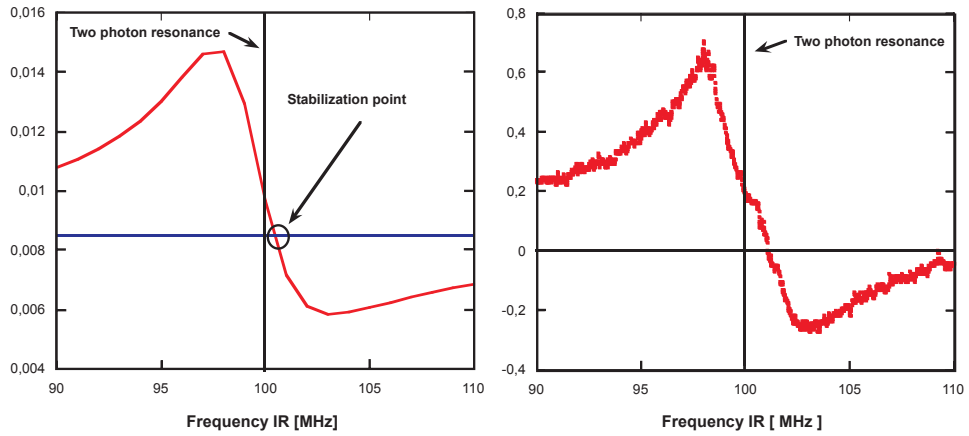

Figure 5.12: *The 881 nm laser is frequency stabilized to the two photon resonance of the ladder system $\nu_{881} = -\nu_{285}$ =100 MHz. This ensures a maximal population transfer to the $(3s3d)$ ^{1}D$_2$. Left part of the figure shows the $(3s3p)^1P_1$ excited state fraction obtained from the optical Bloch equations. The right part shows the experimental photomultiplier signal.*

The actual experiment was done with the Ti:sapphire laser generating light at 880 nm. The light was sent through an AOM that allowed the light to be amplitude modulated at 1 kHz and run at a 20% duty cycle. A $\lambda/2$ plate and a polarization beam splitter allowed us to change the 880 nm power. Just before the MOT chamber a $\lambda/4$ plate could be inserted in order to check the two circular polarizations. A interference filter was used to insure the photomultiplier tube was insensitive to 880 nm light. With the 880 nm light being modulated a change in the UV fluorescence was observed. This was observed on a oscilloscope. Since the 880 nm AOM was modulated with a square TTL pulse the observed fluorescence had a similar step. The size of the step was mapped out and is shown in figure 5.12 along with a theoretical

solution to the OBE. Since no frequency reference was available when the experiment was carried out, the laser was frequency stabilized to the two photon resonance by observing the change in the fluorescence as the 880 nm light was modulated. The two photon resonance was mapped out for several different IR Rabi frequencies and the experimental values of equation 5.17 as a function of the IR Rabi frequency is shown in figure 5.13 where the helicity is the same as for the MOT. For figure 5.14 here the polarization is opposite to the MOT helicity.

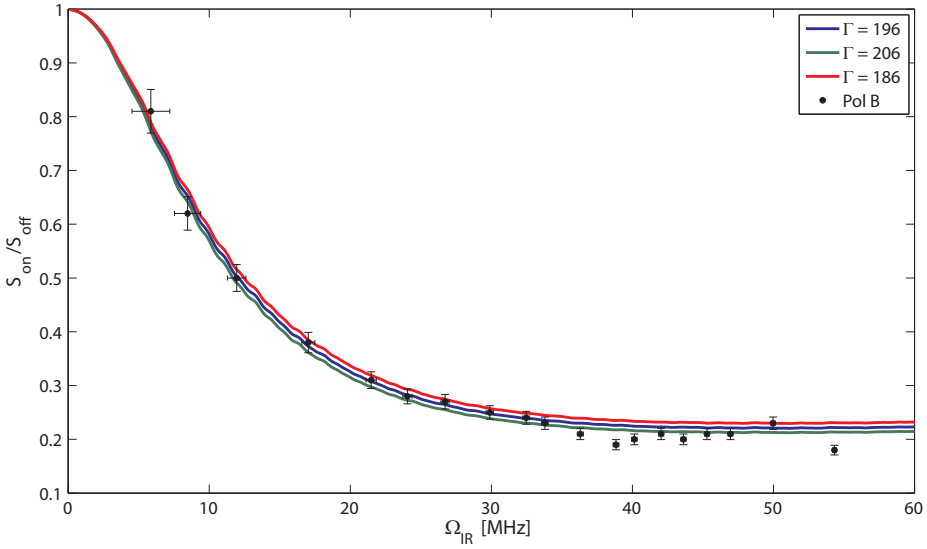

Figure 5.13: *Experimental results of the ratios $\frac{S^{on}}{S^{off}}$ for various values of the IR Rabi frequency and circularly polarized light. Also plotted are the corresponding simulated curves for various values of Γ with $\delta_{UV} = 100$ MHz, $\Omega_{UV} = 20$ MHz, $\alpha = 0.175$, corresponding to the MOT operating conditions. The vertical errorbars shown are $\pm 5\%$ and the horizontal errorbars correspond to an uncertainty in determination of the 881 nm power of 0.1 mW.*

The experimental values with the polarization corresponding to the MOT helicity support a value of $\Gamma_{21} + \Gamma_{22} = (196 \pm 10)$ s^{-1} in good agreement with theoretical calculations [77]. When using the polarization opposite to the MOT helicity we find a $\Gamma = (150 \pm 15)$ s^{-1}. By using $\epsilon = 2/3$ found in [77] we get $\Gamma = 2/3\Gamma_{21} + \Gamma_{22} = 153$ s^{-1} and by using simple 1D models of the MOT we obtain $\Gamma_{21} = 138$ s^{-1} and $\Gamma_{22} = 57$ s^{-1}

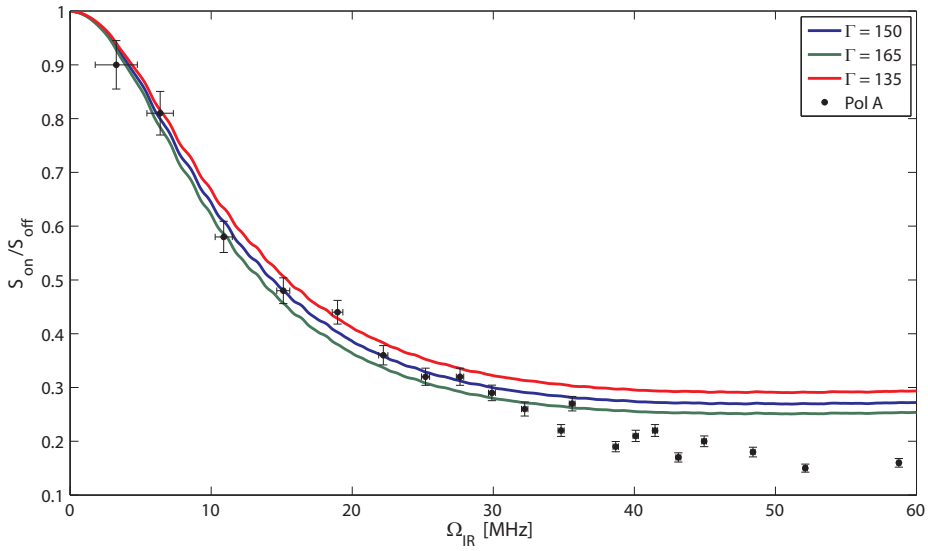

Figure 5.14: *Experimental results of the ratios* $\frac{S^{on}}{S^{off}}$ *for various values of the IR Rabi frequency and circularly polarized light. Also plotted are the corresponding simulated curves for various values of* Γ *with* $\delta_{UV} = 100$ *MHz,* $\Omega_{UV} = 20$ *MHz,* $\alpha = 0.175$*, corresponding to the MOT operating conditions. The vertical errorbars shown are* $\pm 5\%$ *and the horizontal errorbars correspond to a uncertainty in determination of the 881 nm power of 0.1 mW.*

5.4 Determination of the (3s3p)^{3}P$_2$ Lifetime

In the following section I will describe the measurement of the ^{3}P$_2$ lifetime and the results. The experiment was carried out in the setup described in section 5.1 where a sample of metastable atoms were prepared and trapped in the magnetic trap. A sample of atoms in the ^{3}P$_2$ state will not be confined forever in such a trap. The main losses are due to collisions with the background gas that typically give the sample a lifetime of 10-20 s. Another type of loss is due to decay of atoms in the ^{3}P$_2$ state back to the ground state. The ^{3}P$_2$ state however is a long lived state with a expected lifetime of approximately 2000 s. There is another loss mechanism caused by ^{3}P$_2$ atoms colliding inelastically and this is examined later. The most obvious way to determine the lifetime would be to plot the exponential decay of atoms out of the ^{3}P$_2$ state. A exponential fit to this will however just show the lifetime due to the background gas as this is much shorter than the ^{3}P$_2$ lifetime due to the magnetic quadropole transition. It should be noted that the lifetime of 3 s for neutral magnesium in the UV MOT is considerably shorter due to two photon ionization and collisions with the thermal beam so the MOT is therefore not limited by the background pressure. A more clever way is to count the number of atoms decaying from the sample. If the total number of atoms is known then the decay rate, γ can be found from

$$\frac{dN_{^3P_2}(t)}{dt} = -\Gamma \cdot N_{^3P_2}(t) \tag{5.18}$$

From 5.18 it is apparent that if the fraction

$$\frac{\frac{dN_{^3P_2}(t)}{dt}}{N_{^3P_2}(t)} = \Gamma \tag{5.19}$$

is known then gamma can be determined at any time, t. In our case, the number of atoms in the magnetic trap is roughly 10^6 which would emit

10^6 photons in all solid angles. The photons that would enter our detector would then be roughly 10^3 photons which means the detector need to use single photon counting. We utilize the UV MOT where atoms decaying from the $^3P_2$ state are captured by the overlapping UV MOT. An atom in the UV MOT that absorbs a UV photon is excited into the $^1P_1$ state and from there it will decay back to $^1S_0$. Since the UV transition is a closed loop a atom can emit millions of photons given by the scattering rate of the UV transition. This generate a much larger signal since a single atom scatter many photons while a atom decays only emits a single atom. This allows us to detect the number of atoms decaying from $^3P_2$ into $^1S_0$ with a PMT.

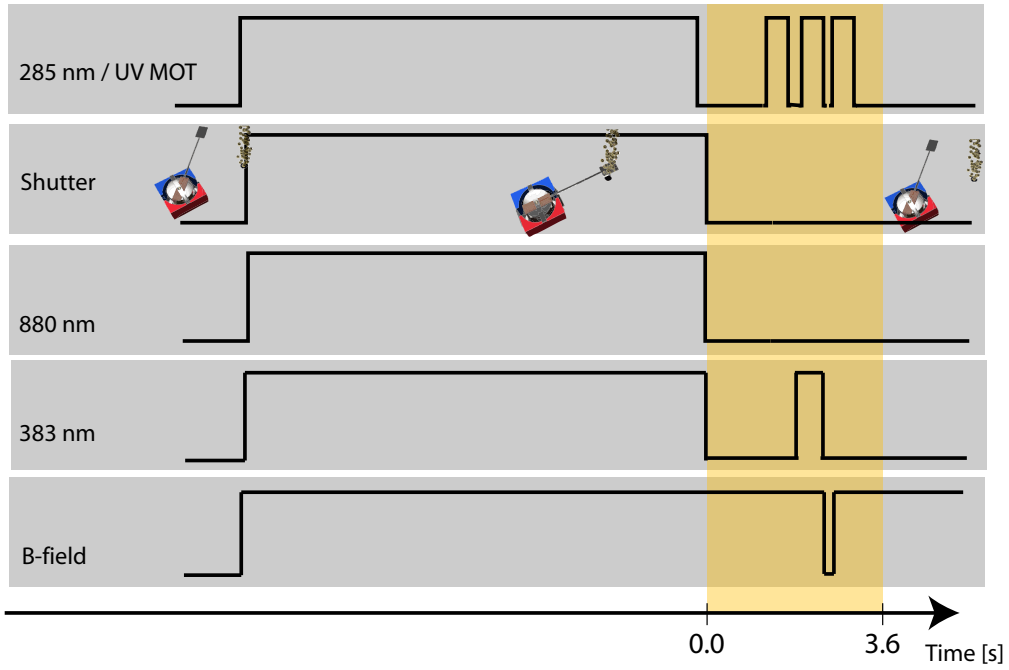

Figure 5.15: *The time-line of the experiment. The computer controls the UV light, 880 nm light, 383 nm light, atomic beam shutter, B-field, and the high gain PMT is sqitched on in the highlighted area.*

The actual experiment is carried out in a looped sequence which is sketched in figure 5.15. The sequence consist of first loading up a UV MOT for 5 s while it is being exposed to 880 nm light during the whole loading. As the

UV MOT is exposed to 880 nm light the atoms has a probability to be in the $^1D_2$ state that decays into the metastable states. For this experiment ρ_{aa} is optimized since this is proportional to the load into the metastable magnetic trap, see section 5.3. Once a metastable sample had been prepared the UV and 880 nm laser beams were switched off. With the light forces gone the UV MOT would ballistically expand and after a 10-20 ms no atoms would be observed if the UV MOT were switched back on. In order to be certain that no atoms from the MOT were in the MOT region we waited 200 ms before proceeding. Right after switching off the UV MOT the atomic beam shutter was closed. After 200 ms the UV laser beams were switched on again, however, since the beam shutter was closed, there should not be any load into the UV MOT. When the UV beams were switched on again the high gain PMT was also switched on. The consequent signals observed is shown in figure 5.16 which is the last part of the sequence shown in figure 5.15. The metastable atoms confined in the magnetic trap will decay back to the ground state and since the magnetic trap and the UV MOT are spatially overlaying they will be recaptured into the UV MOT.

The UV MOT therefore experiences a load as seen in figure 5.16 part A with a load roughly linear on this timescale. Next we determine the remaining number of atoms by switching on the 383 nm laser. The 383 nm light is tuned to the $^3P_2$ to $^3D_2$ transition which cause the atoms to be rapidly pumped into the $^3P_1$ state. This state will decay into the ground state with a lifetime of 4 ms. The transfer efficiency is measured to be 66.7% and is investigated later. As the atoms are transferred back into the UV MOT they can be detected with the same high gain PMT. This means that the parameters like the solid angle, quantum efficiency, and gain on the detected signal is identical to the parameters used to observed the slope in Part A. The ratio in 5.19 can therefore be evaluated and from the ratio gamma can be determined. Unfortunately the load into the UV MOT in part A was not only given by the decaying atoms. If the sequence ran without the 880 nm laser on a load was still observed. This load came from background gas consisting of neutral magnesium that was let into the MOT chamber when the atomic beam shutter was open. A beam dump was put into the

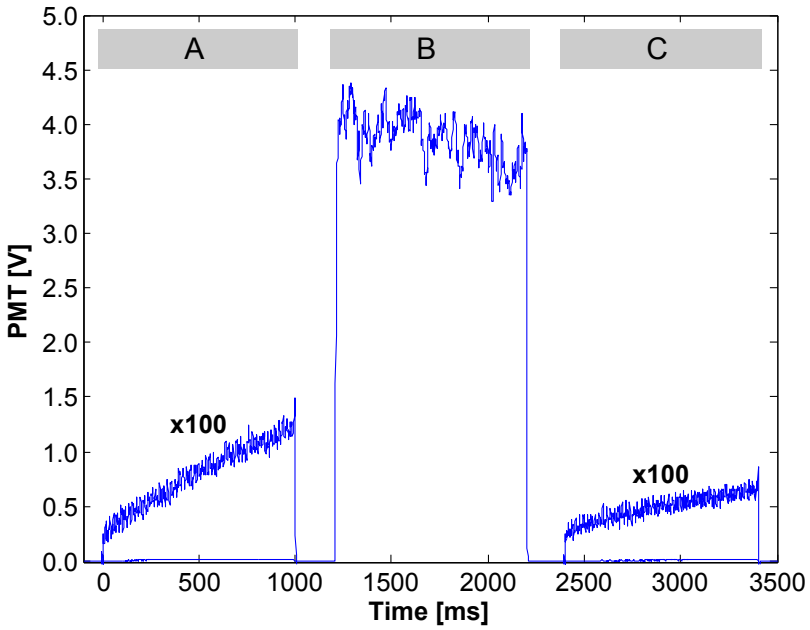

Figure 5.16: *UV fluorescence observed on the high gain PMT from metastable atoms decaying back into the UV MOT. In A the atoms decaying from the $^3P_2$ state are observed. In B all $^3P_2$ state atoms are flashed back into the ground state by the 383 nm laser. In part C the background load without the presence of metastable atoms is observed.*

chamber in order to minimize the background gas from the atomic beam. The beam dump itself consist of a wedged piece of copper that is in thermal contact to a copper feedthrough allowing for cooling of the beam dump. The introduction of a beam dump removed 90% of the background gas however it was not eliminated completely, even when cooling the beam dump with liquid nitrogen. In order to correct for this background load a third pulse of UV light was turned on as shown in figure 5.16 part C. From the changing slope the load of the background gas into part A could be corrected for. The amount of magnesium background gas in the chamber decreased after the shutter was closed due to pumping and is therefore timedependent. Since the background load is determined in part C the actual background load in part A is higher the the measured load in part C. In figure 5.16 a sequence

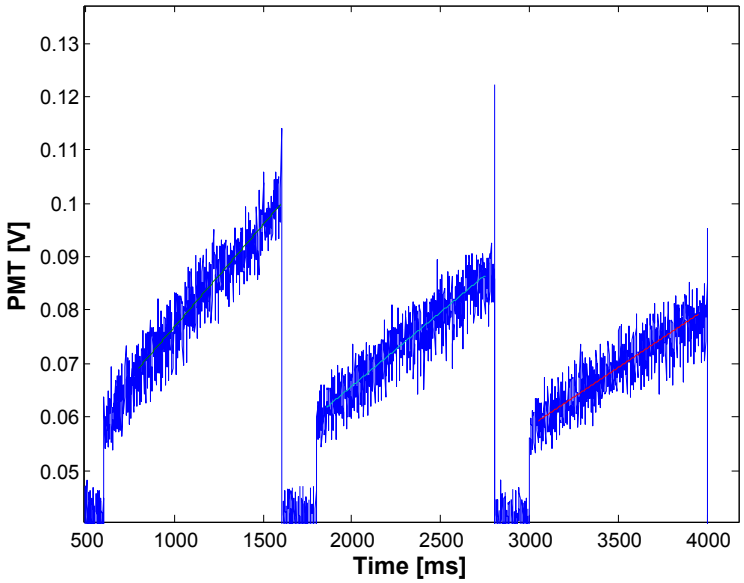

Figure 5.17: *Calibration of the load from the background gas. The load is seen to be time dependent since the slope changes. The longer the atomic shutter has been closed the smaller the slope is.*

similar to 5.15 however without the 880 nm laser on. This time the only load into the UV MOT is from the background gas. As time progressed each load into the MOT decreases as seen in figure 5.17. The exponential decaying load rate was fitted and with the time constant known the load rate in figure 5.16 part A could be corrected for background load.

Since the sequence where the measurement take place is over a 3 s period some corrections to the measured values are needed. For example we measure the remaining atoms in part B however we need to know the total number of atoms in Part A. In order to determine the total number of atoms in part A we determine the lifetime of the metastable atoms trapped in the magnetic trap. We investigated the lifetime in the magnetic trap in several ways. For example it is possible to determine the lifetime by varying the different times in the sequence. We loaded metastable atoms into a magnetic trap and then watched the decay back into the UV MOT and let it run for 100 s. The time evolution of the number of atoms in the MOT is given by the load into

the MOT, the loss of ground state atoms due to two photon ionization and background collisions(α_0), and the decay of the magnetic trapped atoms due to background collisions (α_2). The rate equations for the load and decay can be written:

$$\frac{dN_2}{dt} = -(\alpha_2 + \Gamma_2)N_2 \tag{5.20}$$

$$\frac{dN_0}{dt} = -\alpha_0 N_0 + \Gamma_2)N_2 \tag{5.21}$$

Where N_0 are the number of atoms in the ground state and N_2 are the number of ^{3}P$_2$ atoms. When assuming the number of atoms to initially be zero in the UV MOT, the solution of 5.20 and 5.21 is given by

$$N_0(t) = \frac{N_2^0 \cdot \Gamma_2}{\alpha_2 + \Gamma_2 - \alpha_0}(e^{-\alpha_0 t} - e^{-(\alpha_2+\Gamma_2)t}) \tag{5.22}$$

The fit of 5.22 to the measured data is shown in figure 5.18. The fitted values are found to be $1/\alpha_0 = 3$ seconds and $1/\alpha_2 = 16$ seconds. Since $\Gamma >> \alpha_2$ it is unfortunately not possible to find the value of Γ through this fit.

With the decay constants known it is now possible to calculate the number of atoms in the magnetic trap at any time. In order to correct for the time difference between the slope measured in Part A and the remaining atoms in Part B we have $N(t_A) = 1.055 \cdot N(t_B)$.

This principle has been used in other experiments to determine the lifetime [85]. However, given the complicated dynamics of a MOT and different behavior of the various magnetic substates ^{3}P$_1$ (m = 0; $\pm$1) in the MOT quadrupole field, we find it necessary to measure directly the recapture fraction not assuming it to be unity. In a steady state situation where the MOT is running with the optical (3s3p)^{1}P$_1$ - (3s3d)^{1}D$_2$ pumping on, we switch the 383 nm re-pumper on and off on a two second time scale. This leads to a

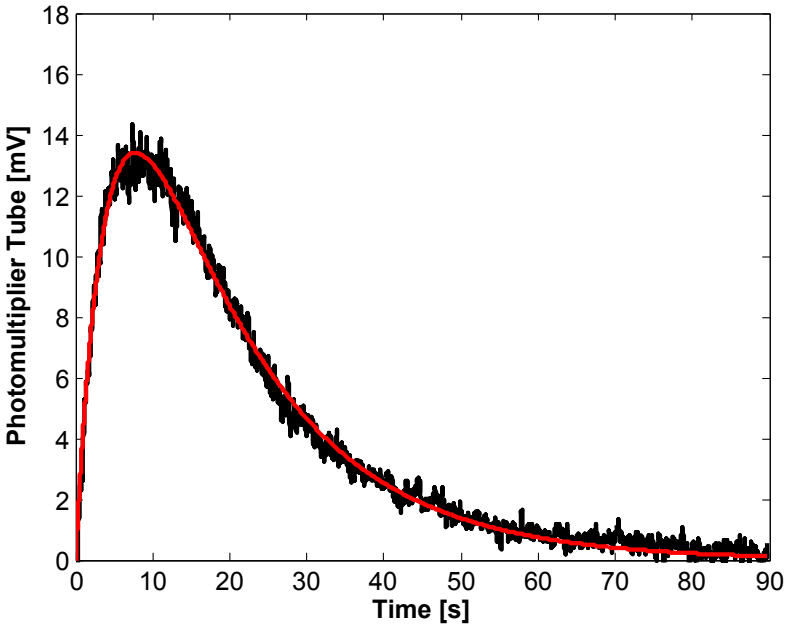

Figure 5.18: *The observed UV fluorescence of metastable atoms being recaptured into the UV MOT. The load from the decaying atoms and the lifetime of the magnetic trap are fitted to the data.*

decay of the MOT signal when 383 nm laser is switched off, since atoms are captured in the $(3s3p)^3P_2$ state and a load when the 383 nm laser is turned back on, since $(3s3p)^3P_2$ atoms are transferred back to $(3s3p)^3P_1$ and a fraction is recaptured in the MOT. The ratio of the load to the decay constants yields exactly the recapture fraction in our experiments. We find this factor to be 1.5 ± 0.1. Insufficient knowledge of this recapture fraction will lead to a non-neglectable systematic effect.

With this information the lifetime could be calculated for each time the sequence ran. We ran the sequence 93 times where the Γ for each sequence is shown in figure 5.19.

As seen in figure 5.20 the mean lifetime is 1914 ± 40 s. For the systematic effect we have the transfer efficiency as the main source of error.

We have investigated several parameters to see if there was a variation in the measured lifetime. One of these is the detuning of the 383 nm laser.

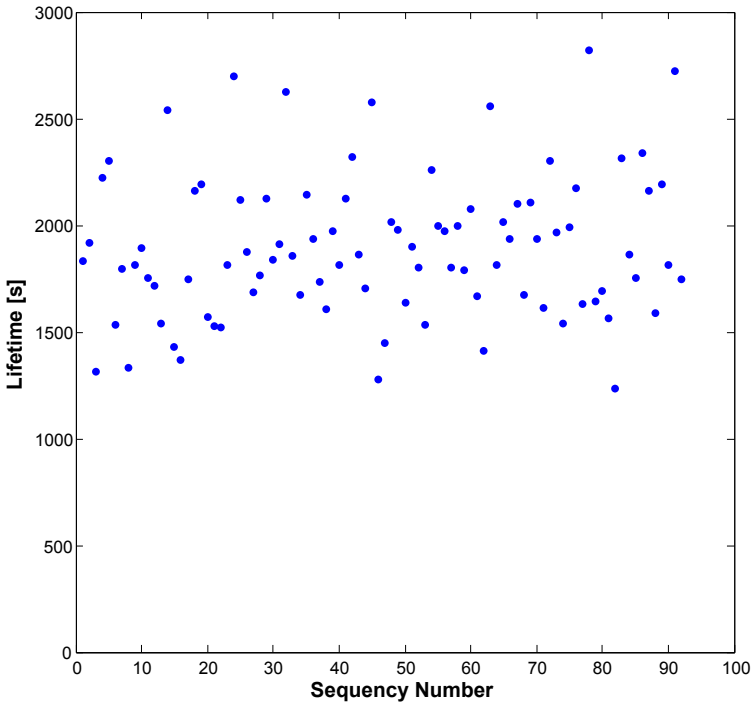

Figure 5.19: *A total of 93 measurement of the lifetime was taken and the spread in the data is shown here.*

If the exact frequency of the 383 nm laser causes the transfer efficiency to change, the experiment could be sensitive to drift of this laser. In figure 5.21 the measured lifetime is shown as a function of the 383 nm detuning away from resonance. It is seen that the lifetime remains constant over a large frequency range. Since the estimated uncertainty in the frequency lock from the beamline is 1.2 MHz which is a very small contribution to the systematic error of the measured lifetime. This is also what we would expect since we expose the $^3P_2$ atoms for a long time compared to the 6 ns lifetime of the 2-2 transition. Any detuning will cause the saturation parameter S to drop however, only a few cycles are needed to pump the atom into the $^3P_1$ state. This will still transfer the whole population into $^3P_1$ in a much shorter time then the exposure time.

The dependence of the magnetic trap on the lifetime was measured. Since not all atoms that are transferred to the $^3P_1$ state are magnetically trapped

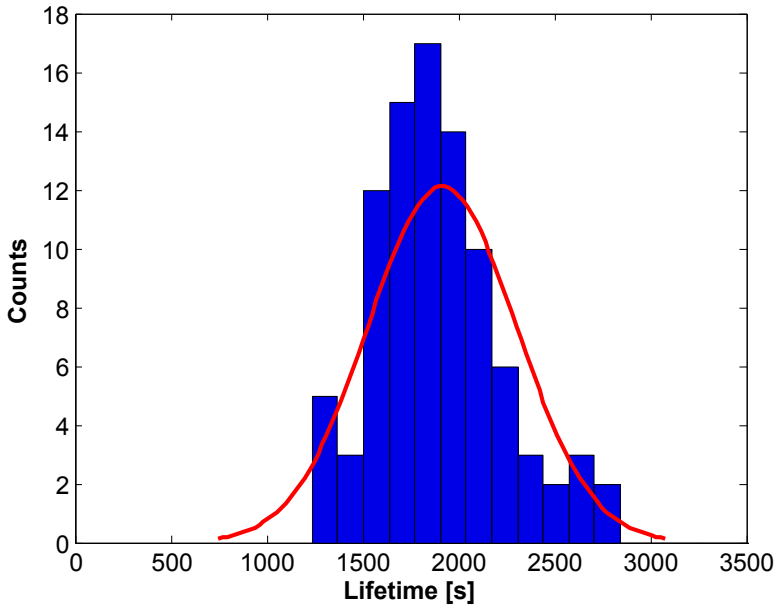

Figure 5.20: *The measured lifetimes are shown in a histogram and a gaussian is fitted to the data.*

there will be a dependence of the magnetic field gradient. With a UV MOT temperature of about 4 mK some atoms will be able to escape the trap before they decay to the ground state and recaptured into the UV MOT. The recapture ratio of non magnetically trapped atoms show a slight dependence on the magnetic gradient as seen in figure 5.21. We therefore used the same magnetic gradient for all lifetime measurements and calibrated the recapture fraction for that particular gradient. As the magnetic field gradient is increased the density increases and according to theoretical calculations there should be inelastic collisions between the atoms in $^3P_2$ causing a drop in the total population. The fact we see a slight increase seem to indicate a lack of inelastic collisions, see section 5.6.

The lifetime is determined to be 1914 seconds with a statistical uncertainty of ±40. The systematic uncertainty is however much larger due to the difficulty in determining the transfer efficiency. The error budget is shown in table 5.2 with the total error on the lifetime estimated to be 10.0% or ±191

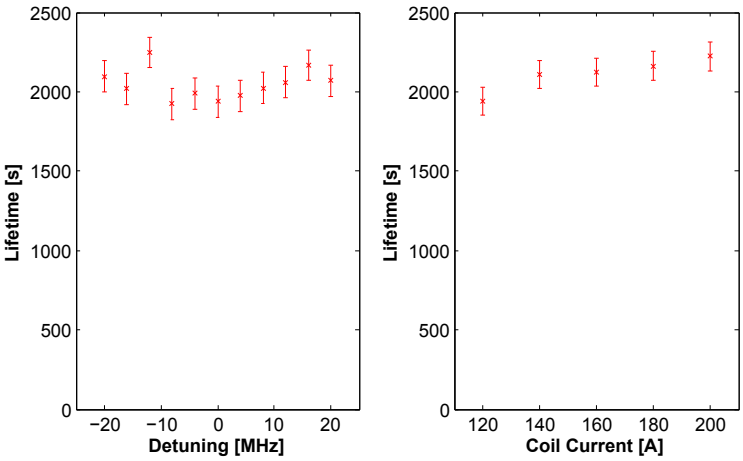

Figure 5.21: *The dependence of the detuning of the 383 nm laser on the measured lifetime and the dependence of the magnetic field on the measured lifetime.*

seconds.

source	**Uncertainty [%]**
Recapture fraction	9.8
Photomultiplier linearity	0.2
MOT fluctuations	2
Magnetic trap lifetime	0.1
Total	**10.0**

Table 5.2: *The statistical errors associated with the determined lifetime. The total statistical error is found to be 10.0% or corresponding to ±191 seconds.*

5.5 Estimate of the spin-forbidden decay rate $(3s3p)^1P_1 \rightarrow (3s3p)^3P_2$

When earlier stated that the $^1S_0$ - $^1P_1$ were a ideal closed two level system this in not entirely correct. There is a very small chance atoms can decay from the $^1P_1$ to the triplet ^3P states. The $^1P_1$ - $^2P_3$ is a M1 magnetic dipole transition requiring in addition a low probability spin flip to occur. The resulting linewidth of the transition is in μHz. We have tried some initial measurements of the transition however the decay rate could not be resolved. The fact we were unable to detect the decay rate sets a upper limit on it. If we assume we have a UV MOT running with N_0 atoms then the number of atoms that has decayed into trapped metastable states given by:

$$N_2 = (\rho_{aa} N_0)\Gamma_a \frac{2}{5}\Delta T \tag{5.23}$$

When the atoms decay back to the $^1S_0$ they produce a signal S_2 on the PMT.

$$S_2 = \frac{\rho_{aa}}{\tau} N_2 \omega \eta_{PMT2} \tag{5.24}$$

ω is here the solid angle viewed by the high gain PMT. η_{PMT2} is the quantum efficiency of the high gain PMT.

The MOT signal seen by the low gain PMT is given by:

$$S_0 = \frac{\rho_{aa}}{\tau} N_0 \omega \eta_{PMT1} \tag{5.25}$$

By preparing a small MOT that both PMTs are able to observe without saturating the high gain PMT it is possible to calibrate the two PMTs against eachother. The relative quantum efficiency can then be determined accurately. If the ratio of the two signals is taken this gives:

$$\frac{S_2}{S_0} = \frac{N_2}{N_0}\frac{\eta_{PMT2}}{\eta_{PMT1}} = \rho_{aa}\Gamma_a \frac{2}{5}\Delta T \frac{\eta_{PMT2}}{\eta_{PMT1}} \tag{5.26}$$

from which we can estimate Γ_a to be

$$\Gamma_a \quad < \quad \frac{S_2}{S_0}\frac{5}{2\rho_{aa}\Delta T}\frac{\eta_{PMT1}}{\eta_{PMT2}} = 4 \cdot 10^{-4} \ \mathtt{s}^{-1} \tag{5.27}$$

when using $S_2 < 1$ mV, $S_0 = 5$ V, $\frac{\eta_{PMT2}}{\eta_{PMT1}} = 10$, $\Delta T = 5$ s, and $\rho_{aa} = 0.05$. This determined upper limit on the lifetime of the $^1P_1$ - $^2P_3$ transition is close to the theoretical calculated lifetime of $1.4 \cdot 10^{-4}$ $\mathtt{s}^{-1}$. It is therefore hopeful that improvements to the system can be made in order to increase the resolution of the measurement. The biggest obstacle is the background load that limit the S/N. Possible solutions to reduce the background load is to operate the oven at a lower temperature. The loss in flux could be compensated by better alignment of the UV MOT beams. More UV power could also increase ρ_{aa}.

Finally, it could be recommended to increase the initial delay between the first UV pulse after closing the atomic shutter. Since the background load decays after the atomic beam is turned off, it is possible to get a better signal if waiting for 1 - 2 seconds. The atoms in the magnetic trap has a lifetime of 16 seconds so after 2 seconds 88% of the metastable atoms are still confined in the magnetic trap. The background gas however has a shorter lifetime given by the pumping on the system. Increasing the delay between the atomic beam and the first pulse therefore increases the S/N ratio. A S/N of 4 should be possible to a obtained with the suggestions listed above.

5.6 Estimate of Collision rate

When performing the lifetime measurements on the $(3s3p)^3P_1$ state, section 5.2, and $(3s3p)^3P_2$ state, section 5.4, it was noted that collisions happened between the metastable population and the thermal atomic beam. For future experiments these cross-sections can set limits on the number of atoms trapped in the metastable state and reduce signal to noise ratios. The

metastable states are of great importance to high resolution spectroscopy and a estimate of the cross-sections is therefore given here.

5.6.1 Experiment with Collisions

There are several mechanisms that can cause atoms trapped in the magnetic quadropole field to be lost. Collisions with the background gas and collisions with the thermal beam depends linear on the number of atoms in the thermal beam. The $(3s3p)^3P_2$ state is the most likely candidate to test for collisions as it is possible to trap and decay slowly enough that collisions can be detected. The $(3s3p)^3P_2$ state has the highest energy of the metastable states and is possible to populate with the two photon transition described in section 5.3. There will also be radiative decay from the $(3s3p)^3P_2$ state however with a lifetime of about 2000 seconds this can safely be neglected. The rate equation for the system is therefore given by:

$$\frac{dN_{^3\mathrm{P}_2}(t)}{dt} = -(\alpha_{\mathrm{bg}} + \alpha_{\mathrm{beam}} + \alpha_{\mathrm{decay}}) \cdot N_{^3\mathrm{P}_2}(t) + L \qquad (5.28)$$

where L is the load form the two photon transition. α_{bg} is the loss from the background which here can be estimated to be roughly similar to the background loss of the UV MOT of around 20 seconds. α_{bg} was determined in section 5.4 to be about 16 seconds in agreement to values found for the UV MOT. If the atomic beam is switched off after the metastable MOT has been loaded then it is possible to turn off the load and we can neglect the load L aswell.

The solution will be a simple exponential decay function:

$$N_{^3\mathrm{P}_2}(t) = N_0 \cdot e^{-(\alpha_{\mathrm{bg}} + \alpha_{\mathrm{beam}})t} \qquad (5.29)$$

If the magnesium flux in the thermal beam is high enough the loss will be dominated by collisions from the thermal beam.

5.6.2 Results

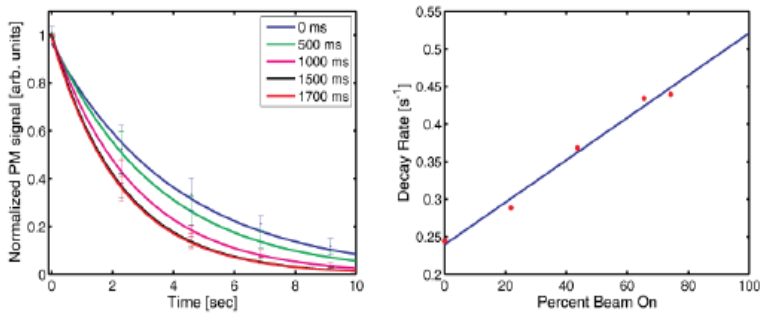

Figure 5.22: *Observed decay of atoms in the $(3s3p)^3P_2$ state for different exposures to the thermal beam. The exposure time are relative to the total measurement time of 2290 ms.*

In figure 5.22 the data from the experiment is shown. From the figure there is a clear effect of the neutral thermal beam on the cold sample of metastable atoms. The data seen in figure 5.22 is with a oven at 710 K. The magnesium flux at this temperature is estimated to be $4{\cdot}10^{12}$ s^{-1} cm^{-2} at the MOT region. The vacuum pressure in the MOT chamber was $7{\cdot}10^{-10}$ mbar. As the effective time the thermal beam is on the lifetime of atoms in the $(3s3p)^3P_2$ state is seen to decrease. Due to technical problems it was not possible to determine the lifetime with a thermal beam on all the time, it could however be extrapolated to 100%. When the beam is on continuously, the decay rate was found to be $\alpha_{beam} = 0.28$ s^{-1}. This is in excellent agreement with previous measurements using another method, giving a value of $\alpha_{beam} = 0.3$ s^{-1}.

From the measured decay rate a cross-section can be determined for the thermal magnesium beam that is colisions between $(3s3p)^3P_2$ and $(3s^2)^1S_0$. The loss rate is given by

$$dN_{^3\mathrm{P}_2}(t) = \sigma_{\mathrm{beam}} F \mathrm{N}_{^3\mathrm{P}_2} \tag{5.30}$$

Where F is the Flux of magnesium atoms. For a flux of $4 \cdot 10^{12}$ s^{-1} cm^{-2}, as stated in section 5.1, the cross-section can be calculated to $7 \cdot 10^{-14}$ m^2 or

700 Å^2. Which gives a large collision rate comparable to the load rate.

5.7 Conclusion

In conclusion we have generated a cold sample of metastable magnesium atoms in the $(3s3p)^3P_{1,2}$ states. Several properties of the metastable state has been determined.

The spin-forbidden decay from the $^1D_2$ into the triplet states has been measured. The decay constant of $\Gamma_{22} + \Gamma_{21} = 196 \pm 10$ s$^-$1 is in excellent agreement with theoretical calculations.

For the first time the lifetime of the $^3P_2$ decay to the ground state has been measured for magnesium. The measured lifetime of $1914 \pm 40 \pm 191$ seconds is close to the theoretical calculations. Furthermore the lifetime dependence on detuning of the 383 nm optical pumping and the magnetic field has been determined.

We have also tried to measure the even slower $^1P_1$ decay rate into the $^3P_2$ state. Since the signal could not be distinguished from the background a upper limit on the lifetime has been estimated. It is possible that this value can be determined in the near future.

No collisions were observed between atoms in the $^3P_2$ state. However we have observed collisions between the thermal beam of neutral magnesium atoms and the magnetic trapped atoms in the $^3P_2$ state. These cross-sections are of great importance to the operation of the 383 nm MOT and slowing of metastable atoms in a zeeman slower as described in chapter 6.

CHAPTER 6

Cooling of Metastable Magnesium

As seen in chapter 5 there are several advantages of having a cold and confined sample of metastable magnesium. In contrary to the approach of chapter 3 we have investigated the possibility of creating a MOT by slowing and capturing atoms coming from a metastable source described in chapter 3.

A MOT loaded directly from the metastable source could capture a larger number of atoms. The possibility to generate a cold sample of atoms opens the possibility to dipole trap the atoms or generate a condensate. The doppler temperature of the $^3p_2$ - $^3D_3$ transition is estimated to be 600 μK.

In the previous chapters several properties have been investigated that are crucial for future experiments with metastable magnesium for example the possibility of generating a 383 nm MOT and some initial measurements of collision cross-sections for the possibility of generation a BEC. Other properties such as 1D cooling and optical pumping has been carried out. For example the level structure of ^{25}Mg is important to know if one is to look for a possible cooling scheme of the isotope. The following chapter look as some aspects and initial experiments of cooling on the triplet states.

6.1 ^{3}P - ^{3}D transition for cooling Metastable Magnesium

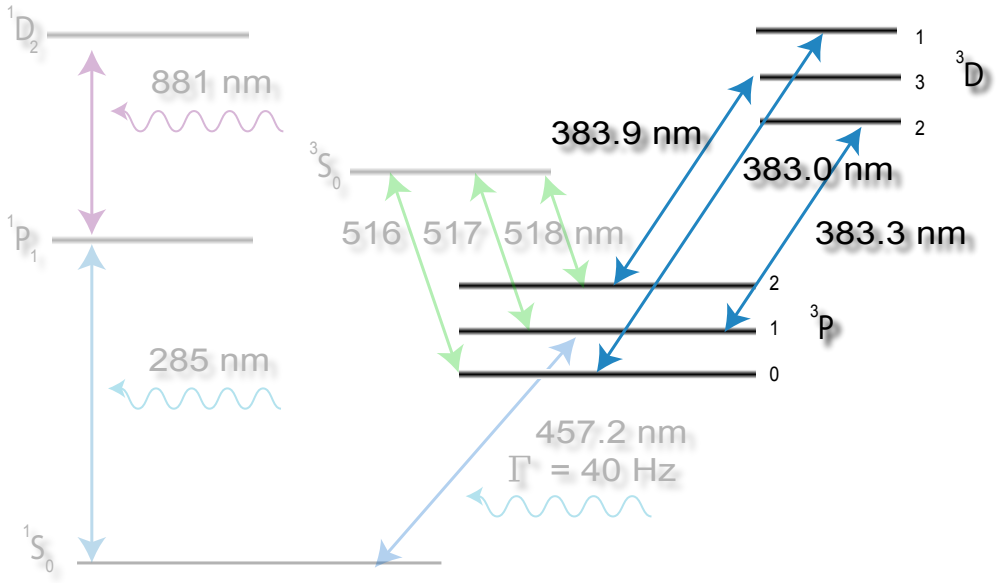

Figure 6.1: *The level diagram of magnesium. The singlet states are on the left and the triplet states are to the right..*

As seen in figure 6.1 the ^{3}P$_j$ states have many dipole allowed transitions to higher lying states. The relative large linewidth of these transitions and consequently short lifetimes mean that using these transitions for slowing Mg atoms is possible. The magnesium atoms are also light atoms compared to for example Rb and Sr which mean that Mg atoms can be stopped on shorter distances and therefore reduce the required length of a zeeman slower. As seen in previous chapters the level structure of ^{25}Mg is more complicated and some lines are not know well. In the following chapter I will focus on cooling of ^{24}Mg unless where otherwise specified. The transitions linking the ^{3}P$_j$ and ^{3}D$_{j'}$ are UV transitions at 383 nm where the scattering rate is given by $F = \frac{\hbar k \Gamma}{2}$ which for the ^{3}P$_2$ - ^{3}D$_3$ transition corresponds to a acceleration of $3.5 \cdot 10^6$ m/s^2. Most of the transitions out of the ^{3}P$_j$ states

are not closed by optically pumping on 1 transition however with 1 or 2 laser acting as repumpers some of them will be closed. The most promising cooling transition is the $^3P_2$ - $^3D_3$ transition since the $^3D_3$ state can only decay back to the $^3P_2$ state. The large force given by the $^3P_2$ - $^3D_3$ transition will unfortunately also give it a higher doppler temperature then the other transitions, however, there are possibility for subdoppler cooling for this J = 2 to J = 3 transition.

For cooling on the $^3P_2$ - $^3D_3$ transition there are unfortunately other lines that are close. The $^3P_2$ - $^3D_2$ transition is 532 MHz red detuned from the cooling transition and with a linewidth of 6.4 MHz has a finite probability of being excited. On the blue side of the cooling transition, with a blue detuning of 379 MHz, the $^3P_2$ - $^3D_1$ transition is located. This transition has a linewidth of 0.7 MHz and therefore atoms in the $^3P_2$ state has a much smaller probability of being excited to the $^3D_1$ state when exciting the cooling transition as seen in figure 6.1. Calculating the excitation probability using

$$\frac{1}{2}\rho_{^3D_2} = \frac{\frac{S_0}{2}}{1 + S_0 + (\frac{2\cdot\Delta}{\Gamma})^2} \tag{6.1}$$

on the $^3P_2$ - $^3D_2$ transition with a linewidth of 6.4 MHz and $S_0 = 4$ yields a lifetime of 0.9 ms when optically pumping the cooling transition with S_0 = 1. Here I have corrected the scattering rate with a factor 3/8 given the probability of decaying out of the $^3P_2$ state. The corresponding lifetime if the only leak is caused by exciting the $^3D_1$ is consequently 32 ms. These lifetimes are without the presence of a repumper and obviously the most probable state to excite is the $^3D_2$ however this state can decay back to either $^3P_2$ or $^3P_1$ which means a extra laser to excite the $^3P_1$ - $^3D_2$ transition would remove this leak and subsequently increasing the lifetime to about 32 ms. Finally one could excite the $^3P_0$ - $^3D_1$ transition with another laser which would ultimately close the cycle.

For the case of ^{25}Mg not only are several fine splitting levels located relatively close to each other which complicate the optical pumping and cooling, but there will also be a presence of hyperfine levels due to the nuclear spin of

I = 5/2. Unfortunately the most promising cooling transition from J = 2 to J = 3 has 15 transitions linking different hyperfine levels. As seen in earlier chapters these levels were not possible to resolve but several of these would most likely require additional repump lasers.

6.2 Zeeman slowing

In order to capture metastable atoms and confine them in a MOT, the atoms will first have to be slowed down to the capture veloicty of the MOT. As shown in section 4.2 the discharge changes the velocity distribution from a maxwell-boltzmann distribution, and very effectively remove all slow moving atoms. This means that it will not be possible to load a MOT directly from a hot beam as done in the neutral Mg MOT. The well known technique of slowing atoms using the zeeman shift is described for metastable magnesium [86], [88]. At the end of the chapter the results from some initial tests are presented.

6.2.1 Design

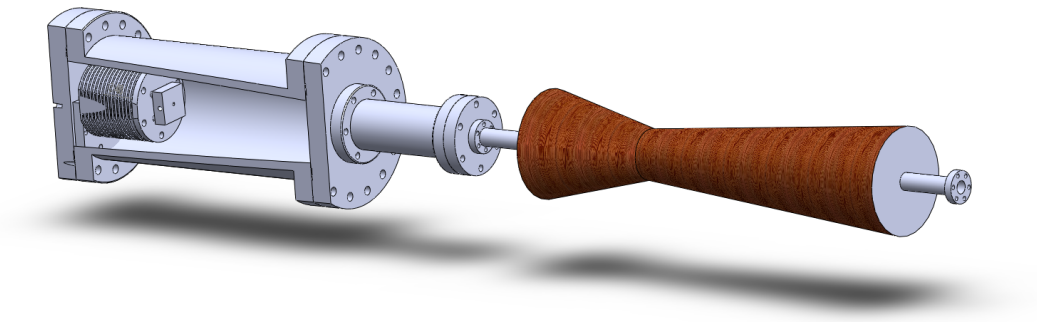

Figure 6.2: *Sketch of the Zeeman slower. The actual zeeman slower is 42 cm long winded up on a 50 cm long tube.*

By changing the magnitude of a magnetic field as the atoms are slower it is possible to keep the laser near resonant during the whole period of slowing. As the atoms slow down a different zeeman shift is needed and this is achieved by having a spatially varying magnetic field that fit the ballistic trajectory of the atoms being slowed. The two main types of zeeman slowers are the ones using either σ_+ or σ_- polarized light. A σ_+ zeeman slower which is also the one we choose to build is shown in figure 6.2. There are several considerations and design issues that need to be addressed and the actual design of a zeeman slower will therefore vary. I assume general knowledge of the working principles and will go in detail with the considerations when slowing metastable magnesium. Slowing metastable magnesium will at first hand look very promising since Mg is a light atom. The fact that the most promising transition is a UV transition with a 6.2 ns lifetime also means that the force will by large. This gives a large deceleration of $3.5 \cdot 10^6 \frac{m}{s^2}$ which means that the length of the zeeman slower can be short or give a high capture velocity. For a capture velocity of 850 m/s the theoretical length needed for slowing is 21 cm at S = 1. It should be noted that a large capture velocity of the zeeman slower mean that in order to shift a resonant laser (B = 0 V = 0) to hit the velocity group at 850 m/s a detuning of 2.2 GHz is required corresponding to 1600 gauss. The large magnetic field required in order to zeeman shift the slowing laser put technical requirements on the coils used. Another serious issue is that the larger light force makes the unhooking at the end of the zeeman slower more difficult since the gradient need to change rapidly. The normal condition for slowing has to be violated at the unhooking point.

Another consideration is the proximity of other lines close to the cooling transition. For example the fine splitting of the ^3D_j levels are 380 MHz and 532 MHz away at B = 0. The fine splitting as a function of magnetic field for some of the transitions is shown in figure 6.3. When cooling in a magnetic field a level crossing occur between the $^3P_2$ to $^3D_3$ and $^3P_2$ to $^3D_1$ transition at 78 gauss. This means that the two transistions are both resonant and as describer earlier, exciting the $^3D_1$ level will cause atoms to fall out of the cooling cycle. As the magnetic field is increased, the $^3P_2$ to $^3D_3$ transition

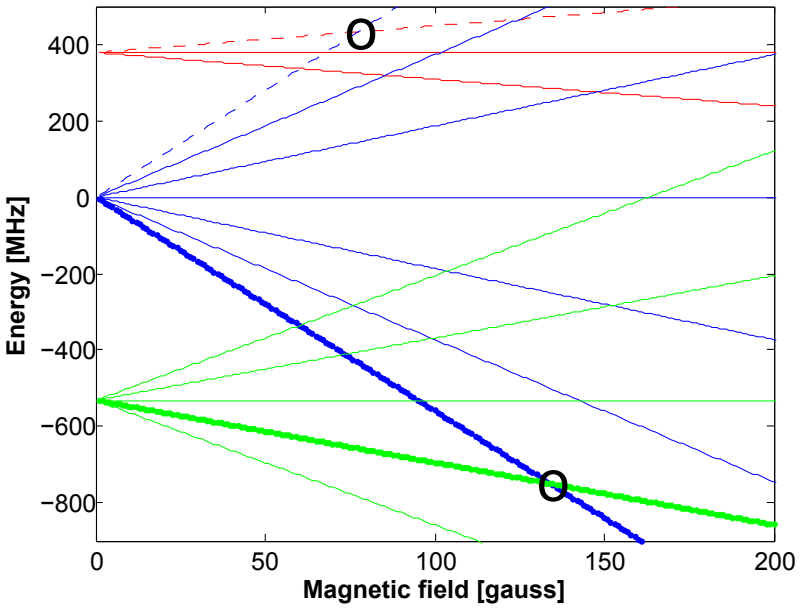

Figure 6.3: *The fine splitting of the* ^3P_j *to* $^3D_{j'}$ *transitions vs magnetic field. The red lines are the* $^3P_2$ *to* $^3D_3$ *green are* $^3P_2$ *to* $^3D_1$ *and the blue are the* $^3P_2$ *to* $^3D_2$ *transitions.*

is split further away from the other transitions causing the induced loss due to optical pumping to decrease. At magnetic fields larger then 78 gauss the main cooling transition is therefore suitable for laser cooling. Atoms moving down the slower will be pumped by σ_+ light and so the atoms will be spin polarized as they propagate down the slower. The atoms being slowed will therefore be in the $m_j = +2$ state as they are pumped by the slowing beam. The only possible level crossing is therefore the $m_j = +2$ to $m_j = +1$ for the $^3\mathrm{D}_1$ states. This transition however requires that the light has right handed helicity and the probability of exciting this state is neiglible in theory with light having a pure left handed helicity. In the actual slower however this is not true as the polarization is not a pure σ_+ polarization.

Due to the fact that we wanted to use the same laser for both cooling the MOT and as a slowing beam means the laser frequency has to be near resonance. The detuning needed for running a MOT would roughly be about 50 MHz and given the frequency shift of the AOM by 90 to 110 MHz mean the

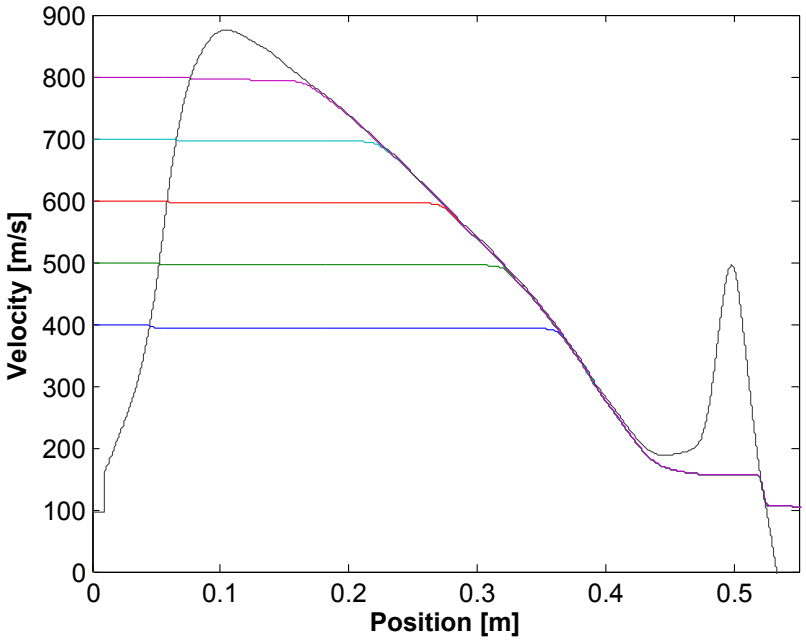

Figure 6.4: *Simulation of the Velocity of atoms starting at different initial velocities.*

slowing beam will be 140 MHz - 160 MHz red detuned. The extra detuning that the AOM provides reduces the light force on the atoms in the MOT from the slowing beam that otherwise could push atoms out of the trap. The detuning of the slowing beam is relatively small compared to the detuning required in order to compensate for the doppler shift of about 2.2 GHz. The slower will therefore have to start with a large magnetic field to compensate the doppler shift and decrease as the atoms are decelerated toward the final velocity where the magnetic field will be only a few hundred gauss depending on the exact detuning of the laser. Normally the extraction coils increases the magnetic field when the final velocity has been reached so that the slowing beam comes out of resonance with the slow atoms. This reduces the light force on the atoms and sets the final velocity. When the atoms leave the slower the magnetic field falls to near zero. The extraction coils provide a rapidly changing magnetic field to avoid interacting with the atoms when the magnetic field goes to zero or pumped to other states so the final velocity

is not affected. The large light force from the UV slowing beam however requires a gradient of more then 500 gauss/cm which is difficult to obtain. It is however also possible to exploit the very effective optical pumping that happens at 78 gauss to set the final velocity. As the magnetic field is lowered and it gets close to 78 gauss the lifetime of the $^3P_2$ state due to optical pumping will decrease due to the level crossing of the $^3P_2$ to $^3D_3$ and $^3P_2$ to $^3D_1$ transitions. The cooling cycle will now no longer be closed and there is a large possibility of atoms being pumped into $^3P_{0,1}$. After a few cycles the atoms will be in the $^3P_0$ or $^3P_1$ state and since there states are hundreds of GHz away they will no longer be affected by the slowing beam and will move undisturbed into the MOT region. Atoms decaying into the $^3P_1$ state are undesirable since they will decay back to the ground state with a lifetime of only 4 ms. A repumper is therefore needed on the $^3P_1$ to $^3D_2$ transition to put these back into the cooling cycle. With a repumper on the $^3P_1$ to $^3D_2$ transition that is spatially overlapping the slowing beam will not only help keep the cooling cycle closed but can also work as a repump laser on the MOT. A MOT running on the $^3P_2$ to $^3D_3$ transition can in theory have a capture velocity of more then 60 m/s depending on beam size and the magnetic gradient. This capture velocity is larger then that of the 285 nm MOT see 5.1 since it is not restricted by two photon ionization and larger light intensity can be utilized. A capture velocity of more then 60 m/s however requires a magnetic gradient of 150 gauss/cm. The magnetic field from the MOT can easily be several mK deep and slow atoms coming from the Zeeman slower can be deflected from this potential. An advantage for atoms in the $^3P_0$ is the lack of a magnetic moment and they are therefore not affected by the MOT field. The $^3P_0$ atoms will therefore move unaffected directly into the MOT region where with the presence of a repumper from $^3P_0$ to $^3D_1$ can put them back into a cooling cycle.

The actual slower that we have build is shown in figure 6.2. The length of the coils is 42 cm which is about twice the length of the theoretical calculated length required, with S = 1 and V_{cap} = 850 m/s. The coil is coiled around a 50 cm long CF16 extension tube with CF16 flanges at each end. The bias coils consist of copper wire with a diameter of 1 mm where the profile and

extraction coils consist of copper wire with a 2 mm diameter. The typical currents needed through the bias coil is 4 A which generate a 800 gauss bias field. The profile coil with the 2 mm wire requires a current of 16 A that will increase the magnetic field in the begining of the slower to about 1600 gauss and at the end of the slower the two fields will almost cancel each other out. The actual current used in the bias and profile coil can be used to set the final velocity were either the extraction coils are used or optical pumping at 78 gauss set the final velocity. The extraction coils using the 2 mm wire can operate at a maximum of about 6 A which generate a gradient of 600 gauss/cm.

The currents that are needed through the coils does generate a significant amount of heat. For example the bias coil alone generate 180 W of heat at 4 A. The profile coil generates 480 W of heat which gives a total amount of heat generate from the slower of 660 W. This heat need to be dissipated effectively, since a normal coil contain air pockets can isolate parts of the inner coil. For effective heat dissipation a 3 mm thich copper tube was placed between the bias and profile coils with cooling water passing through it. This reduced the effective thickness of the coil to about half the thickness thereby reducing the temperature gradient needed across the coil layers. In order to remove the air pockets and ensure good thermal transport thermally conducting epoxy was used between the layers which has a higher thermally conductivity then thermal paste. The thermal conducting epoxy ensures that no part of the coil exceeds 80 C°. avoiding temperature buildups is important since the resistance of the copper wire increases by about 40% pr 100 degree which can fast cause a runaway reaction.

6.2.2 Initial tests

Unfortunately the Ti:Sapphire laser generating light at 383 nm stopped working during the testing of the zeeman slower and we are currently working on the lasers for this experiment. I will however show some of the initial tests of the velocity distribution with the presence of a slowing beam. The setup is shown in figure 6.2 where 383 nm laser beams tuned to the $^3P_2$ to $^3D_3$ are

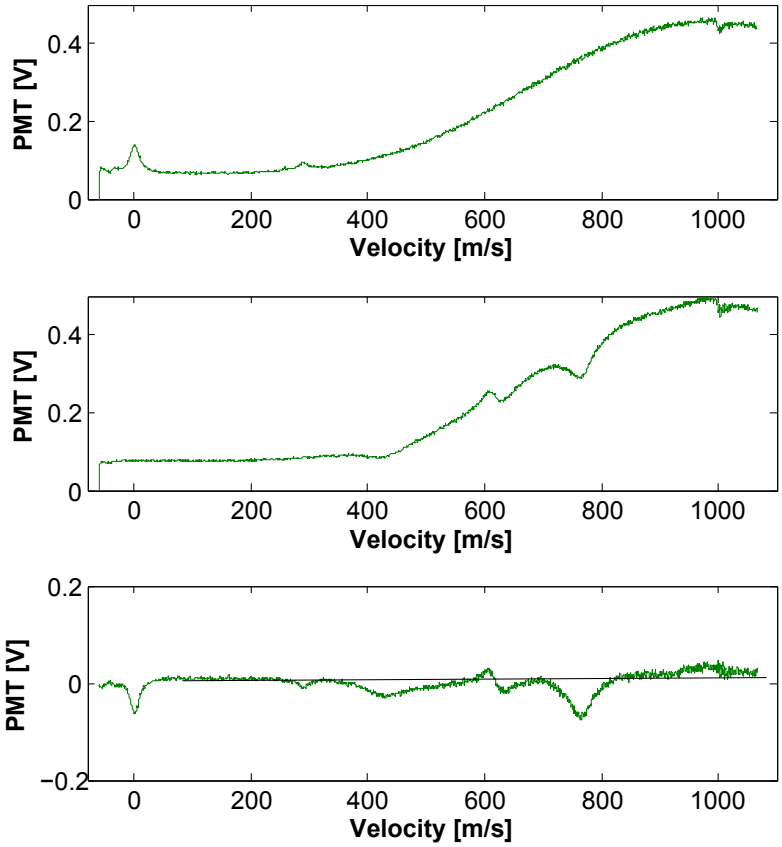

Figure 6.5: *The Velocity distribution of atoms comming out of the zeeman slower. Seen here is the actual photomultiplier signal of the fluorescence from the beam. top. The signal without a slowing beam. Middle. The observed signal with the presence of a slowing beam. Bottom. The two signals subtracted showing the cooling of the* $^3P_2$ *to* $^3D_3$ *transition.*

intersecting the atomic beam in a 45 deg angle to the beam axis. The $^3P_2$ to $^3D_3$ transition will now have a different doppler shift for each velocity class. When the laser is scanned the velocity distribution is mapped out as seen in figure 6.5. In the setup a small amount of the 383 nm light is also sent in perpendicular to the beam. The perpendicular beam generate a peak at the $^3P_2$ to $^3D_3$ and $^3P_2$ to $^3D_2$ transition that is known to be separated by 532 MHz. These transition peaks allow for a calibration of the velocity scale when the experiment is being performed. In figure 6.5 the slowing beam used is red

detuned 1600 MHz corresponding to a doppler shift of 614 m/s. A dip in the fluorescence at 614 m/s is seen in figure 6.5 where atoms with this velocity is slowed to about 600 m/s where a peak is seen. Subtracting the plot with and without a slower beam on is shown in figure 6.5 where the area of the peak at 600 m/s is roughly the same as the area of the dip at 614 m/s meaning the number of atoms is conserved. There is however another dip at 819 m/s which is the $^3P_2$ to $^3D_2$ transition located $(819-614)\text{m/s} \cdot 2.6\frac{\text{MHz}}{\text{m/s}} = 533$ MHz blue detuned from the $^3P_2$ to $^3D_3$ transition in agreement with previous measured data. The $^3P_2$ to $^3D_1$ transition is also observed at 468 m/s corresponding to 380 MHz red detuned. At the location of the $^3P_2$ to $^3D_1$ and $^3P_2$ to $^3D_1$ transitions both have dips where no cooling can be observed since the atoms quickly drop out of the cooling cycle.

6.2.3 Alternative cooling transitions

For slowing metastable atoms through the slower the most obvious transition to use is the closed $^3P_2$ to $^3D_3$ transition. The doppler temperature of this transition is about 600 μK which is not a lot colder then the UV transition at 285 nm. There are transitions between the ^3P and the ^3D states that give lower doppler temperatures. The $^3P_2$ to $^3D_1$ transition with a libnewidth of 0.7 MHz would give a much lower doppler temperature. The $^3P_2$ to $^3D_1$ transition is not a closed transition and so 3 lasers are required to close the cooling cycle. Since more then one laser is needed this means that the doppler temperature reached will be a weighted average of the lifetimes. The transitions from the ^3P to ^3S state would also require three lasers but the doppler temperature of these are much lower. In table 6.1 the doppler temperature is calculated for some of the triplet-triplet transitions. Since the transitions at about 517 nm have less momentum and narrower linewidths these transitions will have lower doppler temperatures. None of the 517 nm transitions are however closed and they will require 3 lasers to address $^3P_{0,1,2}$.

Transition	Wavelength	Linewidth	Lifetime	I_{sat}	$T_{Doppler}$	T_{recoil}
	[nm]	[MHz]	[ns]	[mW/cm^2]	[μK]	[μK]
$^3P_0 \rightarrow {}^3S_1$	516.876	1.8	88.5	1.7	43	2.97
$^3P_1 \rightarrow {}^3S_1$	517.413	5.4	29.7	5.1	129	2.96
$^3P_2 \rightarrow {}^3S_1$	518.505	8.9	17.8	8.4	214	2.95
$^3P_0 \rightarrow {}^3D_1$	383.044	14.3	11.1	33.3	343	5.40
$^3P_1 \rightarrow {}^3D_1$	383.339	10.7	14.8	24.9	257	5.39
$^3P_1 \rightarrow {}^3D_2$	383.339	19.3	8.3	44.7	462	5.39
$^3P_2 \rightarrow {}^3D_1$	383.938	0.7	223.2	1.6	17	5.37
$^3P_2 \rightarrow {}^3D_2$	383.938	6.4	24.8	14.8	154	5.37
$^3P_2 \rightarrow {}^3D_3$	383.938	25.6	6.2	59.2	615	5.37

Table 6.1: *Data for the transitions originating from the $^3P_{0,1,2}$ states [87].*

6.3 Conclusion

In conclusion we have made initial tests of a zeeman slower for generation a slow beam of metastable atoms. A decrease in fluorescence has been observed for the $^3P_2$ to $^3D_1$ and $^3P_2$ to $^3D_2$ transition while the $^3P_2$ to $^3D_3$ transition showed slowing with small loss of atoms.

CHAPTER 7

Conclusion and outlook

7.1 Conclusion

The experiments described in this thesis is part of a ongoing quest to realize a atomic clock based on magnesium. The experiments evolve around two main experiments. Those conducted in the magnesium MOT by cooling the singlet state and those using the metastable magnesium beam. Several schemes to cool magnesium has been tested like the two photon cooling described in section 5.3. Despite these efforts the coldest samples of magnesium probed are around 1 mK.

Spectroscopy on the beamline has been carried out in order to determine isotope shifts, hyperfine splittings and to provide a frequency reference for the different transitions.

The UV MOT was used to determine several decay rates and lifetimes of states of interest. The weak decay rates are unaffected by the high temperatures as long as they are possible to trap unlike probing transitions are limited by the doppler effect. This allowed us to measure the spin-forbidden decay rate $(3s3d)^1D_2 \rightarrow (3s3p)^3P_{1,2}$. The lifetimes of the two magnetically trapped $(3s3p)^3P_{1,2}$ states were measured. Collisions between magnesium atoms in the $(3s^2)^1S_0$ and $(3s3p)^3P_2$ state has been observed and surrently limit the number of atoms obtained in the metastable state.

7.2 Outlook

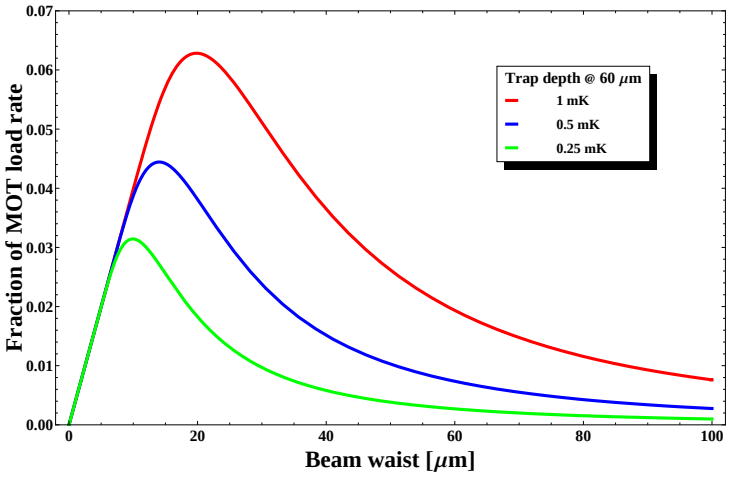

Figure 7.1: *Load rate into the optical trap given as a fraction of the MOT load rate as a function of beam waist.*

Following the experiments on the beamline and the experiments conducted in the UV MOT, we are now working on slowing metastable magnesium atoms in order to trap and confine metastable magnesium. The theoretical doppler temperatures of the 517 nm transitions are well below the mK temperatures obtained using the 285 nm UV transition. There are also several interesting transitions at 383 nm that could generate a cold sample of magnesium.

The reason for trying to obtain a colder sample of magnesium is the need to dipole trap the magnesium atoms for a optical lattice clock. Dipole traps are unfortunately not very deep and typically have potentials smaller then 1 mK. The depth of the trap is of course dependent on the intensity available. It is therefore a balance between having a very tightly focused beam with a deep trap or a larger and more shallow trap while overlap spatially more

with the MOT. In figure 7.1, the fraction of MOT load rate into the dipole trap is shown as a function of the beam waist for 3 different dipole depths. For a very small waist the trap becomes sensitive to vibrations and the load rate also drop if the spatially overlap becomes too small. The load drops for very small waists as the load is generated by optically pumping the atoms at the trap center into a dark state [89].

7.3 Acknowledgement

I wish to acknowledge the financial support from the Lundbeck Foundation.

Measurement of the Spin-forbidden Decay rate $(3s3d)^1D_2 \rightarrow (3s3p)^3P_{2,1}$ in ^{24}Mg

K. T. Therkildsen,* B. B. Jensen, C. P. Ryder, N. Malossi, and J. W. Thomsen

The Niels Bohr Institute, Universitetsparken 5, 2100 Copenhagen, Denmark

(Dated: December 19, 2008)

Abstract

We have measured the spin-forbidden decay rate from $(3s3d)^1D_2 \rightarrow (3s3p)^3P_{2,1}$ in ^{24}Mg atoms trapped in a magneto-optical trap. The total decay rate, summing up both exit channels $(3s3p)^3P_1$ and $(3s3p)^3P_2$, yields (200 ± 10) s^{-1} in excellent agreement with resent relativistic many-body calculations of [S.G. Porsev et al., Phys. Rev. A. **64**, 012508 (2001)]. The characterization of this decay channel is important as it may limit the performance of quantum optics experiments carried out with this ladder system as well as two-photon cooling experiments currently explored in several groups.

PACS numbers: Valid PACS appear here

*Electronic address: kaspertt@fys.ku.dk

I. INTRODUCTION

The interest in alkaline earth systems has increased significantly over the past years. One of the main interests in these systems is their applications to high resolution spectroscopy and atomic frequency standards, as they offer very narrow electronic transitions [1]. Another attractive feature of the two-electron systems is their very simple energy level structure, for bosonic isotopes, free of both fine and hyperfine structure. This simple structure opens for detailed comparison between theory and experiment [2]. Recent advances in *ab initio* relativistic many-body calculations of two-electron systems have provided very accurate values for atomic structure and properties such as the electric-dipole transitions of Mg, Ca, and Sr[3]. However, in the case of Mg relatively few experiments have been reported in literature motivating the studies in this Brief Report.

In a series of papers two photon cooling in ladder schemes have been proposed to lower the temperature below the doppler limit of alkaline earth elements [4, 5, 6]. The magnesium and calcium systems are of particular interest since cooling is limited to a few mK. Experimental evidence for two-photon cooling has been established, but the effect is rather modest contrary to theoretical predictions [7, 8]. One important mechanism to take into account in these studies are leaks from the ladder system, limiting the number of atoms that eventually can be cooled.

In this this Brief Report we present the first measurements of the spin forbidden decay from the magnesium $(3s3d)^1D_2$ state to $(3s3p)^3P_1$ and $(3s3p)^3P_2$. Using atoms trapped in a magneto-optical trap we optically prepare the atoms in the $(3s3d)^1D_2$ state and measure the decay to $(3s3p)^3P_{2,1}$ manifold by trap loss measurements. This enables us to deduce the absolute decay rate for these transitions and compare our results to state of the art theoretical calculations.

II. TRAP LOSS MEASUREMENTS

In figure 1, we show the relevant energy levels and transitions in our experiment. The 285 nm transition is used for coolingand trapping the atoms while the 881 nm transition is used to populate the $(3s3d)$ $^1D_2$ state. From this state the atoms may decay to the $(3s3p)^3P_1$

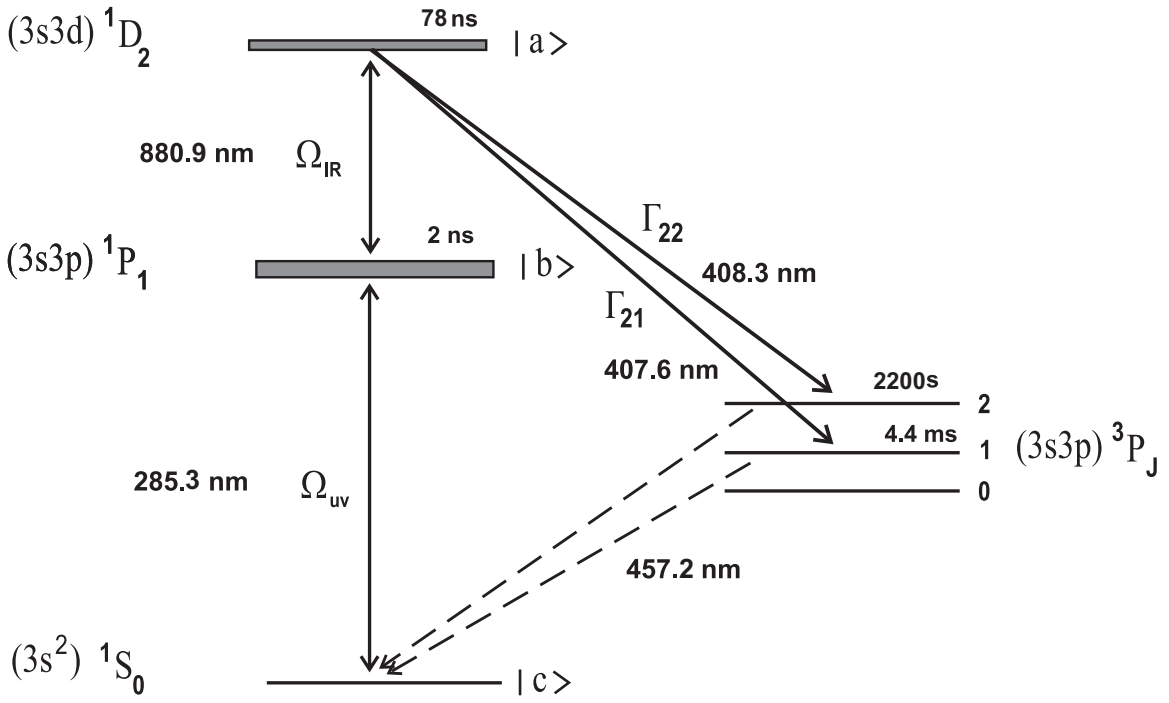

FIG. 1: Energy levels relevant for the $(3s3d)^1D_2 \rightarrow (3s3p)^3P_{2,1}$ decay measurement in ^{24}Mg.

state (407.6 nm) with rate Γ_{21} or to the $(3s3p)^3P_2$ state (408.3 nm) with rate Γ_{22}, or simply back to $(3s3p)^1P_1$. By neglecting decay to the $(3s3p)^3P_0$ state, which is weaker by orders of magnitude, no other decay channels are open. When the 881 nm laser is switched off we express the steady state number of atoms N_0 as the ratio of the load rate to linear losses L/α. Here we neglect intra-MOT collisions since we are working at relative low atom densities. The equation for the number of atoms trapped in the MOT with 881 nm light present can be written as:

$$\dot{N} \;=\; L - \rho_{aa}\,(\Gamma_{22} + \Gamma_{21})N - \alpha\, N. \tag{1}$$

Experimentally we determine the total loss rate $\Gamma_{22} + \Gamma_{21}$. In our case the linear loss rate α is dominated by resonant photo-ionization of $(3s3p)^1P_1$ at 285 nm [9]. Photo-ionization from the $(3s3d)$ $^1D_2$ level is below 1 Mb and will not be considered here[10]. The steady state becomes

$$N^{on} = \frac{L}{\rho_{aa}\,(\Gamma_{22} + \Gamma_{21}) + \alpha^{on}}, \tag{2}$$

and

$$N^{off} = \frac{L}{\alpha^{off}}. \tag{3}$$

The ratio of signal with 881 nm turned on and off is proportional to ρ_{bb}^{on}, ρ_{bb}^{off} respectively. We find finally

$$\frac{S^{on}}{S^{off}} = \frac{\alpha^{off}\,\rho_{bb}^{on}/\rho_{bb}^{off}}{\rho_{aa}\left(\Gamma_{21}+\Gamma_{22}\right)+\alpha^{off}\,\frac{\rho_{bb}^{on}}{\rho_{bb}^{off}}}, \tag{4}$$

as the α-coefficient is dominated by resonant photo-ionization and thus proportional to the fraction of atoms in the $(3s3p)^1P_1$ state. So far we assumed that all atoms decaying to the $(3s3p)^3P_J$ manifold are lost. This is indeed the case for the $(3s3p)^3P_2$ final states due to their long lifetime exceeding 2200 seconds [11]. On the time scale of the experiment, being only a few seconds, we consider the atoms from this state lost. However, for the $(3s3p)^3P_1$ states atoms in the $|J=1, m_j=+1\rangle$ magnetic sub state will be trapped in the magnetic quadrupole field of the MOT and most likely be recaptured when decaying back to the $(3s^2)^1S_0$ ground state. Atoms in $|J=1, m_j=0,-1\rangle$ magnetic sub states are expected to be lost since the rms velocity of the trapped atoms exceed 1 m/s leading to a rms travelled distance of more than 5 mm, which is large compared to our MOT beam diameter of only a few mm. The total decay rate will thus be modified to $\gamma\Gamma_{21}+\Gamma_{22}$. The actual value of γ depend strongly on the polarization of the 285 nm beam and the 881 nm beam.

If we assume a standard one dimensional model for the MOT we can determine the influence of the constant γ. This is a good approximation as the 881 nm beam is directed along one of the uv MOT beams, but not retro reflected. Consider atoms on the $-z$ side, see figure 2. These atoms will mainly populate the $|J=1, m_j=0,-1\rangle$ state. Further excitation of the collinear 881 nm laser will drive the atoms to the left (blue line) or right (red line) depending on the helicity of the 881 nm laser. This creates an anisotropy in the decay to the $(3s3p)^3P_1$ state. Atoms driven along the blue line, i.e., with same polarization helicity as the MOT beams, will only populate non-trapped states. Experiments performed in this configurations is thus insensitive to the re-trapping dynamics as described above. Using the Clebsch Gordan coefficients shown in figure 2 we find the rate $(1/2\cdot 1 + 1/2\cdot(1/2+1/2))\Gamma_{21} = \Gamma_{21}$, as expected. For the opposite polarization we find a reduction $(1/2\cdot 1/2 + 1/2\cdot(2/3+1/6))\Gamma_{21} = 2/3\Gamma_{21}$. We now Consider a more general case where all three magnetic sub states $|J=1, m_j=+1,0,-1\rangle$ are populated. The populations are denoted n_+ n_0 and with $n_+ + n_0 + n_- = 1$. We find the effective decay constant as $(1-n_+/6)\Gamma_{21}$ for MOT polarization. The n_+ coefficient is expected to be small compared to the sum of the two other terms. However, even in an extreme case where all sub states

are populated equally Γ_{21} is effected only by about 5%.

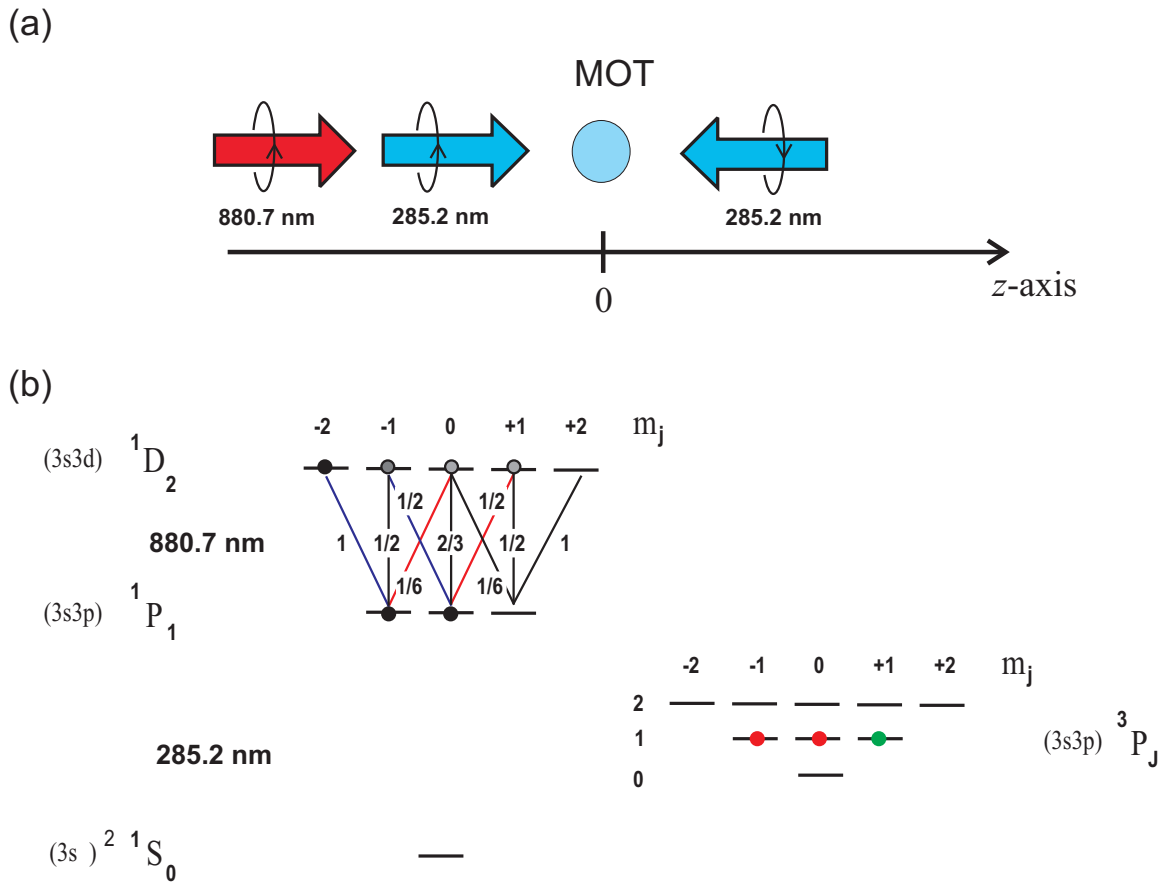

FIG. 2: (color online)(a) Experimentally the 881 nm beam is co-linear with one of the MOT beams. The polarization state can be selected similar to the MOT helicity, as shown in the figure, or opposite. (b) Polarization dependent pumping of atoms in the MOT. Assuming a one dimensional representation of the MOT the 881 nm polarization, represented by blue line (= MOT helicity) or red line, optical pumping will drive the atoms such that anisotropy in the decay rate will emerge. The green dot represents atoms trapped in the MOT quadrupole magnetic field, while red dots represents atoms in non-trapped states. The Clebsch Cordan coefficients shown will also apply to the $(3s3d)\ ^1D_2 \rightarrow (3s3p)^3P_1$ decay.

With a 881 nm helicity opposite to that of the MOT beam, marked in red color on figure 2, will ultimately result in a destruction of the trapping force as the 881 nm laser intensity increases. This effect is expected as a result of destructive reshuffling of the atoms into "wrong" magnetic sub states.

III. EXPERIMENTAL SETUP AND RESULTS

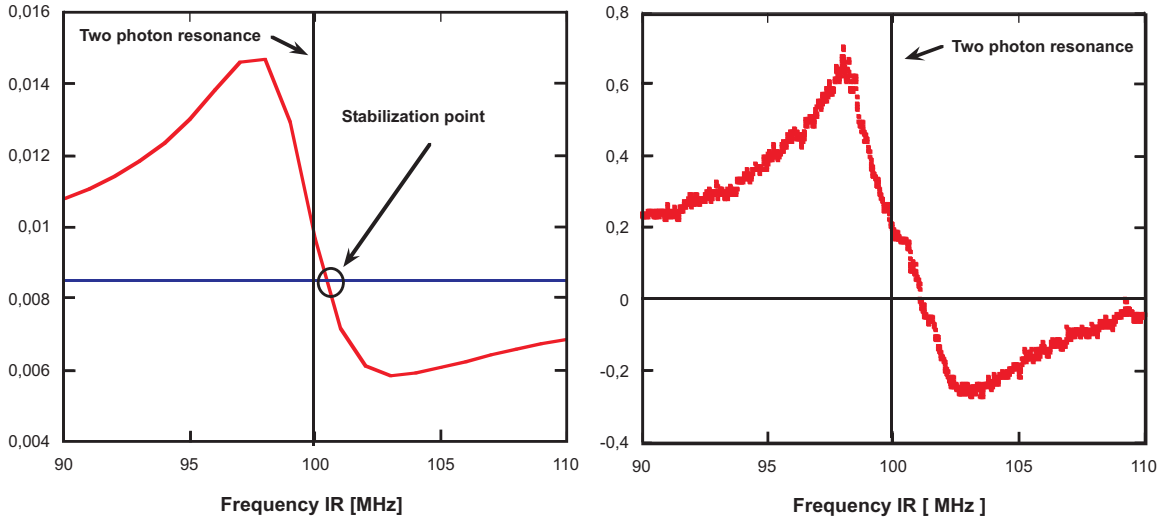

FIG. 3: (color online)The 881 nm laser is frequency locked to the two photon resonance of the ladder system $\nu_{881} = -\nu_{285}$ =100 MHz. This ensures a maximal transfer of population to the $(3s3d)$ $^1D_2$. Left part of the figure shows the $(3s3p)^1P_1$ excited state fraction obtained from the optical Bloch equations. Right part shows the experimental lock signal.

The main part of the experimental setup has been described in [12]. In our experiment the 285 nm MOT is probed by 881 nm light produced by a Ti:Sapphire laser. The 881 nm light is power and frequency controlled by an AOM. A $\lambda/4$ plate controls the helicity of the light. Presence of the 881 nm light will change the 285 nm light level recorded by a PM (not sensitive to 881 nm light). This we use to lock the 881 nm laser frequency close to the two photon resonance $\nu_{881} = -\nu_{285}$ =100 MHz during the experiments, see figure 3. Increasing the rabi frequency of the 881 nm light causes a minor change in the locking point. In our power range this corresponds to about 1 MHz and not considered important at this level of accuracy.

Typically 10^7 atoms are captured in the MOT, with a rms diameter of 1 mm and temperatures from 3 to 5 mK. The Doppler cooling limit for the MOT is 2 mK as sub-Doppler cooling is not supported in this system.

The number of emitted 285 nm photons when the IR laser was on and off respectively, was measured for each of the two circular polarizations states. The 881 nm light was sent through the AOM, which was modulated with a square wave at 1 kHz, with a duty cycle

of 20 %. The photomultiplier signal was measured and average over 32 periods with the light respectively on and off, thus providing values for S^{on} and S^{off}. At the same time these signals provided a lock of the Ti:S laser to the two photon resonance, see figure 3. This measurement was repeated for different IR intensities (Rabi frequencies), while the MOT was running in steady state mode.

Experimental values for the ratio $\frac{S^{on}}{S^{off}}$ as a function of the 881 nm Rabi frequency are show in figure 4. As expected the fraction starts out at 1 and gradually decreases as the Rabi frequency is increased. In figure 4 the 881 nm polarization corresponds to the MOT helicity (blue line in figure 2) and polarization opposite to the MOT helicity. The solid curves are results from a simulation based on the optical Bloch equations including the MOT magnetic field. Experiments with this helicity clearly supports a value of $\Gamma = (200 \pm 10)$ s^{-1} in good agreement with calculations performed in [3], where $\Gamma = \Gamma_{22} + \Gamma_{21} = (57.3 + 144)$ s^{-1}. For the opposite 881 nm polarization (red line in figure 2) we observe a reduced decay constant of $\Gamma = (150 \pm 10)$ s^{-1} as substates . Using values of [3] and the coefficient deduced above we obtain $\Gamma = \Gamma_{22} + 2/3\Gamma_{21} = 153$ s^{-1} in favor of the one dimensional model described above.

IV. CONCLUSION

In conclusion we have measured the total spin forbidden decay rate $(3s3d)^1D_2 \rightarrow (3s3p)^3P_{2,1}$ in ^{24}Mg. We find a rate of $\Gamma = (200 \pm 10)$ s$^-1$ supporting state of the art relativistic many-body calculations. Assuming a simple one dimensional model for the MOT we find the differential decay constants $(3s3d)^1D_2 \rightarrow (3s3p)^3P_1$, and $(3s3d)^1D_2 \rightarrow (3s3p)^3P_2$ as $\Gamma_{21} = 150$ s^{-1} and $\Gamma_{22} = 50$ s^{-1} supporting the above mentioned calculations.

Acknowledgments

We wish to acknowledge the financial support from the Lundbeck Foundation and the Carlsberg Foundation.

---

[1] T. P. Heavner, S. R. Jefferts, E. A. Donley, J. H. Shirley, T. E. Parker, Metrologia **42**, 411 (2005).

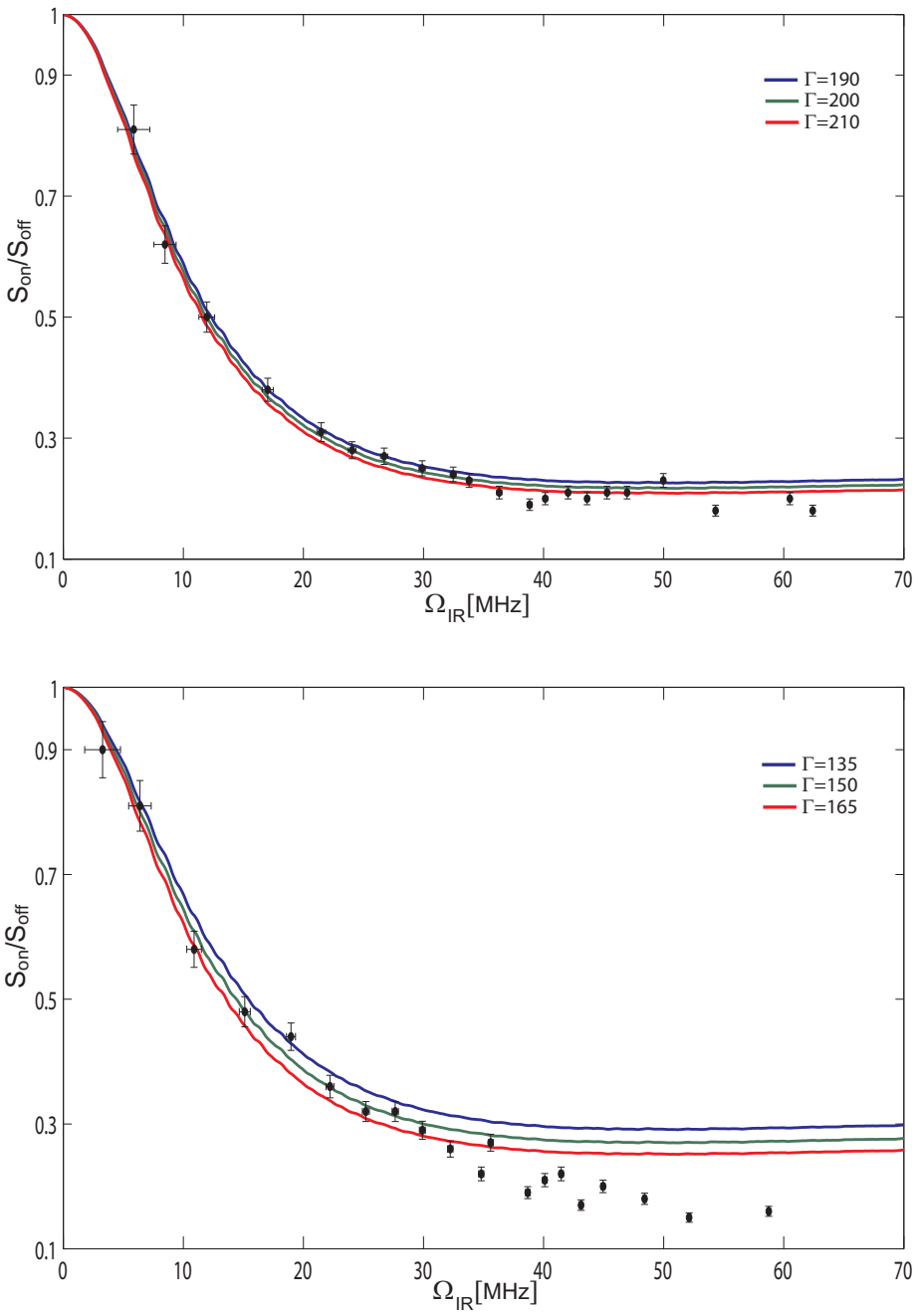

FIG. 4: (color online) Experimental values for the ratio $\frac{S^{on}}{S^{off}}$ as a function of the 881 nm rabi frequency. (top) Here the circular polarization corresponds to the MOT helicity (blue lines in figure 2). The solid curves are results from a simulations based on the optical Bloch equations, including the magnetic field of the MOT, at different decay constants $\Gamma = \Gamma_{22} + \Gamma_{21} = 190\ \mathrm{s}^{-1}$, 200 s^{-1}, 210 s^{-1}. Experiments with this circular helicity supports a value of $\Gamma = (200 \pm 10)\ \mathrm{s}^{-1}$.(bottom) Experiment with 881 nm polarization opposite to the MOT helicity. At a Rabi frequency of about 30 MHz the MOT is being destroyed by the destructive optical pumping effects of the 881 nm laser. Only data points below 30 MHz should be considered.

S. Bize et al., J. Phys. B **38**, S449 (2005)

L. Hollberg et al., J. Phys. B **38**, S469 (2005)

M. M. Boyd et al., Science **314**, 1430 (2006)

W. H. Oskay et al., Phys. Rev. Lett. **97**, 020801 (2006)

[2] Mette Machholm, Paul S. Julienne and Kalle-Antti Suominen. Phys. Rev A. **59**, R4113 (1999)

[3] Porsev, S. G. and Kozlov, M. G. and Rakhlina, Yu. G. and Derevianko, A. Physical Review A **64**, 012508 (2001)

[4] Wictor C. Magno, Reinaldo L. Cavasso Filho, and Flavio C. Cruz. Phys. Rev. A **67**, 043407 (2003)

[5] Josh W. Dunn, J. W. Thomsen, Chris H. Greene, and Flavio C. Cruz. Phys. Rev. A **76**, 011401 (2007)

[6] Giovanna Morigi and Ennio Arimondo. Phys. Rev. A **75**, 051404 (2007)

[7] N. Malossi, S. Damkjr, P. L. Hansen, L. B. Jacobsen, L. Kindt, S. Sauge, J. W. Thomsen, F. C. Cruz, M. Allegrini, and E. Arimondo. Phys. Rev. A **72**, 051403 (2005)

[8] T. E. Mehlstäubler, K. Moldenhauer, M. Riedmann, N. Rehbein, J. Friebe, E. M. Rasel, and W. Ertmer. Phys. Rev. A **77**, 021402 (2008)

[9] Madsen D. N. and Thomsen J. W. J. Phys. B **33**, 4981 (2000)

[10] T. K. Fang and Kozlov, T. N. Chang Physical Review A **61**, 052716 (2000)

[11] Sergey G. Porsev and Andrei Derevianko. Phys. Rev. A **69**, 042506 (2004)

[12] Loo F. Y., Brusch A., Sauge S., Allegrini M., Arimondo E., Andersen N., Thomsen J. W. J. Opt. B: Quantum Semiclass. Opt. **6**, 81 (2004)

Measurement of the $3s3p\ ^3P_1$ lifetime in magnesium using a magneto-optical trap

P. L. Hansen,[1] K. T. Therkildsen,[1] N. Malossi,[1] B. B. Jensen,[1] E. D. van Ooijen,[1] A. Brusch,[1] J. H. Müller,[1] J. Hald,[2] and J. W. Thomsen[1,*]

[1]*The Niels Bohr Institute, Universitetsparken 5, 2100 Copenhagen, Denmark*

[2]*Danish Fundamental Metrology, Ltd., Matematiktorvet 307, DK-2800 Lyngby, Denmark*

(Received 30 October 2007; published 2 June 2008)

We demonstrate an accurate method for measuring the lifetime of long-lived metastable magnetic states using a magneto-optical trap (MOT). Through optical pumping, the metastable $(3s3p)\ ^3P_1$ level is populated in a standard MOT. During the optical pumping process, a fraction of the population is captured in the magnetic quadrupole field of the MOT. When the metastable atoms decay to the $(3s^2)\ ^1S_0$ ground state they are recaptured into the MOT. In this system no alternative cascading transition is possible. The lifetime of the metastable level is measured directly as an exponential load time of the MOT. We have experimentally tested our method by measuring the lifetime of the $(3s3p)\ ^3P_1$ of ^{24}Mg. This lifetime has been measured numerous times previously, but with quite different results. Using our method we find the $(3s3p)\ ^3P_1$ lifetime to be (4.4 ± 0.2) ms. Theoretical values point toward a lower value for the lifetime.

DOI: 10.1103/PhysRevA.77.062502 PACS number(s): 32.70.Jz, 78.20.Ls, 32.70.Cs, 37.10.De

I. INTRODUCTION

In many spectroscopic experiments, beam line and cell measurements have played an important role, however, the workhorse of today is atom traps such as the magneto-optical trap (MOT), magnetic traps or various types of dipole traps. In these traps large numbers of atoms or molecules (10^9-10^{12}) can be stored with lifetimes exceeding 300 s at submilli-K temperatures [1–7]. Following this development a large amount of new high precision spectroscopic data on atoms and molecules has emerged. Parallel to these achievements theory has been developing new accurate models of atoms and molecules and single species and mixed species [8,9].

Compared to alkali elements collision and spectroscopic properties of the alkaline earth elements are less understood. In particular the lack of high precision radiative data prevents decisive conclusions on new accurate *ab initio* many-body calculations and models for two electron atoms [10]. Pioneering experiments on neutral Ca and Sr have provided new accurate data of the $^1P_1$, $^3P_1$, and $^3P_2$ lifetimes down to a 1% level [11–14]. These methods and the method presented in this paper are to some extent a variation of the well-known electron shelving experiments carried out with ions [15,16]. With photoassociation studies, lifetime measurements have greatly improved, yet the results are somewhat model dependent. Here we demonstrate the use a MOT for precision measurements of long-lived magnetic metastable lifetimes, by studying the metastable $(3s3p)\ ^3P_1$ state of ^{24}Mg. For this state we only consider decay to the ground state as the 0.5 mHz transition $(3s3p)\ ^3P_1 \rightarrow (3s3p)\ ^3P_0$ is strongly forbidden and suppressed. The lifetime of the $(3s3p)\ ^3P_1$ state has been measured several times, however, the various experimental results differ significantly and range from 4 ms to about 5 ms for the most recent measurement in 1992 [17–20]. Theoretical calculations support a value in the range 2.8 to 3.6 ms [10,21–23], however, not all theories were targeting high precision for this particular lifetime.

II. THEORY OF MEASUREMENT

In Fig. 1, we show the relevant energy levels and transitions for our experiment. The 285 nm transition is used for cooling the atoms, while the 457 nm transition is used to populate the metastable $(3s3p)\ ^3P_1$ state. Having cooled the atoms close to the Doppler temperature limit of approximately 2 mK, we expose the atoms to a millisecond pulse of 457 nm light. During this pulse most of the cold ensemble is transferred to the $(3s3p)\ ^3P_1$ state. Statistically about 1/3 of these can be transferred into the magnetically trapped $^3P_1$ state $|J=1, m_j=+1\rangle$ and held by the MOT quadrupole magnetic field. Experimentally, we transfer as much as 85% of the ground state by aligning the MOT to a point of nonzero magnetic field parallel to the propagation direction of the 457 nm. In this case optical pumping with circularly polarized light will only populate one of the magnetic substates $|J=1, m_j=\pm 1\rangle$ depending on the helicity of the 457 nm light and the direction of the magnetic field.

To model our system we have solved the optical Bloch equations for the three level scheme shown in Fig. 1. Special care must be taken in solving the equations numerically as the difference in the two upper state lifetimes differ by about a factor of 1000000. Figure 2 displays the calculated 285 nm fluorescence, monitored in the experiment, as a function of time. In Fig. 2(A) we have normal MOT operation, whereas in Fig. 2(B) we flash the MOT with the 457 nm pulse, and prepare a steady state population in the $(3s3p)\ ^3P_1$ state. It

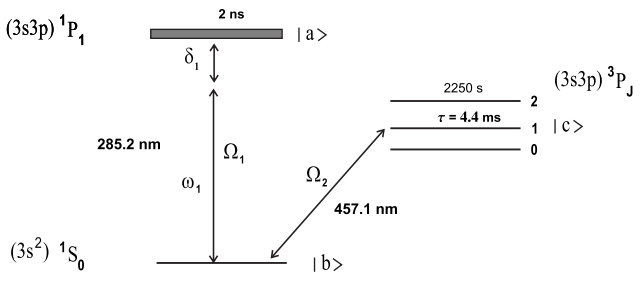

FIG. 1. Energy levels relevant for the lifetime measurement of the metastable $(3s3p)\ ^3P_1$ state of the 24 magnesium isotope. The involved levels are labeled $|a\rangle$, $|b\rangle$, and $|c\rangle$ respectively.

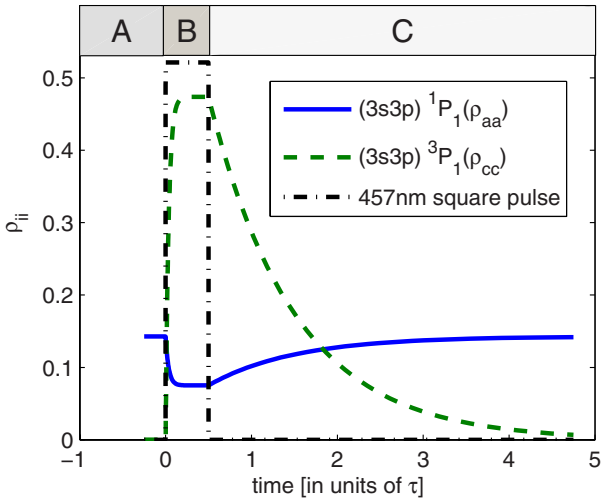

FIG. 2. (Color online) The number of atoms in the excited $(3s3p)\ ^1P_1$ (ρ_{aa}) and $(3s3p)\ ^3P_1$ (ρ_{cc}) states during the pulsed experiment. Time is in units of τ. The signal monitored in our experiment is proportional to the fluorescence determined by (ρ_{aa}).

can be shown that the 285 nm fluorescence in Fig. 2(B) decays exponentially. The time constant of this decay is controlled by the Rabi frequencies Ω_1 and Ω_2 as well as the lifetimes of the $(3s3p)\ ^1P_1$ and $(3s3p)\ ^3P_1$ states,with 2 ns and a few ms, respectively. In principle this may be used to obtain the lifetime of the $(3s3p)\ ^1P_1$ state as Fig. 2(C) yields the metastable lifetime. Practically determining the lifetime in this way is difficult as it requires precise knowledge of the involved Rabi frequencies, i.e., laser intensities at the MOT region.

In Fig. 2(C) the 285 nm fluorescence signal rises exponentially according to

$$S(t) = N_0(1 - e^{-t/\tau}), \tag{1}$$

with a time constant of the metastable lifetime τ. In the experiment $(3s3p)\ ^3P_1$ atoms decaying to the $(3s^2)\ ^1S_0$ ground state are recaptured in the MOT. Here we monitor them as they emit fluorescence at 285 nm. Three important time scales control the dynamics of the system, the metastable state lifetime of about 4 ms, the MOT lifetime 4 s and finally the magnetic trap lifetime of more than 20 s. However, the time scale of interest to this experiment is only about 40 ms $(\sim 10\tau)$, and contributions to the signal from a finite magnetic trap lifetime may safely be disregarded. By including the linear losses from the MOT due to collisions with background atoms, photoionization [24], etc., here described by α, we obtain

$$\dot{N} = \frac{N_0}{\tau}(e^{-t/\tau}) - \alpha N(t), \tag{2}$$

where N_0 is the number of metastable atoms trapped in the magnetic trap. The solution of Eq. (2) becomes

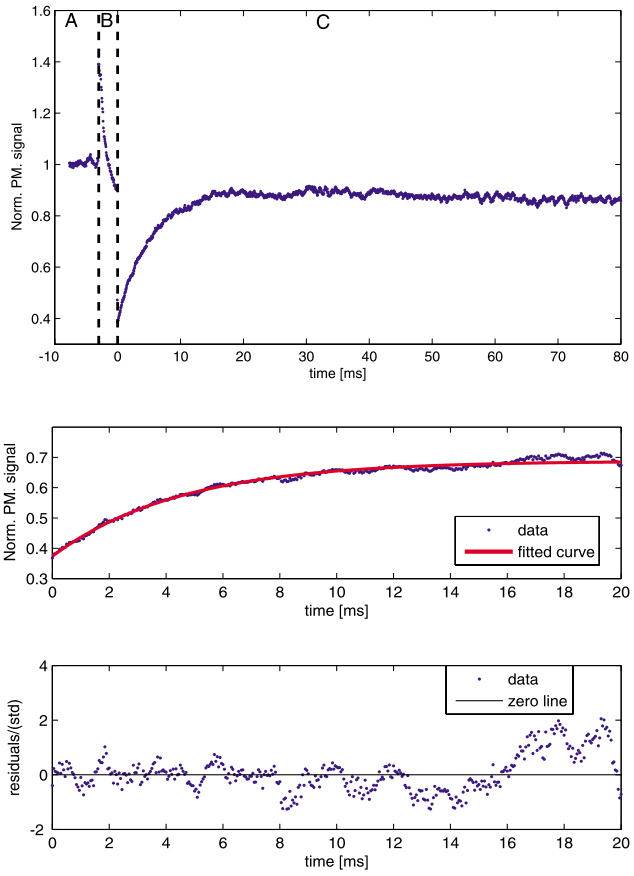

FIG. 3. (Color online) Typical MOT fluorescence measurement, here normalized to the uv power level. The interval marked with dashed lines show the 457 nm pulse. As the 457 nm light is turned on additional background photons are observed. After a load period of about 10 ms the signal is slowly decays due to the 4–5 s MOT lifetime. Lower two graphs: the red curve is a fit to Eq. (3), giving 4.4 ms. The lower part shows the residuals of the fit.

$$N(t) = \frac{\gamma_{cc}}{\gamma_{cc} - \alpha} N_0(e^{-\alpha t} - e^{-\gamma_{cc} t}), \tag{3}$$

with $\gamma_{cc} = 1/\tau$. As γ_{cc} is a factor 1000 larger than α we neglect linear losses of the magnetic trapped atoms during the time interval of the measurement $\sim 10\tau$. For time scales longer than 40 ms this is no longer true as seen in Fig. 3.

III. EXPERIMENTAL SETUP

The main part of the experimental setup has been described in Ref. [25]. A standard magneto-optical trap is intersected by a circularly polarized 457 nm light beam. The beam is overlapped with a MOT beam in the plane perpendicular to the MOT coil symmetry axis. An amplified 914 nm diode is used for generation of 457 nm light by frequency doubling in $KNbO_3$ in a standard four mirror cavity [26]. The 914 nm diode is antireflection coated with feedback from an external grating in a Littrow configuration, and it provides an output of approximately 40 mW. The amplifier consist of an AR coated broad-area laser diode (BAL). Normally we have

about 350 mW output from the 914 nm system and 125 mW of 457 nm light. The 457 nm laser is free running during the experiment (effective linewidth 1 MHz) and is tuned to resonance manually by minimizing the 285 nm fluorescence. In free running mode the 457 nm laser is stable for minutes, however, it is nevertheless tuned before each individual decay experiment. The combined power broadening of 457 and 285 nm transitions, added with the Doppler effect, makes the metastable state easily populated without the need for a narrow-linewidth 457 nm laser. In order to control the pulse of the blue light, the beam is sent through an AOM. The 457 nm beam has a diameter comparable to the UV beams (1.5 mm) used for the MOT and is sent through one of the UV mirrors overlapping the UV beam. Experiments were performed for both a single and a retro reflected beam, with no detectable difference on the outcome.

The experiment is fully controlled by computer using a sequence program in LABVIEW. Our main parameters for this experiment include: 457 nm pulse time 0.1–5 ms, coil current 100–200 A, corresponding to a coil symmetry gradient of 108–216 Gauss/cm. Just before the blue 457 nm pulse is sent we close the atomic beam shutter which remains closed during period C to prevent loading from the thermal beam source. Typically 10^7 atoms are captured in the MOT (load rate 3×10^6 s^{-1}), with a rms diameter of 1 mm and temperatures from 3–5 mK. The Doppler cooling limit for the MOT is 2 mK as sub-Doppler cooling is not supported in this system.

In our experiment, the $|J=1,m_j=+1\rangle$ atoms are captured in the MOT magnetic quadrupole field. The Zeeman energy shift yields $g_j\mu_B m_j/k_B=100.8$ μK/Gauss ($g_j=3/2$) giving 1.7 mK/mm at 172.8 Gauss/cm, our typical operating gradient on the coil symmetry axis. As the MOT temperature is 3–5 mK and the laser beam diameter a 3 mm ($1/e^2$), most $|J=1,m_j=+1\rangle$ atoms remain trapped within the MOT volume.

IV. EXPERIMENTAL RESULTS AND DISCUSSION

In Fig. 3 we present a typical experimental result with MOT operation, 457 nm flash, and reload clearly visible. Small oscillations in the fluorescence signal are visible and are due to a poor servo loop of the UV cavity. To minimize these oscillations we divide the observed fluorescence signal with a normalizing power signal taken from one of the uv beams. The dashed lines show when the 457 nm pulse is on. During this period we observe an overall increased signal due to scattered 457 nm photons on vacuum windows, etc., not being coated for this wavelength. In the reload period we recover 85% of the atoms. The last 15% may be lost due to imperfect polarization of the 457 nm light or possibly if the MOT temperature is outside our recapture range. Hot atoms trapped magnetically may decay outside the MOT capture region defined by the laser beams, here 3 mm. Our maximal range is 5.1 mK/mm (2.6 mK/mm perpendicular to the symmetry axis of the coils) and barely sufficient for a 5 mK MOT temperature. After about 10 ms we notice a weak decay of the reloaded signal. This is due to linear loss mechanisms reducing the MOT lifetime to 4–5 s, limited mainly by two photon ionization induced by the 285 nm MOT light. The lifetime of the magnetic trap is estimated to be about 20 s at our present background pressure of 10^{-9} mbar.

Figure 3, lower panel shows data from the reload period. The red curve is Eq. (3) fitted to the data giving $\tau=4.4$ ms. A total of 80 measurements were taken at different settings, exploring systematic effects (magnetic field gradient, power of the 457 nm pulse, pulse duration and polarizations) and maximum signal-to-noise ratio and recapture fraction. The measurements at maximum field gradient 200 Gauss/cm gave the best signal to noise ratio and only these 34 measurements are used in the quoted lifetime. Our measurements gave a final value of (4.4 ± 0.2) ms here quoted with the statistical uncertainty being the standard deviation divided $\sqrt{N}$, N=34. We found the standard deviation of 0.9 ms for the 34 measurements and thus an uncertainty of 0.16 ms, here rounded to 0.2 ms.

Looking at the fit in Fig. 3 middle panel, we would expect a better uncertainty than the quoted 0.2 ms. However, noise fluctuations on the same time scale as the lifetime will give shot to shot fluctuations. This could be caused by fluctuations in the laser intensity, but we rather attribute this effect to the dynamics of the atoms in the trap, however, indirectly linked to the laser intensity fluctuations. Atoms exited to $|J=1,m_j=+1\rangle$ state, experiencing an attractive potential, would perform an oscillating motion with a characteristic frequency determined by the gradient of the magnetic field and the initial temperature of the MOT. The latter is sensitive to intensity fluctuation of the laser. Simple 1D numerical simulations show, that for our setup with an estimated MOT temperature of about 3–5 mK corresponding to a mean velocity of close to 2 m/s, this would induce oscillations in the observed fluorescence peaking on time scales close to the lifetime. The amplitude of the oscillations is proportional to the number of atoms in the $|J=1,m_j=+1\rangle$, which explains why these oscillations are not observed at times much later than the lifetime. Improving the uv intensity stability by a lock, servoed using, e.g., an AOM, could to some extend lower the MOT temperature to improve the accuracy of the measurements.

In Table I we have collected experimental and theoretical investigations of the $(3s3p)\ ^3P_1$ lifetime. Experimentally, there is a good agreement between the different methods. The latest experimental value [17] seems somewhat higher compared to the present work, but still overlapping at the 1σ level. More recent theoretical calculations point toward a lower value for the lifetime. The difference seems not to be linked to a particular experimental or theoretical method, but appear as a general trend. Possible errors could be caused by accidental resonance to other excited states. For the magnesium energy levels no resonant transitions is present at half or double of the 457 nm wavelength. Closest we find $3s4p\ ^1P_1 \rightarrow 3s10d\ ^1D_2$ at 901.6 nm and $2p^6 3s^2\ ^1S_0 \rightarrow 3s4p\ ^1P_1$ at 202.6 nm which both can be ruled out here. Another possible mechanism could be magnetic field induced mixing to near by P states. Using first order perturbation theory we write the $^3P_1$ state in terms of $^1P_1$ and ^3P_J contributions [27]

TABLE I. Collection of most recent calculated and measured $(3s3p)\ ^3P_1$ lifetimes.

Theoretical			Experimental		
Reference	Year	τ [ms]	Reference	Year	τ [ms]
[21]	2004	2.8(1)	This work	2006	4.4(2)
[22]	2002	3.8	[17]	1992	5.3(7)
[10]	2001	3.6	[18]	1982	4.8(8)
[23]	1979	4.60(4)	[19]	1975	4.5(5)
			[20]	1975	4.0(2)

$$|^3P_1'\rangle = \alpha|^3P_0\rangle + \beta|^3P_1\rangle + \gamma|^3P_2\rangle + \delta|^1P_1\rangle. \quad (4)$$

Evaluating the involved matrix elements gives $\alpha = (3/2)^{1/2}\mu_B B/\hbar\Delta_0$, $\beta=1$, $\gamma=(3/2)^{1/2}\mu_B B/\hbar\Delta_1$, and $\delta = (6)^{1/2}\mu_B B/\hbar\Delta_3$. Here Δ_0 is the energy difference $^3P_0$-$^3P_1$, Δ_1 is the energy difference $^3P_1$-$^3P_2$, etc, μ_B is the Bohr magneton and B the magnetic field. The Δ values are $\Delta_0 = 600$ GHz, $\Delta_1 = 1200$ GHz, and $\Delta_2 = 395.3$ THz, see Fig. 1. However, our magnetic field is below 22 Gauss within the atom cloud giving coefficients of magnitude 10^{-8} to 10^{-10} and the mixing effect can be neglected here.

V. CONCLUSION

In conclusion we have measured the metastable II4 magnesium $(3s3p)\ ^3P_1$ lifetime using a magneto-optical trap by loading the metastable atoms into a magnetic quadrupole trap. Our value (4.4 ± 0.2) ms is the most accurate to date and in good agreement with recent experimental work on an 1σ level. Theoretically, several recent calculations point toward a significantly lower value and the general discrepancy between theory and experiment is presently not understood.

ACKNOWLEDGMENTS

We would like to thank Gretchen K Campbell for stimulating discussions and for a careful reading of the manuscript. We wish to acknowledge the financial support from the Lundbeck Foundation and the Carlsberg Foundation.

[1] R. Grimm, M. Weidemuller, and Y. B. Ovchinnikov, Adv. At., Mol., Opt. Phys. **42**, 95 (2000).
[2] J. Doyle, B. Friedrich, R. V. Krems, and F. Masnou-Seeuws, Eur. Phys. J. D **31**, 149 (2004).
[3] J. D. Weinstein, R. deCarvalho, T. Guillet, Br. Friedrich, and J. M. Doyle, Nature (London) **395**, 921 (1998).
[4] D. Egorov, W. C. Campbell, B. Friedrich, S. E. Maxwell, E. Tsikata, L. D. van Buuren, and J. M. Doyle, Eur. Phys. J. D **31**, 307 (2004).
[5] S. V. Nguyen, S. Doret, C. B. Connolly, R. A. Michniak, W. Ketterle, and J. Doyle, Phys. Rev. A **72**, 060703(R) (2005).
[6] H. L. Bethlem, G. Berden, and G. Meijer, Phys. Rev. Lett. **83**, 1558 (1999).
[7] K. M. R. van der Stam, E. D. van Ooijen, R. Meppelink, J. M. Vogels, and P. van der Straten, Rev. Sci. Instrum. **78**, 013102 (2007).
[8] J. Weiner, V. S. Bagnato, S. Zilio, and P. S. Julienne, Rev. Mod. Phys. **71**, 1 (1999).
[9] K. M. Jones, E. Tiesinga, P. D. Lett, and P. S. Julienne, Rev. Mod. Phys. **78**, 1041 (2006).
[10] S. G. Porsev, M. G. Kozlov, Yu. G. Rakhlina, and A. Derevianko, Phys. Rev. A **64**, 012508 (2001).
[11] G. Zinner, T. Binnewies, F. Riehle, and E. Tiemann, Phys. Rev. Lett. **85**, 2292 (2000).
[12] M. Yasuda and H. Katori, Phys. Rev. Lett. **92**, 153004 (2004).
[13] P. G. Mickelson, Y. N. Martinez, A. D. Saenz, S. B. Nagel, Y. C. Chen, T. C. Killian, P. Pellegrini, and R. Cote, Phys. Rev. Lett. **95**, 223002 (2005).
[14] T. Zelevinsky, M. M. Boyd, A. D. Ludlow, T. Ido, J. Ye, R. Ciurylo, P. Naidon, and P. S. Julienne, Phys. Rev. Lett. **96**, 203201 (2006).
[15] W. Nagourney, J. Sandberg, and H. Dehmelt, Phys. Rev. Lett. **56**, 2797 (1986).
[16] J. C. Bergquist, R. G. Hulet, W. M. Itano, and D. J. Wineland, Phys. Rev. Lett. **57**, 1699 (1986).
[17] A. Godone and C. Novero, Phys. Rev. A **45**, 1717 (1992).
[18] H. S. Kwong, P. L. Smith, and W. H. Parkinson, Phys. Rev. A **25**, 2629 (1982).
[19] P. S. Furcinitti, J. J. Wright, and L. C. Balling, Phys. Rev. A **12**, 1123 (1975).
[20] C. J. Mitchell, J. Phys. B **8**, 25 (1975).
[21] R. Santra, K. V. Christ, and C. H. Greene, Phys. Rev. A **69**, 042510 (2004).
[22] I. M. Savukov and W. R. Johnson, Phys. Rev. A **65**, 042503 (2002).
[23] C. Laughlin and G. A. Victor, Astrophys. J. **234**, 407 (1979).
[24] D. N. Madsen and J. W. Thomsen, J. Phys. B **33**, 4981 (2000).
[25] F. Y. Loo, A. Brusch, S. Sauge, M. Allegrini, E. Arimondo, N. Andersen, and J. W. Thomsen, J. Opt. B: Quantum Semiclassical Opt. **6**, 81 (2004).
[26] V. Ruseva and J. Hald, Appl. Opt. **42**, 5500 (2003).
[27] I. I. Sobelman, *Atomic Spectra and Radiative Transitions* (Springer-Verlag, Berlin, 1992).

Amplification and ASE suppression in a polarization-maintaining ytterbium-doped all-solid photonic bandgap fibre

C. B. Olausson[1,2*], C. I. Falk[3], J. K. Lyngsø[1,2], B. B. Jensen[3], K. T. Therkildsen[3], J. W. Thomsen[3], K. P. Hansen[1], A. Bjarklev[2] and J. Broeng[1]

[1] Crystal Fibre A/S, Blokken 84, DK-3460 Birkerød, Denmark
[2]DTU Fotonik, Ørsteds Plads, building 343, 2800 Kgs. Lyngby, Denmark
[3]Niels Bohr Institute, Universitetsparken 5, 2100 København, Denmark
[*]Corresponding author: cbo@crystal-fibre.com

Abstract: We demonstrate suppression of amplified spontaneous emission at the conventional ytterbium gain wavelengths around 1030 nm in a cladding-pumped polarization-maintaining ytterbium-doped all-solid photonic crystal fibre. The fibre works through combined index and bandgap guiding. Furthermore, we show that the peak of the amplified spontaneous emission can be shifted towards longer wavelengths by rescaling the fibre dimensions. Thereby one can obtain lasing or amplification at longer wavelengths (1100 nm – 1200 nm) as the amount of amplification in the fibre is shown to scale with the power of the amplified spontaneous emission.

OCIS codes: (060.2280) Fiber design and fabrication; (060.2270) Fiber characterization; (060.2400) Fiber properties; (060.2420) Fibers, polarization-maintaining; (060.5295) Photonic crystal fibers; (060.3510) Lasers, Fiber.

References and links

1. G. Bouwmans, L. Bigot, Y. Quiquempois, F. Lopez, L. Provino, and M. Douay, "Fabrication and characterization of an all-solid 2D photonic bandgap fiber with a low-loss region (< 20 dB/km) around 1550 nm," Opt. Express **13**, 8452-8459 (2005).
2. G. Canat, J. C. Mollier, J. P. Bouzinac, G. L. M. Williams, B. Cole, L. Goldberg, G. Kulcsar, Y. Jaouen, "Power limitations of fiber lasers at 1.5 µm by parasitic lasing effects," in *Conference on Lasers and Electro-Optics/Quantum Electronics and Laser Science and Photonic Applications Systems Technologies*, Technical Digest (CD) (Optical Society of America, 2004), paper CMK6.
3. A. Shirakawa, J. Ota, H. Maruyama, and K. -I. Ueda, "Linearly-Polarized Yb-Doped Fiber Laser Directly Operating at 1178 nm for 589-nm Generation," in *Advanced Solid-State Photonics*, OSA Technical Digest Series (CD) (Optical Society of America, 2007), paper MD1.
4. S. Sinha, C. Langrock, M. Digonnet, M. Fejer, and R. Byer, "Efficient yellow-light generation by frequency doubling a narrow-linewidth 1150 nm ytterbium fiber oscillator," Opt. Lett. **31**, 347-349 (2006).
5. N. Malossi, S. Damkjaer, P. L. Hansen, L. B. Jacobsen, L. Kindt, S. Sauge, J. W. Thomsen, F. C. Cruz, M. Allegrini, and E. Arimondo, "Two-photon cooling of magnesium atoms," Phys. Rev. A **72**, 051403 (2005).
6. A. Wang, A. K. George, and J. C. Knight, "Three-level neodymium fiber laser incorporating photonic bandgap fiber," Opt. Lett. **31**, 1388-1390 (2006).
7. V. Pureur, L. Bigot, G. Bouwmans, Y. Quiquempois, M. Douay, and Y. Jaouen, "Ytterbium-doped solid core photonic bandgap fiber for laser operation around 980 nm," Appl. Phys. Lett. **92**, 061113 (2008).
8. R. Goto, K. Takenaga, K. Okada, M. Kashiwagi, T. Kitabayashi, S. Tanigawa, K. Shima, S. Matsuo, and K. Himeno, "Cladding-Pumped Yb-Doped Solid Photonic Bandgap Fiber for ASE Suppression in Shorter Wavelength Region," in *Optical Fiber Communication Conference and Exposition and The National Fiber Optic Engineers Conference*, OSA Technical Digest (CD) (Optical Society of America, 2008), paper OTuJ5.
9. T. Birks, F. Luan, G. Pearce, A. Wang, J. Knight, and D. Bird, "Bend loss in all-solid bandgap fibres," Opt. Express **14**, 5688-5698 (2006).
10. K. P. Hansen, C. B. Olausson, J. Broeng, K. Mattsson, M. D. Nielsen, T. Nikolajsen, P. M. W. Skovgaard, M. H. Sørensen, M. Denniger, C. Jakobsen, and H. R. Simonsen, "Airclad fiber laser technology," Proc. SPIE **6873**, 687307 (2008).

#98542 - $15.00 USD Received 8 Jul 2008; revised 15 Aug 2008; accepted 17 Aug 2008; published 20 Aug 2008

11. W. J. Wadsworth, R. M. Percival, G. Bouwmans, J. C. Knight, T. A. Birks, T. D. Hedley, and P. S. J. Russell, "Very High Numerical Aperture Fibers," IEEE Photonics Tech. Lett. **16**, 843-845 (2004).
12. A. Cerqueira S. Jr., F. Luan, C. Cordeiro, A. George, and J. Knight, "Hybrid photonic crystal fiber," Opt. Express **14**, 926-931 (2006).
13. J. K. Lyngsø, B. J. Mangan, and P. J. Roberts, "Polarization Maintaining Hybrid TIR/Bandgap All-Solid Photonic Crystal Fiber," in *Conference on Lasers and Electro-Optics/Quantum Electronics and Laser Science Conference and Photonic Applications Systems Technologies*, OSA Technical Digest (CD) (Optical Society of America, 2008), paper CThV1.
14. N. M. Litchinitser, S. C. Dunn, B. Usner, B. J. Eggleton, T. P. White, R. C. McPhedran, and C. Martijn de Sterke, "Resonances in microstructured optical waveguides," Opt. Express **11**, 1243-1251 (2006).

1. Introduction

In photonic bandgap (PBG) fibres light is confined within a low-index core by a microstructured cladding typically formed by silica and air. In this work an all-solid PBG fibre is used in which the PBG cladding is made by a triangular lattice of germanium-doped high-index micro-rods in a silica background, which raise the overall cladding index as in [1], while the core consists of a single ytterbium-doped micro-rod as gain medium. Combining the wavelength filtering effect of PBG confinement with an ytterbium-doped core results in efficient suppression of amplified spontaneous emission (ASE) at the conventional ytterbium gain wavelengths around 1030 nm and thus a reduction in parasitic lasing outside the bandgap, which typicially limits the operation of long wavelength fibre lasers and amplifiers [2]. Frequency doubled fibre lasers and amplifiers around 1180 nm [3,4] are of interest for yellow light generation in medical and astronomical application, while frequency quadrupling of fibre lasers can generate narrow linewidth UV light in the range 255 nm – 295 nm for applications in atomic physics [5]. Previous work on the use of the photonic bandgap filtering effect for shorter wavelength laser operation at 907 nm and 980 nm is reported in [6,7].

In this paper, we demonstrate suppression of ASE for two different all-solid PBG fibres with different bandgap positions. We show that the ASE peak can be shifted towards longer wavelengths by rescaling the dimensions of the fibre and thereby moving the bandgap. It has been shown that the ASE peak of an all-solid PBG fibre can be shifted towards longer wavelengths by reducing the coiling diameter [8], however, this method works by and suffers from significant bend losses [9]. With the present approach, we show that tight coiling of the fibre is not necessary in order to shift towards longer wavelengths. Furthermore, we demonstrate that the amplification in the fibres scales with the ASE power for a given wavelength.

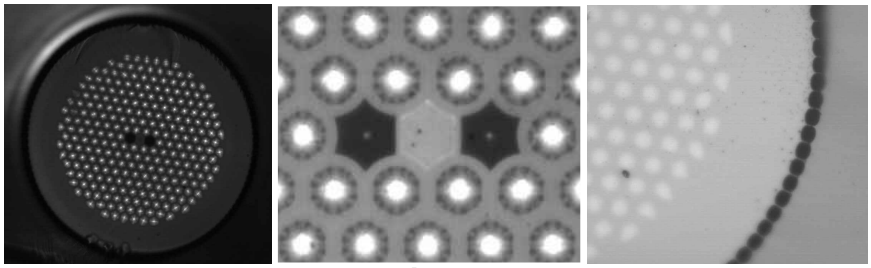

Fig. 1. (a) Microscope image of the fibre structure. The lighter regions are the germanium-doped rods constituting the pump-cladding, while the two darker regions are the boron rods. (b) Microscope image of the core region. (c) Microscope image of the airclad surrounding the pump-cladding structure.

2. Fibre properties

Two all-solid photonic PBG fibres were fabricated with a cladding pitch of 9.45 μm and 9.80 μm, respectively. The signal core consists of an ytterbium-doped rod, which is index matched to the silica background. The core is surrounded by the PBG pump-cladding structure made

by an eight period triangular lattice structure of high-index germanium-doped rods. For the two fibres we measured the diameter of the cladding to 214 μm and 220 μm, respectively. Both fibres have pump absorption of 1.1 dB/m at 976 nm. Furthermore, the PBG pump cladding is surrounded by an airclad structure providing the pump guide with a large numerical aperture of 0.57, allowing for efficient high-power cladding-pumping [10,11].

The polarization-maintaining properties of the fibre are obtained by incorporating two low index boron-doped rods on either side of the core. The boron-doped rods act as stress applying parts, inducing high birefringence in the fibre while the lower index results in confinement by total internal reflection (TIR) in one direction and bandgap guiding in other directions [12]. The birefringence is on the order of 10^{-4}.

Microscope images of the fibre structure, the core and the airclad structure surrounding the pump cladding are shown in Fig. 1. The lighter regions are the germanium-doped rods, while the two darker regions near the core are the boron rods.

Core properties of the fibre have been determined by performing measurements on a fibre which is identical to the fibre in question in terms of pump cladding and core properties, but without the surrounding airclad. Near-field measurements at 1150 nm yield a $1/e^2$ mode field diameter of 10.0 μm in the axis parallel to the stress rods, a mode field diameter of 10.8 μm in the axis perpendicular to the stress rods and an average numerical aperture of 0.1. A near field image taken in the third order bandgap using 1150nm light is shown in Fig. 2. The lack of an anti-resonant tail of light in the boron-doped stress rods on either side of the core is evidence of index guiding in the direction of the stress rods and bandgap guiding in the other direction. A passive version of this type of hybrid TIR / bandgap fibre has been reported in [13].

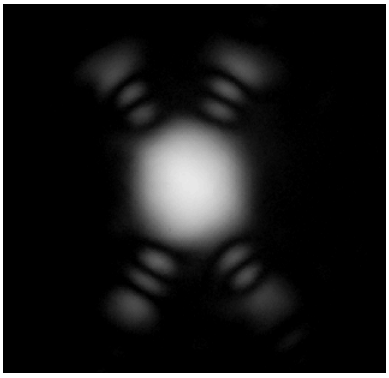

Fig. 2. Near field CCD image taken in the third order bandgap using 1150 nm light, where the stress rods are in the horizontal direction. An anti-resonant tail of light is visible in the surrounding high-index germanium-doped rods, but not in the boron-doped stress rods.

Recently, ASE suppression in an ytterbium-doped all-solid photonic PBG fibre for long wavelength applications has been demonstrated [8]. The present fibre design is polarization-maintaining and holds potential for higher power due to the airclad surrounding the pump cladding.

3. Suppression of amplified spontaneous emission

The transmission spectrum of the fibres is measured using the setup in Fig. 3(a). In order to only transmit light in the core, light from a white light source is launched into 1 m of single-mode large mode area (LMA) fibre with a core size of 10 um, which is then butt-coupled to the 10 μm core of 30 m of the ytterbium-doped all-solid PBG fibre. The light from the core of the PBG fibre is subsequently collected by a high NA 10 μm core fibre in order to limit light collected by the optical spectrum analyzer (OSA) to the core region.

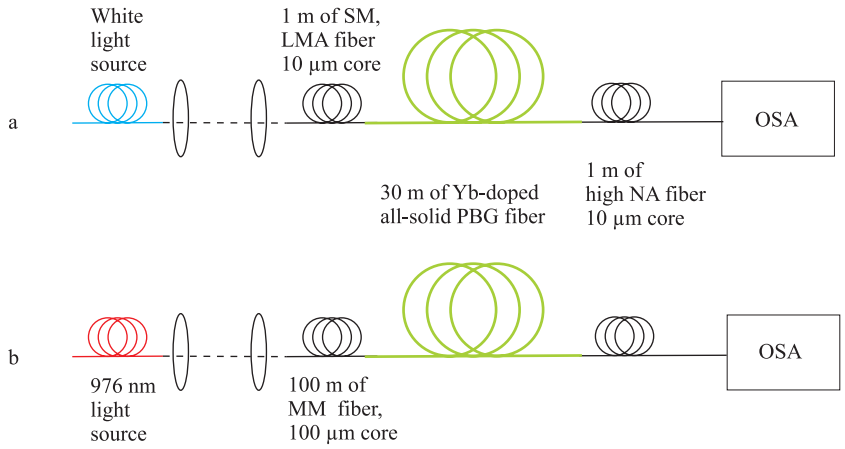

Fig. 3. (a) Experimental setup for measuring the bandgap transmission spectrum and (b) setup for measuring the ASE spectrum.

The ASE spectrum in the core is measured using the setup shown in Fig. 3(b). The 976 nm pump light is launched into the pump cladding of the PBG fibre using a multi-mode fibre with a core size of 100 µm and the output core light is collected by the same high NA fibre and detected by the optical spectrum analyzer.

Figure 4 shows the ASE spectrum (red) of a PBG fibre with a bandgap centered around 1140 nm (grey). Compared to the ASE spectrum of an index-guiding photonic crystal fibre (black), the PBG fibre shows significant suppression of ASE outside the bandgap.

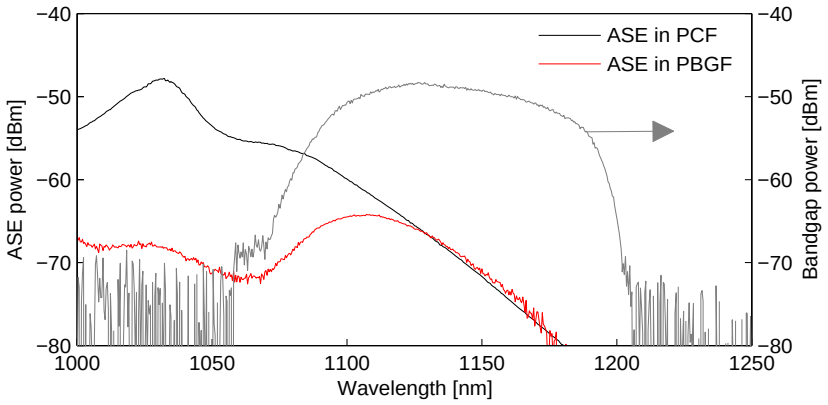

Fig. 4. ASE spectrum of an ytterbium-doped all-solid PBG fibre (red) showing suppression of ASE outside the bandgap (grey) compared to the ASE spectrum of an index guiding photonic crystal fibre (black).

Figure 5 shows the ASE spectra of the two different ytterbium-doped all-solid PBG fibres, one designed with a bandgap centered at 1140 nm (red) and another designed with a bandgap centered at 1180 nm (black). Results show that the peak of the ASE spectrum can be shifted towards longer wavelengths by moving the bandgap position in the fibre. This is done by rescaling the fibre dimensions in the drawing process.

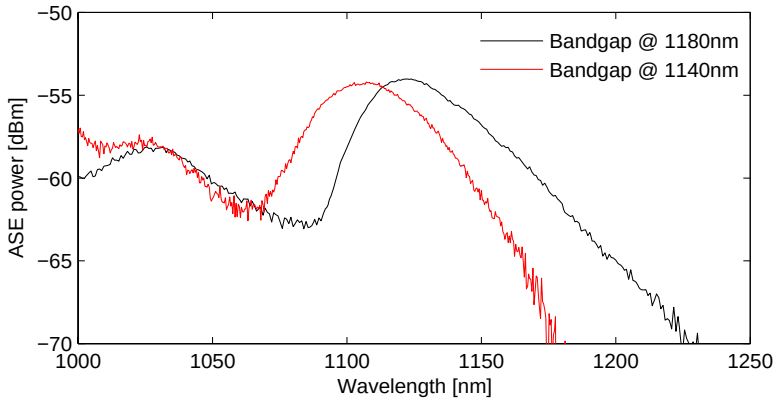

Fig. 5. ASE spectra of two ytterbium-doped all-solid PBG fibres with bandgap positions centered at 1140nm (red) and 1180nm (black). The peak of the ASE spectrum is shifted towards longer wavelengths by moving the bandgap.

4. Amplification and laser properties

The amplification properties of the fibres are measured using the forward seeded amplification setup depicted in Fig. 6. The PBG fibre is pumped with up to 3 W of 980 nm light and seeded with 2 mW of 1080 nm – 1145 nm light from a laser cavity created from 30 m of the same PBG fibre and a laser dispersing prism. The seed laser cavity is tuned using a mirror. Furthermore, the pump light is launched at an angle in order to reduce guidance in the high-index rods and obtain maximum pump absorption.

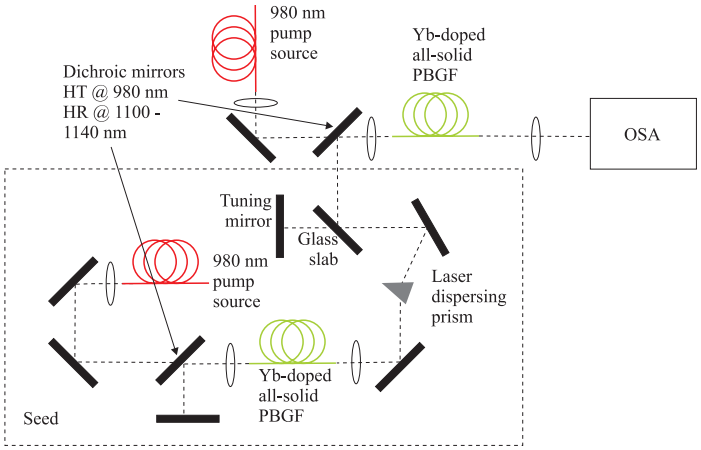

Fig. 6. Amplification setup using forward seeding with a seed setup tunable in the range 1080 nm – 1145 nm.

The amplification results for the two PBG fibres are presented in Fig. 7. For both fibres results show that the amplification for a given wavelength scales with the ASE power. For the specified pump power an amplification of up to 15dB is obtained in both fibres. Peak amplification occurs at the wavelengths that experience the least loss due to the bandgap combined with the highest gain due to their emission cross section. Increasing the pump power will shift the ASE peak, and hence also the peak amplification, towards the left bandgap edge.

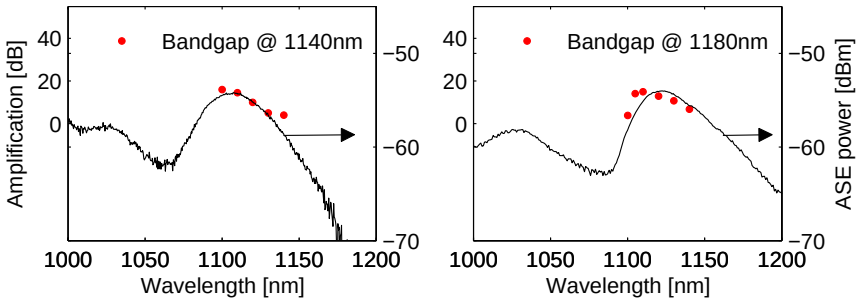

Fig. 7 The amplification properties of the fibres (red dots) are seen to follow the ASE profiles (black).

Laser properties of the fibres are presented in Fig. 8. The fibre with the bandgap centered at 1140 nm is pumped with 1.1 W of 980 nm light while the fibre with the bandgap centered at 1180 nm is pumped with 2.5 W. Approximately 17 dB of pump light is absorbed at 980 nm while 2 dB of pump light is trapped in the high-index rods due to imperfect angled incoupling. The fibres are tunable as shown in Fig. 8(a) with optimum wavelengths at approximately 1100 nm and 1120 nm for the two fibres. These wavelengths lie at the top of the left bandgap edge. The bandgap widens as the cladding pitch is increased [14], which causes the left bandgap edge to shift less than the bandgap center and hence reduces the shift of the optimum lasing wavelength to 20 nm compared to the 40 nm shift of the bandgap center. Furthermore, in Fig. 8(b) the ASE suppression is apparent in the output power spectrum outside the bandgap, when the fibre with a bandgap centered at 1180 nm is lasing at exactly the edge of the bandgap. Comparing the level of ASE inside the bandgap to the level of ASE outside the bandgap, we measure an ASE suppression of 15dB at the bandgap edge.

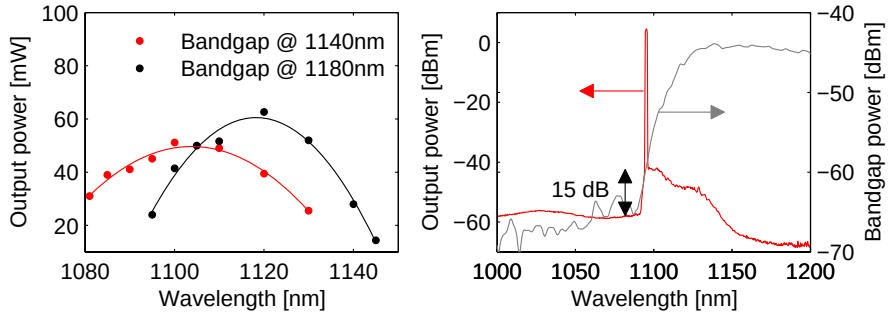

a **b**

Fig. 8. (a) Laser properties of the two fibres. (b) Power spectrum of the PBG fibre with a bandgap centered at 1180nm (red) lasing at the edge of the bandgap (grey). ASE suppression of 15 dB is apparent in the power spectrum outside the bandgap.

5. Conclusion

Experimental results show ASE suppression in two different ytterbium-doped all-solid PBG fibres and the ability to shift the ASE peak towards longer wavelengths by rescaling of the fibre design. In addition to the control of the ASE suppression, amplification measurements for the two fibres have shown that also the amplification properties can be controlled by design as the amplification is seen to scale with the ASE power. These features can be useful when designing fibres with potential for even longer wavelength lasing and amplification and can open new possibilities for high-power ytterbium-doped fibre lasers and amplifiers lasing at longer wavelengths above the conventional ytterbium gain wavelengths.

Metastable Magnesium fluorescence spectroscopy using a frequency-stabilized 517 nm laser

Ming He, Brian B. Jensen, Kasper T. Therkildsen, Anders Brusch, and Jan W. Thomsen*

Niels Bohr Institute, University of Copenhagen, Universitetsparken 5, DK-2100 Copenhagen,
**Corresponding author: jwt@fys.ku.dk*

Abstract: We present a laser operating at 517 nm for our Magnesium laser-cooling and atomic clock project. A two-stage Yb-doped fiber amplifier (YDFA) system generates more than 1.5 W of 1034 nm light when seeded with a 15 mW diode laser. Using a periodically poled lithium niobate (PPLN) waveguide, we obtained more than 40 mW of 517 nm output power by single pass frequency doubling. In addition, fluorescence spectroscopy of metastable magnesium atoms could be used to stabilize the 517 nm laser to an absolute frequency within 1 MHz.

OCIS codes: (190.2620) Frequency conversion; (140.3510) Lasers, fiber; (020.7010) Trapping

References and links

1. T. P. Heavner, S. R. Jefferts, E. A. Donley, J. H. Shirley, and T. E. Parker, "NIST-F1: recent improvements and accuracy evaluations," Metrologia **42**, 411-422 (2005).
2. S. Bize, P. Laurent, M. Abgrall, H. Marion, I. Maksimovic, L. Cacciapuoti, J. Grünert, C. Vian, F. Pereira dos Santos, P. Rosenbusch, P. Lemonde, G. Santarelli, P. Wolf, A. Clairon, A. Luiten, M. Tobar, and C. Salomon, "Cold atom clocks and applications," J. Phys. B: Atomic, Mol. Opt. Phys. **38**, S449-S468 (2005).
3. U. Sterr, C. Degenhardt, H. Stoehr, Ch. Lisdat, H. Schnatz, J. Helmcke, F. Riehle, G. Wilpers, Ch. Oates, and L. Hollberg, "The optical calcium frequency standards of PTB and NIST," C. R. Physique **5**, 845-855 (2004).
4. C. Degenhardt, H. Stoehr, Ch. Lisdat, G. Wilpers, H. Schnatz, B. Lipphardt, T. Nazarova, P. Pottie, U. Sterr, J. Helmcke, and Fritz Riehle, "Calcium optical frequency standard with ultracold atoms: Approaching 10^{-15} relative uncertainty," Phys. Rev. A **72**, 062111 (2005).
5. G. Wilpers, C. W. Oates, and L. Hollberg, "Improved uncertainty budget for optical frequency measurements with microkelvin neutral atoms: Results for a high-stability ^{40}Ca optical frequency standard," Appl. Phys. B **85**, 31-44 (2006).
6. D. Ludlow, T. Zelevinsky, G. K. Campbell, S. Blatt, M. M. Boyd, M. H. G. de Miranda, M. J. Martin, J. W. Thomsen, S. M. Foreman, Jun Ye, T. M. Fortier, J. E. Stalnaker, S. A. Diddams, Y. Le Coq, Z. W. Barber, N. Poli, N. D. Lemke, K. M. Beck, and C. W. Oates, "Sr lattice clock at 1×10^{-16} fractional uncertainty by remote optical evaluation with a Ca clock," Science **319**, 1805-1808 (2008).
7. R. L. Targat, X. Baillard, M. Fouche, A. Brusch, O. Tcherbakoff, G. D. Rovera, and P. Lemonde, "Accurate optical lattice clock with ^{87}Sr atoms," Phys. Rev. Lett. **97**, 130801 (2006).
8. M. Takamoto and H. Katori, "Spectroscopy of the $^1S_0$-$^3P_0$ clock transition of ^{87}Sr in an optical lattice," Phys. Rev. Lett. **91**, 223001 (2003).
9. M. M. Boyd, A. D. Ludlow, S. Blatt, S. M. Foreman, T. Ido, T. Zelevinsky, and J. Ye, "^{87}Sr lattice clock with inaccuracy below 10^{-15}," Phys. Rev. Lett. **98**, 083002 (2007).
10. N. Poli, Z. W. Barber, N. D. Lemke, C. W. Oates, L. S. Ma, J. E. Stalnaker, T. M. Fortier, S. A. Diddams, L. Hollberg, J. C. Bergquist, A. Brusch, S. Jefferts, T. Heavner, and T. Parker, "Frequency evaluation of the doubly forbidden $^1S_0$-$^3P_0$ transition in bosonic ^{174}Yb," Phys. Rev. A **77**, 050501 (2008).
11. Z. W. Barber, C. W. Hoyt, C. W. Oates, L. Hollberg, A. V. Taichenache, and V. I. Yudin, "Direct excitation of the forbidden clock transition in neutral ^{174}Yb atoms confined to an optical lattice," Phys. Rev. Lett. **96**, 083002 (2006)
12. H. C. Chui, S. Y. Shaw, M. S. Ko, Y. W. Liu, J. T. Shy, T. Lin, W. Y. Cheng, R. V. Roussev, and M. M. Fejer, "Iodine stabilization of a diode laser in the optical communication band," Opt. Lett. **30**, 646-648 (2005).

#107734 - $15.00 USD Received 26 Feb 2009; revised 17 Apr 2009; accepted 19 Apr 2009; published 24 Apr 2009

13. H. M. Pask, R. J. Carman, D. C. Hanna, A. C. Tropper, C. J. Mackechinie, P. R. Barber, and J. M. Dawes, "Ytterbium-doped silica fiber lasers: Versatile sources for the 1-1.2μm region," IEEE J. Sel. Top. Quantum Electron. **1**, 2-12 (1995).
14. P. C. Becker, N. A. Olsson, and J. R. Simpson, *Erbium-Doped Fiber Amplifier*, (Academic 1999).
15. M. Dekker, *Rare-Earth-Doped Fiber Lasers and Amplifier*, (2nd Edition 2001).
16. G. Giusfredi, A. Godone, E. Bava, and C. Novero, "Metastable atoms in a Mg beam: Excitation dynamics and velocity distribution," J. Appl. Phys. **63**, 1279-1285 (1988).
17. C. Novera and A. Godone, "Wavelength and Isotopic shift measurements of the 3S (3s4s) – 3P (3s3p) MgI transitions," Z. Phys. D **17**, 33-35 (1990).
18. L. Hallstadius and J. E. Hansen, "Experimental Determination of Isotope Shifts in MgI," Z. Phys. A **285**, 365-370 (1978).
19. W. Y. Cheng, J. T. Shy, T. Lin, and C. C. Chou, "Molecular Iodine spectra and laser stabilization by frequency-doubled 1534nm diode laser," Jpn. J. Appl. Phys. **44**, 3055-3058 (2005).

1. Introduction

The developments in laser cooling and trapping of atoms have opened the doors for a variety of research fields in precision measurements and its applications. Access to atoms in an ultra-cold regime has resulted in tremendous improvements in precision spectroscopy and the development of a new class of atomic clocks. Alkali atoms have been the first choice for laser cooling and trapping, due to the single unpaired electron structure and transitions easily accessible with diode lasers. Laser cooled cesium atoms are currently used to define the SI second [1, 2]. The Cs fountain clocks of today are approaching an accuracy and stability level of a few parts in 10^{16}, equivalent a clock losing only one second in 300 million years.
Alkaline-Earth and Alkaline-Earth-like atoms are excellent candidates for future optical frequency standards, as the internal level structure allows for laser cooling and narrow clock transitions. The main effort has concentrated on the cooling of Magnesium, Calcium, Strontium and Ytterbium atoms. So far, accurate optical atomic clocks have been realized using Ca [3-5], Sr [6-9] and Yb [10, 11].

In this letter, we report a 517 nm laser source suitable for our Magnesium laser cooling and atomic clock project. The laser system is intended for optically pumping atoms between the (3s3p) $^3P_{0,1,2}$ states by addressing the (3s3p) $^3P_j \rightarrow$ (3s4s) $^3S_1$ transitions. The 517 nm second harmonic generation (SHG) system is constructed using a two-stage Yb-doped fiber amplifier (YDFA) system and a periodically poled lithium niobate (PPLN) waveguide [12]. In this setup, we can get an output power of more than 40 mW at 517 nm. In addition, fluorescence spectroscopy of metastable magnesium atoms is used to stabilize the 517 nm SHG system to within 1 MHz on an absolute scale.

2. Experiment and results

A schematic diagram of the experiment is shown in Fig. 1. The seed laser is an external-cavity diode laser in Littrow configuration operating at 1034 nm. After a 40 dB optical isolator, the laser power is measured to be 15 mW. A telescope is used to optimize the fiber-coupling efficiency of the 1034 nm laser. The Yb-doped fiber amplifier used in our laboratory is a polarization maintaining (PM) fiber, providing amplification of light with wavelengths ranging from 1030 nm to 1120 nm. The YDFA has an Yb-doped single-mode core with a 10 μm diameter, and a large multimode pump guiding cladding with a 125 μm diameter. The pump laser wavelength is 976 nm for the maximum absorption efficiency of YDFA. The fiber lengths of both the YDFA are about 2.5 meters with a cladding pump laser absorption of 6 dB/m. Dichroic Mirrors (DM) are employed to overlap and couple both 976 nm and 1034 nm lasers into the YDFA. An interference filter (IF) transmitting 1034 nm light is placed after the two-stage the YDFA, to remove the 976 nm pump light from the output.

In Fig. 2, the blue points show the gain of the one-stage YDFA at 1034 nm, which is measured as a function of pump power at a coupled seed laser power of 8 mW. It is observed that the gain saturates at a pump power of about 4.5 W. We get a maximum 1034 nm output of around 400 mW from the one-stage YDFA, limited by spontaneous emission of the Yb-

#107734 - $15.00 USD Received 26 Feb 2009; revised 17 Apr 2009; accepted 19 Apr 2009; published 24 Apr 2009

Doped fiber centered at 1035 nm [13]. The typical output of the two-stage YDFA is shown with the red circles in Fig.2, where a maximum output of 1.5 W at 1034 nm is reached. The coupling efficiency between Yb-doped cores of the 1st stage and 2nd stage YDFA is around 50 %.

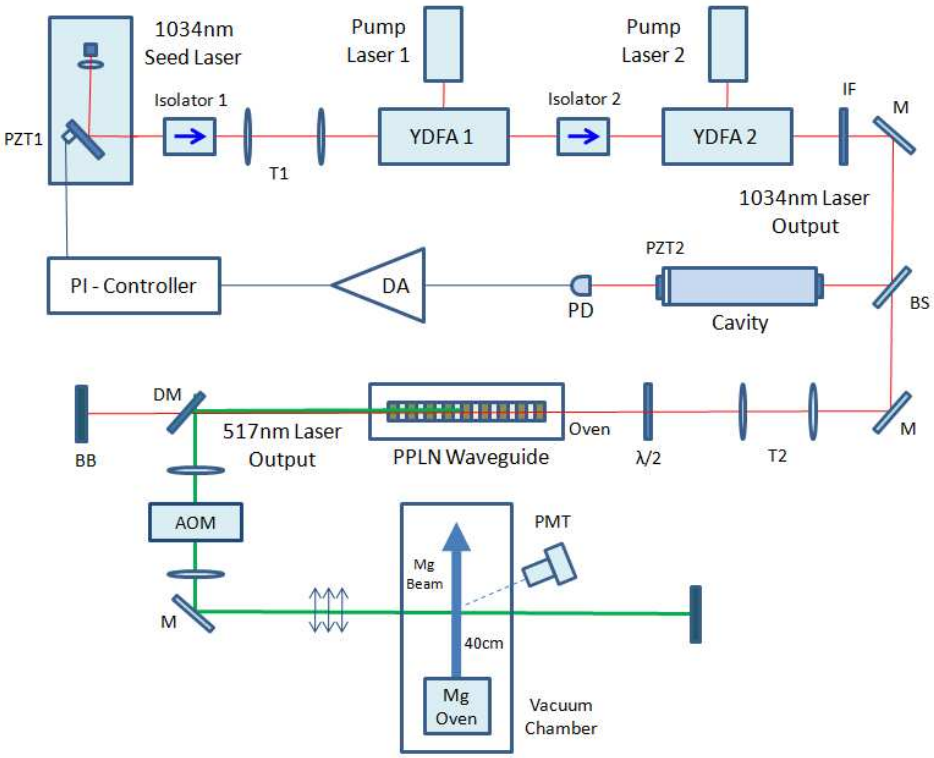

Fig. 1. Schematic diagram of 517 nm laser system: T, telescope; DM, dichromatic mirror; IF, interference filter; M, mirror; λ/2, half waveplates; BS, beam splitter; AOM, acousto-optic modulator; PMT, photomultiplier tube; PD, photodiode; BB, beam block; DA, differential amplifier; PZT, piezoelectric actuator. A two stage YDFA system is used for 1034 nm amplification, and a PPLN waveguide produces second harmonic generation (SHG) at 517 nm. The PPLN temperature is about 35 °C, and 40 mW of 517 nm SHG output is obtained with 1.4 W of incident 1034 nm laser. An external cavity is used to stabilize the two-stage YDFA system, and spectroscopy is performed on a metastable magnesium beam.

The 1034 nm output from the two-stage YDFA is collimated and then focused into the PPLN waveguide, with a beam waist of 30 µm. The domain period of the PPLN waveguide is 6.37 µm with a quasi-phase matching temperature around 35 °C and temperature coefficient of 0.09 nm/K. An oven is used to stabilize the PPLN's temperature within 0.01 °C. A half waveplate controls the polarization direction of the 1034 nm laser to optimize the SHG output of the PPLN waveguide.

A TEM_{00} Gaussian laser beam at 517 nm is obtained from the PPLN waveguide. In Fig. 3, we show the generated 517 nm power (blue points) with simply single pass, where a maximum of 40 mW is obtained with 1.4 W of incident power at 1034 nm. In this plot, the wavelength of the input laser is 1034.860 nm, and the quasi-phase temperature is 34.2 °C. The red circles in Fig. 3 show the frequency doubling efficiency as a function of incident 1034 nm power. We observe a decreasing doubling efficiency, from 2.5 % $W^{-1}cm^{-1}$ to about 2 % $W^{-1}cm^{-1}$ at high power output. This is due to increased amplified spontaneous emission (ASE) of YDFA [14,15]. A dichroic mirror is used to reflect the 517 nm output and transmit the

#107734 - $15.00 USD Received 26 Feb 2009; revised 17 Apr 2009; accepted 19 Apr 2009; published 24 Apr 2009

infrared 1034 nm laser. We have chosen to use a single pass SHG compared to frequency doubling in an external cavity, as it provides the possibility of pumping several ^{25}Mg hyperfine transitions simultaneously by rapidly scanning the laser frequency. Frequency doubling in an external cavity can provide significantly higher output powers, however, for the repumping purposes intended, the 40 mW demonstrated here by single pass frequency doubling is more than sufficient.

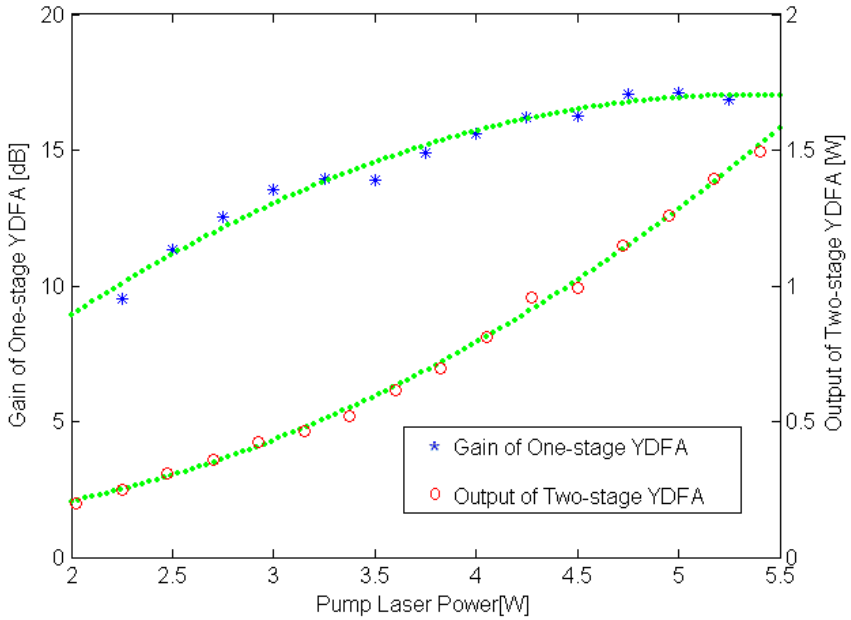

Fig. 2. The blue points show 1034 nm gain of one-stage YDFA as a function of pump laser power. The red circles show 1034 nm output of two-stage YDFA, where 1.5 W output obtained. The green lines are added as a guide for the eye .

An external enhancement cavity is used to stabilize the two stage YDFA system by fringe locking. The cavity is constructed by two high reflective concave mirrors coated for 1034 nm. 60 μW of the IR laser beam is coupled into this cavity, the transmitted signal is collected by a photodiode. After a differential amplifier and a PI-controller circuit, the output signal is sent to the piezoelectric actuator (PZT) of the seed laser, to stabilize the 517 nm SHG system. The FWHM linewidth of the 517 nm laser is measured to be 1.2 MHz.

An oven containing magnesium is operated at T = 793 K and produces an effusive magnesium beam which after the discharge region has a non-maxwellian velocity distribution with a mean velocity of 1000 m/s and total output of 10^{13} atoms/s. Metastable magnesium atoms are produced by electron impact in a self sustained discharge which runs at a stable current of one ampere. The metastable Mg beam setup is similar to the one described in [16] and has a generation efficiency of metastable magnesium atoms of 40 %.

#107734 - $15.00 USD Received 26 Feb 2009; revised 17 Apr 2009; accepted 19 Apr 2009; published 24 Apr 2009

Isotope shifts of the $(3s3p)\ ^3P_{0,1,2}$-$(3s4s)\ ^3S_1$ Mg I transitions

Ming He, Kasper T. Therkildsen,* Brian B. Jensen, Anders Brusch, and Jan W. Thomsen
The Niels Bohr Institute, Universitetsparken 5, 2100 Copenhagen, Denmark

Sergey G. Porsev†
Petersburg Nuclear Physics Institute, Gatchina, Leningrad District 188300, Russia

(Received 21 April 2009; published 12 August 2009)

We report measurements of the isotope shifts of the $(3s3p)\ ^3P_{0,1,2}$-$(3s4s)\ ^3S_1$ Mg I transitions for the stable isotopes ^{24}Mg (I=0), ^{25}Mg (I=5/2), and ^{26}Mg (I=0). Furthermore, the ^{25}Mg $^3S_1$ hyperfine coefficient $A(^3S_1)=(-321.6\pm1.5)$ MHz is extracted and found to be in excellent agreement with state-of-the-art theoretical predictions giving $A(^3S_1)=-325$ MHz and $B(^3S_1)\simeq10^{-5}$ MHz. Compared to previous measurements, the data presented in this work are improved up to a factor of 10.

DOI: 10.1103/PhysRevA.80.024501 PACS number(s): 32.30.Jc, 31.30.Gs, 32.10.Fn

I. INTRODUCTION

Accurate measurements of atomic transitions play an important role in many parts of physics and astronomy. They form a basis for state-of-the-art atomic structure calculations and provide important reference data for spectroscopic measurements. Accurate spectroscopic measurements have a wide range of applications covering astrophysical [1] and laboratory-based experiments including optical cooling schemes and atomic clocks [2,3]. With the access to new and improved spectroscopic data, detailed models using relativistic many-body methods of atomic structure calculations and models may advance significantly [4,5]. For the alkaline-earth elements, some transitions are very well known, but most transitions are relatively unknown or known only with a modest accuracy.

The magnesium atom is interesting for a number of reasons. Magnesium has a particularly simple level structure among the two electron systems studied such as Ca, Sr, Ba, and Yb. This opens for detailed comparison to theoretical models [6,7]. Most of the transitions are in the blue part of the spectrum which makes the magnesium atom ideal for optical clock purposes. The black body shift, currently limiting the Sr atomic clock [3], is expected to be factor of 100 lower compared to the Sr case [8]. However, exploiting the magnesium system for an optical clock has been restricted due to lack of ultracold magnesium atoms. In the magnesium system, cooling to low temperatures using the intercombination line is not feasible and other methods has failed to efficiently cool samples below one mK [9,10]. The 517 nm transitions studied in this paper are suited for repumping purposes and can in combination with a cooling laser on the $(3s3p)\ ^3P_2$-$(3s3d)\ ^3D_3$ be used to efficiently cool magnesium atoms to micro-kelvin temperatures.

In the search for a possible temporal drift of the fine-structure constant $\alpha=\frac{e^2}{4\pi\varepsilon_0\hbar c}$, accurate spectroscopic measurements on distant quasars have been carried out [12]. One of the sources of possible systematic effects is the difference between isotopic abundance ratios in gas clouds in the early universe compared to those on earth. To test this possibility, it is necessary to have accurate isotope shifts for the relevant atomic transitions. Here, the $(3s3p)\ ^3P_{0,1,2}$-$(3s4s)\ ^3S_1$ transitions (see Fig. 1) play an important role and new data on the isotope shifts will be helpful [4]. An improvement of the experimental determination of the isotope shift will reflect on the precision of theoretical calculations, since magnesium is often used as a test ground for different methods of atomic calculations. The need for accurate isotope shifts is further motivated by the wish to study the isotopic evolution of the universe. The isotopic abundances of gas clouds may be measured independently of a variation of α [11]. This is important for testing models of nuclear reactions in stars and supernovae and of the chemical evolution of the universe.

In this Brief Report, we present measurements for the isotope shift and hyperfine structure splitting of the $(3s3p)\ ^3P_{0,1,2}$-$(3s4s)\ ^3S_1$ Mg I transitions around 517 nm in a metastable atomic magnesium beam. We improve previous

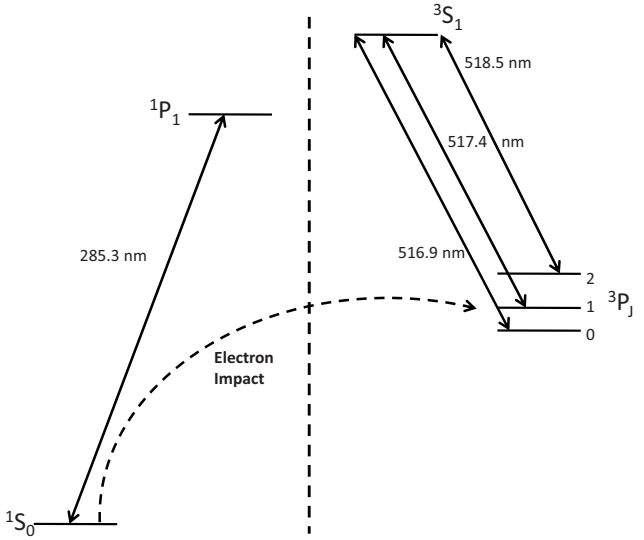

FIG. 1. Level diagram for ^{24}Mg showing transitions relevant for this Brief Report. There are three stable magnesium isotopes ^{24}Mg, ^{25}Mg, and ^{26}Mg with nuclear spins of I=0, I=5/2, and I=0, respectively. Dashed line indicates the separation between the singlet and triplet spin states. Note that for ^{25}Mg, hyperfine structure is present.

*kaspertt@fys.ku.dk
†Present address: School of Physics, University of New South Wales, Sydney, NSW 2052, Australia.

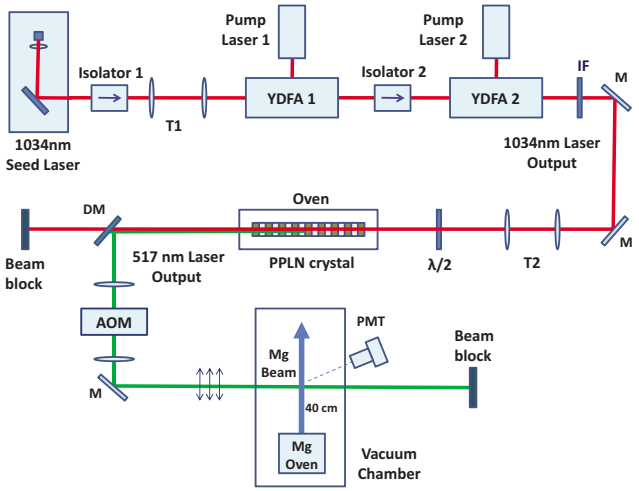

FIG. 2. (Color online) Schematic diagram of the laser system: T, telescope; DM, dichroic mirror; IF, interference filter; M, mirror; λ/2, half wave plates; BS, beam splitter; AOM, acousto-optic modulator; PMT, photomultiplier tube. A two-stage YDFA system is used for 1034 nm laser amplification and is single pass frequency doubled in a PPLN crystal. Fluorescence spectroscopy is performed on a metastable magnesium beam, approximately 40 cm from the oven orifice.

measurements by up to a factor of 10 for the stable isotopes ^{24}Mg (I=0), ^{25}Mg (I=5/2), and ^{26}Mg (I=0). For ^{25}Mg $^3S_1$, we extract the hyperfine coefficient $A(^3S_1)$ and compare the result to state-of-the-art relativistic many-body calculations.

II. EXPERIMENTAL SETUP

Figure 2 shows the experimental setup used for spectroscopy on metastable magnesium atoms. The Mg oven is operated around 520 °C and produces an effusive magnesium beam with mean velocity 1000 m/s and flux of $\sim 10^{13}$ atoms/s. Electron impact initiates the discharge which runs at a stable current of about 1 A in a setup similar to the one described in [13]. Using the main 285.3 nm $(3s^2)\ ^1S_0$-$(3s3p)\ ^1P_1$ transition and switching the discharge, we estimate about 40% of the atoms are in a metastable state, distributed among the $^3P_{0,1,2}$ levels. The 517 nm light is produced from a fiber amplified diode laser centered at 1034 nm [14]. We use an external cavity diode laser in a Littrow configuration followed by a 40 dB optical isolator. Typically, the output after the isolator is 15 mW and about 10 mW is injected into a two-stage Yb-doped fiber amplifier (YDFA) system. The fiber consists of a highly doped single-mode core of 10 μm diameter with a peak absorption of 1200 dB/m at 976 nm and a large multimode pump guiding cladding of 125 μm in diameter. The fibers are pumped with up to 5 W at 976 nm. After the amplifier stage, 1.5 W of 1034 nm light is generated. The 1034 nm light is single pass frequency doubled in a periodically poled lithium niobate (PPLN) crystal generating up to 40 mW at 517 nm. The domain period of the PPLN crystal is 6.37 μm with a quasi-phase-matching temperature around 35 °C and temperature coefficient of 0.09 nm/K. An oven is used to stabilize the PPLN temperature within 0.01 °C in order to achieve optimal phase matching. After the frequency doubling, a dichroic mirror is used to separate the 517 nm light from the 1034 nm light.

Spectroscopy is performed 40 cm from the oven orifice using linearly polarized light. The imaging system collects fluorescence from an area of about 8 mm^2 within the atomic beam limiting the residual Doppler effect to 60 MHz. A 275–400 MHz acousto-optic modulator (AOM) is used for frequency scale calibration. The absolute AOM frequency is controlled below 1 kHz rms and was verified using a precision counter. For calibration, both zero- and first-order beams from the AOM are overlapped producing a double set of spectra. Changing the dc offset of the AOM enables us to test the degree of linearity of the frequency scan. The intrinsic linewidth of the 517 nm light has been measured to be below 3 MHz using a high finesse cavity. Each spectrum is averaged 32 times and 30 different spectra are recorded for each transition.

III. METHOD OF CALCULATION

The method used for calculation of the magnetic-dipole and electric-quadrupole hyperfine structure constants A and B for the $^3S_1$ state is a combination of the configuration-interaction (CI) method with many-body perturbation theory (MBPT) [15]. Initially, the method was developed for calculating energy levels. The MBPT was used to construct an effective Hamiltonian for valence electrons. Then the multiparticle Schrödinger equation for valence electrons was solved in the frame of the CI method. Following the earlier works, we refer to this approach as the CI+MBPT formalism.

In this approach, the energies and wave functions are determined from the equation

$$H_{\mathrm{eff}}(E_n)\Phi_n = E_n\Phi_n,$$

where the effective Hamiltonian is defined as

$$H_{\mathrm{eff}}(E) = H_{\mathrm{FC}} + \Sigma(E).$$

Here, H_{FC} is the Hamiltonian in the frozen core approximation and Σ is the energy-dependent correction, which takes into account virtual core excitations.

In order to calculate other atomic observables, one needs to construct the corresponding effective operators for valence electrons [16–18]. In particular, the effective operator of the hyperfine interaction used in this work accounts for the core-valence and core-core correlations. To account for shielding of an externally applied field by core electrons, we have solved random-phase approximation (RPA) equations, summing a certain sequence of many-body diagrams to all orders of MBPT [16,19].

We consider Mg as a two-electron atom with the core $[1s^2,\ldots,2p^6]$. On the whole, the one-electron basis set for Mg consists of $1s-13s$, $2p-13p$, $3d-12d$, and $4f-11f$ orbitals, where the core and $3,4s$, $3,4p$, $3,4d$, and $4f$ orbitals are Dirac-Hartree-Fock (DHF) ones, while all the rest are the virtual orbitals. The orbitals $1s-3s$ are constructed by solving the DHF equations in V^N approximation, $3p$ orbital is

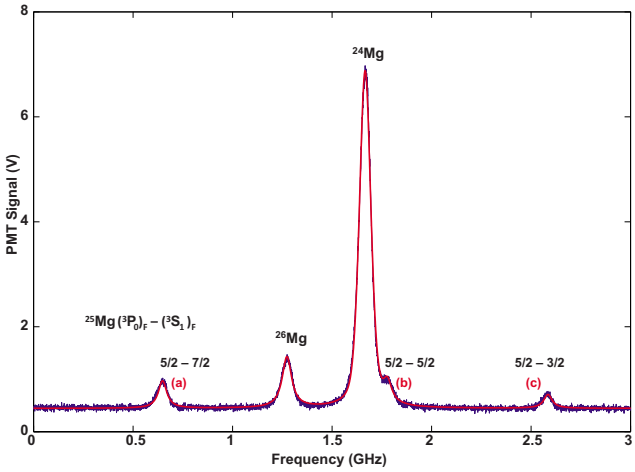

FIG. 3. (Color online) Fluorescence signal from the $^3P_0$-$^3S_1$ transition. Blue curve represents the experimental data and red curve is a fit to the data. The hyperfine splittings of $^{25}\mathrm{Mg}(^3P_0)_F$-$(^3S_1)_F$ are indicated as (a)–(c).

obtained in V^{N-1} approximation, and $4s$, $4p$, $3,4d$, and $4f$ orbitals are constructed in V^{N-2} approximation. We determined virtual orbitals using a recurrent procedure similar to Ref. [20] and described in detail in [17,18]. Configuration-interaction states were formed using this one-particle basis set which is sufficiently large to obtain numerically converged CI results. An extended basis set, used at the stage of MBPT calculations, included $1s-19s$, $2p-19p$, $3d-18d$, $4f-15f$, and $5g-11g$ orbitals.

The results obtained in the frame of the CI+MBPT method for the hyperfine structure (hfs) constants A and B are $A(^3S_1)=-325$ MHz and $B(^3S_1)\simeq 10^{-5}$ MHz. The theoretical value for the magnetic-dipole constant A is in a good agreement with the experimental value obtained in this work $A(^3S_1)=-321.6\pm 1.5$ MHz.

The electric-quadrupole hfs constant $B(^3S_1)$ is very close to zero. In the absence of configuration interaction of the $3s4s$ configuration with other configurations (such as $3snd$ and nd^2 configurations, where $n\geq 3$), the hfs constant B would be exactly equal to zero, but (very weak) configuration interaction leads to a nonzero value of B, though very small.

IV. RESULTS AND DISCUSSION

Figures 3–5 show typical fluorescence spectra as a function of laser frequency for the $^3P_{0,1,2}$-$^3S_1$ transitions. The blue curve is the raw data and the red curve is a Voigt profile fit to the data. For ^{24}Mg, we obtain a full width at half maximum (FWHM) linewidth of 55 MHz in agreement with our beam and detector geometry. From the spectra, we clearly identify the isotope shift and the hyperfine components $(^3P_{0,1,2})_F$-$(^3S_1)_F$ of ^{25}Mg. The hyperfine coefficients of the $^3P_{1,2}$ levels could be extracted from the data, however, we use the values measured in [21] due to the very high precision of these measurements to extract the hyperfine coefficient $A(^3S_1)$. We find the hyperfine coefficient

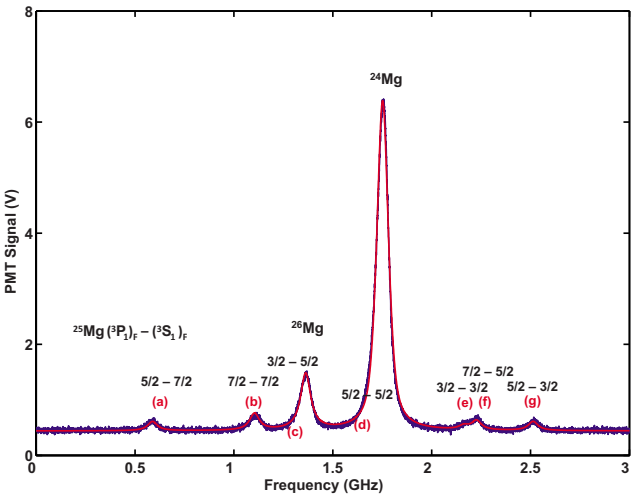

FIG. 4. (Color online) Fluorescence signal from the $^3P_1$-$^3S_1$ transition. Blue curve represents the experimental data and red curve is a fit to the data. The hyperfine splittings of $^{25}\mathrm{Mg}(^3P_1)_F$-$(^3S_1)_F$ are indicated as (a)–(g).

$A(^3S_1)=(-321.6\pm 1.5)$ MHz. As described in Sec. III, the electric-quadrupole hfs constant $B(^3S_1)$ is significantly smaller than the resolution of the experiment and is therefore set to zero in the fitting procedure. Table I summarizes our findings and compares to previous measurements. Different systematic errors have been investigated as mentioned in Sec. II, all of which have been determined to be lower than the statistical error. Errors listed in Table I are pure statistical errors. Here, it can be seen that the value for the hyperfine coefficient $A(^3S_1)$ and the isotope shifts agree with previous measurements within the uncertainty.

We observe the ^{24}Mg-^{26}Mg shift to be almost constant which indicates that relativistic isotope shift effects are small or comparable to the statistical error in our measurement. Our measured isotope shifts are accounted for by pure mass effect. In this case, the ratio between the ^{24}Mg-^{26}Mg and ^{24}Mg-^{25}Mg shifts can be expressed as [23]

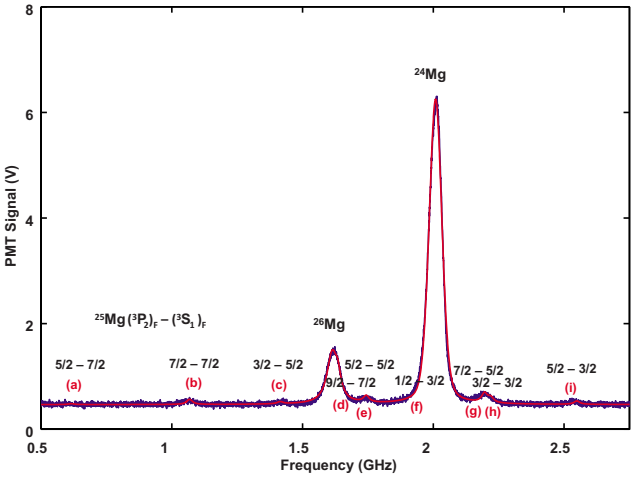

FIG. 5. (Color online) Fluorescence signal from the $^3P_2$-$^3S_1$ transition. Blue curve represents the experimental data and red curve is a fit to the data. The hyperfine splittings of $^{25}\mathrm{Mg}(^3P_1)_F$-$(^3S_1)_F$ are indicated as (a)–(i).

TABLE I. Measured isotope shift and $^3S_1$ hyperfine structure constant. The errors listed are the statistical errors.

	$^3P_0$-$^3S_1$		$^3P_1$-$^3S_1$		$^3P_2$-$^3S_1$		
	Δ^{24-26} (MHz)	Δ^{24-25} (MHz)	Δ^{24-26} (MHz)	Δ^{24-25} (MHz)	Δ^{24-26} (MHz)	Δ^{24-25} (MHz)	$A(^3S_1)$ (MHz)
Ref. [22] (1949)	414 ± 9		366 ± 45		414 ± 12		-322 ± 6
Ref. [23] (1978)	396 ± 6	210 ± 36	391 ± 4.5	201 ± 21	393 ± 7.5	204 ± 7.5	-329 ± 6
Ref. [24] (1990)	391 ± 10	214 ± 10	393 ± 10	215 ± 10	397 ± 10	217 ± 10	-322 ± 6
This work (2009)	391.3 ± 1.7	205.7 ± 1.5	390.1 ± 1.4	209.1 ± 1.3	394.4 ± 0.8	205.7 ± 0.8	-321.6 ± 1.5

$$\frac{\Delta(^{24}\mathrm{Mg} - {}^{26}\mathrm{Mg})}{\Delta(^{24}\mathrm{Mg} - {}^{25}\mathrm{Mg})} = \frac{26-24}{26\cdot 24}\frac{25\cdot 24}{25-24} = \frac{25}{13} \simeq 1.92. \quad (1)$$

We obtain the ratios $^3P_0 \rightarrow {}^3S_1$ 1.90 ± 0.02, $^3P_1 \rightarrow {}^3S_1$ 1.87 ± 0.01 and $^3P_2 \rightarrow {}^3S_1$ 1.92 ± 0.01. These values are consistent with previous results [23,24].

V. CONCLUSION

In this paper, we present improved data for the isotope shift of the Mg $^3P_{0,1,2}$-$^3S_1$ and the hyperfine coefficient $A(^3S_1)$ for the ^{25}Mg isotope. We find good agreement between state–of-the-art many-body theory and experimental results. Experimental values reported here are improved by up to a factor of 10 compared to previous studies.

ACKNOWLEDGMENTS

We would like to acknowledge financial support from the Lundbeck foundation and the Carlsberg foundation. The authors also gratefully acknowledge Kjeld Jensen for technical assistance and Julian Berengut for editing this Brief Report.

[1] M. Aldenius, J. D. Tanner, S. Johansson, H. Lundberg, and S. G. Ryan, Astron. Astrophys. **461**, 767 (2007).
[2] T. Rosenband *et al.*, Science **319**, 1808 (2008).
[3] A. D. Ludlow *et al.*, Science **319**, 1805 (2008).
[4] J. C. Berengut, V. V. Flambaum, and M. G. Kozlov, Phys. Rev. A **72**, 044501 (2005).
[5] J. C. Berengut, V. A. Dzuba, V. V. Flambaum, and M. G. Kozlov, Phys. Rev. A **69**, 044102 (2004).
[6] K. T. Therkildsen, B. B. Jensen, C. P. Ryder, N. Malossi, and J. W. Thomsen, Phys. Rev. A **79**, 034501 (2009).
[7] P. L. Hansen, K. T. Therkildsen, N. Malossi, B. B. Jensen, E. D. van Ooijen, A. Brusch, J. H. Müller, J. Hald, and J. W. Thomsen, Phys. Rev. A **77**, 062502 (2008).
[8] S. G. Porsev and A. Derevianko, Phys. Rev. A **74**, 020502(R) (2006).
[9] N. Malossi, S. Damkjaer, P. L. Hansen, L. B. Jacobsen, L. Kindt, S. Sauge, and J. W. Thomsen, F. C. Cruz, M. Allegrini and E. Arimondo, Phys. Rev. A **72**, 051403(R) (2005).
[10] T. E. Mehlstäubler, K. Moldenhauer, M. Riedmann, N. Rehbein, J. Friebe, E. M. Rasel, and W. Ertmer, Phys. Rev. A **77**, 021402(R) (2008).
[11] M. G. Kozlov, V. A. Korol, J. C. Berengut, V. A. Dzuba, and V. V. Flambaum, Phys. Rev. A **70**, 062108 (2004).
[12] J. K. Webb, V. V. Flambaum, C. W. Churchill, M. J. Drinkwater, and J. D. Barrow, Phys. Rev. Lett. **82**, 884 (1999); J. K. Webb *et al.*, *ibid.* **87**, 091301 (2001); M. T. Murphy *et al.*, Mon. Not. R. Astron. Soc. **327**, 1208 (2001); **327**, 1237 (2001); J. K. Webb, M. T. Murphy, V. V. Flambaum, and S. J. Curran, Astrophys. Space Sci. **283**, 565 (2003).
[13] G. Giusfredi, A. Godone, E. Bava, and C. Novero, J. Appl. Phys. **63**, 1279 (1988).
[14] M. He, B. B. Jensen, K. T. Therkildsen, A. Brusch, and J. W. Thomsen, Opt. Express **17**, 7682 (2009).
[15] V. A. Dzuba, V. V. Flambaum, and M. G. Kozlov, Phys. Rev. A **54**, 3948 (1996).
[16] V. A. Dzuba, M. G. Kozlov, S. G. Porsev, and V. V. Flambaum, Zh. Eksp. Teor. Fiz. **114**, 1636 (1998); J. Exp. Theor. Phys. **87**, 885 (1998).
[17] S. G. Porsev, Yu. G. Rakhlina, and M. G. Kozlov, Phys. Rev. A **60**, 2781 (1999).
[18] S. G. Porsev, Yu. G. Rakhlina, and M. G. Kozlov, J. Phys. B **32**, 1113 (1999).
[19] D. Kolb, W. R. Johnson, and P. Shorer, Phys. Rev. A **26**, 19 (1982).
[20] P. Bogdanovich and G. Zukauskas, Sov. Phys. Collect. **23**, 13 (1983).
[21] A. Lurio, Phys. Rev. **126**, 1768 (1962).
[22] M. F. Crawford, F. M. Kelly, A. L. Schawlow, and W. M. Gray, Phys. Rev. **76**, 1527 (1949).
[23] L. Hallstadius and J. E. Hansen, Z. Phys. A **285**, 365 (1978).
[24] C. Novero and A. Godone, Z. Phys. D: At., Mol. Clusters **17**, 33 (1990).

Iodine spectroscopy based on metastable Mg I spectroscopy of (3s3p) 3P - (3s4s) 3S transitions

Ming He[†], Brian B. Jensen, Anders Brusch, Kasper T. Therkildsen, and Jan W. Thomsen[*]

Niels Bohr Institute, University of Copenhagen, Universitetsparken 5, DK-2100 Copenhagen,

[*]Corresponding author: jwt@fys.ku.dk

Abstract: We report precise measurement of the iodine absorption spectroscopy around 516.9, 517.4 and 518.5 nm, based on our previous measurements on the isotope shift and hyperfine structures of the metastable Mg I (3S3P) ^{3}P - (3S4S) ^{3}S transitions. In addition, we demonstrated the Doppler-free Iodine hyperfine spectrum, which can be used to improve laser frequency stabilization. Moreover, the measurement of the Iodine spectrum and the metastable Mg I spectroscopy is valuable for the Mg atomic clock project.

OCIS codes: (300.6320) Spectroscopy, high-resolution; (020.7010) Laser trapping

References and links

1. B. Bodermann, G. Bönsch, H. Knöckel, A. Nicolaus and E. Tiemann, Wavelenghth measurements of three iodine lines between 780 nm and 795 nm, Metrologia **35**, 105-113(1998).
2. S. Gerstenkorn and P. Luc, "ATLAS DUUU SPECTRE DABSORPTION DE LA MOLECULE 14800 – 20000 cm^{-1} ", Laboratoire AIME-COTTON CNRS II – 91405 ORSAY.
3. H. Knöckel, B. Bodermann, and E. Tiemann, "High precision decription of the rovibronic structure of the I_2 B-X spectrum", Eur. Phys. J. D **28**, 199-209 (2004).
4. T. J. Quinn, "Practical realization of the definition of the metre, including recommended radiation of other optical frequency standards (2001)", Metrologia **40**, 103-133 (2003).
5. L. Chen, W. Y. Cheng, and J. Ye, "Hyperfine interactions and perturbation effects in the B0u$^+$($3\pi_u$) state of $^{127}I_2$", J. Opt. Soc. Am. B **21**, 820-832 (2004).
6. J. P. Wallerand, L. Robertsson, L.S. Ma, and M. Zucco, "Absolute frequency measurement of molecular iodine lines at 514.7 nm, interrogated by a frequency-doubled Yb-doped fibre laser", Metrologia **43**, 294-298 (2006)
7. W. Y. Cheng, L. Chen, T. H. Yoon, J. L. Hall, and J. Ye, "Sub-Doppler molecular-iodine transitions near the dissociation limit (523-498 nm)", Opt. Lett. **27**, 571-573 (2002).
8. K. Sengstock, U. Sterr, J. H. Müller, V. Rieger, D. Bettermann, and W. Ertmer, "Optical Ramsey spectroscopy on laser-trapped and thermal Mg atoms", Appl. Phys. B **59**, 99-115 (1994).
9. F. Y. Loo, A. Brusch, S. Sauge, M. Allegrini, E. Arimondo, N. Andersen, and J. W. Thomsen, "Investigations of a two-level atom in a magneto-optical trap using magnesium", J. Opt. B **6**, 81-85 (2004).
10. P. L. Hansen, K. T. Therkildsen, N. Malossi, B. B. Jensen, E. D. van Ooijen, A. Brusch, J. H. Müller, J. Hald, and J. W. Thomsen, "Measurement of the 3s3p $^3P_1$ lifetime in magnesium using a magneto-optical trap", Phys. Rev. A **77**, 062502 (2008).
11. S. G. Porsev and A. Derevianko, "Multipolar theory of blackbody radiation shift of atomic energy levels and its implications for optical lattice clocks", Phys. Rev. A **74**, 020502(R) (2006).
12. M. He, K. T. Therkildsen, B. B. Jensen, A. Brusch, J. W. Thomsen, and S. G. Porsev, "Isotope shifts of the (3s3p)$^3P_{0,1,2}$ – (3s4s)$^3S_1$ Mg I transitions", Phys. Rev. A **80**, 024501(2009).
13. C. Nevedo and A.Godone, "Wavelength and isotopic shift measurements of the 3S(3s4s) – 3P(3s3p) MgI transitions", Z. Phys. D **17**, 33-35 (1990)
14. M. He, B. B. Jensen, K. T. Therkildsen, A. Brusch, and J. W. Thomsen, "Metastable Magnesium fluorescence spectroscopy using a frequency-stabilized 517 nm laser", Opt. Express **17**, 7682-7687 (2009).
15. Wolfgang Demtröder, "Laser Spectroscopy", Springer-Verlag GmbH, 2nd edition, 1995.
16. V. Kaufman and W. C. Martin, "Wavelengths and Energy level Classifications of Magnesium Spectra for All Stages of Ionization (Mg I through Mg XII)", J. Phys. Chem. Ref. Data 20, 83-152 (1991).
17. S. Gerstenkorn and P. Luc, "Description of the absorption spectrum of iodine recorded by means of Four Transform Spectroscopy: the (B-X) system", J. Physique **46**, 867-881 (1985).

18. L. Cheng, "High-precision spectroscopy of molecular iodine: from optical frequency standards to global descriptions of hyperfine interactions and associated electronic structure", Ph.D thesis, Univesity of Colorado, 2005.

1. Introduction

The spectrum of the iodine molecule have often been chosen as a frequency reference from the green to the near infrared region (500 nm – 900 nm). While atomic spectra usually consist of only a few lines over a large spectral range, the iodine molecular spectrum is much denser because of the additional rotational and vibrational degrees of freedom [1]. The iodine atlas by S. Gerstenkorn and P. Luc [2] permits frequency calibration using Doppler-broadened lines at the GHz level. However, Doppler-free iodine lines can be used as a frequency references at an accuracy of 10^{-9} or better [3]. Today some of these lines are recommended as wavelength standards by the *Comité International des Poids et Mesures* (CIPM) [4]. Recently, high-precision measurement of Doppler-free iodine lines, in the wavelength range of 500 nm – 517 nm, has been investigated [5-7]. This work demonstrates a great future potential for an all solid state based optical frequency standards suitable for demanding environments such as space flight.

Magnesium atoms, with comparably simple level structure among the alkaline earth elements, are a good candidate for an optical frequency standard [8-10]. Moreover, its internal level structures allows laser cooling and features narrow clock transitions insensitive to black body radiation frequency shifts at the 10^{-17} fractional level [11]. For our magnesium laser cooling and atomic clock experiments, we have constructed a green CW laser source and referenced it to an iodine spectrometer in the 516 nm - 518 nm region. In this letter, we present precise measurement of the iodine absorption spectrum around 516.9, 517.4 and 518.5 nm, corresponding to our previous measurements on the isotope shifts and hyperfine structure of Mg I (3s3p) ^{3}P - (3s4s) ^{3}S transitions [12]. This is a factor of 10 improvement compared to previous measurements [13]. Doppler-free iodine hyperfine spectrum is obtained, allowing absolute frequency calibration of magnesium transitions at the 10^{-9} level.

2. Experiment & Results

The schematic diagram of the experiment is shown in Fig. 1. The seed laser is a homemade external-cavity diode laser centered at 1034 nm. The Yb-doped fiber amplifier (YDFA) used is a polarization maintaining (PM) fiber, providing amplification of light with wavelengths ranging from 1000 nm to 1150 nm. The YDFA has an Yb-doped single mode core with a diameter of 10 μm, and a large multimode pump guided cladding with a diameter of 125 μm. The pump laser wavelength is 976 nm, for the maximum absorption efficiency of YDFA. After a two stage YDFA, an interference filter (IF) centered at 1034 nm is used to remove the 976nm part in the output. 1.5 W of infrared laser power can be obtained after the two-stage YDFA system. Second harmonic generation (SHG) is achieved in a periodically poled lithium niobate (PPLN) crystal. An oven is used to stabilize the PPLN's temperature with an accuracy of 0.01^{o}C, and a half waveplate is employed to control the polarization direction of the 1034 nm laser and to optimize the SHG output of PPLN crystal. The FWHM linewidth of the green laser is measured to be close to 1 MHz. We obtain around 40 mW of green laser power, with a doubling efficiency of approximately 2% per$W^{-1}cm^{-1}$ [14].

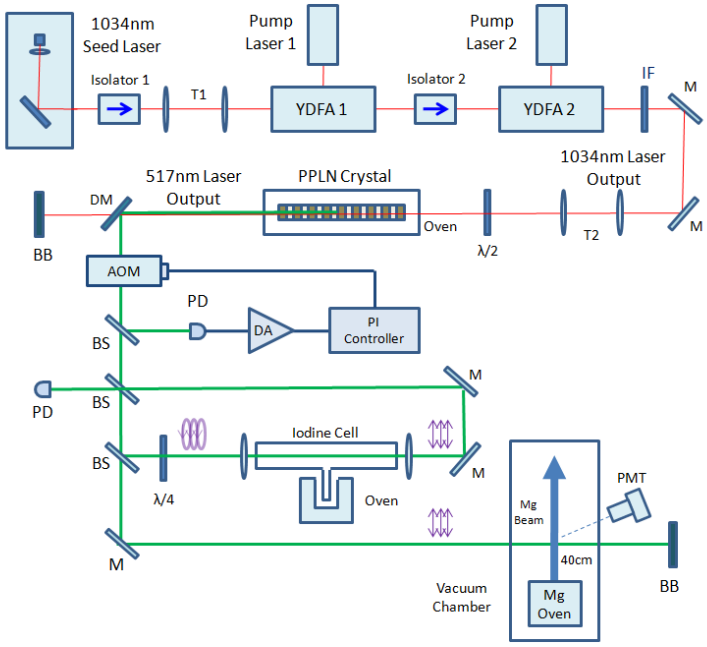

Fig. 1. Schematic diagram of 517 nm laser system: T, telescope; DM, dichroic mirror; IF, interference filter; BB, beam block; M, mirror; λ/2, half waveplates; λ/4, quarter waveplates; BS, beam splitter; AOM, acousto-optic modulator; PD, photodiode; DA, differential amplifier; PMT, photomultiplier tube. A two stage YDFA system is used for 1034 nm amplification, followed by the 517 nm second harmonic generation in the PPLN crystal. The Iodine spectroscopy signal is recorded by a photodiode. The absorption spectroscopy of metastable magnesium beam is obtained by a photomultiplier tube.

An acousto-optic modulator (AOM) is used to stabilize the green laser output power with a rms deviation of less than 1 %. About 10 mW is available after the AOM for iodine polarization spectroscopy [15]. The circular polarized probe beam and the linearly polarized pump beam counter propagate through a 6-cm-long iodine cell. The beam diameter inside the cell is ~ 0.1 mm, and the probe/pump intensity ratio is about 1/3. An oven is employed to adjust the cold finger temperature of iodine cell from -10 ^{o}C to room temperature to increase the signal-to-noise ratio of the spectra. The green laser is frequency modulated at ~ 80 kHz with a peak-to-peak amplitude of about 1MHz, by applying a dither signal to the seed laser current driver. A lock-in amplifier is used to demodulate the photodiode signal to obtain the Doppler-free iodine signal. A linearly polarized green laser beam with 2 mm diameter and 1 mW power is used for metastable Mg I spectroscopy. The Mg oven is operated at T = 793 K and produces an effusive magnesium beam with mean velocity 1000 m/s and flux of typically 10^{14} atoms/ssr [12].

In Fig. 2, the blue line shows the fluorescence signal taken with a photomultiplier tube, of the metastable Mg $(3s4s)^3S_1$-$(3s3p)^3P_2$ transitions at 518.5 nm. The red line is the Voigt profile fit of the raw data. The ^{24}Mg and ^{26}Mg isotope shift of 394.4 ± 0.8 MHz [12], is used for frequency scale calibration. The green line is the Doppler iodine molecular absorption spectrum taken by a photodiode detector, and three iodine absorption profiles are observed close to the Mg I spectra. In ref [2], the iodine lines are calibrated by means of uranium spectrum. In Fig. 2, the ^{24}Mg peak with wavenumber of 19286.225 cm^{-1} [16] is used to

calibrate the wavenumbers of the iodine lines. The iodine line positions are found by fitting a sum of Gaussian functions to the profiles of the iodine spectrum. The resonances A, B and C are found to be 19286.0731 ± 0.0006 cm^{-1}, 19286.1115 ± 0.0007 cm^{-1} and 19286.1471 ± 0.0009 cm^{-1} respectively. As shown in Table 1, the resonances A and B are identical to lines 3360 and 3361 in ref [2], with wavenumber of 19286.0825 ± 0.0009 cm^{-1} and 19286.1187 ± 0.0004 cm^{-1}. To identify the iodine lines, i.e., the vibrational and rotational molecular constants, we used the method described in [2, 17]. We list our calculated values in Table 1.

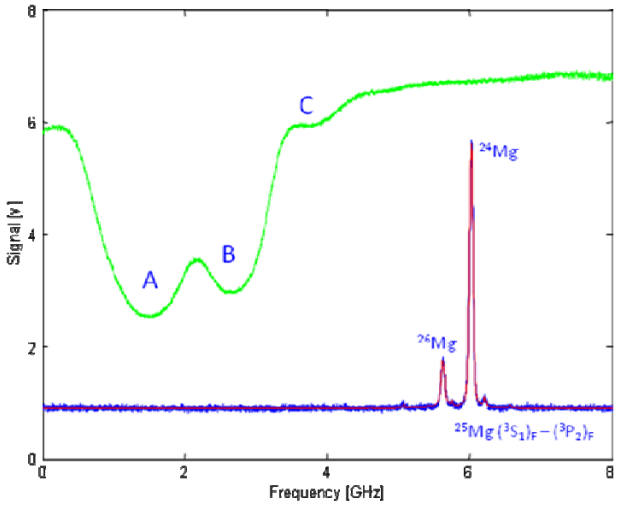

Fig. 2. Absorption spectroscopy of molecular Iodine and metastable Mg $(3s4s)^3S_1$-$(3s3p)^3P_2$ transitions simultaneously at 518.5 nm. The blue line is the fluorescence signal recorded by a photomultiplier tube, and the red line is the fitted curve. The isotope shift of ^{24}Mg and ^{26}Mg, and the hyperfine structure of ^{25}Mg can be observed. The green line is the Doppler absorption spectra of Iodine molecular indicated as A-C.

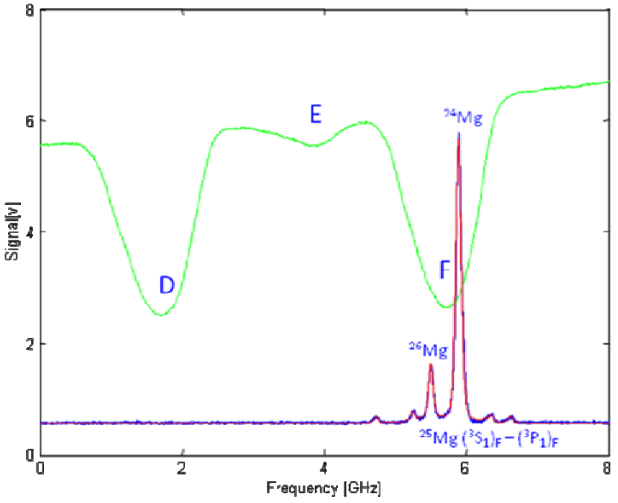

Fig. 3. Absorption spectroscopy of molecular Iodine and metastable Mg $(3s4s)^3S_1$-$(3s3p)^3P_1$ transitions simultaneously at 517.4 nm. The blue line is the fluorescence signal recorded by a photomultiplier tube, and the red line is the fitted curve. The isotope shift of ^{24}Mg and ^{26}Mg, and the hyperfine structure of ^{25}Mg can be observed. The green line is the Doppler absorption spectra of molecular Iodine indicated as D-F.

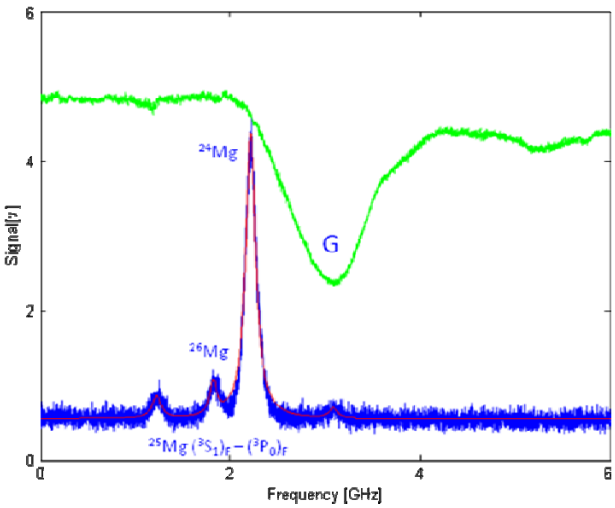

Fig. 4. Absorption spectroscopy of molecular Iodine and metastable Mg $(3s4s)^3S_1$-$(3s3p)^3P_0$ transitions simultaneously at 516.9 nm. The blue line is the fluorescence signal recorded by a photomultiplier tube, and the red line is the fitted curve. The isotope shift of ^{24}Mg and ^{26}Mg, and the hyperfine of ^{25}Mg can be observed. The green line is the Doppler absorption spectrum of molecular Iodine, indicated as G.

In Fig. 3 and Fig. 4, the blue lines show the fluorescence signal of the metastable Mg (3s4s) $^3S_1$-(3s3p) $^3P_{1,0}$ transitions at 517.4 nm and 516.9 nm respectively. The isotope shift values of 390.1 ± 1.4 MHz for $^3S_1$-$^3P_1$ transition (Fig.3) and 391.3 ± 1.7 MHz for $^3S_1$-$^3P_0$ transition (Fig.4) [12] are used for frequency scale calibration, and the ^{24}Mg peak with wavenumber of 19326.939 cm^{-1} (Fig.3) and 19346.998 cm^{-1} (Fig.4) [16] are used to calibrate the iodine lines positions. In Fig. 3, the lines D, E and F are measured to be 19326.7984 ± 0.0006 cm^{-1}, 19326.8696 ± 0.0004 cm^{-1}, and 19326.9327 ± 0.0003 cm^{-1}. In Fig. 4, the line G is measured to be 19347.0265 ± 0.0008 cm^{-1}. The experimental results and calculations are listed in Table 1.

Table 1. Measured Iodine Lines around 516.8, 517.4 and 518.5 nm, corresponding to the metastable Mg I (3S3P) ^{3}P - (3S4S) ^{3}S transitions.

Assignments	Measurement (cm^{-1})	Calculation (cm^{-1})	Ref [2] (cm^{-1})
A: (3360)P(57) 41-0	19286.0731 ± 0.0006	19286.0733	19286.0825 ± 0.0009
B: (3361)R(23) 40-0	19286.1115 ± 0.0007	19286.1122	19286.1187 ± 0.0004
C: R(79) 48-1	19286.1471 ± 0.0009	19286.1404	- -
D: (3560)P(57) 42-0	19326.7984 ± 0.0006	19326.7955	19326.8054 ± 0.0007
E: P(26) 46-1	19326.8696 ± 0.0004	19326.8735	- -
F: (3561)R(59) 42-0	19326.9327 ± 0.0003	19326.9267	19326.9373 ± 0.0006
G: R(111) 57-1	19347.0265 ± 0.0008	19347.0310	- -

An example of a measured iodine hyperfine spectrum is shown in Fig. 5. The figure demonstrates the transition of R(23) 40-0, corresponding to the line 3361 in ref [2]. The measurements have been made in an iodine cell maintained at room temperature. The laser frequency is slowly swept over the transition by scanning the seed laser PZT voltage. During

the measurement, the sweep time is 50 s and the time constant of the lock-in amplifier is 100 ms. The frequency scale is given by estimating the Doppler absorption linewidth of the iodine spectroscopy. The odd vibration quantum number of J"=23 results in 21 hyperfine components, as show in Fig. 5. The observed linewidth of the hyperfine components is 2.6 ± 0.3 MHz, which is consistent with the expect value due to pressure and power broadening [7, 18] for our experimental parameters.

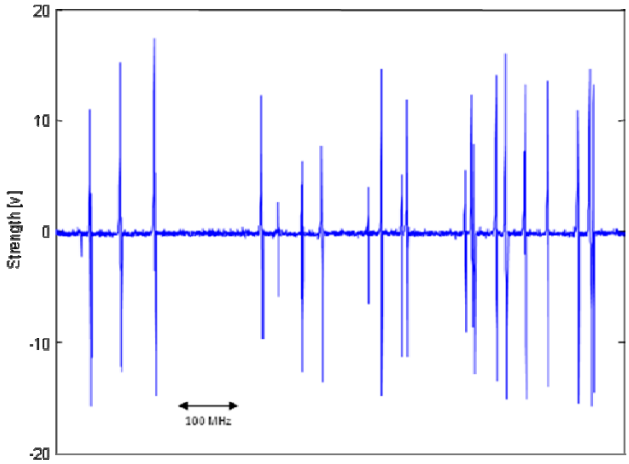

Fig. 5. Hyperfine structure of Iodine line R(23)(40-0) at 518.5 nm. The frequency sweep time is 50 s, and the time constant of Lock-In amplifier is 100 ms.

3. Conclusion & Discussion

In conclusion, we have performed the first time precise measurement of the iodine absorption spectroscopy around 516.9, 517.4 and 518.5 nm, using our previous measurements on the isotope shift and hyperfine spectra of the Mg I (3S3P) ^{3}P - (3S4S) ^{3}S transitions as frequency references. Experimental values reported here are consistent with calculations and reference data. In addition, we have demonstrated the Doppler-free Iodine hyperfine spectrum, which can be used to improve the laser frequency stability to the sub-kHz level. The constructed iodine spectrometer and metastable MgI spectrometer, with optical frequency comb generator, allows us for absolute frequency calibration at 10^{-9} level or even better.

Acknowledgement

We would like to acknowledge financial support from Lundbeckfonden and Carlsbergfondet. The authors also gratefully acknowledge Kjeld Jensen for technical assistance.

† Present address, Center for Cold Atom Physics, State Key Laboratory of Magnetic Resonance and Atomic and Molecular Physics, Wuhan Institute of Physics and Mathematics, Chinese Academy of Science, Wuhan 430071, China.

Experimental determination of the ^{24}Mg I $(3s3p)^3P_2$ lifetime

B. Bak Jensen, He Ming, K. Gunnarsson, M. H. Madsen, A. Brusch, J. Hald, J. Ye, and J. W. Thomsen*
The Niels Bohr Institute, Universitetsparken 5, 2100 Copenhagen, Denmark
(Dated: September 10, 2009)

We present the first measurement of the electric-dipole forbidden $(3s3p)^3P_2 \rightarrow (3s^2)^1S_0$ (M2) transition rate in ^{24}Mg and compare to state of the art theoretical predictions. Our measurement exploits a magnetic trap isolating the sample from perturbations and a magneto-optical trap as an amplifier converting each $^3P_2 \rightarrow {}^1S_0$ decay event into millions of photons readily detected. The transition rate is determined to $5.224{\cdot}10^{-4}$ s^{-1} corresponding to a $^3P_2$ lifetime of 1914 $\pm$ 40 seconds. This value is in excellent agreement with recent theoretical predictions.

PACS numbers: Valid PACS appear here

I. INTRODUCTION

Alkaline Earth elements have attracted considerable attention, theoretical as a well as experimental, over the past years. One of the main motivations for studying these atoms is their use for optical atomic clocks and high precision measurements [ref]. Especially the 87 strontium atom has enjoyed success and now forms a basis for neutral atoms clocks that surpass the best ^{133}Cs primary standards [ref]. The high precision achieved rely on long lived metastable states where a doubly forbidden intercombination transition ^{1}S$_0 \rightarrow {}^3$P$_0$ provides a narrow resonance with mHz natural linewidth.

Despite considerable efforts forbidden transitions of alkali Earth atoms remain relatively unknown, in particular for the magnesium system [Derivianko]. Unlike energy separation of atomic levels weak transition rates offers a more challenging test of modern theory, where accurate determination of matrix elements can serve as a benchmark test of atomic structure models. Today's atomic structure calculations based on modern ab initio methods aims at predicting basic properties of low-lying states with a precision below 1% [Sergey]. In this connection reliable values for allowed and in particular weak transitions plays a key role for the further advancement of modern theory.

Effective isolation of a quantum system dramatically increases the ability to make precise measurements on it. Magnetic, optical and magnetic-optical trapping of neutral atoms in ultra high vacuum environments forms an important basis for many of today's precision measurements. These traps provide an effective isolation of perturbing effects and offer reduction of a number of systematic effects. Some of the main advantages include: minimize or entirely eliminate the Doppler effect, localized sample allowing controlled interactions, minimize contact with surroundings which can lead to population depletion and heating.

In a pioneering work the lowest ^{3}P$_2$ life time was measured for ^{88}Sr yielding 520^{+310}_{-140} s about a factor of two below theoretical predictions [ref]. Similar results for other Earth alkali elements are, to our knowledge, not reported in literature. The measurements using ^{88}Sr atoms where complicated by quenching induced by room temperature Black Body Radiation (BBR). Optical pumping at 2 μm connecting the ^{3}P$_2$ state to the ^{3}D$_J$ manifold resulted in an unwanted depletion of trapped atoms and a complex data analysis was required. This temperature dependence is absent in the magnesium system. Here resonance transitions are considerably more energetic rendering the system practically immune to black body effects at room temperature. This is also a key feature behind proposals of magnesium for a future atomic clock since it has one of the lowest BBR contributions among optical atomic clock candidates [ref].

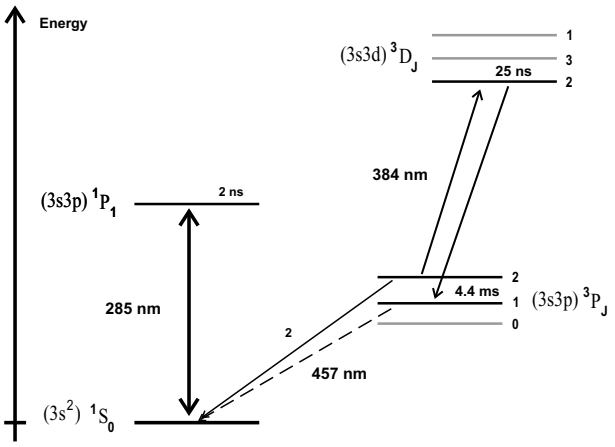

FIG. 1: Energy level diagram for ^{24}Mg. Atoms magnetically trapped in the ^{3}P$_2$ state decay to the ^{1}S$_0$ state by a magnetic quadrupole (M2) transition. Here atoms are recaptured into the MOT (285 nm) and a strong fluorescence level emerges. Atoms may be transferred efficiently to the ^{1}S$_0$ state by optical pumping at 384 nm. Atoms decaying from the ^{3}D$_2$ state have a branching ratio of 3:1 in favor of ^{3}P$_1$ compared to ^{3}P$_2$ as a final state.

A long metastable lifetime may result in sub μHz optical spectroscopy pushing optical clocks to new levels. Recently an EIT optical clock scheme was proposed [Thomas Zanon-Willette] where the ^{3}P$_0$ state is cou-

*Electronic address: jwt@fys.ku.dk

pled to the strong main transition though $^1P_1$. Similar schemes can be envisioned with the $^3P_2$ state. With the $^3P_2$ state as an effective ground state it has been speculated if evaporative cooling could be carried out aiming at BEC in these systems. For Ca and Sr this seems not to be possible due to destructive collisions resulting in an unfavorable ratio between elastic and inelastic collision rates thus preventing evaporative cooling [Hemmerich, Killian]. In the case of magnesium calculations predicts the same outcome but, to our knowledge, no experiments have been performed yet.

The very long life time of the $^3P_2$ state is a result of quantum mechanical selection rules, which excludes direct single photon decay to first order by dipole transitions (E1) and to second order by magnetic dipole transitions (M1) or electric quadrupole transitions (E2). By a third order process single photon decay to the ground state is allowed via a magnetic quadrupole (M2) transition. Decay probabilities for (M1,E2) transitions to $^3P_1$ and $^3P_0$ are slower by many orders of magnitude [Derivianko, Green].

The principle of our measurement relies on counting the amount of atoms decayed after a time interval t relative to the remaining $^3P_2$ atoms. This ratio is independent of initial population in the magnetic trap and yield the transition rate directly. Depending on the initial observation time t small corrections must be included. A sample of $^3P_2$ atoms will shrink as a result of two effects, firstly, the decay to the ground state $^1S_0$ with a rate Γ_2, secondly, atoms will be ejected out of the magnetic trap as a result of collisions with the background gas by a rate α_2. Assuming no collisional losses between atoms in the traps we find the rate equations for $^3P_2$ atoms N_2 and $^1S_0$ atoms N_0:

$$\frac{dN_2}{dt} = -(\alpha_2 + \Gamma_2)N_2 \quad (1)$$

$$\frac{dN_0}{dt} = -\alpha_0 N_0 + \Gamma_2 N_2, \quad (2)$$

where N_2 is the $^3P_2$ population and N_0 the MOT population. Notice the magnetic trap lifetime $1/\alpha_2 = 20$ seconds is different from the MOT lifetime $1/\alpha_0 = 3$ seconds [DNM]. Here we assume the MOT is started initially with no atoms.

The MOT fluorescence signal a time t, $t \ll 1/\alpha_2$ is then given by $S_1 = \eta\Gamma_2 N_2^0 t$ while the remaining atoms transferred to the MOT would give the signal $S_2 = \eta(1-\alpha_2 t)N_2^0 \cong \eta N_2^0$. Here η represents the fluorescence detector efficiency and N_2^0 the initial $^3P_2$ sample size. Consequently, the ratio of the signals S_1 and S_2 would yield the decay rate Γ_2 independent of N_2^0. This ratio can be measured with high precision but small corrections must be applied to account for the decay of the MOT and the magnetic trap sample during measurements.

The solution to Eqn. (2) is given by:

$$N_0(t) = \frac{N_2^0 \cdot \Gamma_2}{\alpha_2 + \Gamma_2 - \alpha_0}(e^{-\alpha_0 t} - e^{-(\alpha_2+\Gamma_2)t}). \quad (3)$$

Figure 2 shows experimental results for the decay of $^3P_2$ atoms to $^1S_0$ recorded over a 60 seconds period. The signal measured is the MOT fluorescence proportional to $N_0(t)$. At short time scales the signal is dominated by $^3P_2$ decay rate. For longer times scales the finite lifetime of the MOT and magnetic trap dominates. This excludes extracting the rate Γ_2 directly from this data by fitting Eqn. (3).

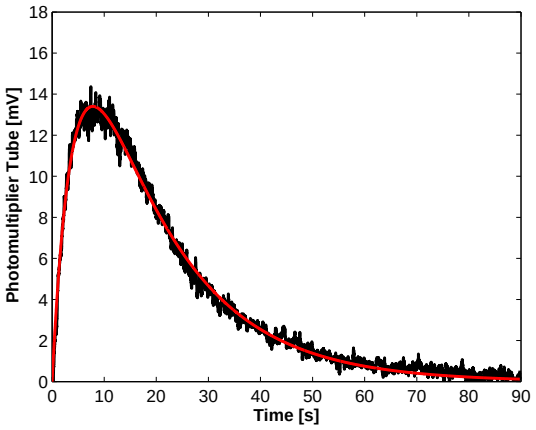

FIG. 2: (color online)Experimental data for $^3P_2$ decay back to the $^1S_0$ ground state. Here atoms are recaptured in the MOT and a strong fluorescence level emerges. The red curve is a fit of Eqn. 3 to the data. The first 1-2 seconds is dominated by spontaneous decay from $^3P_2$ state. Later time scales are controlled by the finite lifetime of the MOT ($\sim$ 3 s) and magnetic trap ($\sim$ 20 s).

We operate a MOT of approximately $4{\cdot}10^7$ ^{24}Mg atoms at temperatures of around 3 mK. By optical pumping on the (3s3p) $^1P_1$ - (3s3d) $^1D_2$ transition we prepare a sample of 10^6 $^3P_2$ atoms magnetically trapped in the MOT quadrupole field. From the (3s3d) $^1D_2$ state atoms may decay to (3s3p) $^3P_2$ at a rate of 50 s^{-1} [Therkildsen]. The magnetically trapped sample has a lifetime close to 20 seconds.

The experimental cycle begins by loading the magnetic trap for 5 seconds. We switch of the MOT for 100 ms sufficient to empty it and turned it back on again. During the next second we monitor the decay of the $^3P_2$ atoms back into the $^1S_0$ state though the MOT fluorescence. In this period about 500 atoms are reloaded into the MOT. Using optical pumping via the $^3D_2$ state we transfer all the remaining $^3P_2$ atoms back to the $^1S_0$ ground state. Resonant 384 nm light couples the $^3P_2$ state with the $^3D_2$ state. Since the involved branching ratio is 3:1, see figure 1, it takes only two 384 nm photons on average to transfer atoms back to the $^3P_1$ state where they decay

back to the $^1S_0$ in about 4 ms [Per]. Finally we measure the eventual load from back ground gas during one second starting with an empty magnetic trap and MOT. This allows us to correct for eventual residual atoms recaptured during the one second load time initiating our measurement sequence. We have carried out more than 90 measurements.

Fig. 3 shows a typical data recording of the MOT fluorescence induced by spontaneous decay to $^1S_0$ state (A), after optical pumping back to $^1S_0$ (B) and finally background load measurement (C). The curve in (A) and (C) has been multiplied by a factor of 100 to fit all three signals on the same scale. Decay of the MOT and magnetic trap during data taking can be corrected with Eqn. (3) and the solution to Eqn. (1). This yield a more pure ratio and value for the rate coefficient. However, the correction is only a 1 - 2 % scale, see table 1.

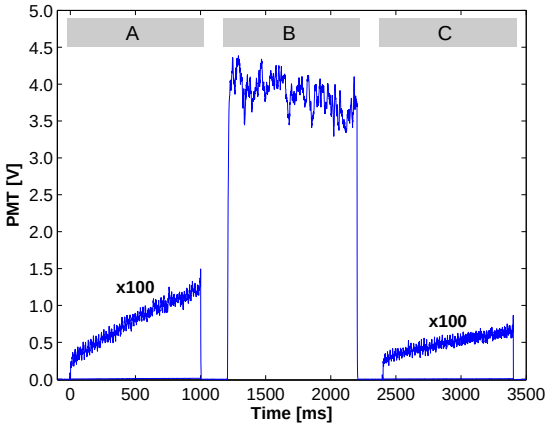

FIG. 3: (color online)Raw fluorescence signal of $^3P_2$ atoms after decay (A) or optical transfer (B) to $^1S_0$ ground state. The decay (A) and background signal (C) are multiplied with a factor of 100 to fit all three curved on the same plot. In order to extract the true signal ratio at time $t = 1$ s we correct for finite lifetime of the MOT and magnetic trap. Especially the MOT lifetime is visible in (B) where the population is decaying over one second. From the measured signal we can extrapolate signals backwards in time to $t = 1$ s for a more accurate ratio.

In principle the lifetime is given by the ratio of the back ground corrected load signal to the signal of back transferred population. This technique has been used in other experiments to determine the lifetime [Katori]. However, given the complicated dynamics of a MOT and different behavior of the various magnetic substates $^3P_1$ ($m = 0, \pm 1$) in the MOT quadrupole field, we find it necessary to measure directly the recapture fraction not assuming it to be unity. In a steady state situation where the MOT is running with the optical pumping populating the $^3P_2$ state we switch the 384 nm laser on and off on a two second time scale. This leads to a decay of the MOT signal when the 384 nm laser is switched off, since atoms are captured in the $^3P_2$ state and a load when the 384 nm laser is turned back on, since $^3P_2$ atoms are transferred back to $^3P_1$ and a fraction is recaptured in the MOT. The ratio of the load to the decay constant yields exactly the recapture fraction in our experiments. We find this factor to be 1.5 ± 0.1. Insufficient knowledge of this recapture fraction will lead to a non neglect able systematic effect.

In figure 4 we have compiled our measurements corrected with the factor of 1.5. We obtain 1914 ± 40 second for the lifetime, the error quoted being only the statistical uncertainty. In addition to the statistical uncertainty in the data we have listed a number of errors in table 1.

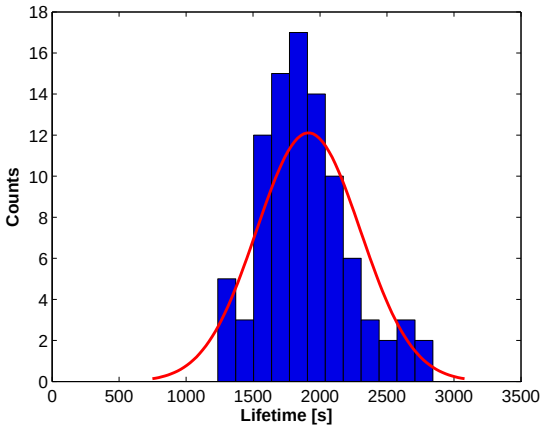

FIG. 4: (color online)Compilation of 93 measurements of the $^3P_2$ lifetime. The red curve is a gaussian fit to the data.

Re-pumping efficiency was tested by repeatedly applying a sequence of pulses of a given time length to one $^3P_2$ sample. The amount of atoms transferred to the MOT by second and third pulse was found to be below 0.5%. The typical re-pumping time was measured to be less than 100 μs but typically pulses are applied from 50-100 ms. In figure 5 we show the life time measurement as a function of re-pumper detuning. We observe no significant effect of re-pumper detuning on the value of the lifetime.

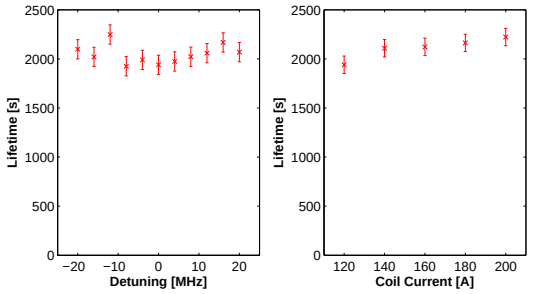

FIG. 5: Lifetime ratio as a function of re-pumper detuning.

Quadrupole-quadrupole long-range interactions may play a role in the presence of a magnetic field as has been

TABLE I: Error budget for the $^3P_2$ life time measurement.

Source	Uncertainty [%]
Recapture fraction	5
Photomultiplier linearity	<1
MOT fluctuations	2
Magnetic trap lifetime	2
MOT lifetime	1.5
Total	6.0

demonstrated for the Ca and the Sr systems [Hemmerich, Kilian]. Keeping the number of $^3P_2$ atoms constant and changing the magnetic field gradient enables us to change the volume by a factor 8 and thus the intra MOT collision rate by a factor of 64. Figure 5 shows data as a function of magnetic field in the MOT coils. We observe no effects related to the magnetic field which could be expected for these low atom numbers [Greene].

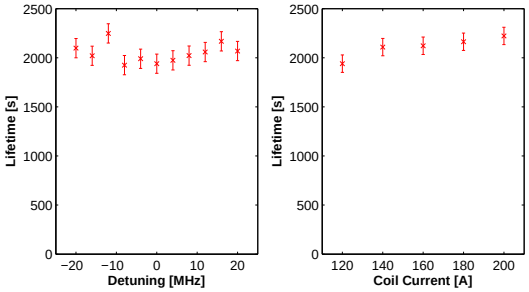

FIG. 6: Lifetime measurements as a function of the magnetic field. The magnetic field gradient measured in gauss/cm is 1.1 times the ampere-scale.

In addition to the statistical uncertainty in the data (1.3%), we include a number of independent contributions to the error budget shown in Table I.

Acknowledgments

We wish to acknowledge the financial support from the Lundbeck Foundation and the Carlsberg Foundation.

[1] T. P. Heavner, S. R. Jefferts, E. A. Donley, J. H. Shirley, T. E. Parker, Metrologia **42**, 411 (2005).
S. Bize et al., J. Phys. B **38**, S449 (2005)
L. Hollberg et al., J. Phys. B **38**, S469 (2005)
M. M. Boyd et al., Science **314**, 1430 (2006)
W. H. Oskay et al., Phys. Rev. Lett. **97**, 020801 (2006)

[2] Mette Machholm, Paul S. Julienne and Kalle-Antti Suominen. Phys. Rev A. **59**, R4113 (1999)

[3] Porsev,S. G. and Kozlov,M. G. and Rakhlina,Y. G. and Derevianko,A. Physical Review A **64**, 012508 (2001)

[4] Wictor C. Magno, Reinaldo L. Cavasso Filho, and Flavio C. Cruz. Phys. Rev. A **67**, 043407 (2003)

[5] Josh W. Dunn, J. W. Thomsen, Chris H. Greene, and Flavio C. Cruz. Phys. Rev. A **76**, 011401(R) (2007)

[6] Giovanna Morigi and Ennio Arimondo. Phys. Rev. A **75**, 051404(R) (2007)

[7] N. Malossi, S. Damkjær, P. L. Hansen, L. B. Jacobsen, L. Kindt, S. Sauge, J. W. Thomsen, F. C. Cruz, M. Allegrini, and E. Arimondo. Phys. Rev. A **72**, 051403 (2005)

[8] T. E. Mehlstäubler, K. Moldenhauer, M. Riedmann, N. Rehbein, J. Friebe, E. M. Rasel, and W. Ertmer. Phys. Rev. A **77**, 021402(R) (2008)

[9] Madsen D. N. and Thomsen J. W. J. Phys. B **33**, 4981 (2000)

[10] T. K. Fang, T. N. Chang Physical Review A **61**, 052716 (2000)

[11] Sergey G. Porsev and Andrei Derevianko. Phys. Rev. A **69**, 042506 (2004)

[12] Loo F. Y., Brusch A., Sauge S., Allegrini M., Arimondo E., Andersen N., Thomsen J. W. J. Opt. B: Quantum Semiclass. Opt. **6**, 81 (2004)

Bibliography

[1] M. G. Mayer, Physical Review **78**, 16 (1950).

[2] H. Katori, M. Takamoto, V. G. Palchicov, and V. D. Ovsiannikov. Physical Review Letters, **91**, 173005 (2003).

[3] F. Sorrentino, G. Ferrari, N. Poli, R. Drullinger and G. M. Tino. Mod. Phys. Lett. B 20, 1287 (2006).

[4] A. D. Ludlow, T. Zelevinsky, G. K. Campbell, S. Blatt, M. M. Boyd, M. H. G. de Miranda, M. J. Martin, J. W. Thomsen, S. M. Foreman, Jun Ye, T. M. Fortier, J. E. Stalnaker, S. A. Diddams, Y. Le Coq, Z. W. Barber, N. Poli, N. D. Lemke, K. M. Beck, and C. W. Oates. Science, **319**, 1805 (2008).

[5] A. D. Ludlow, M. M. Boyd, T. Zelevinsky, S. M. Foreman, S. Blatt, M. Notcutt, T. Ido, and J. Ye. Phys. Rev. Lett., **96**, 033003 (2006).

[6] R. Le Targat, X. Baillard, M. Fouch, A. Brusch, O. Tcherbakoff, G. D. Rovera, and Pierre Lemonde. Phys. Rev. Lett., **97**, 130801 (2006).

[7] Z. W. Barber, C. W. Hoyt, C. W. Oates, L. Hollberg, A. V. Taichenachev, and V. I. Yudin. Phys. Rev. Lett., **96**, 083002 (2006).

[8] X. Baillard, M. Fouch, R. Le Targat, P. G. Westergaard, A. Lecallier, Y. Le Coq, G. D. Rovera, S. Bize, and Pierre Lemonde. Optics Letters, **32**, 1812 (2007).

[9] J. R. Guest, N. D. Scielzo, I. Ahmad, K. Bailey, J. P. Greene, R. J. Holt, Z.-T. Lu, T. P. OConnor, and D. H. Potterveld. Physical Review Letters, **98**, 093001 (2007).

[10] J. R. de Laeter, J. K. Böhlke, P. De Bivre, H. Hidaka, H. S. Peiser, K. J. R. Rosman and P. D. P. Taylor, Pure Appl. Chem., Vol. **75**, 683 (2003).

[11] T. W. Hänsch and A. L. Schawlow, Optics Communications, **13**, 68 (1975).

[12] R. Santra, K. V. Christ, and Ch. H. Greene: Properties of meta- stable alkaline-earth-metal atoms calcuaed using an accurate effective core potential. Phys. Rev. A **69**, 042510 (2004).

[13] H. Marion, F. Pereira Dos Santos, M. Abgrall, S. Zhang, Y. Sortais, S. Bize, I. Maksimovic, D. Calonico, J. Grünert, C. Mandache, P. Lemonde, G. Santarelli, Ph. Laurent, A. Clairon, and C. Salomon. Search for variations of fundamental constants using atomic fountain clocks. Phys. Rev. Lett., **90**, 15080114 (2003).

[14] H. Katori, M. Takamoto, V. G. Palchikov, and V. D. Ovsiannikov, Ultrastable Optical Clock with Neutral Atoms in an Engineered Light Shift Trap, Phys. Rev. Lett. **91**, 173005 (2003).

[15] Martin M. Boyd, Tanya Zelevinsky, Andrew D. Ludlow, Sebastian Blatt, Thomas Zanon-Willette, Seth M. Foreman, and Jun Ye Phys. Rev. A **76**, 022510 (2007)

[16] E. L. Raab, M. Prentiss, Alex Cable, Steven Chu, and D. E. Pritchard. Phys. Rev. Lett., **59**, 2631 (1987).

[17] R. Blatt, W. Ertmer, and J.L. Hall. Prog. Quant. Electr., **8**, 237 (1984).

[18] M. Kasevich, E. Riss, S. Chu, and R. De Voe. Physical Review Letters, **63**, 612 (1989).

[19] K. Gibble and S. Chu. Metrologia, **29**, 201 (1992).

[20] A. Clairon, C. Salomon, S. Guellati, and W. Phillips. Europhys. Letters, **16**, 164 (1991).

[21] C. Cohen-Tannoudji. Proceedings of the International School of Physics Enrico Fermi -Laser Cooling of Atoms an Ions. Elsevier Science Publishers B.V, 1991.

[22] W. D. Philips. Proceedings of the International School of Physics Enrico Fermi -Laser Cooling of Atoms an Ions. Elsevier Science Publishers B.V, 1991.

[23] Harold J. Metcalf and Peter van der Straten. Laser Cooling and trapping. Springer, second edition, 2001.

[24] Hidetoshi Katori, Tetsuya Ido, Yoshitomo Isoya, and Makoto Kuwata-Gonokami. Physical Review Letters, **82**, 1116 (1999).

[25] Xinye Xu, Thomas H. Loftus, John L. Hall, Alan Gallagher, and Jun Ye. Journal of the Optical Society of America B: Optical Physics, **20**, 968 (2003).

[26] T. Binnewies, G. Wilpers, U. Sterr, F. Riehle, J. Helmcke, T. E. Mehlstaubler, E. M. Rasel, and W. Ertmer. Physical Review Letters, **87**, 123002 (2001).

[27] E. A. Curtis, C. W. Oates, and L. Hollberg. Physical Review A, **64**, 031403 (2001).

[28] P. S. Julienne and F. H. Mies. Collisions of ultracold trapped atoms. J.Opt.Soc.Am. B, **6**, 2257 (1989).

[29] S. G. Porsev and A. Derevianko. Phys. Rev. A, **65**, 020701 (2002).

[30] M.Machholm, P. S. Julienne, and K.-A. Souminen. Physical Review A, **65**, 23401 (2002).

[31] Timothy P. Dinneen, Kurt R. Vogel, Ennio Arimondo, John L. Hall, and Alan Gallagher. Physical Review A, **59**, 1216 (1999).

[32] G. Zinner, T. Binnewies, F. Riehle, and E. Tiemann. Physical Review Letters, **85**, 2292 (2000).

[33] Robin Santra, Kevin V. Christ, and Chris H. Greene. Physical Review A, **69**, 042510 (2004).

[34] S. G. Porsev, M. G. Kozlov, Yu. G. Rakhlina, and A. Derevianko. Physical Review A, **64**, 012508 (2001).

[35] Th. Udem, R. Holzwarth, and T. W. Hänsch. Nature, **416**, 233 (2002).

[36] Xinye Xu, Thomas H. Loftus, Matthew J. Smith, John L. Hall, Alan Gallagher, and Jun Ye. Physical Review A (Atomic, Molecular, and Optical Physics), **66**, 011401 (2002).

[37] B. H. Brandsen and C. J. Joachain, Physics of Atoms and Molecules, Pear- son Education Limited, second edition ed., 2003.

[38] G. Breit and L. A. Wills, Hyperfine structure in intermediate coupling, Physical Review **44**, 0470 (1933).

[39] S. G. Porsev and A. Derevianko, Physical Review A **74**, 020502 (2006).

[40] Steven Chu, L Hollberg, J. E. Bjorkholm, Alex Cable, and A. Ashkin. Physical Review Letters, **55**, 48 (1985).

[41] P. D. Lett, W. D. Phillips, S. L. Rolston, C. E. Tanner, R. N.Watts, and C. I.Westbrook. Optical molasses. J. Opt. Soc. Am. B, **6**, 2084, (1989).

[42] S. Gerstenkorn and P. Luc. Atlas du Spectre dAbsorption de la Molcule dIode, 14800 - 20000 cm-1. Laboratoire Aim Cotton, CNRS II, Orsay, 1978.

[43] Wolfgang Demtröder. Laser Spectroscopy. Springer-Verlag GmbH, second edition, 1995.

[44] Dorthe Nørgård Madsen. Experimental Studies of Cold Magnesium Atoms. PhD thesis, Niels Bohr Institute, (2001).

[45] T. W. Hänsch. Laser frequency stabilization by polarization spectroscopy of a reflecting reference cavity. *Optics Communications*, **35** (1980).

[46] Valentina Ruseva. Design of high-power frequency-doubled diode laser systems for experiments on laser cooled Magnesium. PhD thesis, Niels Bohr Institute, 2005.

[47] R. W. P. Drever, J. L. Hall, F. V. Kowalski, J. Hough, G. M. Ford, A. J. Munley, and H. Ward. Laser phase and frequency stabilization using an optical resonator. Appl. Phys. B, **31**, 97 (1983).

[48] Frequency Standards - Basics and Applications, F. Riehle, Wiley (2004)

[49] H. M. Pask, R. J. Carman, D. C. Hanna, A. C. Tropper, C. J. Mackechinie, P. R. Barber, and J. M. Dawes, Ytterbium-doped silica fiber lasers: Versatile sources for the 1-1.2m region, IEEE Journal of Selected Topics in Quantum Electronics, 2-12 (1995)

[50] M. Dekker, Rare-Earth-Doped Fiber Lasers and Amplifier (M. J. F. Digonnet, Editor), New York, 2nd Edition (2001)

[51] P. A. Franken, A. E. Hill, C. W. Peters and G. Weinreich. Phys. Rev. Lett., **7**, 118 (1961).

[52] K. Schneider, S. Schiller, J. Mlynek, M. Bode and I. Freitag. Opt. Lett., **21**, 1999 (1996).

[53] Yariv. Optical Electronics, Saunders, Philadelphia, 1991.

[54] U. Brinkmann, J. Goschler, A. Steudel and H. Walther, Z. Phys. A, **228**, 427 (1969)

[55] U. Brinkmann, J. Kluge, and K. Pippert, J. Appl. Phys. **51**, 4612 (1980)

[56] S. Garpman, G. Lidö, S. Rydberg and S. Svanberg, Z. Phys. A, **241**, 217 (1971)

[57] S. Ishii and W. Ohlendorf, Rev. Sci. Instrum. **43**, 1632 (1972)

[58] P. E. Jessop and F. M. Pipkin, Phys. Rev. A **20**, 269 (1979)

[59] G. Brink, A. glassman and R.gupta, Opt. Commun. **33**, 17 (1980)

[60] L. Pasternack and P.J. Dagdigian, Rev. Sci. Instrum. **48**, 226 (1977)

[61] G. Giusfredi, P. Minguzzi, F. Strumia and M. Tonelli, Z. Phys. A, **274**, 279 (1975)

[62] G. Giusfredi, A. Gondone, E. Bava and C. Novero, J. Appl. Phys. **63**, 1279 (1987)

[63] Atomic and Molecular Beam Methods, volume 1, edited by G. Scoles, Oxford University Press, (1988).

[64] A. Lurio, Hyperfine Structure of the ^3P States of Zn^{67} and Mg^{25}, *Phys. Rev.* **126**, 1768 (1962)

[65] M. F. Crawford, F. M. Kelly, A. L. Schawlow, W. M. Gray, *Phys. Rev.* **76**, 1527 (1949)

[66] L. Hallstadius and J. E. Hansen, Experimental Determination of Isotope Shifts in Mg I, *Z. Phys. A* **285**, 365 (1978)

[67] C. Novero and A. Godone, *Z. Phys. D* **17**, 33 (1990)

[68] Nicola Malossi. Studies of cold magnesium atoms in a magneto-optical trap: towards a novel optical frequency standard. PhD thesis, Niels Bohr Institute, 2008.

[69] Alessandro Cosci. Raffreddamento e confinamento di atomi di magnesio in trappola magneto-ottica. Masters thesis, Universita degli Studi di Firenze, Facolta di Scienze Matematiche Fisiche e Naturali, (2006).

[70] F. Y. Loo, A .Brusch, S. Sauge, M. Allegrini, E. Arimondo, N. Andersen, and J.W. Thomsen. Investigations of a two-level atom in a magneto-optical trap using magnesium. Journal of Optics B: Quantum and Semi-classical Optics, **6**, 81 (2004).

[71] M. Inguscio, S. Stringari, and C. E. Wieman, editors. Making, Probing and Understanding Bose-Einstein Condensates (1999). Proceedings of the International School of Physics Enrico Fermi, Course CXL.

[72] L. You and M. Holland. Ballistic Expansion of Trapped Thermal Atoms. Phys. Rev. A **53**, R1 (1996).

[73] D.N. Madsen and J.W. Thomsen. Measurment of absolute photoionization cross sections using magnesium magneto-optical traps. J. Phys. B., **35**, 2173 (2002).

[74] Per Lunnemann Hansen. Experimental determination of metastable $^3P_1$. Master thesis, Niels Bohr Institute, 2006.

[75] Robin Santra and Kevin V. Christ and Chris H. Greene. Physical Review A **69** 042510 (2004)

[76] I. M. Savukov and W. R. Johnson. Physical Review A **65** 042503 (2002)

[77] S. G. Porsev, M. G. Kozlov, Y. G. Rakhlina and A. Derevianko. Many-body calculations of electric-dipole amplitudes for transitions between low-lying levels of Mg, Ca, and Sr. Physical Review A, 64, 012508 2001

[78] C. Laughlin and G. A. Victor. The Astrophysical Journal **234** 407 (1979)

[79] A. Godone and C. Novero. Physical Review A **45** 1717 (1992)

[80] H. S. Kwong and Peter L. Smith and W. H. Parkinson. Physical Review A. **25** 2629 (1982)

[81] Remeasurement of the Mg $^3P_1$-state lifetime P. S. Furcinitti, J. J. Wright, and L. C. Balling. Phys. Rev. A **12**, 1123 (1975)

[82] C. J. Mitchell. J. Phys. B **8** 25 (1975)

[83] N. Malossi, S. Damkjær, P. L. Hansen, L. B. Jacobsen, L. Kindt, S. Sauge, J. W. Thomsen, F. C. Cruz, M. Allegrini, and E. Arimondo, Phys. Rev. A **72**, 051403 (2005)

[84] O. Scully and S. Zubairy, Quantum Optics, Cambridge University Press, 1997.

[85] M. Yasuda and H. Katori, Phys. Rev. Lett. **92**, 153004 (2004).

[86] J . V. Prodan and W. D. Philipps. Prog. Quant. Elect., **8**, 231 (1984).

[87] Kasper T. Therkildsen. Investigation of metastable Magnesium Atoms. PhD thesis, Niels Bohr Institute, (2009).

[88] J. V. Prodan, W. D. Phillips, and H. Metcalf. Physical Review Letters, **49**, 1149 1982.

[89] Anders Brusch. Horloge a reseau optique a atomes de strontium, et etude des effets dhyperpolarisabilite dus au pieges laser. These de doctorat de l'universite paris IV.